Niklas Säfström

Modeling and simulation of rigid body and rod dynamics via geometric methods

◉ NTNU
Norwegian University of
Science and Technology

Preface

This thesis is submitted in partial fulfillment of the requirements for the degree of philosophiae doctor (PhD) at the Norwegian University of Sciences and Technology (NTNU) in Trondheim. The research was supported by grant from NTNU and the Faculty of Information Technology, Mathematics and Electrical Engineering (IME).

Acknowledgements

I want to thank the Department of Mathematical Sciences and the Faculty of Information Technology, Mathematics and Electrical Engineering (IMF) for making the work presented in this thesis possible.

I am very grateful to my supervisor Associate Professor Elena Celledoni for her continuous encouragement and guidance throughout my years as a PhD student at NTNU. I am also thankful that I had the opportunity to collaborate with Associate Professor Francesco Fassò, Professor Thor I. Fossen, Doctoral student Gullik Jensen, Doctor Tu Duc Nguyen and Professor Antonella Zanna. Especially Gullik Jensen for his hospitality, letting me occupy a decent part of his office at the Department of Engineering Cybernetics, during our pleasant and interesting collaboration.

I would like to thank all the colleagues and friends at the Department of Mathematical Sciences. Further, I thank Sverre and Øyvind for the lunch breaks and the more or less relevant discussions.

Finally, I thank my family, friends, my wife Åsa and my daughter Hedda for their love and support.

<div align="right">

Niklas Säfström
Trondheim, November 2009

</div>

Structure of the thesis

This thesis consists of an introduction and the following five papers:

- **Paper I:** *Efficient time-symmetric simulation of torqued rigid bodies using Jacobi elliptic functions*, E. Celledoni and N. Säfström.
  Published in Journal of Physics A, Vol. 39, 5463–5478, 2006.

- **Paper II:** *The Exact Computation of the Free Rigid Body Motion and Its Use in Splitting Methods*, E. Celledoni, F. Fassò, N. Säfström and A. Zanna.
  Published in SIAM Journal on Scientific Computing, Vol. 30, No. 4, 2084–2112, 2008.

- **Paper III:** *Modeling and Control of Offshore Pipelay Operations Based on a Finite Strain Pipe Model*, G. A. Jensen, N. Säfström, T. D. Nguyen and T. I. Fossen.
  Published in Proceedings of American Control Conference–ACC2009, 2009.

- **Paper IV:** *A Nonlinear PDE Formulation for Offshore Vessel Pipeline Installation*, G. A. Jensen, N. Säfström, T. I. Fossen and T. D. Nguyen.
  To appear in Journal of Ocean Engineering.

- **Paper V:** *Hamiltonian and multi-symplectic structure of a rod model using quaternions*, E. Celledoni and N. Säfström.
  Preprint Numerics No. 8/2009, Departments of Mathematical Sciences, NTNU, 2009.

All the articles comprise both programming and analysis work. My contribution to these articles has been substantial in both respects.

Contents

Chapter 1

Introduction

The use of Lie groups and differential geometry has in the last few years gained importance in several branches of applied engineering, such as robot technology, structural mechanics and marine control system. Symmetries and geometric features, like for example the symplectic structure of Hamiltonian systems, play a central role in stability analysis and in the understanding of the system's physical characteristics. Yet it is not always easy to determine which of the geometric properties are the most fundamental in the various particular problems at hand. Even simple mechanical systems can exhibit unexpected or chaotic dynamical behavior which is well worth investigating. Sometimes these properties can be revealed by sophisticated analytical methods or clever geometric numerical methods, see e.g. [11, 13, 24].

In structural mechanics and flexible body dynamics, complicated real life structures are often simulated by numerical discretization of the modeled governing continuous equations. The building blocks for numerical discretizations are often proper combinations of simpler mechanical systems, e.g. systems of rigid or elastic bodies linked by reciprocal force influences, and it is desirable that the finite dimensional discretized equations inherit the key geometrical features of their continuous counterparts. Since a physical system is featured and sometimes completely determined by its geometrical properties, also its numerical treatment should be tailored to the problem. This suggests that the modeling, geometrical analysis and numerical approximation of a mechanical problem play interactive roles in the solution process and geometric considerations have therefore been the course of action, both in the modeling and in the numerical techniques, through out this thesis.

Paper I [7] and II [6] in this thesis focus on rigid body dynamics, systems of rigid bodies that are exposed to external forces. An implementation based on the

exact solution of the free rigid body motion is adopted in splitting methods for rigid body dynamics. Besides being an interesting subject in it self, the geometry of rigid body dynamics also constitutes a basic understanding of the elastic model considered in papers III–V.

Paper III [17] and IV [16] addresses applications within offshore engineering, in particular pipelay operations. Pipelines constitute one of the major components within offshore oil and gas industry. As the exploiting in deep water fields becomes more common, the installation of pipelines and flowlines has become some of the most challenging offshore operations handled. In fact, recent trends in deep water installation have developed pipelaying into an engineering discipline of its own accord [18]. As the engineering complexity and costs increase with water depth and pipe diameter, accurate mathematical models and geometrically correct numerical simulations have become more important. The simulations are used to analyze the pipelay operation and identify possible critical strains on the pipe during the installation to maintain the overall safety levels. This has motivated the development of dynamic models and geometrically correct numerical methods to better understand the problem and predict the behavior of the mechanical system. Some already existing commercially developed computer program, such as for example OFFPIPE [23], SIMLA [28] and RIFLEX [10], have become the universal tools for simulating pipelay operations. However, high reliability models and numerical methods, suited for closed loop automatic control assistance in the pipelay, are still an interesting subject of research. Paper III [17] and IV [16] in this thesis address the problem of modeling and simulating the pipelay operation. By adding external forces, such as gravity, buoyancy and hydrostatic damping to a well established nonlinear elastic rod model [25], we obtain a dynamic model for an elastic pipe submerged in water. A mathematical model of a vessel is finally attached to the pipe-model as a boundary condition.

In Paper V [8], we formulate both a symplectic and a multi-symplectic formulation of the elastic rod model used in paper III and IV.

In the following section we will give an introduction of the free rigid body and rotations in space. This is not only of interests for the papers on rigid body dynamics, but also for the understanding the kinematics of the elastic rod model used for the pipelay simulations. We will also give an introduction to some geometrical and structural numerical methods that will be used in the papers.

1.1 $SO(3)$ and the rigid body dynamics

One of the most fundamental mechanical problems is the motion of the rigid body, whose configuration space is the Lie group of rotations in space, $SO(3)$. The rich geometry of rigid body dynamics often appears in a more general form in solid mechanics and plays a important role for more advanced theories for

modeling rods, beams and shells [25, 26].

For a comprehensive description of rigid body motions see e.g. [2, 22]. A rigid body is defined by a set of points in space $\mathcal{B} \subset \mathbb{R}^3$, such that the distance between two arbitrary points of the body remains constant as the body moves. The motion of a free rigid body, without any influence of gravity or external forces, can be described by linear translations and rotations about the center of mass. However, for simplicity it is usual to neglect the translational motions and consider only body rotations about a fixed point in space.

Let $\{E_1, E_2, E_3\}$ be an orthonormal basis attached to the rotating body, referred as the *body frame*, with its origin placed at the center of mass. Further, let $\{e_1, e_2, e_3\}$ be an orthonormal *spatial basis* fixed in space, having its origin at the body center of mass. Thus, any point given in body coordinates $X \in \mathcal{B}$ (uppercase letters), in the body fixed basis E_i, can be transformed to its spatial coordinates x (lowercase letters) in the basis $\{e_i\}_{i=1,\ldots,3}$ by a 3×3 rotation matrix $\Lambda \in SO(3)$,

$$SO(3) := \{\Lambda \in 3 \times 3 \text{ real matrix} \,|\, \Lambda\Lambda^T = I_{3\times3}, \ \det \Lambda = 1\},$$

where $I_{3\times3}$ is the 3×3 identity matrix and Λ^T is the transpose of Λ. The motion of a point $X \in \mathcal{B}$ in the spatial coordinates is therefore described by $x(t) = \Lambda(t)X$, where t is the time. Differentiating x with respect to t gives the velocity of the point in spatial coordinates, $\dot{x} = \dot{\Lambda}X = \dot{\Lambda}\Lambda^T x$, and from the identity $\Lambda\Lambda^T = I_{3\times3}$,

$$\frac{d}{dt}\Lambda\Lambda^T = \dot{\Lambda}\Lambda^T + \Lambda\dot{\Lambda}^T = \dot{\Lambda}\Lambda^T + (\dot{\Lambda}\Lambda^T)^T = 0,$$

it follows that $\dot{\Lambda}\Lambda^T$ must be a skew-symmetric matrix

$$\widehat{w} := \begin{pmatrix} 0 & -w_3 & w_2 \\ w_3 & 0 & -w_1 \\ -w_2 & w_1 & 0 \end{pmatrix} = \dot{\Lambda}\Lambda^T, \quad w = (w_1, w_2, w_3)^T \in \mathbb{R}^3,$$

where w is called the *spatial angular velocity* (aligned with the axis of rotation, see figure 1.1). It is readily seen that the matrix-vector multiplication $\widehat{w}x$ can be interpreted as the vector product of w and x, i.e. $\dot{x} = \widehat{w}x = w \times x$. The velocity can also be expressed in body basis $\Lambda^T \dot{x} = \Lambda^T \dot{\Lambda}X$, the *convective velocity*, and we define the skew symmetric matrix

$$\widehat{W} := \Lambda^T \dot{\Lambda}, \quad W \in \mathbb{R}^3,$$

where W is the *body angular velocity* and it follows

$$\dot{\Lambda} = \widehat{w}\Lambda = \Lambda\widehat{W}. \tag{1.1}$$
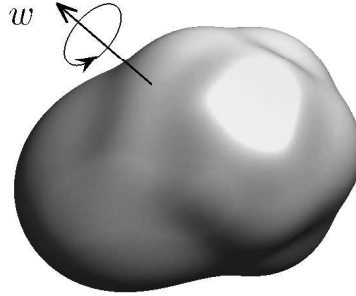
Figure 1.1: Geometrical interpretation of the angular velocity w in space coordinates

By the definition of kinetic energy in classical mechanics one finds the kinetic energy for the rotating rigid body

$$T = \frac{1}{2} \int_{\mathcal{B}} \rho(X) \|\dot{\Lambda} X\|^2 \, d^3 X = \frac{1}{2} \int_{\mathcal{B}} \rho(X) \|\widehat{W} X\|^2 \, d^3 X = \frac{1}{2} \langle W, JW \rangle,$$

where ρ is the density, $\langle \, \cdot \, , \, \cdot \, \rangle$ denotes the Euclidean inner product and J is a symmetric positive definite matrix. The inertia matrix J can be made diagonal, $J = \mathrm{diag}(J_1, J_2, J_3)$ by an appropriate choice of body basis E_i. In that case J_i, $i = 1, \ldots, 3$, are referred to as the *principal moments of inertia*.

From the Lagrangian L, defined by $L = T - U = (1/2)\langle JW, W \rangle$, one obtains the equations of motion via the reduced variational principle,

$$\delta \int_{t_0}^{t_1} L \, dt = \delta \int_{t_0}^{t_1} \frac{1}{2} \langle JW, W \rangle \, dt = 0. \tag{1.2}$$

However, the variations has to be done with care using consistent variations such that $\delta W = \dot{\Sigma} + W \times \Sigma$, for arbitrary $\Sigma(t) \in \mathbb{R}^3$ satisfying the boundary conditions $\Sigma|_{t_0} = \Sigma|_{t_1} = 0$, see e.g. [22]. The variational problem (1.2) yields the *Euler equations*, $J\dot{W} = (JW) \times W$, and together with the rotational kinematics (1.1) one obtains the equations of motions for a free rigid body

$$J\dot{W} = (JW) \times W, \tag{1.3}$$

$$\dot{\Lambda} = \Lambda \widehat{W}. \tag{1.4}$$

The Euler equations (1.3) can also be obtained from the Noether's theorem [2, 24, 13]. By Noether's theorem one can prove that the components of the
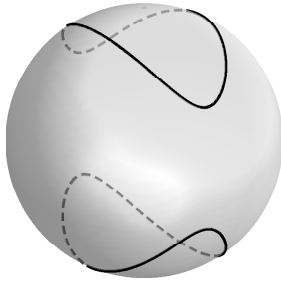
Figure 1.2: The solution on the momentum sphere

spatial angular momentum m,

$$m := \Lambda M = \Lambda JW, \quad M := JW,$$

are preserved quantities, i.e. $m = \text{constant}$. This implies

$$\frac{d}{dt}m = \frac{d}{dt}(\Lambda M) = \Lambda \widehat{W} M + \Lambda \frac{d}{dt} M = 0,$$

or

$$\frac{d}{dt}M = M \times W = M \times (J^{-1}M), \tag{1.5}$$

equivalent to (1.3).

From the two preserved quantities (*invariants*): the total angular momentum, $C := \|M\|^2/2$, and the total energy, $E := M^T(J^{-1}M)/2$, one observes that the solution of the Euler equations must lay on the intersection of the two level surfaces of momentum C (sphere) and energy E (ellipsoid), see figure 1.2. Using the two invariants one obtains the well known solution of the Euler equations, that dates back to Legendre and Jacobi [15], given in terms of *Jacobi elliptic functions*.

The geometry of rigid bodies also appear in the elastic rod model described in [25], whose configuration space is

$$\mathcal{C} = \{(\varphi, \Lambda) \,|\, S \in [0, L] \to \mathbb{R}^3 \times \mathrm{SO}(3) \,|\, \langle \varphi'(S), \Lambda e_3 \rangle > 0\}.$$

The kinematics for the rigid rotations of the undeformed cross sections along the line of centroids φ is given by

$$\partial_S \Lambda(S, t) = \widehat{\omega}\Lambda = \Lambda\widehat{\Omega}, \quad \partial_t \Lambda(S, t) = \widehat{\mathrm{w}}\Lambda = \Lambda\widehat{W},$$

where w is the angular velocity and ω is the bending and torsional strain in spatial basis (lowercase letters), respectively, and W, Ω their analogues in material basis. The governing equations (excluding external forces) in spatial basis are

$$\rho_A \partial_t^2 \varphi = \partial_S n \tag{1.6}$$

$$I_\rho \partial_t w + w \times (I_\rho w) = \partial_S m + (\partial_S \varphi) \times n, \tag{1.7}$$

where n, m are internal stress forces and stress couple (in spatial basis), respectively, and

$$\rho_A := \int_{\mathcal{A}} \rho_0 \, dA, \quad I_\rho := \Lambda J_\rho \Lambda^T, \quad J_\rho = \mathrm{diag}(J_1, J_2, J_3).$$

Defining the momentum densities $P := \rho_A \Lambda^T (\partial_t \varphi)$, $\Pi := J_\rho W$ we obtain the reduced equations in material coordinates [27]

$$\partial_t P + (J_\rho^{-1} \Pi) \times P = \partial_S N + (C_2^{-1} M) \times N, \tag{1.8}$$

$$\partial_t \Pi + (J_\rho^{-1} \Pi) \times \Pi = \partial_S M + (C_2^{-1} M) \times M + (C_1^{-1} N + e_3) \times N. \tag{1.9}$$

From the kinematics of the rotations differentiating in turn with respect to t and S we also obtain

$$C_1^{-1} \partial_t N - \rho_A^{-1} \partial_S P = (C_1^{-1} N + e_3) \times (J_\rho^{-1} \Pi) + (C_2^{-1} M) \times (A_\rho^{-1} P),$$

$$C_2^{-1} \partial_t M - J_\rho^{-1} \partial_s \Pi = (C_2^{-1} M) \times (J_\rho^{-1} \Pi).$$

The latter formulation, equations (1.8)-(1.9), has strong similarities with the Euler equations of rigid body dynamics (1.5).

1.2 Integrators on manifolds

A common geometric property for the physical phenomena we are interested in is that their solutions evolve on a given smooth manifold. For the definition of a manifold see e.g. [19], however in most applications it is sufficient to consider a manifold as the zero-set in $\mathbb{R}^n$ of a smooth map $g : \mathbb{R}^n \to \mathbb{R}^{n-m}$, $m \leq n$, i.e.

$$M = \{y \,|\, g(y) = 0\}, \quad g : \mathbb{R}^n \to \mathbb{R}^{n-m},$$

and M is said to be m-dimensional.

Assume a problem formulated by the differential equation

$$\dot{y} = f(t, y), \quad f(t, y) \in T_y M, \tag{1.10}$$

where $T_y M$ is the tangent space at $y \in M$ such that $y(t)$, for $t \geq t_0$, belongs to the m-dimensional manifold M for $y(t_0) \in M$. In particular we are interested in manifolds acted upon by a Lie group.

Definition 1.2.1. *[24] A Lie group is a smooth manifold G that is also an algebraic group, with a smooth binary group operation $m : G \times G \to G$ and a smooth inversion map $i : G \to G$*

$$m(g, h) = g \cdot h \in G, \quad i(g) = g^{-1} \in G, \quad \forall g, h \in G.$$

If G is a Lie group, its tangent space $T_e G$ at the identity, $e \in G$, is a linear vector space with the same dimension as G. This tangent space obey certain algebraic properties and is called the Lie algebra associated to the Lie group G, denoted $\mathfrak{g} := T_e G$.

Definition 1.2.2. *A Lie algebra $\mathfrak{g}$ is a linear vector space together with a bilinear operation, $[\,\cdot\,,\,\cdot\,] : \mathfrak{g} \times \mathfrak{g} \to \mathfrak{g}$, called the Lie bracket, that is 1) Bilinear, 2) Skew-symmetric and 3) satisfies the Jacobi identity.*

The theory of Lie groups and Lie algebras is found in e.g. [3, 9, 12].

Definition 1.2.3. *[24] Let M be a smooth manifold, G a Lie group with the identity e and U be a subset of $G \times M$ containing e such that $\{e\} \times M \subset U \subset G \times M$. A local group of transformations acting on M is given by a Lie group G and a smooth map (Lie group action) $\Psi : U \to M$ with the following properties:*

1. *$\Psi(e, y) = y, \ y \in M$.*

2. *$(g_1, y), (g_2, y) \in U$, implies*

    $$\Psi(g_1, \Psi(g_2, y)) = \Psi(g_1 \cdot g_2, y),$$

    where $g_1 \cdot g_2 \in G$.

3. *$\Psi(g^{-1}, \Psi(g, y)) = y$.*

The Lie group action is said to be *transitive* if for any two points $y, z \in M$, there is a group element g such that $\Psi(g, y) = z$, or equivalently if the orbit $\Psi(G, y) := \{\Psi(g, y) \mid g \in G\}$ of any point is all of M [19].

Example The group of rotations $SO(3)$ is a Lie group and its associated Lie algebra is denoted $\mathfrak{so}(3)$, which consists of all skew-symmetric matrices. The Lie bracket of $\mathfrak{so}(3)$ is the matrix commutator given by $[\widehat{w}, \widehat{v}] = \widehat{w}\widehat{v} - \widehat{v}\widehat{w}$, $\widehat{w}, \widehat{v} \in \mathfrak{so}(3)$. For the attitude matrix $\Lambda \in SO(3)$, described in the previous section, we have

$$\widehat{W} := \Lambda^T \dot{\Lambda} \in \mathfrak{so}(3), \quad \widehat{w} := \dot{\Lambda}\Lambda^T \in \mathfrak{so}(3).$$

♦

For the numerical solution of problems of the type (1.10) it might be crucial, in some applications, to produce numerical approximations $y_n \approx y(t_n)$ that stay on the given manifold, i.e. $y_n \in M$. A generic numerical method, such as e.g. a classical Runge-Kutta or a multistep method, does not in general have this property. On manifolds acted upon by a transformation group it is possible to use Lie group integrators (see e.g. [11]) in order to ensure that the numerical approximation is on M.

The idea behind Lie group integrators is that the numerical method $\Phi_h : y_i \rightarrow y_{i+1}$ advances the numerical solution on M by using the Lie group action. Lie group integrators relay on the use of a coordinate map, a local diffeomorphism from a neighborhood of the origin in $\mathfrak{g}$ to a neighborhood of the identity in G. A common example is the exponential map,

$$\exp : \mathfrak{g} \rightarrow G. \tag{1.11}$$

Using the coordinate map and the Lie group action it is possible to pullback the original equation from the manifold to the Lie algebra. The transformed equation is then approximated on $\mathfrak{g}$ by means of a classical Runge-Kutta method and the inverse transformation is used to advance the solution on M. An example of Lie group integrator is the Magnus integrator described in [14], which is used in paper I [7] on $SO(3)$ to approximate the attitude of a rigid body. The approach is illustrated in the example below.

Example Recall the linear differential equations for the attitude of the rigid body (1.1) in the form (1.10),

$$\dot{\Lambda} = \widehat{w(t)}\Lambda \quad \widehat{w(t)}\Lambda \in T_\Lambda SO(3), \tag{1.12}$$

here $M = SO(3)$ and $\Lambda(t) \in SO(3)$. Since $\exp : \mathfrak{so}(3) \rightarrow SO(3)$ (1.11) is a local diffeomorphism and the Lie group action is transitive, the solution of (1.12) can be expressed locally as

$$\Lambda(t) = \exp \Omega(t)\Lambda_0, \quad \Lambda_0 = \Lambda(t_0) \in SO(3). \tag{1.13}$$

Differentiating (1.13) with respect to time we obtain

$$\frac{d}{dt} \exp \Omega(t) = \widehat{w(t)} \exp \Omega(t), \quad \Omega(t_0) = 0,$$

and the equation can be written explicitly in Ω as a differential equation in $\mathfrak{so}(3)$. One obtains

$$\dot{\Omega} = d\exp_\Omega^{-1}(\widehat{w(t)}) = \sum_{k=0}^{\infty} \frac{B_k}{k!} \mathrm{ad}_\Omega^k(\widehat{w(t)}), \tag{1.14}$$

where

$$\text{ad}_\Omega^k(A) = [\text{ad}_\Omega^{k-1}(A), A], \quad \text{ad}_\Omega^0(A) = \Omega,$$

and B_k are the Bernoulli numbers defined by $\sum_{k \geq 0}(B_k/k!)x^k = x/(e^x - 1)$ [1]. The firsts Bernoulli numbers are $B_0 = 1$, $B_1 = -1/2$, $B_2 = 1/6$. Applying Picard's fixed point iteration to (1.14) [21],

$$\Omega(t) = \lim_{m \to \infty} \Omega_m(t), \quad \Omega_{m+1} = \Omega_0 + \int_{t_0}^t d\exp_{\Omega_m}^{-1}(\widehat{w(\tau)})\, d\tau,$$

where $\Omega_0 = \Omega(t_0) = 0$, yields the so called Magnus series

$$\Omega(t) = \int_{t_0}^t \widehat{w(\tau)}\, d\tau - \frac{1}{2}\int_{t_0}^t\int_{t_0}^{\tau_1}\left[\widehat{w(\tau_2)}, \widehat{w(\tau_1)}\right] d\tau_2\, d\tau_1$$

$$+ \frac{1}{4}\int_{t_0}^t\int_{t_0}^{\tau_1}\int_{t_0}^{\tau_2}\left[\left[\widehat{w(\tau_3)}, \widehat{w(\tau_2)}\right], \widehat{w(\tau_1)}\right] d\tau_3\, d\tau_2\, d\tau_1 + \cdots, \quad (1.15)$$

for $\|t - t_0\|$ sufficiently small. To get an approximate solution $\widetilde{\Omega} \approx \Omega$, in $\mathfrak{so}(3)$, one truncates the Magnus expansion (1.15) and approximates the integrals by Gaussian quadrature [14]. The numerical solution to (1.12), $\Lambda_1 \approx \Lambda(t_0 + h) \in SO(3)$, is

$$\Lambda_1 = \exp(\widetilde{\Omega})\Lambda_0 \in SO(3).$$

and its order of accuracy depends on $\|\widetilde{\Omega} - \Omega\| = \mathcal{O}(h^{p+1})$. Using one point Gauss quadrature,

$$\widetilde{\Omega} = h\,\widehat{w}(t_0 + h/2),$$

one obtains a second order Lie group method, $p = 2$. For a fourth order method

$$\widetilde{\Omega} = h(A_1 + A_2)/2 - h^2\frac{\sqrt{3}}{12}[A_1, A_2],$$

where $A_{\{1,2\}} = \widehat{w}(t_0 + h(1/2 \mp \sqrt{3}/6))$. Besides being a Lie group integrator, these second and fourth order methods also become time-symmetric, such that the numerical method, $\Phi_h : \Lambda_0 \to \Lambda_1$, satisfies $\Phi_h \circ \Phi_{-h} = $ identity mapping. Symmetric methods usually show good behavior in long time integration [11]. A complete treatment of Magnus methods can be found in [5] and in references therein.

♦

1.3 Symplectic integrators

Symplectic integrators or Poisson integrators are specially designed numerical schemes for Hamiltonian systems which preserve the symplectic structure and have excellent behavior on long-time integration. Under appropriate assumptions, symplectic methods can also be shown to ensure approximate conservation of energy over exponentially long times [4].

For a mechanical system with n degrees of freedom $q = (q_1, \ldots, q_m)^T$, the equations of motion are given by the solution of the Euler-Lagrange equations

$$\frac{d}{dt} \partial_{\dot{q}} L(q, \dot{q}) = \partial_q L(q, \dot{q}), \tag{1.16}$$

where $L = T(q, \dot{q}) - U(q)$, T is the kinetic- and U the potential energy, here assumed to depend only on q. By the Legendre transform one defines the conjugate momenta $p_i := (\partial/\partial \dot{q}_i) L$ to get the Hamiltonian formalism of the problem. Solving the Lagrange equations (1.16) is equivalent to solve the (canonical) Hamiltonian system

$$\dot{z} = \mathcal{J} \nabla_z H(z), \quad \mathcal{J} = \begin{pmatrix} 0 & I_{m \times m} \\ -I_{m \times m} & 0 \end{pmatrix}, \tag{1.17}$$

where $H : \mathbb{R}^{2m} \to \mathbb{R}$ is the Hamiltonian function, $H := p^T \dot{q}(p, q) - L(q, \dot{q}(p, q))$, $z = (q, p)^T \in \mathbb{R}^{2m}$ and $\mathcal{J}$ is called structure matrix. By the definition of H one can readily see that the Hamiltonian is a preserved quantity, i.e. $\dot{H} = 0$. An other special property of this formulation is that the solution of (1.17) preserves the symplectic two form

$$\omega := dp \wedge dq = \sum_{i=1}^{n} dp_i \wedge dq_i,$$

which is equivalent to say that

$$\left(\frac{\partial z(t)}{\partial z_0} \right)^T \mathcal{J} \left(\frac{\partial z(t)}{\partial z_0} \right) = \mathcal{J}, \quad \forall\, t > 0. \tag{1.18}$$

A *symplectic integrator* is a numerical method $\Phi_h : z_0 \to z_1$, $z_n = (q_n, p_n)$, where $z_1 = \Phi_h(z_0)$ is an approximation of $z(t_1) = z(t_0 + h)$, satisfying the condition

$$\left(\frac{\partial z_1}{\partial z_0} \right)^T \mathcal{J} \left(\frac{\partial z_1}{\partial z_0} \right) = \mathcal{J}.$$

Not all mechanical systems obey the canonical Hamiltonian formalism described above. For example the free rigid body equations do not fit into this

framework. Hamiltonian systems can however be generalized to the so called *Poisson systems*, having the form

$$\dot{z} = \mathcal{J}(z)\nabla_z H(z), \tag{1.19}$$

where $z \in \mathbb{R}^n$ and $H(z)$ is the Hamiltonian function, with a non-constant structure matrix $\mathcal{J}(z)$. A Poisson system is endowed with a Poisson bracket

$$\{F, H\} := \nabla_z F(z)^T \mathcal{J}(z)\nabla_z H(z),$$

and the system (1.19) can be written as $\dot{z}_i = \{z_i, H\}$ $i = 1, \ldots, n$. In particular, if $\mathcal{J}_{ij}$ depends linearly on z, $\mathcal{J}_{ij} = C_{ij}^k z_k$, the system is said to be a Lie-Poisson system (the bracket is called Lie-Poisson bracket).

Example The free rigid body has a Lie-Poisson structure with the Lie-Poisson bracket [22]

$$\{F, G\} = \nabla F(z)^T \widehat{M} \nabla G(z) = -\langle M, \nabla F(z) \times \nabla G(z)\rangle, \tag{1.20}$$

and the Euler equations (1.5) can be obtained from $\dot{M}_i = \{M_i, H\}$, where the Hamiltonian $H = \langle M, J^{-1}M\rangle/2$.

$\blacklozenge$

Similarly to symplectic integrators one defines *Poisson integrators* for non-canonical systems (1.19).

Definition 1.3.1. *(See [11]) A numerical method $\Phi_h : z_0 \to z_1$ is a Poisson integrator for the structure matrix $\mathcal{J}(z)$, if the transformation $z_0 \to z_1$*

- *respects the Casimirs, i.e. invariants C_i that satisfies $\{C_i, H\} = 0$ for all smooth H,*

- *satisfies*

$$\left(\frac{\partial z_1}{\partial z_0}\right)\mathcal{J}(z_1)\left(\frac{\partial z_1}{\partial z_0}\right)^T = \mathcal{J}(z_1),$$

whenever the method is applied to (1.19).

Example One way to obtain a Poisson integrator is to split the Hamiltonian in two parts, $H = H_1 + H_2$, giving rise to two simpler individual systems, $\dot{z} = \mathcal{J}(z)\nabla H_i(z)$, $i = 1, 2$. By integrating those systems exactly and composing their flows appropriately one obtains the numerical approximation, e.g., for a second order method

$$z_1 = \varphi_{h/2}^{[2]} \circ \varphi_h^{[1]} \circ \varphi_{h/2}^{[2]}(z_0),$$

where $\varphi_h^{[1]}(z_0)$ and $\varphi_h^{[2]}(z_0)$ denote the exact solutions $z(h+t_0)$ for a given initial condition $z(t_0) = z_0$. This approach is for example adopted in paper I [7] and II [6] on rigid bodies that are exposed to external forces.

$$\blacklozenge$$

In some cases, it might be convenient to rewrite a non-canonical Poisson system into a canonical system. Given a non-canonical Poisson structure with a structure matrix $\mathcal{J}(z) \in \mathbb{R}^{n \times n}$, if $\mathcal{J}(z)$ has constant rank $2m \leq n$ then, by Darboux' theorem [24], there exist a *local* change of variables $\bar{z} = \bar{z}(z)$ such that the problem assumes the canonical Hamiltonian form (1.17).

Example The Lie-Poisson structure of the free rigid body can be locally rewritten in canonical form in Euler angles $\Phi = (\varphi, \theta, \psi)^T \in \mathbb{R}^3$ [22]. The Euler angles define local coordinates on $SO(3)$. For example, defining elementary rotations,

$$R_x(\alpha) = \begin{pmatrix} 1 & 0 & 0 \\ 0 & \cos\alpha & \sin\alpha \\ 0 & -\sin\alpha & \cos\alpha \end{pmatrix}, \quad R_z(\alpha) = \begin{pmatrix} \cos\alpha & \sin\alpha & 0 \\ -\sin\alpha & \cos\alpha & 0 \\ 0 & 0 & 1 \end{pmatrix}, \quad (1.21)$$

around the x- and the z-axis, respectively, $\Lambda \in SO(3)$ can be formulated by successive simple rotations

$$\Lambda = R(\Phi) := R_z(\psi) R_x(\theta) R_z(\varphi), \quad \Phi = (\varphi, \theta, \psi)^T, \quad (1.22)$$

so called zxz-convention. The latter representation of Λ in Euler angles is not unique, but is just one of several possible conventions (local charts). From the kinematic relation (1.1)

$$\dot{\Lambda} = \widehat{w}\Lambda = \Lambda\widehat{W},$$

where w and W are spatial and body angular velocity, it follows from straightforward calculations,

$$W = \text{skew}^{-1}\left(R(\Phi)^T \frac{d}{dt} R(\Phi)\right), \quad w = \text{skew}^{-1}\left(\left(\frac{d}{dt} R(\Phi)\right) R(\Phi)^T\right),$$

where skew is the bijective mapping skew : $\mathbb{R}^3 \rightarrow \mathfrak{so}(3)$, i.e. $\text{skew}(v) = \widehat{v}$, one obtains the transformations $W = T_W(\Phi)\dot{\Phi}$, $w = T_w(\Phi)\dot{\Phi}$, where e.g.,

$$T_W(\Phi) := \begin{pmatrix} \sin\psi \sin\theta & \cos\psi & 0 \\ -\cos\psi \sin\theta & -\sin\psi & 0 \\ \cos\theta & 0 & 1 \end{pmatrix}. \quad (1.23)$$

From the Lagrangian

$$L = \frac{1}{2}\langle W, JW \rangle = \frac{1}{2}\langle \dot{\Phi}, T_W(\Phi)^T J T_W(\Phi)\dot{\Phi} \rangle$$

one obtains the conjugate momenta

$$P := \frac{\partial L}{\partial \dot{\Phi}} = T_W(\Phi)^T J T_W(\Phi) \dot{\Phi}, \quad P = (p_\varphi, p_\theta, p_\psi)^T. \tag{1.24}$$

However, the Legendre transform (1.24) is only regular and valid for

$$0 < \varphi < 2\pi, \quad 0 < \theta < \pi, \quad 0 < \psi < 2\pi,$$

when $T_W(\Phi)^T J T_W(\Phi)$ is invertible. The Hamiltonian finally defined by $H := P^T \dot{\Phi}(\Phi, P) - L(\Phi, \dot{\Phi}(\Phi, P))$ becomes

$$H = \frac{1}{2} \left(\frac{[(p_\varphi - p_\psi \cos\theta)\sin\psi + p_\theta \sin\theta \cos\psi]^2}{J_1 \sin^2\theta} \right.$$
$$\left. + \frac{[(p_\varphi - p_\psi \cos\theta)\cos\psi - p_\theta \sin\theta \sin\psi]^2}{J_2 \sin^2\theta} + \frac{p_\psi^2}{J_3} \right),$$

and the rigid body equations are written in canonical form (1.17) for $z = (\Phi, P)^T$.

♦

1.4 Summary of papers

Paper I: Efficient time-symmetric simulation of torqued rigid bodies using Jacobi elliptic functions

Elena Celledoni and Niklas Säfström

In this paper we develop an accurate integrator for the dynamics of a free rigid body with distinct principal moments of inertia. The solution of the Euler equations is given by the Jacobi elliptic functions, which are computed to machine precision by using the Arithmetic-Geometric Mean sequence. To approximate the attitude of the body a symmetric Magnus method of order 2 and 4, respectively, is employed. The overall implementation gives a symmetric 2 or 4 order method for the dynamics of the free rigid body. The method is primarily proposed as a part of a symmetric splitting method for problems of rigid bodies subjected to external forces. Experiments on the heavy top and a satellite problem show that the splitting method preforms well and gives a near conservation of energy during long time integration. The use of the highly accurate approximation of the Jacobi elliptic functions is advantageous for perturbed free rigid body problems.

Paper II: The exact computation of the free rigid body motion and its use in splitting methods

Elena Celledoni, Francesco Fassò, Niklas Säfström and Antonella Zanna
Published in SIAM Journal on Scientific Computing, 2008 [6]

This paper is a continuation of the ideas in paper I. Here we consider Jacobi elliptic integrals of the third kind to compute an accurate solution of the attitude of the rigid body. Both rotation matrices and quaternions are used to represent the rotation of the body. We review various algorithms for the computation of the exact solution of the free rigid body equations and provide a common framework. The purpose of the paper is to investigate the benefits of using the exact solution of the free rigid body motion in splitting methods for rigid body dynamics. Various different experiments are performed, e.g., satellite-dynamics problems and molecular dynamics simulation of water molecules. The results are compared against state of the art methods for rigid body dynamics. The conclusion is that the use of exact rigid body motion in splitting methods is competitive as a numerical approach: it is very robust and behaves uniformly well for all choice of the principal moment of inertia and initial conditions, independently of the step-size of integration.

Paper III: Modeling and Control of Offshore Pipelay Operations Based on a Finite Strain Pipe Model

Gullik A. Jensen, Niklas Säfström, Tu Duc Nguyen and Thor I. Fossen
Published in Proceedings of American Control Conference–ACC2009, 2009 [17]

The paper deals with mathematical modeling and simulations within offshore engineering. A model, aimed for prediction and control of offshore pipelay operations from a dynamically positioned surface vessel, is developed. The model is based on a nonlinear elastic rod, capable of undergoing shearing, twist and bending, formulated by J.C. Simo [25]. The elastic rod model, adding hydrostatic damping and gravity, is used to model the pipe submerged in water. A standard vessel model is attached to one end of the pipe model as a dynamic boundary condition. Numerical simulations are included, applying both PD (proportional-derivative) and PID (proportional-integral-derivative) controllers, to give an example of possible application of the model and to illustrate the behavior of the mechanical system.

Paper IV: A Nonlinear PDE Formulation for Offshore Vessel Pipeline Installation

Gullik A. Jensen, Niklas Säfström, Thor I. Fossen and Tu Duc Nguyen
To appear in Journal of Ocean Engineering [16]

This work continues paper III [17]. A seabed as added to the pipe model presented in paper III and the final combined pipe-vessel system is proved to be input-output passive. Numerical experiments are performed, for the static case as well as for a dynamic scenario, which are validated against the natural catenary equation, for the static case, and the commercial finite element method (FEM) code RIFLEX [10], which holds an international leading position in FEM analysis for slender marine structures. The dynamic experiment indicates a very good correlation with the simulation performed by RIFLEX. The conclusion is that the proposed model is well suited for prediction and control of offshore pipelay operations. Since the dynamics of the surface vessel is included in the model, the range of analysis that can be performed using the proposed model extends that of RIFLEX.

Paper V: Hamiltonian and multi-symplectic structure of a rod model using quaternions

Elena Celledoni and Niklas Säfström
Preprint Numerics No. 8/2009,
Departments of Mathematical Sciences, NTNU [8]

A constrained Hamiltonian formulation as well as a multi-symplectic formulation of the elastic rod model [25], adopted in paper III and IV, is presented. The motivation for those formulations is the excellent behavior in long time integration, while applying symplectic or multi-symplectic integrators [20]. Multi-symplecticity is a generalization of classical symplecticity for finite-dimensional Hamiltonian systems to the infinite-dimensional case. Besides global preservation of energy and momentum, the multi-symplectic formulation of a Hamiltonian PDE implies local energy and momentum conservation properties.

Bibliography

[1] M. Abramowitz and I. A. Stegun. *Handbook of mathematical functions with formulas, graphs, and mathematical tables*, volume 55 of *National Bureau of Standards Applied Mathematics Series, 55*. Reprint of the 1972 edition. Dover Publications, Inc., New York, 1992.

[2] V. I. Arnold. *Mathematical methods of classical mechanics.* Graduate Texts in Mathematics. Springer, second edition, 1989.

[3] A. Baker. *Matrix groups. An introduction to Lie group theory.* SUMS. Springer, 2002.

[4] G. Benettin and A. Giorgilli. On the Hamiltonian interpolation of near-to-the identity symplectic mappings with application to symplectic integration algorithms. *J. Stat. Phys.*, 74(5-6):1117–1143, 1994.

[5] S. Blanes, F. Casas, J. A. Oteo, and J. Ros. The Magnus expansion and some of its applications. *Phys. Reports*, 470(5-6):151–238, 2009.

[6] E. Celledoni, F. Fassò, N. Säfström, and A. Zanna. The exact computation of the free rigid body motion and its use in splitting methods. *SIAM J. Sci. Comp.*, 30(4):2084–2112, 2008.

[7] E. Celledoni and N. Säfström. Efficient time-symmetric simulation of torqued rigid bodies using Jacobi elliptic functions. *J. Phys. A*, 39:5463–5478, 2006.

[8] E. Celledoni and N. Säfström. Hamiltonian and multi-symplectic structure of a rod model using quaternions. 2009.

[9] M. L. Curtis. *Matrix groups.* UTX. Springer, second edition, 1984.

[10] I Fylling, C. M. Larsen, N. Sødahl, E Passano, N. A. Bech, A. G. Engseth, H. Lie, and H Ormberg. *RIFLEX User's Manual 3.6, MARINTEK, Trondheim, Norway.* Trondheim, Norway, 2008.

[11] E. Hairer, C. Lubich, and G. Wanner. *Geometric numerical integration*, volume 31 of *Springer series in computational mathematics.* Springer, 2002.

[12] B. C. Hall. *Lie groups, Lie algebras, and representations. An elementary introduction.* GTM. Springer, 2003.

[13] N. H. Ibragimov. *Elementary Lie group analysis and ordinary differential equations.* Wiley, 1999.

[14] A. Iserles and S. P. Nørsett. On the solution of linear differential equations in Lie groups. *R. Soc. Lond. Philos. Trans. Ser. A Math. Phys. Eng. Sci.*, 357(1754):983–1019, 1999.

[15] C. G. J. Jacobi. Sur la rotation d'un corps. *Crelle Journal für die reine und angewandte Matematik*, Bd. 39:293–350, 1849.

[16] G. A. Jensen, N. Säfström, T. I. Fossen, and T. D. Nguyen. A nonlinear PDE formulation for offshore vessel pipeline installation. *J. Ocean Engrg.*, 2009. To appear.

[17] G. A. Jensen, N. Säfström, T. D. Nguyen, and T. I. Fossen. Modelling and control of suspended pipeline during pipelay operation based on a finite strain beam model. In *Proceedings of American Control Conference–ACC2009 St. Louis, Missouri, USA*, June 2009.

[18] S. Kyriakides and E. Corona. *Mechanics of offshore pipelines, Vol I: Buckling and collapse.* Elsevier, first edition, 2007.

[19] J. M. Lee. *Introduction to smooth manifolds.* GTM. Springer, first edition, 2006.

[20] B. Leimkuhler and S. Reich. *Simulating Hamiltonian Dynamics*, volume 14 of *Cambridge Monographs on Applied and Computational Mathematics.* Cambridge University Press, first edition, 2004.

[21] W. Magnus. On the exponential solution of differential equations for a linear operator. *Comm. Pure and Appl. Math.*, 7(4):649–673, 1954.

[22] J. E. Marsden and T. S. Ratiu. *Introduction to mechanics and symmetry.* Texts in applied mathematics. Springer, 1999.

[23] OFFPIPE. http://www.offpipe.com/.

[24] P. J. Olver. *Applications of Lie groups to differential equations.* Springer, second edition, 1993.

[25] J. C. Simo. A finite strain beam formulation. The three-dimensional dynamic problem. Part I. *Comput. Methods Appl. Mech. Engrg.*, 49(1):55–70, 1985.

[26] J. C. Simo and D. D. Fox. On a stress resultant geometrically exact shell model. part i: Formulation and optimal parametrization. *Comput. Methods Appl. Mech. Engrg.*, 72(3):267–304, 1989.

[27] J. C. Simo, J. E. Marsden, and P. S. Krishnaprasad. The hamiltonian structure of nonlinear elasticity: The material and convective representations of solids, rods, and plates. *Arch. Rat. Mech. Anal.*, 104(2):125–183, 1988.

[28] SIMLA - Simulation of Pipelaying. http://www.sintef.no/.

Paper I

Efficient time-symmetric simulation of torqued rigid bodies using Jacobi elliptic functions

E. Celledoni and N. Säfström.

Chapter 2

Efficient time-symmetric simulation of torqued rigid bodies using Jacobi elliptic functions

ABSTRACT. If the three moments of inertia are distinct, the solution to the Euler equations for the free rigid body is given in terms of Jacobi elliptic functions. Using the Arithmetic-Geometric mean algorithm, [1], these functions can be calculated efficiently and accurately. Compared to standard numerical ODE and Lie-Poisson solvers, the overall approach yields a faster and more accurate numerical solution to the Euler equations. This approach is designed for mass asymmetric rigid bodies. In the case of symmetric bodies, the exact solution is available in terms of trigonometric functions, see [5] and [18] and [2] for details.

In this paper we consider the case of asymmetric rigid bodies subject to external forces. We consider a strategy similar to the symplectic splitting method proposed in [18] and [5]. The method here proposed is time-symmetric. We decompose the vector field of our problem in a free rigid body (FRB) problem and another completely integrable vector field. The FRB problem consists of the Euler equations and a differential equation for the 3×3 orientation matrix. The Euler equations are integrated exactly while the matrix equation is approximated using a truncated Magnus series.

In our experiments we observe that the overall numerical solution benefits greatly from the very accurate solution of the Euler equations. We apply the method to the heavy top and the simulation of artificial satellite attitude dynamics.

2.1 Introduction

We consider the Euler equations describing the motion of a free (FRB) rigid body

$$
\begin{aligned}
I_1\dot{\omega}_1 &= (I_2 - I_3)\omega_2\omega_3, \\
I_2\dot{\omega}_2 &= (I_3 - I_1)\omega_3\omega_1, \\
I_3\dot{\omega}_3 &= (I_1 - I_2)\omega_1\omega_2,
\end{aligned}
\tag{2.1}
$$

where I_1, I_2 and I_3 are the principal moments of inertia. These equations are completely integrable. Energy and angular momentum are preserved along the solution, this means that for all times the two quantities

$$
E = \frac{1}{2}\left(I_1\omega_1^2 + I_2\omega_2^2 + I_3\omega_3^2\right), \quad G^2 = I_1^2\omega_1^2 + I_2^2\omega_2^2 + I_3^2\omega_3^2,
\tag{2.2}
$$

are constant, (here E is the energy and G^2 is the total angular momentum). There is also a non canonical symplectic structure (Lie-Poisson structure) preserved by the flow of (2.1), [13]. By using the two constants of motion it is possible to derive the general solution of the equations expressed in terms of Jacobi elliptic functions.

The expression of the exact general solution of the Euler equations can be turned into a numerical method by using efficient numerical approximations of the Jacobi elliptic functions. To impose the initial conditions a constant τ, used to translate time, must be computed prior to the integration, see section 3 for details. In this paper we show that this approach is very competitive and discuss the details of its further use in problems of rigid bodies subject to external forces. We also refer to [3] and [16] for related literature.

The simulation of rigid body motion is interesting for applications in robotics, structural mechanics, molecular dynamics, and also nanotechnology, [8], [10, 19]. Often stable integration over very long times is required in the simulations. It has been shown that the preservation of geometric features, as for example symplecticity and time-symmetry of the flow for Hamiltonian systems, can be crucial for the performance of numerical integrators in long time simulations, [10, 9]. Therefore in some cases geometric integrators are preferred to other existing sophisticated algorithms for multi-body systems.

Lie-Poisson integration methods for the Euler equations have been constructed by various authors, [7, 12, 15, 17], see also [10] and references therein. Many of these methods cannot be straightforwardly generalized to the broader class of non canonical Hamiltonian problems, thus their use is limited to the numerical approximation of the Euler equations. However some of these integrators have successfully been applied in the simulation of rigid body dynamics and of torqued rigid bodies. This is for instance the case in [5] and [18].

For the Euler equations, in [14, 18], the right hand side of (2.1) is split in the following three terms,

$$f_1(\omega) = \begin{bmatrix} 0 \\ I_3\omega_3\omega_1 \\ -I_2\omega_1\omega_2 \end{bmatrix}, \quad f_2(\omega) = \begin{bmatrix} -I_3\omega_2\omega_3 \\ 0 \\ I_1\omega_1\omega_2 \end{bmatrix}, \quad f_3(\omega) = \begin{bmatrix} I_2\omega_2\omega_3 \\ -I_1\omega_3\omega_1 \\ 0 \end{bmatrix}.$$
(2.3)

Each of the three vector fields is Hamiltonian with respect to the rigid body Poisson bracket [13, p. 8], and defines a differential equation which is easy to integrate exactly. The appropriate composition of the corresponding flows produces a (non canonical) symplectic approximation of the problem. There is numerical evidence showing that this Lie-Poisson method is very competitive compared to most of the known and previously proposed integration strategies for the Euler equations [14, 4, 15]. We use this splitting for comparison in our numerical experiments. The generalization to the case of a six-dimensional system modeling torqued rigid bodies, in [18], is achieved by considering a splitting of the Hamiltonian of the problem in four parts, three of them give rise to vector fields analogous to f_1, f_2 and f_3, the last vector field is completely integrable and arises from the potential energy yielding the torque. We will briefly recall this approach in section 4.

The method proposed for torqued rigid bodies in the present paper is time-symmetric, and related to the approach of [18, 5]. We decompose the vector field of our problem in a FRB problem and another completely integrable vector field. The FRB problem is given by the three Euler equations and the differential equations for the orientation matrix. This matrix represents the rotation which the body undergoes with respect to a reference configuration. The numerical approximation of the Euler equations is performed to machine accuracy, while the orientation matrix is approximated by the exponential of a truncated Magnus series (achieving order 2 or 4). The overall splitting is symmetric, but not symplectic. However in many of the considered numerical experiments the new method presents better conservation of energy and better behavior of the numerical solution then the symplectic integrator of [18, 5].

Accurate approximations preserving energy, momentum and the Lie-Poisson structure of the Euler equations, have been recently addressed in [15]. In this work the authors propose a new implementation of the Discrete Moser-Veselov (DMV) algorithm of [17]. By applying an appropriate rescaling of the initial condition, they also obtain new DMV methods of order four and six. The rescaling needs to be performed just once, at the beginning of the integration. The higher order methods present therefore virtually the same computational cost as the second order DMV algorithm.

Our numerical tests show that using the exact solution and computing the Jacobi elliptic functions to machine accuracy leads to a very competitive method for the solution of the Euler equations, also compared to the improved DMV

approach. Both approaches require the computation of some quantities prior to the time stepping, the rescaling factors for the DMV, and the constants for imposing the initial condition in the approach of Jacobi elliptic functions. This implies increased computational cost when the methods are used within a splitting technique for torqued rigid bodies. Our experiments show that the symmetric splitting method proposed in the present paper remains competitive also in the case of torqued rigid bodies.

The outline of the paper is as follows. The new method is presented in section 2. Some technical issues for the implementation of this approach are discussed in section 3. In section 4 we report some numerical experiments comparing the proposed approach to the DMV approach of [15] and the symplectic splitting of [5, 18].

2.2   A symmetric splitting method for torqued rigid bodies

Efficient integrators for the free rigid body can be used in connection with splitting methods in the numerical approximation of more complex rigid body dynamics. The method presented here can also be applied to problems of interacting rigid bodies, rigid body linked by constrains, etc [5, 18].

The Hamiltonian function for our problem is

$$\mathcal{H} = \mathcal{H}(\boldsymbol{\pi}, Q) = \frac{1}{2} \left(\frac{\pi_1^2}{I_1} + \frac{\pi_2^2}{I_2} + \frac{\pi_3^2}{I_3} \right) + V(Q),$$

where $\boldsymbol{\pi} = (I_1\omega_1, I_2\omega_2, I_3\omega_3)^T$ is the angular momentum and Q is the rotation matrix which describes the orientation of the body.

The Hamiltonian $\mathcal{H}$ gives rise to the following system of ordinary differential equations

$$\dot{\boldsymbol{\pi}} = \mathrm{skew}(T^{-1}\boldsymbol{\pi})\, \boldsymbol{\pi} + f(Q), \tag{2.4}$$

$$\dot{Q} = \mathrm{skew}(T^{-1}\boldsymbol{\pi})\, Q, \tag{2.5}$$

where

$$\mathrm{skew}(\boldsymbol{v}) = \begin{pmatrix} 0 & v_3 & -v_2 \\ -v_3 & 0 & v_1 \\ v_2 & -v_1 & 0 \end{pmatrix},$$

f depends on the potential energy $V(Q)$, and

$$T = \begin{pmatrix} I_1 & 0 & 0 \\ 0 & I_2 & 0 \\ 0 & 0 & I_3 \end{pmatrix}$$

is the principal inertia tensor. To derive a symmetric splitting method for the above equations, we start by applying a Störmer/Verlet splitting,

$$\mathcal{H} = \mathcal{H}_1 + \mathcal{H}_2, \quad \mathcal{H}_2 = V(Q),$$

and $\mathcal{H}_1 = \mathcal{H} - \mathcal{H}_2$ is the kinetic energy. The system of differential equation is then split into the two systems,

$$S_1 = \begin{cases} \dot{\boldsymbol{\pi}} = \mathrm{skew}(T^{-1}\boldsymbol{\pi})\,\boldsymbol{\pi}, \\ \dot{Q} = \mathrm{skew}(T^{-1}\boldsymbol{\pi})\,Q, \end{cases} \tag{2.6}$$

corresponding to the kinetic part, and

$$S_2 = \begin{cases} \dot{\boldsymbol{\pi}} = f(Q), \\ \dot{Q} = 0, \end{cases} \tag{2.7}$$

corresponding to the potential part. The Störmer/Verlet scheme is then

$$(\boldsymbol{\pi}, Q)^{(j+1)} = \varphi_{h/2}^{[S_2]} \circ \varphi_h^{[S_1]} \circ \varphi_{h/2}^{[S_2]}((\boldsymbol{\pi}, Q)^{(j)}), \quad j = 0, 1, \dots,$$

where $\varphi_h^{[S_1]}$ and $\varphi_h^{[S_2]}$ represent the exact flows of S_1 and S_2. It is well known that this scheme is symplectic. In the case of symmetric rigid bodies, the exact flow $\varphi_h^{[S_1]}$ can be expressed in terms of trigonometric functions, see [5, 18, 2] for details. This is not true in the asymmetric case. Our splitting is obtained substituting $\varphi_h^{[S_1]}$ with a computationally efficient time-symmetric approximation of the flow of S_1.

The system S_1 is simply a FRB problem. Rewriting the first part of system (2.6) in terms of the angular velocity, $\boldsymbol{\omega} = T^{-1}\boldsymbol{\pi}$ one obtains the Euler equations (2.1). We can now compute $\boldsymbol{\pi}(t)$ to machine accuracy, for any t and any initial value, by using the exact solution of the Euler equations, and computing the Jacobi elliptic functions by the method of Arithmetic-Geometric Mean, see section 3. Hence the update of $\boldsymbol{\pi}$ on the interval $[t_j, t_{j+1}]$ is

$$\boldsymbol{\pi}^{(j+1)} = \mathcal{S}(\boldsymbol{\pi}^{(j)}, h, t_j), \tag{2.8}$$

and is exact. The operator $\mathcal{S} : \mathbf{R}^3 \times \mathbf{R} \times \mathbf{R} \to \mathbf{R}^3$ maps any initial value $\boldsymbol{\pi}(t_j) = \mathbf{v} \in \mathbf{R}^3$ to the solution, $\boldsymbol{\pi}(t_{j+1}) = \mathcal{S}(\mathbf{v}, h, t_j)$, of the Euler equations at time $t_{j+1} = t_j + h$.

The approximation of the orientation matrix $Q^{(j+1)}$ in t_{j+1} is obtained integrating numerically on the interval $[t_j, t_{j+1}]$ the equation

$$\dot{Q} = \mathrm{skew}(T^{-1}\boldsymbol{\pi})\,Q, \quad Q(t_j) = Q^{(j)},$$

using a symmetric Magnus method (of order 2 or 4) [9]. For order 2 this results in the following expression

$$Q^{(j+1)} = \exp\left(h\,\mathrm{skew}\left(T^{-1}\boldsymbol{\pi}^{(j+1/2)}\right)\right)Q^{(j)}, \tag{2.9}$$

where $\boldsymbol{\pi}^{(j+1/2)} = \boldsymbol{\pi}(t_j + h/2)$ is obtained as a by-product of the update $\boldsymbol{\pi}^{(j+1)}$ in (2.8) with little extra cost (see section 3 for details). The exponential in (2.9) is computed by Rodrigues formula [13, p. 291]. Thus, using (2.8) and (2.9), the flow $\varphi_h^{[S_1]}$ is approximated by a second order flow $\phi_h^{[S_1]}$.

Given $f(Q^j)$ the flow $\varphi_h^{[S_2]}$ can be calculated exactly

$$\boldsymbol{\pi}^{(j+1)} = \boldsymbol{\pi}^{(j)} + hf(Q^{(j)}),$$
$$Q^{(j+1)} = Q^{(j)},$$

and the updating (second order) scheme is finally

$$(\boldsymbol{\pi}^{(j+1)}, Q^{(j+1)}) = \varphi_{h/2}^{[S_2]} \circ \phi_h^{[S_1]} \circ \varphi_{h/2}^{[S_2]}((\boldsymbol{\pi}^{(j)}, Q^{(j)})),$$

where

$$\phi_h^{[S_1]}((\boldsymbol{\pi}^{(j)}, Q^{(j)})) = \begin{cases} \boldsymbol{\pi}^{(j+1)} = \mathcal{S}(\boldsymbol{\pi}^{(j)}, h, t_j), \\ Q^{(j+1)} = \exp\left(h\,\mathrm{skew}\left(T^{-1}\boldsymbol{\pi}^{(j+1/2)}\right)\right)Q^{(j)}, \end{cases} \tag{2.10}$$

$$\varphi_h^{[S_2]}((\boldsymbol{\pi}^{(j)}, Q^{(j)})) = \begin{cases} \boldsymbol{\pi}^{(j+1)} = \boldsymbol{\pi}^{(j)} + h\,f(Q^{(j)}), \\ Q^{(j+1)} = Q^{(j)} \end{cases} \tag{2.11}$$

It is easy to verify that $\phi_h^{[S_1]}\phi_{-h}^{[S_1]} = I$ and the overall splitting method has the time-symmetry property,

$$\Phi_h\Phi_{-h} = 1, \quad \Phi_h = \varphi_{h/2}^{[S_2]} \circ \phi_h^{[S_1]} \circ \varphi_{h/2}^{[S_2]}.$$

Note that if we increase the number of terms included in the truncated Magnus series and obtain higher order in the approximation of $\varphi^{[S_1]}$, our scheme will accordingly be a more accurate approximation of the Störmer/Verlet splitting.

2.3   Implementation issues

Consider the values

$$\begin{aligned} a_1^2 &= 2EI_3 - G^2, & a_3^2 &= G^2 - 2EI_1, \\ b_1^2 &= I_2(I_3 - I_2), & b_3^2 &= I_2(I_2 - I_1), \end{aligned} \tag{2.12}$$

where G and E are given in (2.2) and I_1, I_2, I_3 are the principal moments of inertia in the Euler's equations (2.1). Assume $b_3/a_3 \leq b_1/a_1$ (we will have a similar situation if $b_3/a_3 \geq b_1/a_1$), the solutions of the Euler equations are

$$\omega_1 = \frac{a_1 \, \text{cn} \, u}{\sqrt{I_1(I_3 - I_1)}}, \quad \omega_2 = \frac{a_1 \, \text{sn} \, u}{b_1}, \quad \omega_3 = \frac{a_3 \, \text{dn} \, u}{\sqrt{I_3(I_3 - I_1)}}, \tag{2.13}$$

where cn, sn and dn are the Jacobi elliptic functions defined by

$$\text{cn} \, u = \cos\varphi, \quad \text{sn} \, u = \sin\varphi, \quad \text{dn} \, u = \sqrt{1 - k^2 \sin^2\varphi}, \tag{2.14}$$

with $u(t) = \lambda(t - \tau)$, $\lambda = b_1 a_3/(I_2\sqrt{I_1 I_3})$, and τ is a constant of integration. Here the amplitude φ is given implicitly as the solution of the equation

$$F(\varphi|k^2) = u(t), \quad u(t) = \lambda(t - \tau), \tag{2.15}$$

where

$$F(\varphi|k^2) := \int_0^\varphi \frac{d\theta}{\sqrt{1 - k^2 \sin^2\theta}}$$

is an elliptic integral of the first kind with modulus $k = b_3 a_1/(b_1 a_3)$. Assume $\boldsymbol{\omega}^{(j)} = T^{-1}\boldsymbol{\pi}^{(j)}$ is the approximation of the angular velocity produced by the symmetric splitting method at step j. At the next integration step we have to calculate the exact solution of the Euler's equations, $\boldsymbol{\omega}(t)$, at $t = t_j + h$ and $t = t_j + c_i h$, $c_i \in (0, 1)$, and $i = 1, \ldots, s$, taking $\boldsymbol{\omega}(t_j) = \boldsymbol{\omega}^{(j)}$ as initial condition. In the case we integrate the equations for the orientation matrix with a Magnus method of order two we have $s = 1$ and $c_1 = 1/2$, and for order four we have $s = 2$, $c_{1,2} = 1/2 \pm \sqrt{3}/6$.

The first task of the process is to determine τ to satisfy the initial condition $\boldsymbol{\omega}(t_j) = \boldsymbol{\omega}^{(j)}$. To this end, we first find the amplitude $\varphi^{(j)} \in [0, 2\pi]$, which is uniquely determined from the equations

$$\omega_1(t_j) = \frac{a_1 \, \cos\varphi^{(j)}}{\sqrt{I_1(I_3 - I_1)}}, \quad \omega_2(t_j) = \frac{a_1 \, \sin\varphi^{(j)}}{b_1}.$$

Furthermore, from the sign of $\omega_3(t_j)$,

$$\omega_3(t_j) = \frac{a_3 \, \sqrt{1 - k^2 \sin^2\varphi^{(j)}}}{\sqrt{I_3(I_3 - I_1)}},$$

we determine the sign of the constants a_3 and λ. Now from (2.15) we get

$$\tau = t_j - \frac{1}{\lambda} F(\varphi^{(j)}|k^2) \tag{2.16}$$

27

where

$$F(\varphi^{(j)}|k^2) = \int_0^{\varphi^{(j)}} \frac{d\theta}{\sqrt{1 - k^2 \sin^2\theta}}. \tag{2.17}$$

The latter integral can be computed to the desired accuracy using the method of Arithmetic-Geometric Mean of [1], briefly described below. We performed the numerical tests in MATLAB. To the best of our knowledge there is no built-in routine in MATLAB evaluating the integral (2.17) for arbitrary values of $\varphi^{(j)}$. The procedure we implemented is analogous to the one used in the MATLAB function `ellipke` for computing the complete elliptic integrals of the first kind $(F(\pi/2|k^2))$.

Consider the sequence $\{\varphi_n^{(j)}\}_{n=0,1,\dots}$, $\varphi_{n+1}^{(j)} > \varphi_n^{(j)}$ defined by

$$\tan(\varphi_{n+1} - \varphi_n) = \frac{b_n}{a_n} \tan\varphi_n, \quad \varphi_0 = \varphi^{(j)},$$

where a_n, b_n are given by the Arithmetic-Geometric Mean sequence [1], i.e.

$$a_{n+1} = \frac{a_n + b_n}{2}, \quad b_{n+1} = \sqrt{a_n b_n}, \quad c_{n+1} = \frac{a_n - b_n}{2}. \tag{2.18}$$

Taking the initial values

$$a_0 = 1, \quad b_0 = \sqrt{1 - k^2}, \quad c_0 = k,$$

one can show that

$$F(\varphi_0|k^2) = \lim_{n\to\infty} \frac{\varphi_n}{2^n a_n}, \quad \varphi_0 = \varphi^{(j)}. \tag{2.19}$$

The iteration stops when $n = N$ and c_N in (2.18) is less than tolerated error. As the Arithmetic-Geometric Mean sequence, (2.18), converges quadratically, one obtains accurate approximations of $F(\varphi^{(j)}|k^2)$ in very few recursion steps. In our implementation we terminate the iteration when c_N is less then machine epsilon.

From (2.16) we easily obtain τ. At this point to find the solution of the Euler equations at the desired time values we can use the built-in MATLAB function `ellipj`, with input

$$[\lambda(t_j + c_1 h - \tau), \dots, \lambda(t_j + c_s h - \tau), \lambda(t_{j+1} - \tau)]^T.$$

We obtain in output the corresponding values of cn, sn, dn and after appropriate rescaling (2.13), we obtain the values of the solution at $t_j + c_1 h, \dots, t_j + c_s h, t_{j+1}$.

The MATLAB function `ellipj` is based on a similar algorithm as the one described above. In our implementation we reuse the Arithmetic-Geometric Mean sequence obtained in the computation of τ.

Note that φ, from the relation (2.17), can be found explicitly for the special cases $k^2 = 1$ or $k^2 = 0$.

2.4 Numerical experiments

The second order symmetric splitting method proposed in this paper is denoted in the sequel by SEJ and compared with the symplectic method of [5, 18] which we denote in short by MR. We denote with SEJ4 the second order symmetric splitting method where the Magnus method of order 4 in the integration of (2.6) is used. The approach for solving the Euler equations is also compared with the Discrete Moser-Veselov methods of [15] (DMV). The symplectic method MR is based on a splitting of the the Hamiltonian $\mathcal{H}$ into four parts,

$$\tilde{\mathcal{H}}_1 = \frac{\pi_1^2}{2I_1}, \quad \tilde{\mathcal{H}}_2 = \frac{\pi_2^2}{2I_2}, \quad \tilde{\mathcal{H}}_3 = \frac{\pi_3^2}{2I_3}, \quad \tilde{\mathcal{H}}_4 = V(Q).$$

Each of the corresponding Hamiltonian vector fields can be integrated exactly ($\tilde{\mathcal{H}}_1$, $\tilde{\mathcal{H}}_2$, $\tilde{\mathcal{H}}_3$ correspond to the vector fields (2.3)), the symmetric composition of the flows gives rise to the approximation scheme,

$$(\boldsymbol{\pi}, Q)^{(j+1)} = \Phi_M((\boldsymbol{\pi}, Q)^{(j)}),$$

where

$$\Phi_M = \varphi_{4,h/2} \circ \Phi_{T,h} \circ \varphi_{4,h/2}.$$

Here

$$\Phi_{T,h} = \varphi_{1,h/2} \circ \varphi_{2,h/2} \circ \varphi_{3,h} \circ \varphi_{2,h/2} \circ \varphi_{1,h/2}$$

is the contribution from the kinetic parts, $\tilde{\mathcal{H}}_1$, $\tilde{\mathcal{H}}_2$ and $\tilde{\mathcal{H}}_3$. The flows of the kinetic parts correspond to elementary rotations in $\mathbf{R}^3$. For example for $\mathcal{H}_1$

$$\varphi_{1,h}((\boldsymbol{\pi}, Q)^{(j)}) = \begin{cases} \boldsymbol{\pi}^{(j+1)} = R_x(h)\boldsymbol{\pi}^{(j)}, \\ Q^{(j+1)} = R_x(h)Q^{(j)}, \end{cases}$$

where

$$R_x(h) = \begin{pmatrix} 1 & 0 & 0 \\ 0 & \cos(C^{(j)}h) & \sin(C^{(j)}h) \\ 0 & -\sin(C^{(j)}h) & \cos(C^{(j)}h) \end{pmatrix},$$

and

$$C^{(j)} = \frac{\pi_1^{(j)}}{I_1}.$$

While the flow for $\tilde{\mathcal{H}}_4$ is the same as for the system S_2 (2.5) of the previous section, i.e. $\varphi_{4,h} = \varphi_h^{[S_2]}$.
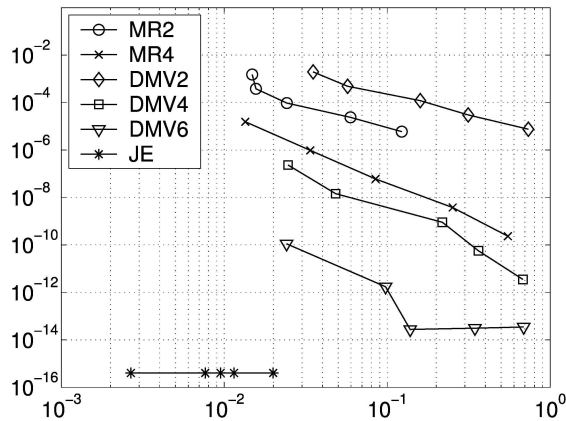
Figure 2.1: Euler equations. Execution times (x-axis) against the norm of the global error at $t = 1$ (y-axis). Integration on the interval $[0, 1]$ with different step sizes. The methods are: MR of order 2 and 4, DMV of order 2, 4 and 6, and the method JE based on the accurate computation of the Jacobi elliptic functions using ellipj in MATLAB. The results are the average over 200 experiments. The initial condition is $\pi_0 = [-1, 0, 2]^T$. The principal moments of inertia are $I_1 = 5$, $I_2 = 4$, $I_3 = 3$.

2.4.1 Free rigid body experiments

In the first experiment we consider the integration of the Euler equations. In this experiment we perform a comparison of the use of `ellipj` in MATLAB for computing the exact solution of the equations (approach here denoted with JE in the figures) with the MR and DMV methods. We refer to [15, 17] for a detailed description of the DMV methods, and recall that the higher order DVM are obtained by computing an appropriate rescaling of the initial condition. In figure 2.1 we plot on the x-axis the execution times employed by the methods to perform the integration on the interval $[0, 1]$, for different choices of the step size, $h = 1/(2^k)$ and $k = 2, \ldots, 6$. On the y-axis we report the corresponding values of the 2-norm of the global error. In all the experiments the reference solution for computing the global error is obtained using the built in function of MATLAB, `ode45`, setting the absolute and relative tolerance equal to $10e - 14$. The MR method in this case involves the computation of the three flows corresponding to the Hamiltonians $\tilde{\mathcal{H}}_1$, $\tilde{\mathcal{H}}_2$, $\tilde{\mathcal{H}}_3$ only.

The JE approach produces, as expected, a very accurate solution of the problem, the error is of the size of 10^{-14} and is independent on the step size of integration. The MR and DMV methods of order 2 and 4 perform similarly with a slight advantage for the MR in the second-order case, and of DVM in the
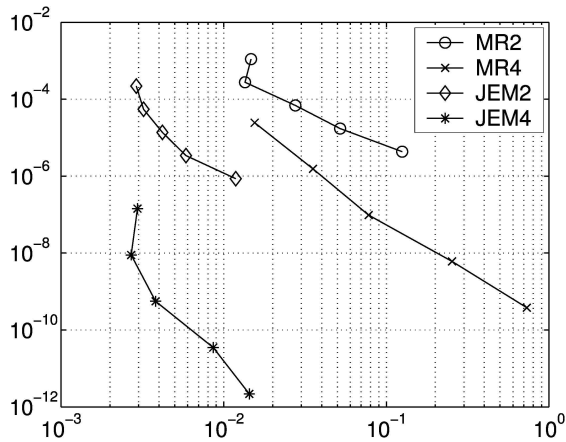
Figure 2.2: FRB equations (2.6). Execution times (x-axis) against the norm of the norm of the global error at $t = 1$ (y-axis). Integration on the interval $[0, 1]$ with different step sizes. The considered methods are MR of order 2 (MR2) and 4 (MR4), and the methods JEM2 and JEM4 (combination of `ellipj` in MATLAB with a Magnus method of order 2 or 4). The results are the average over 200 experiments. The initial conditions are $\pi_0 = [-1, 0, 2]^T$, and Q_0 is equal to the 3×3 identity matrix. The principal moments of inertia are $I_1 = 5$, $I_2 = 4$, $I_3 = 3$.

fourth-order case.

The execution times are computed taking an average over 200 experiments. In this experiment the principal moments of inertia and the initial value are $I_1 = 5$, $I_2 = 4$, $I_3 = 3$ and $\boldsymbol{\pi}_0 = (1, 0, 2)^T$. The cost for computing the rescaling factors in the DMV methods and for the computation of τ in JE are not included in this experiment. The excellent performance of the JE approach, compared to the other considered methods, shows that the Arithmetic-Geometric Mean algorithm is a very efficient method for the evaluation of the Jacobi elliptic functions.

We repeated this experiment, on the interval $[0, 400]$ with step size $h = 0.4$, and considered the energy error as the difference between the constant exact energy, given by $\mathcal{H}$, and the energy obtained from the numerical methods. For the MR method of order 2 and 4 the energy error is oscillating near zero, (the amplitude of the oscillations is about 10^{-3} for order 2, and about 10^{-5} for the method of order 4). The DMV methods give an energy error of the size of 10^{-13}, and the JE approach the energy error is about 10^{-16}.

In the second experiment we consider the integration of the FRB problem (2.6). In figure 2.2 we report the execution times (x-axis) against the norm of the global error at $t = 1$ (y-axis). The integration is performed on the interval
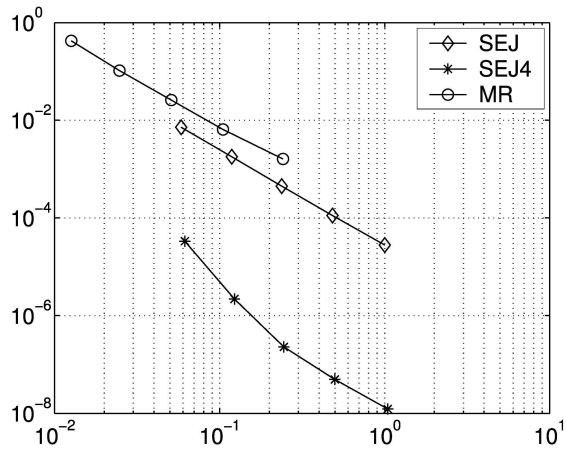
Figure 2.3: Heavy top. Execution times (x-axis) against the norm of the global error at $t = 1$ (y-axis). Integration on the interval $[0, 1]$ with different step sizes. The results are the average over 200 experiments. We consider the symmetric splitting methods SEJ and SEJ4 and the symplectic splitting MR. All the methods have order 2. The initial conditions are $\omega_0 = [10, 10, 10]^T$, $u_0 = [0, 0, 1]^T$. The principal moments of inertia are $I_1 = 1000$, $I_2 = 5000$, $I_3 = 6000$.

$[0, 1]$ with different step sizes. We denote with JEM2 og JEM4 the methods based on the use of `ellipj` in MATLAB, (for the solution of the Euler's equations), combined with a Magnus method for the computation of the orientation matrix, (Magnus method of order 2 (JEM2) and order 4 (JEM4), see section 2). The comparison is made with the MR methods of order 2 and 4. The results are given as an average over 200 repeated experiments. The initial conditions are $\pi_0 = [-1, 0, 2]^T$, Q_0 is equal to the 3×3 identity matrix, and $I_1 = 5$, $I_2 = 4$, $I_3 = 3$. Also in this case the JEM methods perform very well.

2.4.2 Heavy top experiments

In figure 2.3 we report the results of the third experiment. We consider the integration of the heavy top problem which corresponds to taking

$$V(Q) = e_3^T Q \boldsymbol{u}_0,$$

(a) Center of mass u, $h = 0.1$, SEJ

(b) SEJ, $h = 0.1$

(c) Center of mass u, $h = 0.05$, SEJ

(d) SEJ, $h = 0.05$

(e) Center of mass u, $h = 0.01$, SEJ

(f) SEJ, $h = 0.01$
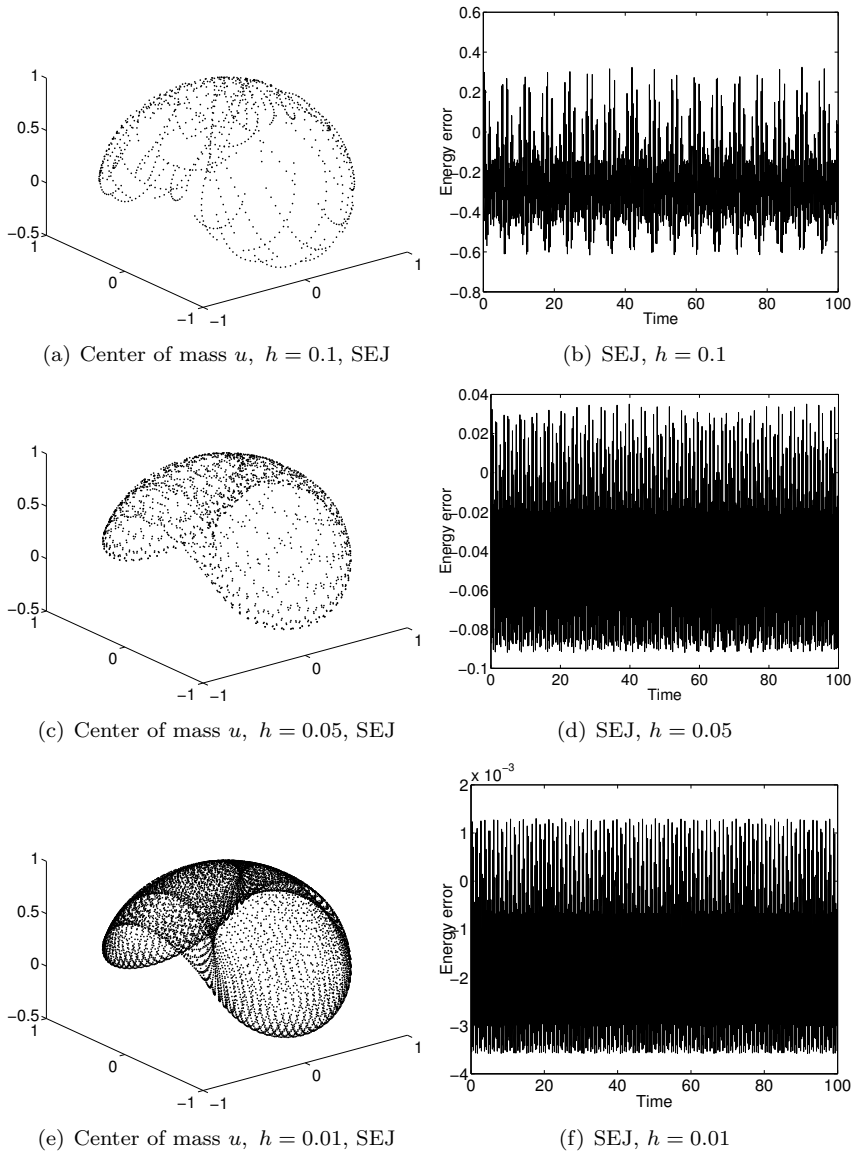
Figure 2.4: Energy error for the heavy top. Integration on the interval $[0, 100]$, using the method SEJ. $I_1 = 1000$, $I_2 = 5000$, $I_3 = 6000$, $\boldsymbol{\omega}_0 = [10, 10, 10]^T$.

(a) Center of mass u, $h = 0.1$, MR

(b) MR, $h = 0.1$

(c) Center of mass u, $h = 0.05$, MR

(d) MR, $h = 0.05$

(e) Center of mass u, $h = 0.01$, MR

(f) MR, $h = 0.01$
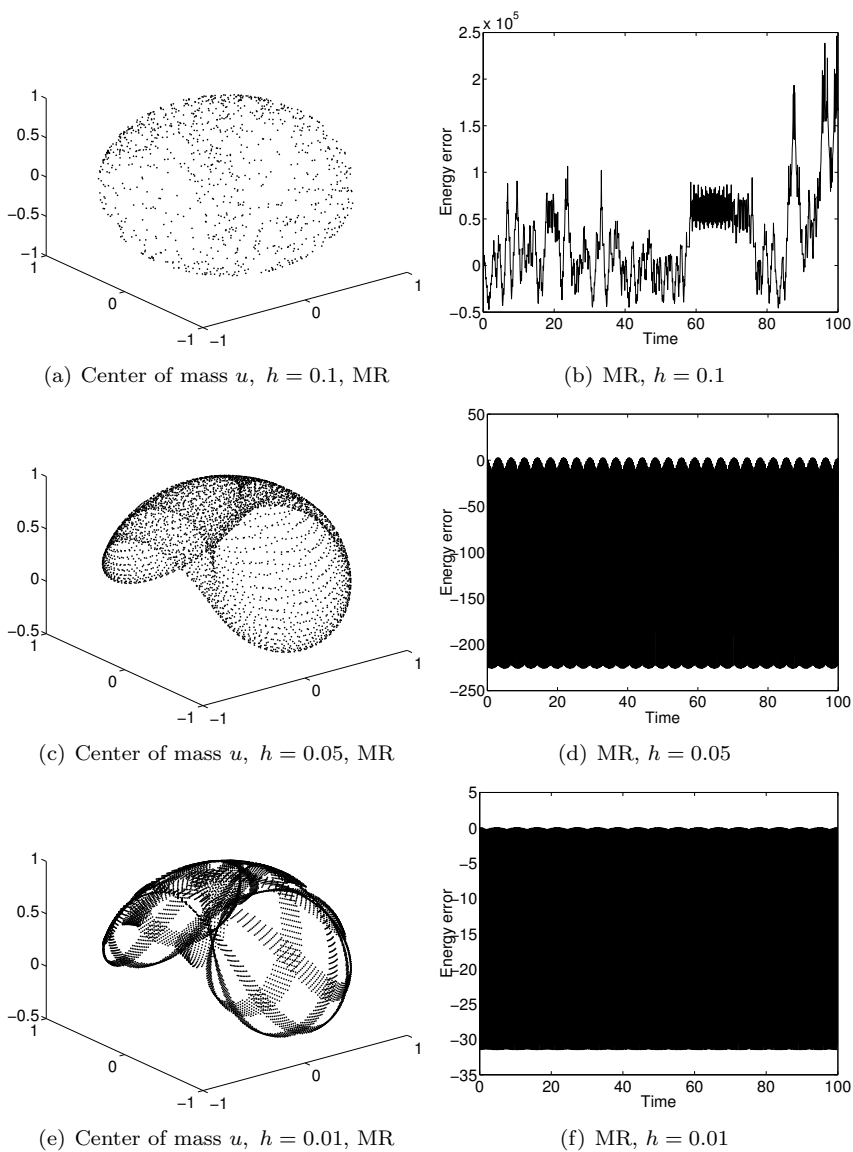
Figure 2.5: Energy error for the heavy top. Integration on the interval $[0, 100]$, using the method MR. $I_1 = 1000$, $I_2 = 5000$, $I_3 = 6000$, $\boldsymbol{\omega}_0 = [10, 10, 10]^T$.

where e_3 is the third canonical vector and u_0 is the initial position of the center of mass of the heavy top. This gives rise to a torque in (2.4) of the form

$$f(Q) = \begin{bmatrix} u_2 \\ -u_1 \\ 0 \end{bmatrix}, \quad \boldsymbol{u}(t) = Q(t)\boldsymbol{u}_0.$$

We use the second order splitting methods MR and SEJ and SEJ4 on the interval $[0, 1]$. The principal moments of inertia are $I_1 = 1000$, $I_2 = 5000$, $I_3 = 6000$, and the initial conditions are $\boldsymbol{\omega}_0 = (10, 10, 10)^T$ and $\boldsymbol{u}_0 = (0, 0, 1)^T$.

We first integrate on the interval $[0, 1]$ and compare the performance of the two splitting methods in terms of execution times against the norm of the global error, figure 2.3. In this case the advantage of the SEJ4 splitting method is quite clear while MR and SEJ perform similarly.

Next we illustrate the qualitative performance of the two methods SEJ and MR. We look at the energy error and at the numerical trajectory describing

(a)   (b)
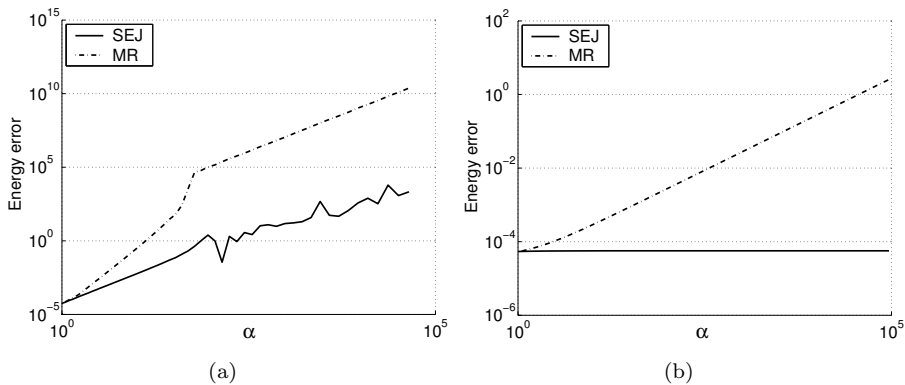
Figure 2.6: Energy error for the heavy top, $u_0 = [0, 0, 1]^T$. Integration on the interval $[0, 10]$, $h = 0.01$. In figure 2.6(a) we vary the initial angular velocity, $\boldsymbol{\omega}_0 = \alpha[1, 2, 3]^T$, and let $I_1 = 1$, $I_2 = 2$, $I_3 = 3$ fixed. In figure 2.6(b) we vary the principal moments of inertia, $I_1 = \alpha$, $I_2 = 2\alpha$, $I_3 = 3\alpha$, and let $\boldsymbol{\omega}_0 = [1, 2, 3]^T$ fixed.

the motion of the center of mass, integrating on the time interval $[0, 100]$. The results are in figures 2.4 and 2.5. We compare the results obtained by using different step sizes for MR and SEJ. For small step sizes we expect the methods to produce similar trajectories. We would like the methods reproduced the correct qualitative behavior of the solution also for bigger step sizes. For step size $h =$

0.01, figures 2.4 (f) and 2.5 (f), the two methods produce trajectories such that

$$\frac{1}{N}\sum_{n=1}^{N}\|u_{\mathrm{SEJ},n} - u_{\mathrm{MR},n}\| = \mathcal{O}(10^{-1}),$$

and $N = 100/0.01$ is the total number of steps. The energy error for SEJ is a factor 10^{-4} smaller than for MR. Increasing the step size to $h = 0.05$ and $h = 0.1$, the amplitude of the oscillations in the energy error increases for both methods. Consistently for all the experiments, SEJ has much smaller energy error than MR, figures 2.4 (b), (d) and (f), 2.5 (b), (d) and (f). For step size $h = 0.1$ the trajectory of the center of mass produced by the MR method is different from the one produced with step size $h = 0.01$, figures 2.5 (a) and (e). For the SEJ method the numerical trajectory of the center of mass maintains the same character for the different step sizes $h = 0.01$, $h = 0.05$ and $h = 0.1$, figures 2.4 (a), (c), (e).

Next, we compare the energy error between the two methods for different values of the angular velocity, figure 2.6 (a), and the inertia tensor figure 2.6 (b). The initial position of the center of mass is $\boldsymbol{u}_0 = (0, 0, 1)$. We consider the time interval $[0, 10]$ and integrate with step size $h = 0.01$. In figure 2.6 we report on the y-axis the average absolute value of the energy error,

$$\frac{1}{N}\sum_{n=1}^{N}|\mathcal{H} - \mathcal{H}_n|,$$

with $\mathcal{H}_n$ the value of the numerical energy for the methods at time step n and $\mathcal{H}$ the exact energy value, and $N = 10/0.01 = 1000$. On the x-axis we report the value of a parameter α used for varying the initial angular velocity $\boldsymbol{\omega}_0 = \alpha[1, 2, 3]^T$, with fixed principal moments of inertia $I_1 = 1$, $I_2 = 2$, $I_3 = 3$, figure 2.6 (a). In figure 2.6 (b) α is instead used to vary the principal moments of inertia $I_1 = \alpha$, $I_2 = 2\alpha$, $I_3 = 3\alpha$ while keeping $\boldsymbol{\omega}_0 = [1, 2, 3]^T$ fixed. From the two plots in figure 2.6 it appears that the energy error for the SEJ method is smaller compared to the MR method in some cases. This happens when the angular velocity or inertia are large, i.e. when the external torque is relatively small compared to the momentum.

2.4.3   Third experiment

Assume μ and r are given constants and the potential energy is given by

$$V(Q) = 3\frac{\mu}{2r^3}(Qe_3)^T TQe_3,$$

where T is the inertia tensor and Qe_3 is the third column of Q. The torque $f(Q)$ in equation (2.5) is here given by

$$f(Q) = 3\frac{\mu}{r^3}(Qe_3) \times (TQe_3).$$

(a) Body frame Qe_3, $h = 0.1$, MR

(b) Relative energy error MR, $h = 0.1$

(c) Body frame Qe_3, $h = 0.1$, SEJ

(d) Relative energy error SEJ, $h = 0.1$

(e) Body frame Qe_3, $h = 0.1$, SEJ4

(f) Relative energy error SEJ4, $h = 0.1$
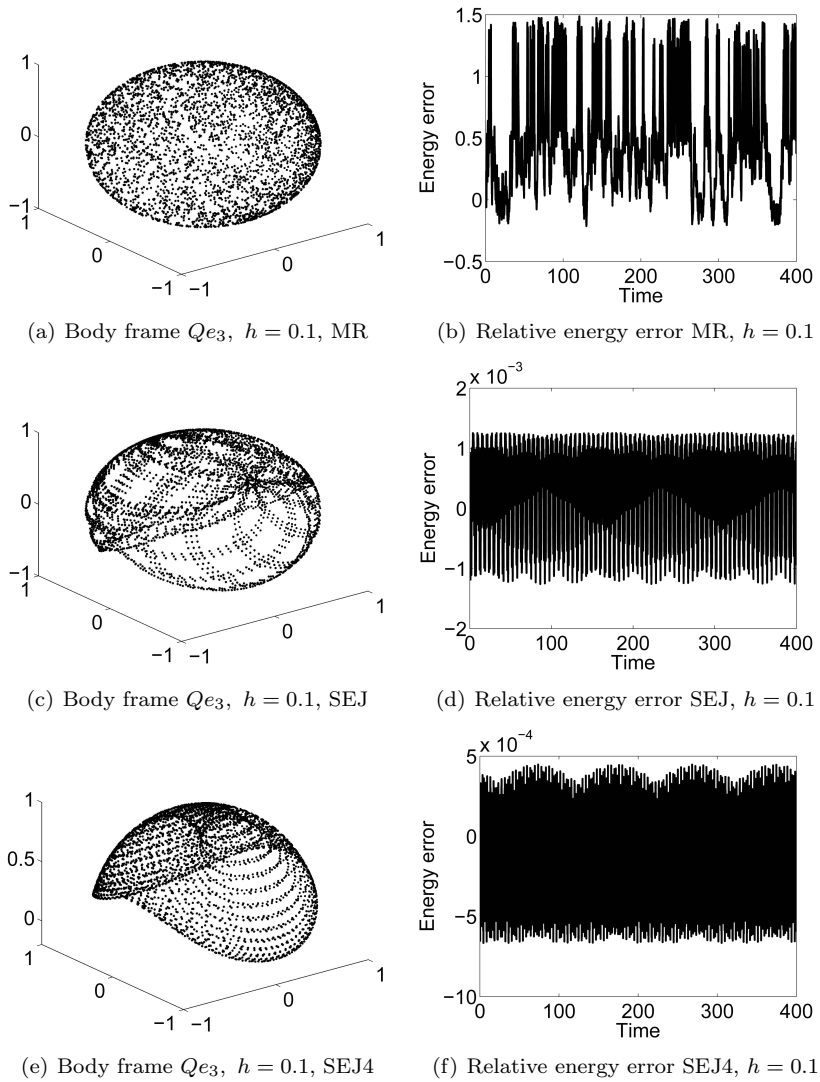
Figure 2.7: Plot of Qe_3 and the relative energy error for the satellite simulation. Integration on the interval $[0, 400]$ with $h = 0.1$, using the method MR, SEJ and SEJ4 (SEJ with Magnus method of order 4 for the rotation matrix Q). The principal moments of inertia are $I_1 = 1.7 \cdot 10^4$, $I_2 = 3.7 \cdot 10^4$, $I_3 = 5.4 \cdot 10^4$. The initial angular velocity is $\boldsymbol{\omega}_0 = [15, -15, 15]^T$ and $Q(0)$ is the 3×3 identity matrix.

This test problem is a simplified version of the model describing the motion of a satellite in a circular orbit of radius r around the earth, [11]. In our test problem the energy is preserved. We take $\mu = GM$ where G is the gravitational constant and M is the mass of the earth.

Recall that we indicate with SEJ4 the second order symmetric splitting method where the rotation matrix Q is approximated with Magnus method of order 4, while for the method SEJ the rotation matrix Q is approximated with a second order Magnus method as in (2.9).

In the first experiment on the satellite model we compare the methods MR, SEJ and SEJ4. The inertia moments are chosen to be

$$I_1 = 1.7 \cdot 10^4, \quad I_2 = 3.7 \cdot 10^4, \quad I_3 = 5.4 \cdot 10^4,$$

the initial condition for the angular velocity is

$$\boldsymbol{\omega}_0 = [15, -15, 15]^T,$$

and $Q(0) = I$ (the identity matrix). Similar values are considered for tests performed in [16]. We have $\mu = GM = 3.986 \times 10^{14}$, $r = 1.5 \times 10^5$. We integrate on the interval $[0, 400]$ for two different step sizes $h = 0.1$ and $h = 0.05$. In figure 2.7, the step size is $h = 0.1$. Figures 2.7 (a), (c), (e) in the left column show the trajectory of described by the vector Qe_3. The method SEJ4 gives the best results.

In the right column of figure 2.7, the energy error for the three methods is presented. Both SEJ and SEJ4 preserve the energy much better than the MR method.

In figure 2.8, the step size is $h = 0.05$. Here the three different methods perform similarly. Also in this case the SEJ methods give better energy preservation compared to MR.

In some of the presented experiments we have considered different orderings of the elementary flows which define the MR methods, this has not given significant differences in the results. An analysis of how different compositions of the flows can influence the size of the energy error can be found in [6]. We do not exclude that appropriate orderings of the flows can give improved performance for the MR splitting in some cases.

2.5   Conclusions

In this paper we presented a symmetric splitting method for the integration of rigid body problems subject to external forces. The numerical strategy is based on the use of available efficient algorithms for the computation of Jacobi elliptic functions. We compared the method with a similar symplectic splitting

method of [18] and [5]. In many of the performed experiments the presented symmetric splitting is more efficient then the symplectic splitting. Moreover the new method presents in many experiments a better energy conservation. This happens especially for problems where the principal moments of inertia are of large size.

2.6 Acknowledgments

Bibliography

[1] M. Abramowitz and I. A. Stegun. *Handbook of mathematical functions with formulas, graphs, and mathematical tables*, volume 55 of *National Bureau of Standards Applied Mathematics Series, 55*. Reprint of the 1972 edition. Dover Publications, Inc., New York, 1992.

[2] G. Benettin, A.M. Cherubini, and F. Fassó. A changing-chart symplectic algorithm for rigid bodies and other hamiltonian systems on manifolds. *SIAM J. Sci. Comp.*, 23(4):1189–1203, 2001.

[3] J. Butcher. *Numerical Methods for Ordinary Differential Equations*. Wiley, second edition edition, 2003.

[4] E. Celledoni and B. Owren. Lie group methods for rigid body dynamics and time integration on manifolds. *Comput. Methods Appl. Mech. Engrg.*, 192:421–438, 2003.

[5] A. Dullweber, B. Leimkuhler, and R. McLachlan. Symplectic splitting methods for rigid body molecular dynamics. *J. Chem. Phys.*, 107:5840–5851, 1997.

[6] F. Fassó. Comparison od splitting algorithms for the rigid body. *Journal of Computational Physics*, 189:527–538, 2003.

[7] Z. Ge and J.E. Marsden. Lie-Poisson Hamilton-Jacobi theory and Lie-Poisson integrators. *Physics Letters A*, 133(3):134–139, 1988.

[8] M. Geradin and A. Cardona. *Flexible Multibody Dynamics*. Wiley and Sons Ltd., 2001.

[9] E. Hairer, C. Lubich, and G. Wanner. *Geometric numerical integration*, volume 31 of *Springer series in compuitational mathematics*. Springer, 2002.

[10] B. Leimkuhler and S. Reich. *Simulating Hamiltonian Dynamics*, volume 14 of *Cambridge Monographs on Applied and Computational Mathematics*. Cambridge University Press, first edition edition, 2004.

[11] M. Leok, T. Lee, and N.H. McClamroch. Attitude maneuvers of a rigid spacecraft in a circular orbit. In *Proc. American Control Conf.*, 2005. Submitted.

[12] D. Lewis and J. C. Simo. Conserving algorithms for the dynamics of Hamiltonian systems of Lie groups. *J. Nonlinear Sci.*, 4:253–299, 1994.

[13] J. E. Marsden and T. S. Ratiu. *Introduction to Mechanics and Symmetry*. Springer-Verlag, 1994.

[14] R. I. McLachlan. Explicit Lie-Poisson integration and the Euler equations. *Physical Review Letters*, 71:3043–3046, 1993.

[15] R. I. McLachlan and A. Zanna. The discrete Moser–Veselov algorithm for the free rigid body, revisited. *Found. of Comp. Math.*, 5(1):87–123, 2005.

[16] J.Wm. Mitchell. *A simplified variation of parameters solution for the motion of an arbirarily torqued mass asymmetric rigid body*. PhD thesis, University of Cincinnati, 2000.

[17] J. Moser and A. Veselov. Discrete versions of some classical integrable systems and factorization of matrix polynomials. *J. of Comm. Math. Phys.*, 139(2):217–243, 1991.

[18] S. Reich. Symplectic integrators for systems of rigid bodies. Integration algorithms and classical mechanics (Toronto, ON, 1993). *Fields Inst. Commun.*, 10:181–191, 1996.

[19] K. Sohlberg, R. E. Tuzunand, G. Sumpter, and D. W. Noid. Application of rigid-body dynamics and semiclassical mechanics to molecular bearings. *Nanotechnology*, 8:103–111, 1997.

(a) Body frame Qe_3, $h = 0.05$, MR

(b) Relative energy error MR, $h = 0.05$

(c) Body frame Qe_3, $h = 0.05$, SEJ

(d) Relative energy error SEJ, $h = 0.05$

(e) Body frame Qe_3, $h = 0.05$, SEJ4

(f) Relative energy error SEJ4, $h = 0.05$
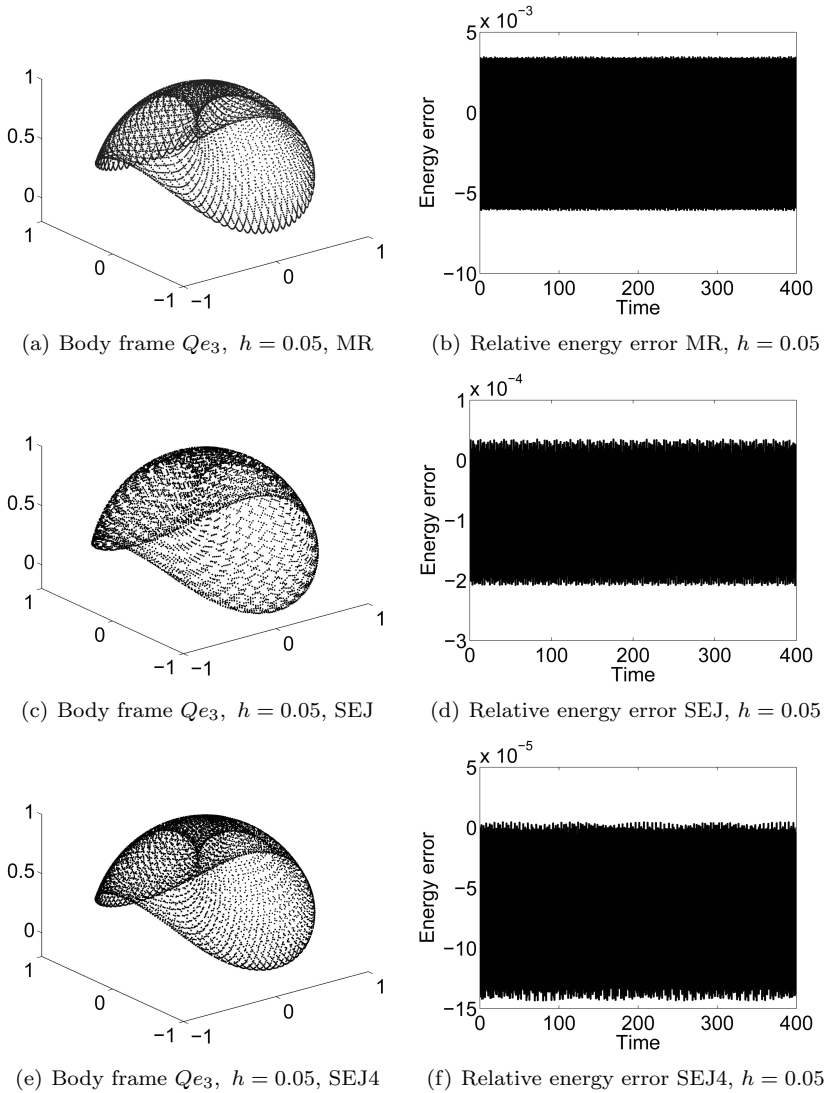
Figure 2.8: Plot of Qe_3 and the relative energy error for the satellite simulation. Integration on the interval $[0, 400]$, using the method MR, SEJ and SEJ4 (SEJ with Magnus method of order 4 for the rotation matrix Q). The principal moments of inertia are $I_1 = 1.7 \cdot 10^4$, $I_2 = 3.7 \cdot 10^4$, $I_3 = 5.4 \cdot 10^4$. The initial angular velocity is $\boldsymbol{\omega}_0 = [15, -15, 15]^T$ and $Q(0)$ is the 3×3 identity matrix.

Paper II

The exact computation of the free rigid body motion and its use in splitting methods

E. Celledoni, F. Fassò, N. Säfström and A. Zanna.

Chapter 3

The exact computation of the free rigid body motion and its use in splitting methods

ABSTRACT. This article investigates the use of the computation of the exact free rigid body motion as a component of splitting methods for rigid bodies subject to external forces. We review various matrix and quaternion representations of the solution of the free rigid body equation, which involve Jacobi elliptic functions and elliptic integrals, and are amenable to numerical computations. We consider implementations which are exact (i.e. computed to machine precision), and semi-exact (i.e. approximated via quadrature formulas). We perform a set of extensive numerical comparisons with state of the art geometrical integrators for rigid bodies, such as the preprocessed discrete Moser–Veselov method. Our numerical simulations indicate that these techniques, combined with splitting methods, *can* be favorably applied to the numerical integration of torqued rigid bodies.

3.1   Introduction

The accurate and efficient integration of the equations of motion of a rigid body under the influence of conservative forces is of great interest in various fields,

particularly mechanics and molecular dynamics (see e.g. [17]). Splitting algorithms are frequently used: the Hamiltonian $H = T + V$, where T is the kinetic energy and V is the potential energy, is written as the sum of integrable terms, whose individual flows can be computed accurately and efficiently (see [11, 21] for background on splitting methods).

If the body has two equal moments of inertia, then the flow of T, namely the flow of the *free rigid body*, involves only trigonometric functions. Therefore splittings based on the computations of the flows of T and of V are widely used, see e.g. [28, 8, 3]. If the body has three different moments of inertia, instead, it is common practice to further split the flow of T in a number of simpler flows, each of which is computable in terms of trigonometric functions, see [28, 20, 26, 8, 9]. However, it is a classical result which dates back to Legendre and Jacobi [13] that, even in the case of three distinct moments of inertia, the flow of the free rigid body can be explicitly integrated in terms of special functions—Jacobi elliptic functions for the angular momentum equation and elliptic integrals or theta functions for the attitude equation, see e.g. [2, 31, 16, 14]. Hence, the flow of T is numerically computable and can be used as a component of splitting algorithms. Because of this there has recently been a renewal of interest in the exact integration of the free rigid body and in its use in splitting methods, see for example [6, 29, 30].

The aim of this article is to investigate the potentialities of this approach through extended comparisons with other existing methods, particularly with those which appear to be the state of the art for the integration of the free rigid body with distinct moments of inertia, that is, a number of splitting algorithms [28, 20, 26, 8] and the so called 'preprocessed discrete Moser–Veselov' method of [12]. The latter method consists of applying the classical discrete Moser–Veselov algorithm, [24], to a free rigid body whose moments of inertia have been suitably modified. This produces high order approximations of the solution of the original free rigid body problem. The modified moments of inertia depend on the initial conditions through the integrals of motion and are given by series expansions in powers of the time-step. Truncations of these series produce integrators of arbitrarily high orders at a very moderate increase in computational cost. See also [22] for an earlier version of this approach.

The rigid body motion can be described in a variety of ways, for example using Euler angles, rotation matrices, and quaternions. A variety of expressions of the solution of the equations of motion has been given in each case. In Section 2 we derive expressions of the solution which are amenable for numerical computations, using both rotation matrices and quaternions (as they are generally preferred to Euler angles in numerical algorithms), and we discuss the link between them. Even though this is of course nothing else than a revisitation of classical material, we add a unified and mathematically precise treatment. We also discuss the relationship to other approaches known in the literature [15, 29].

We consider the implementation of two of these algorithms, one with rotation matrices and one with quaternions. They both use the elliptic integral of the third kind, and to compute this function we consider two strategies. One is *exact*, that is, computes the required functions to machine precision by means of the well-known Carlson's method, [25]. The other, that we call *semi-exact*, uses Gaussian quadrature of arbitrarily high order and produces high order approximations of the solution of the free rigid body. At the price of making the error in the evaluation of the integral depending on the step-size of integration, this allows a substantial reduction of the computational cost.

In section 3 we perform numerical experiments. In particular, in Section 3.2 we consider the free rigid body and compare the methods with those of [12]. We investigate how the different methods perform for different choices of the moments of inertia. It should be noted that, as far as the free rigid body is concerned, an obvious yet important feature of the exact methods is that they can be applied with any value of the time-step, while approximate and semi-exact methods must be applied with small enough time-steps in order to achieve a desired accuracy. Furthermore, implicit methods, like those of [12], use fixed-point iteration, which might require small step-sizes to converge. These numerical comparisons give some indication on the potentiality of exact and semi-exact algorithms as components of splitting methods for forced rigid bodies. In fact, compared to approximate methods, exact and semi-exact methods are more robust in their dependence on the size of the time-step. In particular, these methods perform better, compared to others, when using large step-sizes.

Next, in Sections 3.3 and 3.4 we investigate numerically the use of exact and semi-exact methods as components of splitting methods for the integration of some problems involving rigid bodies subject to external forces. Specifically, we consider some sample cases with and without a fixed point and a case from molecular dynamics. In molecular dynamics situations the large number of particles implies that most of the computation time is spent to evaluate the interacting forces, so that an increase in the time spent to update the individual rigid molecules' state can be compensated by the advantage given by the use of larger step-sizes.

Altogether, our conclusion is that the implementation of the exact solution of the free rigid body is in general a competitive approach compared to other numerical methods, which is worth of consideration.

3.2 The exact solution for the free rigid body

3.2.1 The equations of motion

The configuration of a rigid body with a fixed point is determined by the rotation which transforms a chosen orthonormal frame $\{\boldsymbol{E}_1^s, \boldsymbol{E}_2^s, \boldsymbol{E}_3^s\}$ fixed in space into a chosen orthonormal frame $\{\boldsymbol{E}_1^b, \boldsymbol{E}_2^b, \boldsymbol{E}_3^b\}$ attached to the body, both having the origin in the body's fixed point. We assume that $\boldsymbol{E}_1^b, \boldsymbol{E}_2^b, \boldsymbol{E}_3^b$ are principal axes of inertia of the body. As is customary, we identify all vectors with their representatives in the body base, that we denote with lowercase fonts (that is, $\boldsymbol{v} = (v_1, v_2, v_3)^T$ is the body representative of $\boldsymbol{V} = \sum_i v_i \boldsymbol{E}_i^b$) and denote by $\boldsymbol{e}_1, \boldsymbol{e}_2, \boldsymbol{e}_3$ the vectors of the canonical basis of $\mathbb{R}^3$. The configuration of the body is thus determined by the attitude matrix $Q \in \mathrm{SO}(3)$ which transforms body representives into spatial representatives of vectors; in particular, $Q\boldsymbol{e}_i^s = \boldsymbol{e}_i$ for $i = 1, 2, 3$.

If $\boldsymbol{m} = (m_1, m_2, m_3)^T$ is the body representative of the angular momentum vector and $I = \mathrm{diag}(I_1, I_2, I_3)$ is the inertia tensor, then the equations of motion can be written as

$$\dot{\boldsymbol{m}} = \boldsymbol{m} \times I^{-1}\boldsymbol{m}, \tag{3.1}$$

$$\dot{Q} = Q\,\widehat{I^{-1}\boldsymbol{m}}. \tag{3.2}$$

Here $\times$ denotes the vector product in $\mathbb{R}^3$ and the hat-map $\widehat{\ } : \mathbb{R}^3 \to \mathfrak{so}(3)$ is defined as

$$\boldsymbol{v} = \begin{pmatrix} v_1 \\ v_2 \\ v_3 \end{pmatrix} \quad \mapsto \quad \widehat{\boldsymbol{v}} = \begin{pmatrix} 0 & -v_3 & v_2 \\ v_3 & 0 & -v_1 \\ -v_2 & v_1 & 0 \end{pmatrix}$$

and satisfies $\widehat{\boldsymbol{v}}\boldsymbol{u} = \boldsymbol{v} \times \boldsymbol{u}$ for all $\boldsymbol{u}, \boldsymbol{v} \in \mathbb{R}^3$.

Equation (3.1) is Euler equation (written for the angular momentum rather than for the angular velocity $\boldsymbol{\omega} = I^{-1}\boldsymbol{m}$), while (3.2) is sometimes called Arnold equation. These are the left-trivialized Hamilton equations on $T^*\mathrm{SO}(3) \approx \mathrm{SO}(3) \times \mathbb{R}^3 \ni (Q, \boldsymbol{m})$ with the kinetic energy,

$$T = \frac{m_1^2}{2I_1} + \frac{m_2^2}{2I_2} + \frac{m_3^2}{2I_3},$$

as Hamiltonian. These equations form a completely integrable Hamiltonian system—in fact, a superintegrable or noncommutatively integrable system since, besides the kinetic energy, also the three components of the spatial angular momentum vector $Q\boldsymbol{m}$ are constants of motion (see for instance [10] and references therein). In particular, the norm of the body angular momentum, $G = \|\boldsymbol{m}\|$, is a constant of motion.

As we review in this section, equations (3.1) and (3.2) can be explicitly integrated in terms of elliptic functions. The integration is done in two steps. First, Euler equation (3.1) is integrated to give $\boldsymbol{m}(t)$. Then, Arnold equation (3.2) becomes a time dependent linear equation for $Q(t)$, whose integration exploits in an essential manner the constancy of the spatial angular momentum vector. We shall review different representations of the solution, including some that use quaternions instead of rotation matrices.

Note that, due to the obvious SO(3)-symmetry and scaling invariance of equations (3.1) and (3.2), we may restrict ourselves to describe their solutions with initial conditions $(Q_0, \boldsymbol{m}_0)$ at $t = t_0$ such that

$$Q_0 = \mathbb{1}, \qquad \|\boldsymbol{m}_0\| = 1.$$

We shall indeed do so in order to keep the notational complexity to a minimum, but we shall indicate the changes which give the general solutions. Depending on notational convenience, we shall indifferently write $\boldsymbol{m}(t)$ or $\boldsymbol{m}_t$ for the value at time t of the solution of Euler equation, etc.

From now on, we tacitly assume that the three moments of inertia I_1, I_2, I_3 are pairwise distinct and we order them in ascending order, $I_1 < I_2 < I_3$.

3.2.2 Solution of Euler equation

The integration of Euler equation (3.1) is a standard matter, and we restrict ourselves to provide the result. As is well-known, Euler equation can be viewed as a Hamiltonian system with respect to the Lie–Poisson structure on $\mathbb{R}^3 \approx \mathfrak{so}(3)^*$, and has the energy T and the norm of the angular momentum, $G := \|\boldsymbol{m}\|$, as constants of motion. For given $G > 0$, the phase portrait consists of the six equilibria $\pm G e_j$, $j = 1, 2, 3$, of the four stable/unstable manifolds of the equilibria $\pm G e_2$, which are given by $2TI_2 = G^2$, and of periodic orbits which fill four disconnected regions of the sphere $G = \text{const}$. The periodic orbits satisfy either $2TI_3 > G^2 > 2TI_2$ or $2TI_2 > G^2 > 2TI_1$ and, for given T and G, there are two of them.

The expression of the periodic solutions involve the three Jacobi elliptic functions sn, cn and dn, whose definition is recalled in the Appendix. As mentioned, we consider only solutions with unit norm. Given T, define the positive constants

$$I_{jh} = |I_j - I_h|, \qquad \Delta_j = |1 - 2TI_j|, \qquad B_{jh} = \left(\frac{I_j \Delta_h}{I_{jh}}\right)^{1/2}$$

for $j, h = 1, 2, 3$, $j \neq h$, and

$$k = \left(\frac{\Delta_1 I_{32}}{\Delta_3 I_{21}}\right)^{1/2}, \quad \lambda_1 = \left(\frac{\Delta_1 I_{23}}{I_1 I_2 I_3}\right)^{1/2}, \quad \lambda_3 = \left(\frac{\Delta_3 I_{12}}{I_1 I_2 I_3}\right)^{1/2}$$

that we shall use without reference throughout this section.

49

Proposition 3.2.1. *Let $\boldsymbol{m}_t$ be a solution of Euler equation (3.1) with unit norm and energy T.*

(i) If $2TI_2 > 1 > 2TI_1$, then

$$\boldsymbol{m}_t = \Big(\sigma B_{13}\, \mathrm{dn}(\lambda t - \nu, k)\,,\ B_{21}\, \mathrm{sn}(\lambda t - \nu, k)\,,\ B_{31}\, \mathrm{cn}(\lambda t - \nu; k)\Big)^T, \quad (3.3)$$

with $\lambda = \sigma\lambda_3$, for some $\nu \in \mathbb{R}$ and $\sigma = \pm 1$.

(ii) If $2TI_2 < 1 < 2TI_3$, then

$$\boldsymbol{m}_t = \Big(B_{13}\, \mathrm{cn}(\lambda t - \nu, k^{-1})\,,\ B_{23}\, \mathrm{sn}(\lambda t - \nu, k^{-1})\,,\ \sigma B_{31}\, \mathrm{dn}(\lambda t - \nu, k^{-1})\Big)^T,$$

with $\lambda = \sigma\lambda_1$, for some $\nu \in \mathbb{R}$ and $\sigma = \pm 1$.

(iii) If $2TI_2 = 1$ and $\boldsymbol{m}_t$ is not an equilibrium solution, then

$$\boldsymbol{m}_t = \Big(\sigma' B_{13}\, \mathrm{sech}(\lambda t - \nu)\,,\ \tanh(\lambda t - \nu)\,,\ \sigma' B_{31}\, \mathrm{sech}(\lambda t - \nu)\Big)^T,$$

with $\lambda = \sigma\lambda_3$, for some $\nu \in \mathbb{R}$, $\sigma = \pm 1$ and $\sigma' = \pm 1$.

The proof of these expressions reduces to differentiation, see e.g. [16]. Solutions on the stable/unstable manifolds have been included mostly for completeness, as their need in numerical computations is quite rare. Note that in the first two cases the phase ν can be taken modulo the period of the Jacobi elliptic functions.

Remark: Solutions with norm G are obtained from the formulas of proposition 3.2.1 with the substitutions $\boldsymbol{m} \mapsto G\boldsymbol{m}$ and $T \mapsto T/G^2$.

3.2.3   Integration of the rotation matrix

There are various derivations of the solution $t \mapsto Q_t$ of equation (3.2) for the attitude matrix. They all have in common the use of the constancy of the angular momentum vector in space to reduce the determination of Q_t to the determination of a planar rotation which, thanks to the knowledge of the solution of Euler equation, reduces to the evaluation of the integral of a known function. The procedure is more easily explained in terms of space vectors, rather than of their body representatives.

Let $\boldsymbol{M}$ be the angular momentum vector, that as above we assume of unit norm, $\mathcal{B}^s = \{\boldsymbol{E}_1^s, \boldsymbol{E}_2^s, \boldsymbol{E}_3^s\}$ be the spatial frame and $\mathcal{B}^b = \{\boldsymbol{E}_1^b, \boldsymbol{E}_2^b, \boldsymbol{E}_3^b\}$ be the body frame. $\boldsymbol{M}$ and $\mathcal{B}^s$ are fixed in space, while $\mathcal{B}^b$ changes with time. Consider any rotation $\mathcal{P}_t$ which takes $\boldsymbol{M}$ into the position of $\boldsymbol{E}_3^b$ at time t; this rotation

depends on t and its inverse transforms the body basis $\mathcal{B}^b$ into a certain orthonormal frame $\mathcal{B}_t = \{\boldsymbol{V}_t, \boldsymbol{W}_t, \boldsymbol{M}\}$. Similarly, let $\mathcal{R}$ be a (time-independent) rotation which transforms $\boldsymbol{E}_3^s$ into $\boldsymbol{M}$, and hence the spatial basis $\mathcal{B}^s$ into a certain orthonormal frame $\mathcal{B}' = \{\boldsymbol{V}', \boldsymbol{W}', \boldsymbol{M}\}$. Since the frames $\mathcal{B}'$ and $\mathcal{B}_t$ have the $\boldsymbol{M}$ axis in common, there is a (time-dependent) rotation $\mathcal{Y}_t$ of axis $\boldsymbol{M}$ which transforms the former into the latter. Therefore, the rotation $\mathcal{Q}_t = \mathcal{R} \circ \mathcal{Y}_t \circ \mathcal{P}_t$ transforms the spatial basis into the body basis.

This procedure is not unique in that it depends on the choice of $\mathcal{P}_t$ and $\mathcal{R}$ but has the advantage that, for each such choice, the determination of $\mathcal{Q}_t$ reduces to the determination of a rotation about a known axis, that is, of an angle. Note that, if $\mathcal{Q}_t$ equals the identity at a certain time t_0, as we may and do assume, then it is possible to choose $\mathcal{R} = \mathcal{P}_{t_0}^{-1}$ and, correspondingly, $\mathcal{Y}_{t_0} = \mathbb{1}$.

Translated into body coordinates, this procedure leads to a representation of the attitude matrix Q_t as the product $P_{t_0}^T Y_t P_t$ with $P_t, Y_t \in \mathrm{SO}(3)$ such that

$$P_t \boldsymbol{m}_t = \boldsymbol{e}_3 \quad \text{and} \quad Y_t \boldsymbol{e}_3 = \boldsymbol{e}_3 \quad \forall t, \quad Y_{t_0} = \mathbb{1}. \tag{3.4}$$

We begin by giving an expression for the angle ψ_t of the rotation Y_t as a function of P_t. For shortness, we do it only in case (i) of proposition 3.2.1.

Here and in the following we denote by a dot the Euclidean scalar product in $\mathbb{R}^3$ (and later on also in $\mathbb{R}^4$). Moreover, we use the inner product

$$\langle A, B \rangle := \frac{1}{2} \mathrm{tr}\,(A^T B)$$

on the space of 3×3 skew-symmetric matrices. Note that $\langle \widehat{u}, \widehat{v} \rangle = u \cdot v$ for all $u, v \in \mathbb{R}^3$.

Proposition 3.2.2. *Consider a solution $\boldsymbol{m}_t$ of Euler equation with unit norm. Let $P_t, Y_t \in \mathrm{SO}(3)$ be smooth functions which satisfy (3.4) and write $Y_t = \exp(\psi_t \widehat{\boldsymbol{e}}_3)$ for some real function ψ_t. Then*

$$Q_t := P_{t_0}^T Y_t P_t \tag{3.5}$$

is the solution of (3.2) with initial datum $Q_{t_0} = \mathbb{1}$ if and only if

$$\psi_t = \int_{t_0}^t \left(2T + \langle \widehat{\boldsymbol{e}_3}, P_s \dot{P}_s^T \rangle\right) ds \quad (\mathrm{mod}\, 2\pi) \tag{3.6}$$

or equivalently, if $\boldsymbol{v}_t$ and $\boldsymbol{w}_t$ are the first two columns of P_t^T,

$$\psi_t = \int_{t_0}^t \left(2T + \boldsymbol{w}_s \cdot \dot{\boldsymbol{v}}_s\right) ds \quad (\mathrm{mod}\, 2\pi). \tag{3.7}$$

Proof. Let $\boldsymbol{\omega}_t = I^{-1}\boldsymbol{m}_t$ be the angular velocity. Under hypotheses (3.4), the matrix Q_t as in (3.5) satisfies $Q_{t_0} = \mathbb{1}$ if and only if $\psi_{t_0} = 0$. Thus, it suffices to prove that $Q_t = P_{t_0}^T Y_t P_t$ satisfies $\dot{Q}_t = Q_t\widehat{\boldsymbol{\omega}}_t$ if and only if

$$\dot{\psi}_t = 2T + \langle\widehat{\boldsymbol{e}_3}, P_t\dot{P}_t^T\rangle. \tag{3.8}$$

For simplicity, we omit the indication of the dependency on t. Since $\dot{Y} = \dot{\psi}Y\widehat{\boldsymbol{e}_3}$, differentiating equation (3.5) gives $\dot{Q} = QP^T(\dot{\psi}\widehat{\boldsymbol{e}_3} + \dot{P}P^T)P$. Hence, $\dot{Q} = Q\widehat{\boldsymbol{\omega}}$ if and ony if $\widehat{\boldsymbol{\omega}} = P^T(\dot{\psi}\widehat{\boldsymbol{e}_3} + \dot{P}P^T)P$. Since $P\widehat{\boldsymbol{u}}P^T = \widehat{P\boldsymbol{u}}$ for all $P \in \mathrm{SO}(3)$ and $\boldsymbol{u} \in \mathbb{R}^3$, this condition is equivalent to $\dot{\psi}\widehat{\boldsymbol{e}_3} = \widehat{P\boldsymbol{\omega}} - \dot{P}P^T$, namely $\dot{\psi} = \langle\widehat{\boldsymbol{e}_3}, \widehat{P\boldsymbol{\omega}} + P\dot{P}^T\rangle$ given that the matrices $\widehat{\boldsymbol{e}_1}, \widehat{\boldsymbol{e}_2}, \widehat{\boldsymbol{e}_3}$ form an orthonormal set for the inner product $\langle\ ,\ \rangle$ and $\dot{P}P^T$ is skew-symmetric. The proof of (3.8) is concluded by observing that $\langle\widehat{\boldsymbol{e}_3}, \widehat{P\boldsymbol{\omega}}\rangle = \boldsymbol{e}_3 \cdot P\boldsymbol{\omega} = P^T\boldsymbol{e}_3 \cdot \boldsymbol{\omega} = \boldsymbol{m} \cdot \boldsymbol{\omega} = 2T$.

Let us now prove (3.7). From $P^T\boldsymbol{e}_3 = \boldsymbol{m}$ it follows that $P = [\boldsymbol{v}, \boldsymbol{w}, \boldsymbol{m}]^T$ with orthonormal vectors $\boldsymbol{v}, \boldsymbol{w}, \boldsymbol{m}$ and one computes $P\dot{P}^T = -\boldsymbol{w}\cdot\dot{\boldsymbol{m}}\widehat{\boldsymbol{e}_1} + \boldsymbol{v}\cdot\dot{\boldsymbol{m}}\widehat{\boldsymbol{e}_2} - \boldsymbol{v}\cdot\dot{\boldsymbol{w}}\widehat{\boldsymbol{e}_3}$. Thus $\langle\widehat{\boldsymbol{e}_3}, P\dot{P}^T\rangle = -\boldsymbol{v}\cdot\dot{\boldsymbol{w}} = \dot{\boldsymbol{v}}\cdot\boldsymbol{w}$. $\qquad\square$

Note that any unit vector $\boldsymbol{v}_t$ orthogonal to $\boldsymbol{m}_t$ can be used to construct the matrix $P_t = [\boldsymbol{v}_t, \boldsymbol{w}_t, \boldsymbol{m}_t]^T$, where $\boldsymbol{w}_t = \boldsymbol{m}_t \times \boldsymbol{v}_t$. Since $\|\boldsymbol{m}_t\| = 1$ implies that $\dot{\boldsymbol{m}}_t$ is orthogonal to $\boldsymbol{m}_t$, a possible choice is that of taking $\boldsymbol{v}_t$ aligned with $\dot{\boldsymbol{m}}_t$. We specialize the expression of the angle ψ_t corresponding to this choice. For another choice, see section 2.6. The expression of ψ uses the elliptic integral of the third kind, Π, and the amplitude function am, whose definitions are recalled in the Appendix.

Corollary 3.2.3. *Consider a solution $\boldsymbol{m}_t$ of Euler equation as in (3.3), with unit norm and energy T such that $2TI_2 > 1 > 2TI_1$. If, in proposition 3.2.2, $\boldsymbol{v}_t = \|\dot{\boldsymbol{m}}_t\|^{-1}\dot{\boldsymbol{m}}_t$ then*

$$\psi_t = 2T(t - t_0) + \frac{\Delta_2}{\lambda I_2}\left[\Pi\big(\mathrm{am}(\lambda t - \nu), n, k\big) - \Pi\big(\mathrm{am}(\lambda t_0 - \nu), n, k\big)\right] \tag{3.9}$$

with k, λ and ν as in (3.3) and $n = B_{23}^{-1}$.

Proof. The orthogonality of $\boldsymbol{w} = \boldsymbol{m} \times \boldsymbol{v}$ and $\dot{\boldsymbol{m}}$ implies $\boldsymbol{w} \cdot \dot{\boldsymbol{v}} = \boldsymbol{w} \cdot \ddot{\boldsymbol{m}}/\|\dot{\boldsymbol{m}}\|$. Since $\ddot{\boldsymbol{m}} = \frac{d}{dt}(\boldsymbol{m} \times \boldsymbol{\omega}) = \dot{\boldsymbol{m}} \times \boldsymbol{\omega} + \boldsymbol{m} \times \dot{\boldsymbol{\omega}}$ and $\dot{\boldsymbol{\omega}} = \|\dot{\boldsymbol{m}}\|I^{-1}\boldsymbol{v}$, this gives $\boldsymbol{w} \cdot \dot{\boldsymbol{v}} = \boldsymbol{v} \cdot I^{-1}\boldsymbol{v} - \boldsymbol{\omega} \cdot \boldsymbol{m} = \boldsymbol{v} \cdot I^{-1}\boldsymbol{v} - 2T$. But from proposition 3.2.2 we know that $\dot{\psi} = 2T + \boldsymbol{w} \cdot \dot{\boldsymbol{v}}$. Hence $\dot{\psi} = \boldsymbol{v} \cdot I^{-1}\boldsymbol{v}$. Inserting $\dot{\boldsymbol{m}} = \boldsymbol{m} \times I^{-1}\boldsymbol{m}$ into $\boldsymbol{v}$ this becomes

$$\dot{\psi} = \frac{I_1(I_{23}m_2m_3)^2 + I_2(I_{13}m_1m_3)^2 + I_3(I_{12}m_1m_2)^2}{(I_1I_{23}m_2m_3)^2 + (I_2I_{13}m_1m_3)^2 + (I_3I_{12}m_1m_2)^2}.$$

Using the constancy of T and G^2 $(= 1)$ to express m_1^2 and m_3^2 in terms of T and m_2^2, and then using the expression of m_2 from (3.3), this gives

$$\dot{\psi} = 2T - \frac{I_2 \Delta_1 \Delta_2 \Delta_3}{I_2^2 \Delta_1 \Delta_3 - I_{12} I_{23} m_2^2} = 2T + \frac{\Delta_2 / I_2}{1 - B_{23}^{-2} \operatorname{sn}^2(\lambda t - \nu)} \; .$$

The proof is concluded by integrating between t_0 and t, taking into account equation (3.36) of the Appendix. $\qquad \square$

This algorithm equals that of [16], except for the sign of ψ. A similar algorithm is given in [7].

Remark: If $2TI_3 > 1 > 2TI_2$ then ψ_t is as in (3.9) with k replaced by k^{-1}, with λ and ν as in point (ii) of proposition 3.2.2, and with $n = B_{21}^{-1}$.

3.2.4 The equations of motion in quaternionic form

We consider now the quaternionic formulation of the free rigid body. For general references on quaternions, see e.g. [19]. Quaternions (of unit norm) are the points of the three sphere $S^3 = \{q \in \mathbb{R}^4 \; : \; \|q\| = 1\}$ equipped with a certain Lie group structure. As is customary, we write $q = (q_0, \boldsymbol{q}) \in \mathbb{R} \times \mathbb{R}^3$ and refer to q_0 and $\boldsymbol{q} = (q_1, q_2, q_3)$ as to the scalar and vector parts of q. Then

$$S^3 = \{q = (q_0, \boldsymbol{q}) \in \mathbb{R} \times \mathbb{R}^3 \; : \; q_0^2 + \|\boldsymbol{q}\|^2 = 1\}$$

is a Lie group with product

$$(p_0, \boldsymbol{p})(q_0, \boldsymbol{q}) := (p_0 q_0 - \boldsymbol{p} \cdot \boldsymbol{q}, p_0 \boldsymbol{q} + q_0 \boldsymbol{p} + \boldsymbol{p} \times \boldsymbol{q}). \tag{3.10}$$

The identity element of S^3 is $e = (1, \boldsymbol{0})$ and the inverse of $q = (q_0, \boldsymbol{q}) \in S^3$ is $q^{-1} = (q_0, -\boldsymbol{q})$.

The 'Euler–Rodriguez' map $\mathcal{E} : S^3 \to SO(3)$ defined by

$$\mathcal{E}(q) = \mathbb{1} + 2q_0 \widehat{\boldsymbol{q}} + 2\widehat{\boldsymbol{q}}^2 \tag{3.11}$$

is a $2 : 1$ surjective submersion. It is not injective since $\mathcal{E}(q) = \mathcal{E}(-q)$ and each rotation matrix has two preimages. Hence, S^3 is a double covering of $SO(3)$. If $\mathcal{E}(q)$ is a rotation of angle ψ and axis $\boldsymbol{e} \in \mathbb{R}^3$, $\|\boldsymbol{e}\| = 1$, then $q = (\cos \frac{\psi}{2}, \pm \boldsymbol{e} \sin \frac{\psi}{2})$. Moreover, the map $\mathcal{E}$ is a group homomorphism since

$$\mathcal{E}(qp) = \mathcal{E}(q)\mathcal{E}(p) \quad \forall q, p \in S^3.$$

Thus, the quaternionic formulation of the equations of motion of the rigid body is a formulation on a covering space. Each motion of the rigid body in $SO(3)$

corresponds to two (non-intersecting) motions in S^3, and it is immaterial which one is considered. The 'equation of motion of the rigid body in quaternion form' is the differential equation on T^*S^3 which describes these motions. Analogously to what done in the case of SO(3), we give this equation in left-trivialized form.

The Lie algebra $\mathfrak{s}^3 = T_e S^3$ of S^3 can be identified with $\mathbb{R}^3$ equipped with the cross product as commutator. It is convenient, however, to identify $\mathfrak{s}^3$ with the subspace $\{0\} \times \mathbb{R}^3$ of $\mathbb{R}^4 = \mathbb{R} \times \mathbb{R}^3$,

$$\mathfrak{s}^3 = \left\{ u = (0, \boldsymbol{u}) \ : \ \boldsymbol{u} \in \mathbb{R}^3 \right\},$$

so as to be able to exploit the fact that the quaternion product (3.10) extends to $\mathbb{R}^4$. Note that, if $u = (0, \boldsymbol{u})$ and $v = (0, \boldsymbol{v})$ are in $\mathfrak{s}^3$, then $uv = (-\boldsymbol{u} \cdot \boldsymbol{v}, \boldsymbol{u} \times \boldsymbol{v}) \in \mathbb{R} \times \mathbb{R}^3$ need not be in $\mathfrak{s}^3$. Instead, if $u = (0, \boldsymbol{u}) \in \mathfrak{s}^3$ and $q \in S^3$, then $quq^{-1} \in \mathfrak{s}^3$, see also (3.14) below. We shall also use the Euclidean product of $\mathbb{R}^4$, that we denote by a dot.

A simple calculation shows that the derivative at the identity of the covering map $\mathcal{E} : S^3 \to SO(3)$ is the map $\mathcal{E}_* := T_e \mathcal{E} : \mathfrak{s}^3 \to \mathfrak{so}(3)$ given by

$$\mathcal{E}_*(u) = 2\widehat{\boldsymbol{u}}, \qquad u = (0, \boldsymbol{u}) \in \mathfrak{s}^3. \tag{3.12}$$

If $q_t \in S^3$ and $Q_t = \mathcal{E}(q_t)$, then $q_t^{-1} \dot{q}_t \in \mathfrak{s}^3$, $Q_t^T \dot{Q}_t \in \mathfrak{so}(3)$ and

$$\mathcal{E}_*(q_t^{-1} \dot{q}_t) = Q_t^T \dot{Q}_t. \tag{3.13}$$

By general facts about Lie groups and covering maps, the map $\mathcal{E}_*$ is a Lie algebra isomorphism and hence intertwines the two adjoint representations, that is

$$\mathcal{E}_*(quq^{-1}) = \mathcal{E}(q)\mathcal{E}(u)\mathcal{E}(q)^{-1} \qquad \forall q \in S^3, \ u \in \mathfrak{s}^3.$$

Note that this identity, (which, incidentally, can be easily verified by a direct computation), can also be written as

$$\mathcal{E}_*(quq^{-1}) = 2\widehat{\mathcal{E}(q)\boldsymbol{u}} \qquad \forall q \in S^3, \ u = (0, \boldsymbol{u}) \in \mathfrak{s}^3. \tag{3.14}$$

As a direct consequence of (3.13) and (3.14) we can now state the rigid body equations of motion on S^3:

Proposition 3.2.4. *Assume that $\boldsymbol{m}_t$ is a solution of Euler equation (3.1) and that $q_t \in S^3$ is a smooth function. Then, $Q_t := \mathcal{E}(q_t)$ is a solution of Arnold equation (3.2) if and only if*

$$\dot{q}_t = \frac{1}{2} q_t \omega_t \tag{3.15}$$

with $\omega_t = (0, I^{-1} \boldsymbol{m}_t)$.

Clearly, if q_t is a solution of (3.15) for a certain $\boldsymbol{m}_t$, then so is $-q_t$ and they project onto the same rigid body motion $\mathcal{E}(q_t)$ on SO(3). The choice of the initial condition q_{t_0} unambiguously selects one of the two. Even though we need not using this fact, we note for completeness that, written on $\mathfrak{s}^3$, that is for $m_t = (0, \boldsymbol{m}_t)$, Euler equation becomes $\dot{m}_t = \frac{1}{2}(m_t \omega_t - \omega_t m_t)$.

3.2.5 Integration of the quaternion

Solutions of (3.15) can be searched in a factorized form $q_t = p_{t_0}^{-1} y_t p_t$ analogous to that of section 3.2.3. To this end, it is sufficient to determine p_t and y_t so that $P_t := \mathcal{E}(p_t)$ and $Y_t := \mathcal{E}(y_t)$ satisfy properties (3.4).

Since $\mathcal{E}_*$ is an isomorphism, equation (3.14) shows that if $p \in \mathrm{S}^3$, $u = (0, \boldsymbol{u}) \in \mathfrak{s}^3$ and $v = (0, \boldsymbol{v}) \in \mathfrak{s}^3$ then $\mathcal{E}(p)\boldsymbol{u} = \boldsymbol{v}$ if and only if $pup^{-1} = v$. Thus, if we write

$$m_t = (0, \boldsymbol{m}_t) \in \mathfrak{s}^3, \qquad e_j = (0, \boldsymbol{e}_j) \in \mathfrak{s}^3 \qquad (j = 1, 2, 3),$$

we see that the analogues of conditions (3.4) are

$$p_t m_t p_t^{-1} = e_3 \quad \text{and} \quad y_t e_3 y_t^{-1} = e_3 \quad \forall t, \quad y_{t_0} = e. \tag{3.16}$$

(The choice $y_{t_0} = -e$ would be acceptable as well.) We can now state the analogue of the first part of proposition 3.2.2.

Proposition 3.2.5. *Consider a solution $\boldsymbol{m}_t$ of Euler equation with unit norm. Let $p_t, y_t \in \mathrm{S}^3$ be smooth functions which satisfy (3.16). Then,*

$$q_t := p_{t_0}^{-1} y_t p_t$$

satisfies (3.15) and $q_{t_0} = e$ if and only if $y_t = (\cos \frac{\psi_t}{2}, \boldsymbol{e}_3 \sin \frac{\psi_t}{2})$ with

$$\psi_t = \int_{t_0}^t \left(2T + 2e_3 \cdot p_s \dot{p}_s^{-1} \right) ds \qquad (\mathrm{mod} \, 2\pi). \tag{3.17}$$

Proof. Define $P_t := \mathcal{E}(p_t)$ and $Y_t := \mathcal{E}(y_t)$. The latter is a rotation with axis $\boldsymbol{e}_3$ if and only if $y_t = \pm(\cos \frac{\psi_t}{2}, \boldsymbol{e}_3 \sin \frac{\psi_t}{2})$ for some ψ_t, but the plus sign has to be selected in order to have $y_{t_0} = e$. Since $Y_t = \exp(\psi_t \widehat{\boldsymbol{e}}_3)$, recalling proposition 3.2.2 and observing that $q_t = p_{t_0}^{-1} y_t p_t$ is a solution of (3.15) if and only if $\mathcal{E}(q_t) = P_{t_0}^T Y_t P_t$ is a solution of (3.2), we see that all we have to prove is that the expressions (3.17) and (3.6) of the angle ψ coincide, namely that

$$2e_3 \cdot p\dot{p}^{-1} = \langle \widehat{\boldsymbol{e}}_3, P\dot{P}^T \rangle.$$

Let $P\dot{P}^T = \widehat{\boldsymbol{a}}$ with $\boldsymbol{a} \in \mathbb{R}^3$. Then, equations (3.12) and (3.13) together show that $p\dot{p}^{-1} = (0, \frac{1}{2}\boldsymbol{a})$. Hence $2e_3 \cdot p\dot{p}^{-1} = \boldsymbol{e}_3 \cdot \boldsymbol{a} = \langle \widehat{\boldsymbol{e}}_3, \widehat{\boldsymbol{a}} \rangle$. $\qquad \square$

In order to make the previous result applicable, we need to give conditions on the quaternion p_t which ensure that it satisfies $p_t m_t p_t^{-1} = e_3$ and then to express the angle ψ_t in terms of the components of p_t. This is the content of the following Lemma.

Lemma 3.2.6. *Consider a solution $\boldsymbol{m} = (m_1, m_2, m_3)^T : \mathbb{R} \to \mathbb{R}^3$ of Euler equation with unit norm and $m_3(t) \neq -1$ for all t. Then, four smooth functions $p_0, p_1, p_2, p_3 : \mathbb{R} \to \mathbb{R}$ are the components of a function $p : \mathbb{R} \to S^3$ which satisfies (3.16) if and only if*

$$p_1 = \frac{p_3 m_1 + p_0 m_2}{1 + m_3}, \qquad p_2 = \frac{p_3 m_2 - p_0 m_1}{1 + m_3}, \tag{3.18}$$

$$p_0^2 + p_3^2 = \frac{1 + m_3}{2}. \tag{3.19}$$

In that case

$$2T + 2e_3 \cdot p\dot{p}^{-1} = \frac{2T + I_3^{-1} m_3}{1 + m_3} + 4\frac{p_3 \dot{p}_0 - p_0 \dot{p}_3}{1 + m_3}. \tag{3.20}$$

Proof. A computation shows that the four components of $pm = (-\boldsymbol{p} \cdot \boldsymbol{m}, p_0 \boldsymbol{m} + \boldsymbol{p} \times \boldsymbol{m})$ equal those of $e_3 p = (-\boldsymbol{p} \cdot \boldsymbol{e}_3, p_0 \boldsymbol{e}_3 - \boldsymbol{p} \times \boldsymbol{e}_3)$ if and only p_0, p_1, p_2, p_3 satisfy (3.18). Condition (3.19) ensures that (p_0, p_1, p_2, p_3) has norm one. Next, using (3.18) one computes

$$e_3 \cdot p\dot{p}^{-1} = (p_3 \dot{p}_0 - p_0 \dot{p}_3) + (p_2 \dot{p}_1 - p_1 \dot{p}_2) = 2\frac{p_3 \dot{p}_0 - p_0 \dot{p}_3}{1 + m_3} - \frac{m_1 \dot{m}_2 - m_2 \dot{m}_1}{2(1 + m_3)}$$

and the conclusion follows observing that $m_1 \dot{m}_2 - m_2 \dot{m}_1 = \boldsymbol{e}_3 \cdot \boldsymbol{m} \times (\boldsymbol{m} \times \boldsymbol{\omega}) = 2T m_3 - \omega_3$, where as usual $\boldsymbol{\omega}$ is the angular velocity. $\qquad\square$

Thus, any choice of p_0 and p_3 satisfying (3.19) leads to a quaternionic implementation of the free rigid body motion. For instance, taking $p_0 = c_0 \sqrt{1 + m_3}$ and $p_3 = c_3 \sqrt{1 + m_3}$ with constants c_0 and c_3 such that $c_0^2 + c_3^2 = \frac{1}{2}$ leads to a particularly simple expression for $\dot{\psi}$. Taking for instance $c_0 = \frac{1}{\sqrt{2}}$ and $c_3 = 0$ gives the following:

Corollary 3.2.7. *Consider a solution $\boldsymbol{m}(t)$ of Euler equation as in (3.3), with unit norm and energy T such that $2TI_2 > 1 > 2TI_1$. Then, quaternions $p(t)$ and $y(t) = \left(\cos \frac{\psi(t)}{2}, \boldsymbol{e}_3 \sin \frac{\psi(t)}{2} \right)$ as in proposition 3.2.5 are given by*

$$p(t) = \frac{1}{\sqrt{2}} \left(\sqrt{1 + m_3(t)}, \ \frac{m_2(t)}{\sqrt{1 + m_3(t)}}, \ -\frac{m_1(t)}{\sqrt{1 + m_3(t)}}, \ 0 \right),$$

$$\psi(t) = \frac{t - t_0}{I_3} + \frac{I_{31}}{I_1 I_3 \lambda} \big[\Pi\left(\varphi(t), n, k\right) + f(t) - \Pi\left(\varphi(t_0), n, k\right) - f(t_0) \big],$$

where $\varphi(s) = \text{am}(\lambda s - \nu, k)$ with λ, k and ν as in (3.3), $n = -(B_{31}/B_{13})^2$ and

$$f(s) = B_{21}^{-1} B_{13} B_{31} \arctan\left(B_{13}^{-1} B_{21} \text{sd}(\lambda s - \nu, k)\right) .$$

Proof. If $2TI_2 > 1 > 2TI_1$ then $m_3 > -1$ for all times. With the given choice of p_0 and p_3 the right hand side of (3.20) reduces to $\frac{2T + m_3/I_3}{1 + m_3}$, namely $\frac{1}{I_3} + \frac{\Delta_3/I_3}{1 + m_3}$. From (3.3), $m_3 = a\text{cn}(\lambda t - \nu, k)$ with $a = B_{31}$. Since $0 < a < 1$, $n := \frac{a^2}{a^2 - 1} < 0$ and thus [5, page 215]

$$\int \frac{du}{1 + a\text{cn}(u, k)} = \frac{1}{1 - a^2}\left[\Pi\big(\text{am}(u, k), n, k\big) - af_1(u)\right],$$

with $f_1(u) = C\tan^{-1}(C^{-1}\text{sd}(u, k))$, $C = \left[(1 - a^2)/(k^2 + (1 - k^2)a^2)\right]^{1/2}$. The proof is concluded with a little bit of algebra. $\square$

This is a rescaled version of the algorithm presented by Kosenko in [15]. This is the algorithm we use in the numerical work of the next section.

3.2.6 Relation between quaternion and matrix algorithms

We discuss now very shortly how to translate into quaternionic form $q = p_{t_0}^{-1} y_t p_t$ a given representation $Q_t = P_{t_0}^T Y_t P_t$ of the attitude matrix as in proposition 3.2.2. This clearly reduces to determining a quaternion p_t such that $P_t = \mathcal{E}(p_t)$. This operation involves 'inverting' a two-to-one map and can of course be done only up to the overall sign of p, but this is immaterial in the present context given that the product $p_{t_0}^{-1} y_t p_t$ is independent of the sign of p.

As usual, we assume $\|\boldsymbol{m}\| = 1$ and $2TI_2 > 1 > 2TI_1$. Thus $m_3 \neq \pm 1$ and we can invoke lemma 3.2.6, which implies that a quaternion p such that $\mathcal{E}(p) = P$ is determined, up to the sign, once p_3^2 and the relative signs of p_0 and p_3 are known. If $p = (p_0, p_1, p_2, p_3)$ then, from (3.11),

$$\mathcal{E}(p) = \begin{pmatrix} 1 - 2(p_2^2 + p_3^2) & -2p_0p_3 + 2p_1p_2 & 2p_0p_2 + 2p_1p_3 \\ 2p_0p_3 + 2p_1p_2 & 1 - 2(p_1^2 + p_3^2) & -2p_0p_1 + 2p_2p_3 \\ -2p_0p_2 + 2p_1p_3 & 2p_0p_1 + 2p_2p_3 & 1 - 2(p_1^2 + p_2^2) \end{pmatrix} .$$

Equating the three diagonals entries of this matrix to those of $P = [\boldsymbol{v}, \boldsymbol{w}, \boldsymbol{m}]^T$ gives $4p_1^2 = 1 + v_1 - w_2 - m_3$, $4p_2^2 = 1 - v_1 + w_2 - m_3$ and

$$4p_3^2 = 1 - v_1 - w_2 + m_3. \tag{3.21}$$

If p_0 and p_3 are both nonzero, then their relative sign is determined by the equality

$$4p_0p_3 = v_2 - w_1,$$

which is obtained by equating entries $(1, 2)$ and $(2, 1)$ of the two matrices $\mathcal{E}(p)$ and P. As an example, the algorithm of corollary 3.2.3 uses $\boldsymbol{v} = \|\dot{\boldsymbol{m}}\|^{-1}\dot{\boldsymbol{m}} = \|\dot{\boldsymbol{m}}\|^{-1}\boldsymbol{m} \times I^{-1}\boldsymbol{m}$ and hence $\boldsymbol{w} = \boldsymbol{m} \times \boldsymbol{v} = \|\dot{\boldsymbol{m}}\|^{-1}(2T\boldsymbol{m} - I^{-1}\boldsymbol{m})$. Thus, (3.21) gives

$$p_3^2 = \frac{1 + m_3}{4} + \frac{I_{32}m_2}{4I_2 I_3 \|\dot{\boldsymbol{m}}\|} \left(m_3 - B_{32}\right).$$

The other components of the quaternion p are computed as just explained and the angle ψ is as in corollary 3.2.3.

As another example, take $\boldsymbol{v} = \frac{\boldsymbol{m} \times \boldsymbol{e}_3}{\|\boldsymbol{m} \times \boldsymbol{e}_3\|}$. Then $v_1 = (1 - m_3^2)^{-1/2}m_2$, $w_2 = (1 - m_3^2)^{-1/2}m_2 m_3$ and

$$p_3^2 = \frac{1 + m_3}{4} - \frac{m_2(1 + m_3)}{4\sqrt{1 - m_3^2}}.$$

This produces a quaternion version of the algorithm based on rotation matrices recently considered by van Zon and Schofield [29]. The rotation angle is

$$\psi = \int_{t_0}^{t} \frac{2T I_3 - m_3^2}{I_3(1 - m_3^2)}ds = \frac{t - t_0}{I_3} + \frac{I_{31}}{\lambda I_3 I_1}\left(\Pi(\text{am}(\lambda t - \nu), n, k) - \Pi(\text{am}(\lambda t_0 - \nu, n, k))\right)$$

with $n = -B_{31}^{-2}B_{13}^{-2}$.

Remark: There is another possibility for constructing a quaternion p such that $pmp^{-1} = e_3$, which is used in [15]. This is based on the fact that, given any three orthonormal vectors $\boldsymbol{v}_1, \boldsymbol{v}_2, \boldsymbol{v}_3 \in \mathbb{R}^3$ and a vector $\boldsymbol{m} \in \mathbb{R}^3$ with unit norm, one has

$$pmp^{-1} = v_3 \quad \text{with} \quad p = \frac{v_2 + v_1 m}{\|v_2 + v_1 m\|} \tag{3.22}$$

where, as usual $v_i = (0, \boldsymbol{v}_i)$ and $n = (0, \boldsymbol{m})$. Reference [15] uses $\boldsymbol{v}_3 = \boldsymbol{e}_3$, $\boldsymbol{v}_1 = \gamma_1 \boldsymbol{e}_1 + \gamma_2 \boldsymbol{e}_2$ and $\boldsymbol{v}_2 = \gamma_2 \boldsymbol{e}_1 - \gamma_1 \boldsymbol{e}_2$ with $\gamma_1, \gamma_2 \in \mathbb{R}$. It is elementary to verify (3.22) by direct computation if $\boldsymbol{v}_i = \boldsymbol{e}_i$, $i = 1, 2, 3$. Otherwise, there is a quaternion $s \in \text{S}^3$ such that $\mathcal{E}(s)\boldsymbol{e}_i = \boldsymbol{v}_i$, $i = 1, 2, 3$. Then, $p = k(se_2 s^{-1} + se_2 s^{-1}m)$ with $k = \|se_2 s^{-1} + se_2 s^{-1}m\|^{-1}$ and a simple computation shows that $v_3 p - pm = s\big[e_3(e_2 + e_1 n) - (e_2 + e_1 n)n\big]s^{-1}$ for $n = sms^{-1}$. Here, the term between square brackets vanishes by virtue of the previous observation.

3.3   Numerical experiments

3.3.1   Numerical implementation

The exact algorithms described in this paper require the computation of elliptic integrals of the first and third kind. Elliptic integrals of the first kind are computed very fast by using standard algorithms like AGM (arithmetic geometric

mean) and ascending/descending Landen trasformations [1]. These can be used also for the elliptic integral of the third kind, but their performance is not so uniform and other algorithms are preferred instead. In [29] the authors use a method based on theta functions. Our implementation makes use of Carlson's algorithms `rf`, `rj`, `rc`, that have been acclaimed to produce accurate values for large sets of parameters. These methods are described in detail in [25] and are the most common routines for elliptic integrals of the third kind in several scientific libraries.

As mentioned in the Introduction, an alternative to the exact computation of the elliptic integral of the third kind is the approximation by a quadrature method. We will refer to the methods obtained in this manner as *semi-exact* methods. These, by construction, integrate the angular momentum exactly. They also preserve Qm (because of the properties of the matrix P in Prop. 3.2.2). Moreover, they will be time-symmetric if the underlying quadrature formula is symmetric.

In [30], the integral

$$\int_{u_0}^{u} \frac{ds}{1 - n \operatorname{sn}^2 s}$$

is approximated by a quadrature based on Hermite interpolation, as the function sn and its derivative can be easily computed at the endpoints of the interval. Alternatively, one can write the same integral in the Legendre form,

$$\int_{\operatorname{am}(u_0)}^{\operatorname{am}(u)} \frac{d\theta}{(1 - n \sin^2 \theta)\sqrt{1 - k^2 \sin^2 \theta}}. \tag{3.23}$$

This format is convenient when using quadrature formulae because it requires tabulating the sine function in the quadrature nodes instead of $\operatorname{sn}(\lambda(t - \nu))$. Thus, (3.23) can be approximated as

$$\int_{\operatorname{am}(u_0)}^{\operatorname{am}(u)} f(\theta)\mathrm{d}\theta \approx \sum_{i=1}^{p} b_i f(\varphi_0 + a_i \Delta\varphi),$$

where $\Delta\varphi = \operatorname{am}(u) - \operatorname{am}(u_0)$ and b_i, a_i are weights and nodes of a quadrature formula respectively. We use Gaussian quadrature (i.e. quadrature based on orthogonal polynomials), because of its high order. In particular, Gauss–Legendre quadrature with p points attains the maximal quadrature order, $2p$. The coefficients and weights for Gaussian–Legendre quadrature method of order 10 (5 nodes) used in this paper are reported in the Appendix. Our numerical experiments indicate that this approximation is very effective. For instance, the 5 point Gauss–Legendre quadrature (order 10) gives very accurate results even for moderately large step-sizes, and reduces the overall cost of the methods by 2/3.

With respect to the exact methods, the semi-exact methods obtained with this approach are more directly comparable to the methods of [12].

3.3.2 Free rigid body

In this section we compare the algorithms discussed in this paper with the pre-processed Rattle/discrete Moser–Veselov of Hairer *et al.* [12]. The latter are, in our opinion, the state-of-the-art approximation methods insofar the rigid body is concerned. The comparison is done using FORTRAN routines. The methods we compare are: `dmv6, dmv8, dmv10`, the methods based on the preprocessed Rattle algorithms of order 6, 8 and 10, respectively, the two exact methods with the rotation matrix of Section 2.3 and the rotation quaternion of Section 2.5 along with their semi-exact variants in which the elliptic integral is approximated by Gauss–Legendre quadrature formulae of order 6, 8 and 10. As explained in the Introduction, in order to do these comparison, we integrate the flow of the free rigid body in a time interval $[0, T_{\text{fin}}]$ by repeated application of the time-h algorithms.

In the first experiment, see Figure 3.1 top plot, we display

$$\text{average}_{I, \boldsymbol{m}_0} \log_{10} ||Q_{\text{reference}}(T_{\text{fin}}; I, \boldsymbol{m}_0) - Q_{\text{computed}}(T_{\text{fin}}|h; I, \boldsymbol{m}_0)||_\infty, \quad (3.24)$$

(or the analogous quantity of the quaternion) against the cpu-time averages of the different methods when $T_{\text{fin}} = 10$, with twenty different step-sizes h ranging from about 0.4 down to 0.01. The absolute value of the indicator (3.24) corresponds to the average number of significant digits of the attitude matrix with step-size h at time T_{fin}.[1] The set of initial parameters, shared by all the methods, is determined as follows. We choose a random inertia tensor, normalized so that $I_1 < I_2 < I_3 = 1$, thereafter a random initial normalized angular momentum in the first quadrant. This is not a restriction, as both scaling the inertia tensor and the angular momentum are equivalent to a time reparametrization. The initial condition for the attitude matrix is the identity matrix that, for quaternions, is $(1, 0, 0, 0)$. The reference solution is computed with Matlab's `ode45` routine, setting both relative and absolute error to machine precision. The average cpu is computed as the mean of 100 runs.

Figure 3.1 indicates that the exact methods are clearly more expensive, but they always converge (against 75 successes for the methods `dmv6, dmv8, dmv10`, that are depending on a step-size "small enough" for the fixed point iterations to converge). The diverging runs of the DMV methods are not taken into account when computing averages. Good behaviour is displayed also by the semi-exact

---

[1]Our methods compute exactly the angular momentum, while the DMV methods do not. However both classes of methods preserve exactly the kinetic energy, the norm of the angular momentum, the spatial angular momentum $Q\boldsymbol{m}$, are time-reversible and Lie–Poisson integrators for the angular momentum. The DMV methods and the semi-exact methods are not symplectic.
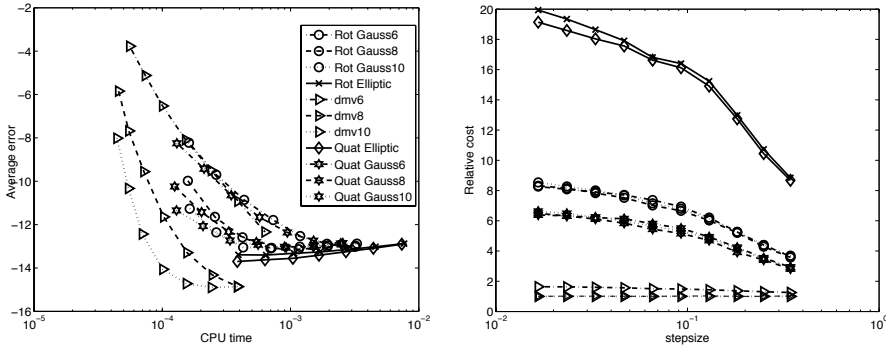
Figure 3.1: Left: Average log of error versus average cpu times in the attitude rotation (100 runs) for random initial conditions and random moments of inertia. Right: Relative cost (with respect to the cheapest method) versus step-size. The methods computing the exact solutions are more expensive then the approximated ones, but their relative cost rate improves for large time-steps. The DMV methods converge 75 out of the 100 runs. The failures are not taken into account when computing the averages.

methods. Their cost is about $1/3$ of the methods using the exact elliptic integral (and this is reasonable, because the exact routines compute 3 elliptic integrals of the third kind: the complete one between 0 and $\pi/2$, and two incomplete ones between 0 and ϕ, where $0 \leq \phi \leq \pi/2$). The right plot in Figure 3.1 displays the relative cost of the methods, computed as

$$\frac{\text{average cost of method X}}{\min_{\text{all methods}} \text{aver. cost of method X}},$$

so that the bottom line equals to one by definition. The DMV are the cheapest methods and their cost increases very slowly with the order of the method. We see that the relative cost of the exact and semi-exact methods is higher for small step-sizes and lower for large step-sizes. This indicates that the exact and semi-exact methods are of interest in numerical simulations that use large step-sizes, for which the DMV might have problems in converging.

The exact and semi-exact methods discussed in this paper reveal a worse accumulation of roundoff error for small step-sizes (see Figure 3.1, left plot). This can be partly explained by the fact that the routines for the attitude rotation make repeated use of the exact solution of the angular momentum. However, with exact methods it is not necessary to perform many tiny steps for integrating to the final time: a single time-stepping is enough, and this avoids the problems related to the accumulation of roundoff error. To improve on propagation of roundoff, it is also possible to perform a simple projection at the end of each
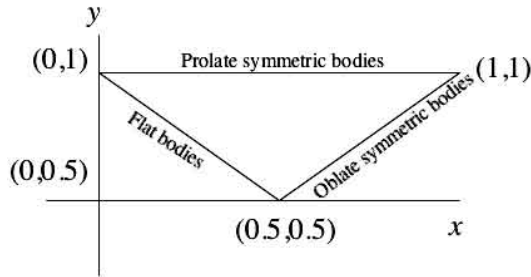
Figure 3.2: Parametrization domain for the matrix of inertia. x-axis: I_1/I_3, y-axis: I_2/I_3.

time-step, in the quaternion case this amounts to divide the attitude quaternion by its norm. In general, when exact and semi-exact methods are applied within a splitting method, the value of the parameters (angular momentum, attitude, energy) will change before and after one free rigid body step, hence we do not foresee problems of roundoff accumulation.

What about the accuracy of the exact methods using matrices or quaternions? Numerical experiments reveal that the accuracy of the two exact methods is very comparable and also their cost. Methods using quaternions to represent rotations are usually faster than their matrix counterpart, but here the computational time is dominated by the evaluation of the elliptic integrals.

Our extensive numerical experiments revealed that the performance of the semi-exact and the DMV methods depended heavily on the matrix of inertia I and the initial condition $\boldsymbol{m}_0$ for the angular momentum. To understand this dependence, we have followed a procedure similar to the one used in [9]. Since normalizing the matrix of inertia is equivalent to a time reparametrization, it is sufficient to consider values of the form $I_1/I_3 < I_2/I_3 < 1$. This reduces to considering two parameters, say $x = I_1/I_3$ and $y = I_2/I_3$. As $I_i + I_j \geq I_k$, the problem is reduced to considering values of x and y in the triangle

$$\mathcal{T} = \{(x,y) \in \mathbb{R}^2 : 0 < 1 - y \leq x < y < 1\},$$

(see Figure 3.2).

We construct a discretization of this triangle by superimposing a rectangular grid (100 points in the x direction and 50 in the y direction). For each point (x,y) in the interior of the triangle, we solve 20 initial value problems with initial condition $\boldsymbol{m}_0$ in the first octant. This set of initial parameters is identical for all the methods. Thereafter, we compute the average (3.24) for each method (non converging runs for the DMV methods are discarded). The results of the
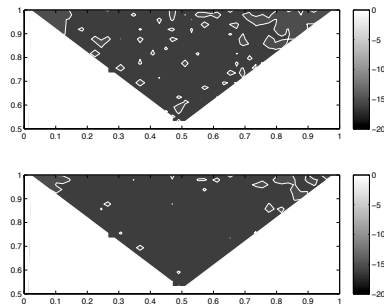
Figure 3.3: Average $\log_{10}$ error for the various values of the matrix of inertia with step-size $h = 0.4$. Comparison of exact methods. Top: Matrix case. Bottom: Quaternion case.

experiments are shown in Figures 3.3, 3.4(a), 3.4(c) and 3.4(e), computed with integration step-size $h = 0.4$, and Figures 3.4(b), 3.4(d) and 3.4(f) computed with integration step-size $h = 0.04$.

For the largest step-size, $h = 0.4$, the exact methods described in this paper perform very similarly and show a uniform accuracy. We compare then the semi-exact methods of order 6, 8, and 10 and the DMV ones of the same order. It should be mentioned that the pictures corresponding to semi-exact methods using matrix rotations or quaternions are virtually indistinguishable from each order, for this reason we only show one of the two. Both the semi-exact and the DMV methods reveal a worse approximation in the proximity of the top left corner

$$0 \approx x = \frac{I_1}{I_3} \ll y = \frac{I_2}{I_3} \approx 1 = \frac{I_3}{I_3}, \tag{3.25}$$

namely when the smallest moment of inertia is much smaller than the two others. This behaviour of the numerical methods is due to the fact that when I_1 goes to zero, one of the periods of the free rigid body motion tends to zero. To resolve these motions accurately, numerical integrators must use small step-sizes. The DMV methods have in average less accuracy and they failed to converge for several initial conditions.

For the next value of the step-size ($h = 0.04$) the exact methods reveal a worse accumulation of roundoff error (not shown), already observed in Figure 3.1. This accumulation disappears if the integration in $[0, T_{\text{fin}}]$ is performed with a single time-step. The DMV, in particular `dmv10`, perform very well in the whole triangle, except for the top left corner.

The conclusion is that exact and semi-exact methods are of interest for large step-sizes, and in particular for values of the moments of inertia in the region (3.25).
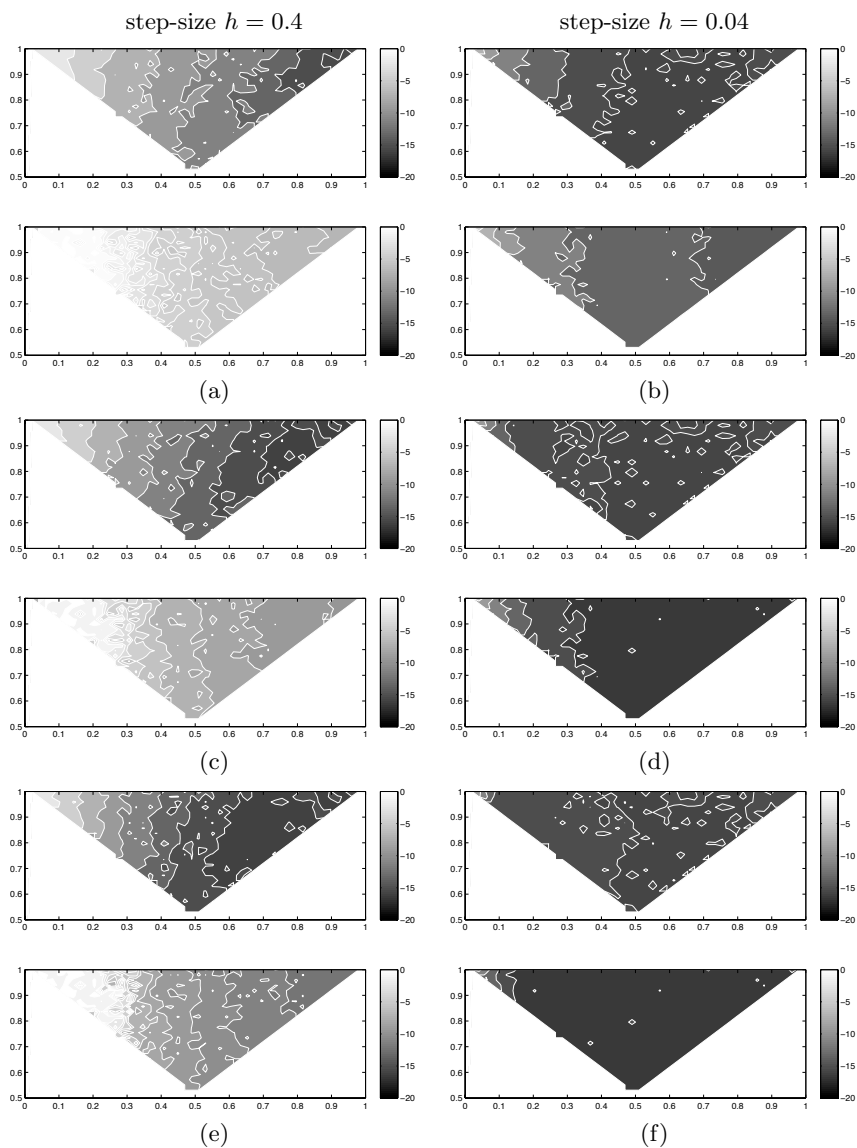
Figure 3.4: Average $\log_{10}$ error for the various values of the matrix of inertia with step-size $h = 0.4$, left, and $h = 0.04$, right:
(a) and (b) order 6. Top: semi-exact with quadrature order 6. Bottom: `dmv6`.
(c) and (d) order 8. Top: semi-exact with quadrature order 8. Bottom: `dmv8`.
(e) and (f) order 10. Top: semi-exact with quadrature order 10. Bottom: `dmv10`.

3.3.3 Torqued systems and perturbations of free rigid body motions

In this section we consider systems of the form

$$H(\boldsymbol{m}, Q) = T(\boldsymbol{m}) + V(Q), \tag{3.26}$$

where T is the kinetic energy of the free rigid body and the potential energy V describes some external torque. As mentioned in the introduction, a standard approach to solve this problem is to split it into a free rigid body motion coming from the kinetic part,

$$S_1 = \begin{cases} \dot{\boldsymbol{m}} = \boldsymbol{m} \times I^{-1}\boldsymbol{m}, \\ \dot{Q} = Q\,\widehat{I^{-1}\boldsymbol{m}}, \end{cases} \tag{3.27}$$

plus a torqued motion, namely

$$S_2 = \begin{cases} \dot{\boldsymbol{m}} = \mathbf{f}(Q), \\ \dot{Q} = 0, \end{cases} \tag{3.28}$$

where $\mathbf{f}(Q) = -\mathrm{rot}(Q^T \frac{\partial V}{\partial Q})$. Here, rot-function maps matrices to vectors, first by associating to a matrix a skew-symmetric one, and then identifying the latter with a vector,

$$\mathrm{rot}(A) = \mathrm{skew}^{-1}(A - A^T),$$

where $\mathrm{skew}(\mathbf{v}) = \hat{\mathbf{v}}$, see also [26].

Thereafter, the flows of the S_1 and S_2 systems are composed by means of a splitting method [21].

The most commonly used is the symplectic second order Störmer/Verlet scheme

$$(\boldsymbol{m}, Q)^{(j+1)} = \varphi_{h/2}^{[S_2]} \circ \varphi_h^{[S_1]} \circ \varphi_{h/2}^{[S_2]}((\boldsymbol{m}, Q)^{(j)}), \quad j = 0, 1, \dots,$$

where $\varphi_h^{[S_1]}$ and $\varphi_h^{[S_2]}$ represent the flows of S_1 and S_2, respectively. Some higher order splitting schemes are presented in the appendix. These are state-of-the-art optimized schemes with very small leading error, [4]. We will use these methods for the remaining experiments. All the remaining experiments are performed in MATLAB. For the rigid body part, we use the rotation-matrix exact method of Section 2.3, which we will call RB for reference.

One of the most popular methods for approximating the free rigid body system (3.27) is a second-order method proposed by McLachlan and Reich (see [8]). This method, that we will call MR, is time-reversible and preserves the Poisson

structure of the system. In brief, the MR method is based on a splitting of the Hamiltonian (3.26) into four parts,

$$\tilde{H}_1 = \frac{m_1^2}{2I_1}, \quad \tilde{H}_2 = \frac{m_2^2}{2I_2}, \quad \tilde{H}_3 = \frac{m_3^2}{2I_3}, \quad \tilde{H}_4 = V(Q).$$

Each of the corresponding Hamiltonian vector fields can be integrated exactly ($\tilde{H}_1$, $\tilde{H}_2$, $\tilde{H}_3$ correspond to the vector field (3.27)), the symmetric composition of the flows gives rise to the approximation scheme,

$$(\boldsymbol{m}, Q)^{(j+1)} = \Phi_{MR}((\boldsymbol{m}, Q)^{(j)}),$$

where

$$\Phi_{MR} = \varphi_{4,h/2} \circ \Phi_{T,h} \circ \varphi_{4,h/2}.$$

Here

$$\Phi_{T,h} = \varphi_{1,h/2} \circ \varphi_{2,h/2} \circ \varphi_{3,h} \circ \varphi_{2,h/2} \circ \varphi_{1,h/2}$$

is the contribution from the kinetic parts, $\tilde{H}_1$, $\tilde{H}_2$ and $\tilde{H}_3$, where the flows of the kinetic parts corresponds to elementary rotations in $\mathbb{R}^3$.

3.3.3.1 The heavy top

As a first study case, we consider a nearly integrable situation, the rigid body with a fixed point in a small constant-gravity field. The Hamiltonian is

$$H = T + \varepsilon V(Q), \qquad 0 < \varepsilon \ll 1, \tag{3.29}$$

with

$$V(Q) = \boldsymbol{e}_3^T Q^T \boldsymbol{u}_0,$$

for a constant vector $\boldsymbol{u}_0$. The vector $\boldsymbol{u} = Q^T \boldsymbol{u}_0$ describes the position of the center of mass times the (normalized) acceleration of gravity. This potential V corresponds to $\mathbf{f}(Q) = (u_2, -u_1, 0)^T$, where u_1 and u_2 are components of $\boldsymbol{u}$.

A symplectic splitting method of order p that treats the free rigid body part exactly would typically have a nearby Hamiltonian of the form

$$\tilde{H} = H + \varepsilon V + \mathcal{O}(\varepsilon h^p),$$

hence, if the step-size of integration is small enough, the numerical error remains smaller with respect to the perturbation parameter, see e.g. [3]. If the rigid body part is resolved by a symplectic method of order r, typically $r \geq p$, the nearby Hamiltonian has the form

$$\tilde{H} = H + \varepsilon V + \mathcal{O}(h^r) + \mathcal{O}(\varepsilon h^p),$$
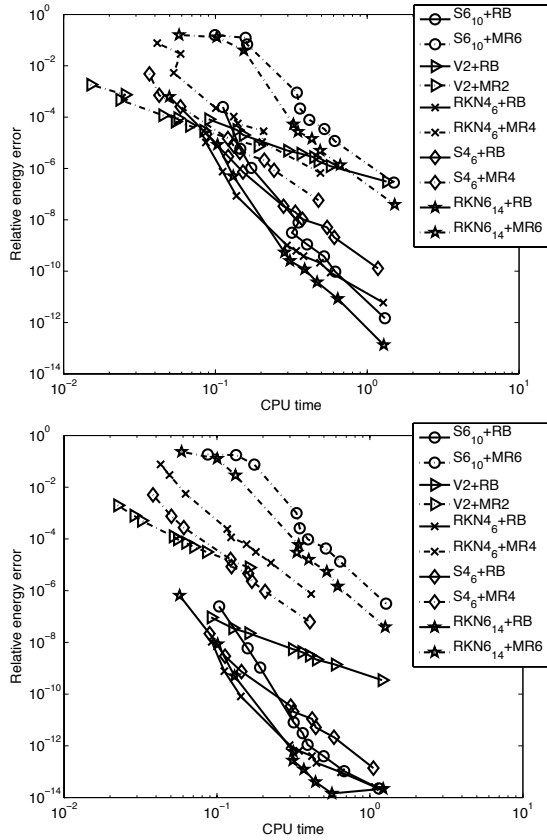
Figure 3.5: Average relative energy errors versus computational time, perturbed rigid body, $\varepsilon = 10^{-3}$ (top plot) and $\varepsilon = 10^{-6}$ (bottom plot). Initial kinetic energy $T_0 = 1$. Solid lines: splitting methods using RB. Dash-dotted lines: splitting methods using MR approximation for the rigid body motion boosted to the same order of the splitting scheme.

thus, in order to have an error that goes to zero as ε goes to zero, one has to take smaller step-sizes h.

This behaviour is displayed in Figure 3.5 for two values of ε (left plot: $\varepsilon = 10^{-3}$, right plot: $\varepsilon = 10^{-6}$). We compare different splitting schemes of various order for the system $S_1 + S_2$. Moreover, we compare the same splitting techniques using an exact method or a further MR splitting for the free rigid body motion. As the MR method has only order two, we boost its order to p (the same as the underlying splitting scheme) using Yoshida's technique [32].

The initial conditions, identical for all the methods, are chosen as follows. Having fixed a value of ε, we choose a random inertia tensor, normalized so that $I_1 = 1$. Having chosen the first two components of $\boldsymbol{m}_0$ randomly, the remaining one is determined to match $T_0 = 1$. The vector $\boldsymbol{u}_0$ is taken equal to $\boldsymbol{e}_3$ and Q_0 is the identity matrix.

Several splitting methods are compared, each timing and relative Hamiltonian error is averaged (mean value) over 20 different initial conditions (each with new $I, \boldsymbol{m}_0$). The methods are implemented so that all the splitting schemes perform the same number of force evaluations. This is done as follows: start with the following basic time-steps: $h \in \{8, 5, 4, 2, 1.75, 1.5, 1.25, 1, 0.5\}$. For a splitting method with s stages (s is the number of evaluations of the force), we use $h_s = c_s h = \frac{s}{10}h$. For instance, for the 6th order 10-stages method $S6_{10}$, $c_s = 1$, for the Störmer-Verlet splitting (V2), $c_s = \frac{1}{10}$. The integration is performed in the interval $[0, 20]$.

Figure 3.5 indicates that, the more we boost the order of the MR scheme, the more the cost of the splitting method becomes similar to the one using the exact solution of the rigid body. This is evident especially for schemes that have a large number of stages ($S6_{10}$, $RKN6_{14}^a$). Moreover, it is also evident that composing MR to a higher order scheme using Yoshida's technique yields methods with high leading error term, that dominates the small error of optimized splitting scheme. Finally, note that only the methods using the exact integrator produce an error that is smaller than ε even for very large choices of the step-size. This is evident for $\varepsilon = 10^{-3}$ but, in particular, for $\varepsilon = 10^{-6}$. The conclusion is that the use of the exact algorithm for the rigid body is definitively of interest in integration of perturbed systems (see also [3], [6]).

3.3.3.2   Second test case

We consider a simplified model describing the motion of a satellite in a circular orbit of radius r around the earth [18]. Denote $\mu = gM$, where g is the gravitational constant and M is the mass of the Earth. The potential energy of this system is given by

$$V(Q) = 3\frac{\mu}{2r^3}(Q^T\mathbf{e}_3) \cdot IQ^T\mathbf{e}_3, \qquad (3.30)$$

where I is the inertia tensor and $\mathbf{e}_3$ is the canonical vector $(0, 0, 1)^T$ in $\mathbb{R}^3$. The torque associated to this potential becomes

$$\mathbf{f}(Q) = 3\frac{\mu}{r^3}(Q^T\mathbf{e}_3) \times I(Q^T\mathbf{e}_3). \qquad (3.31)$$

We simulate the motion of the satellite using the same parameters as in [23], namely

$$I_1 = 1.7 \times 10^4, \qquad I_2 = 3.7 \times 10^4, \qquad I_3 = 5.4 \times 10^4,$$
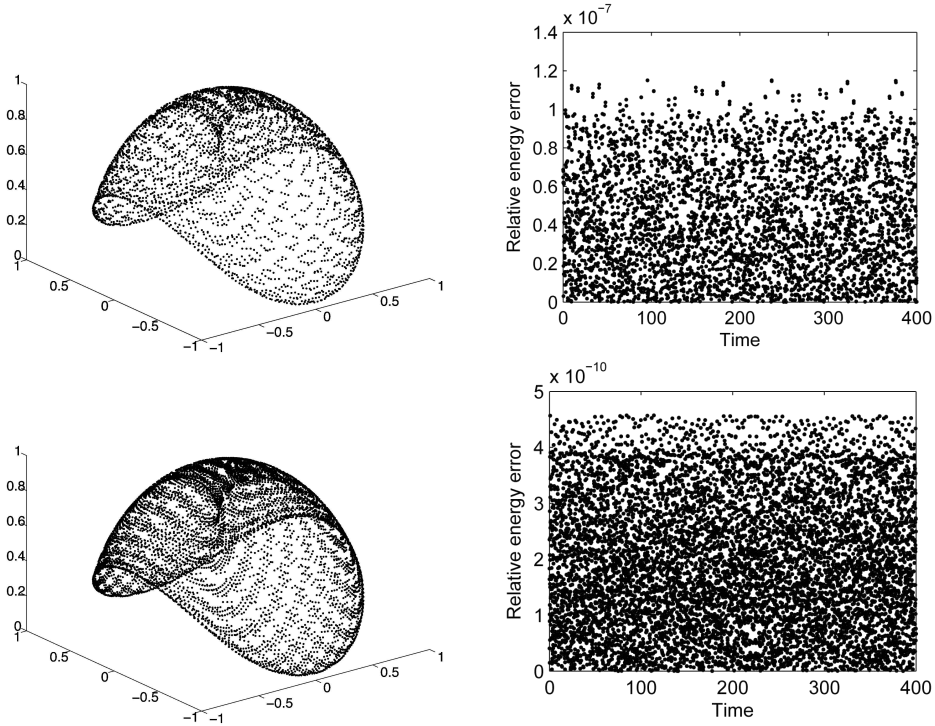
Figure 3.6: Satellite simulation. Left column: Center of mass ($Q^T \mathbf{e}_3$) by the splitting method RKN6$_{14}^a$ with step-size $h = 0.1$ (top) and $h = 0.05$ (bottom). Right: Relative error on the energy corresponding to the same step-sizes. See text for details.

with

$$\mu = 3.986 \times 10^{14}, \qquad r = 1.5 \times 10^5,$$

in the interval $[0, 400]$. The initial angular momentum is $\mathbf{m}_0 = I (15, -15, 15)^T$. The initial attitude Q_0 is the identity matrix. The system has an energy $H_0 = 1.21595664 \times 10^7$, which is conserved in time. This experiment was also considered in [6]. The splitting method based on the exact approximation of the rigid body is very accurate. The motion of the center of mass (left column) and the relative error on the energy H_0 (right column) for the splitting method RKN6$_{14}^a$ employing our exact solution, are shown in Figure 3.6. The integration is performed in the interval $[0, 400]$ with step-size $h = 0.1$ (top) and $h = 0.05$ (bottom). The relative error on the energy (see Figure 3.6), which is of the order of 10^{-7} for $h = 0.1$ and 10^{-10} for $h = 0.05$, indicates that H_0 is preserved to 7 and 10 digits respectively.

The corresponding plots for the evaluation of the flow of T with the MR splitting method are shown in Figure (3.7).
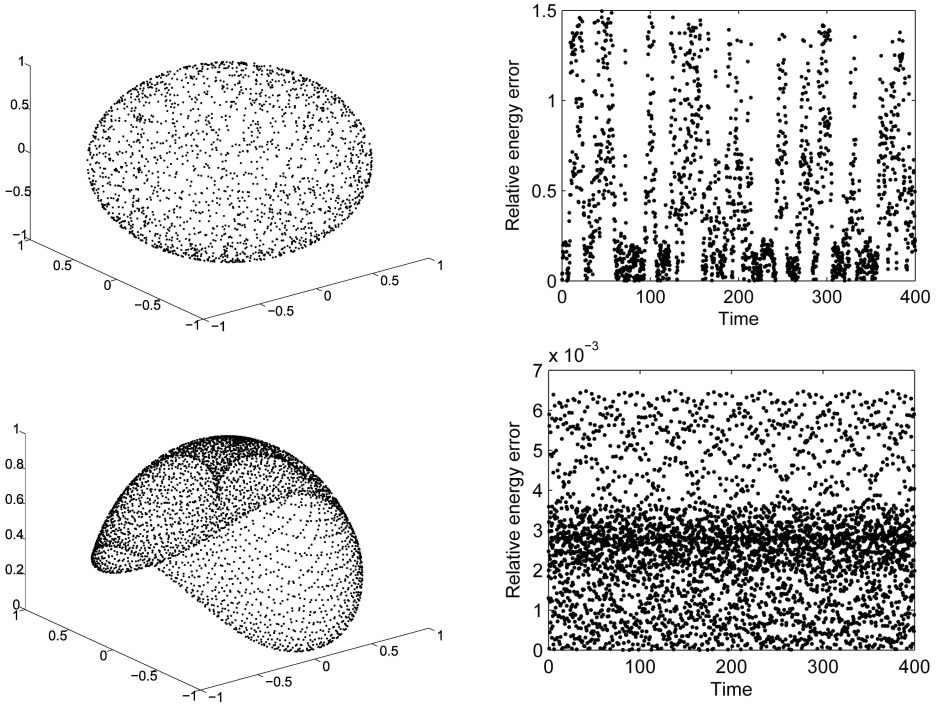
Figure 3.7: Satellite simulation. Left column: Center of mass $(Q^T \mathbf{e}_3)$ by the splitting method MR with step-size $h = 0.1$ (top) and $h = 0.05$ (bottom). Right: Relative error on the energy corresponding to the same step-sizes. See text for details.

3.3.4   Molecular dynamics simulation: Soft dipolar spheres

We consider a molecular dynamics simulation, where molecules are modeled as dipolar soft spheres. This model is of interest because it can be used to study water and aqueous solutions, as water molecules can be described by small dipoles. We consider the system described in example b in Appendix A of [8] which we recall here for completeness. Denote by m_i the total mass of the ith body, by $\mathbf{q}_i$ the position of its center of mass, by $\mathbf{p}_i$ its linear momentum, by $\mathbf{Q}_i$ its orientation and, finally, by $\boldsymbol{m}_i$ its angular momentum in body frame. The system has

70

Hamiltonian

$$H(\mathbf{q}, \mathbf{p}, \boldsymbol{m}, \mathbf{Q}) = T(\mathbf{p}, \boldsymbol{m}) + V(\mathbf{q}, \mathbf{Q}), \tag{3.32}$$

where T refers to the total kinetic energy,

$$T(\mathbf{p}, \boldsymbol{m}) = \sum_i (T_i^{\text{trans}}(\mathbf{p}_i) + T_i^{\text{rot}}(\boldsymbol{m}_i)),$$

consisting of the sum of the translational and rotational kinetic energies of each body,

$$T_i^{\text{trans}}(\mathbf{p}_i) = \frac{\|\mathbf{p}_i\|^2}{2}, \qquad T_i^{\text{rot}}(\boldsymbol{m}_i) = \frac{1}{2}\boldsymbol{m}_i \cdot (I_i^{-1}\boldsymbol{m}_i),$$

where $I_i = \text{diag}(I_{i,1}, I_{,2}, I_{i,3})$ is the inertia tensor of the ith body, while V is the potential energy, describing the interaction between dipoles, that is assumed to depend on the position and orientation only. Furthermore, $V = \sum_{j>i} V_{i,j}$, where $V_{i,j}$ describes the interaction between dipole i and dipole j. We suppose

$$V_{i,j}(\mathbf{q}_i, \mathbf{Q}_i, \mathbf{q}_j, \mathbf{Q}_j) = V_{i,j}^{\text{short}} + V_{i,j}^{\text{dip}},$$

where

$$V_{i,j}^{\text{short}} = 4\epsilon \left(\frac{\sigma}{r_{i,j}}\right)^{12}, \qquad \mathbf{r}_{i,j} = \mathbf{q}_i - \mathbf{q}_j, \quad r_{i,j} = \|\mathbf{r}_{i,j}\|,$$

describes the short range interaction between particles i and j, while

$$V_{i,j}^{\text{dip}} = \frac{1}{r_{i,j}^3}\boldsymbol{\mu}_i \cdot \boldsymbol{\mu}_j - \frac{3}{r_{i,j}^5}(\boldsymbol{\mu}_i \cdot \mathbf{r}_{i,j})(\boldsymbol{\mu}_j \cdot \mathbf{r}_{i,j}),$$

is the term modeling the dipole interaction, where $\boldsymbol{\mu}_i$ being the orientation of the ith dipole vector. If $\bar{\boldsymbol{\mu}}_i$ is an initial fixed reference orientation for the dipole, then $\boldsymbol{\mu}_i = \mathbf{Q}_i\bar{\boldsymbol{\mu}}_i$.

The Hamiltonian (3.32) is separable, as the potential energy is independent of momenta and angular momenta. As before, we split the system as $H = T + V$, yielding

$$\begin{array}{rcl} \dot{\mathbf{q}}_i &=& \frac{\mathbf{p}_i}{m_i}, \\ \dot{\mathbf{p}}_i &=& 0, \\ \dot{\boldsymbol{m}}_i &=& \boldsymbol{m}_i \times (I_i^{-1}\boldsymbol{m}_i), \\ \dot{\mathbf{Q}}_i &=& \mathbf{Q}_i(\widehat{I_i^{-1}\boldsymbol{m}_i}), \end{array} \tag{3.33}$$

and

$$\begin{array}{rcl} \dot{\mathbf{q}}_i &=& 0, \\ \dot{\mathbf{p}}_i &=& -\frac{\partial V}{\partial \mathbf{q}_i}, \\ \dot{\boldsymbol{m}}_i &=& -\text{rot}(\mathbf{Q}_i^\top \frac{\partial V}{\partial \mathbf{Q}_i}) \\ \dot{\mathbf{Q}}_i &=& 0. \end{array} \tag{3.34}$$

We approximate the original system with full Hamiltonian (3.32) by a composition of the flows of (3.33) and (3.34), using some of the optimized splitting schemes introduced earlier. In [30] the authors use a similar approach. The main difference is in the the choice of the splitting schemes (Störmer-Verlet and a fourth-order Forest-Ruth like scheme) and the implementation of the RB method. One of the standard methods, used in several packages for molecular dynamics simulations, for instance the ORIENT package [27], is that described in [8]. The method consists of a Störmer–Verlet splitting plus a further splitting of the rigid body kinetic energy (that is the MR method described earlier in 3.3.3). Here, we will denote the same method by V2+MR.

It is important to stress that, for a sufficiently large number of particles, approximating the rigid body equations by a inexpensive method, like MR, or a more expensive one, like the exact RB, is irrelevant, as the cost of this part grows only linearly with the number of particles. The computationally most demanding part in this simulation is the solution of (3.34), namely the computation of the potential, whose cost grows quadratically with the number of particles.

This appears clearly in our first example: we compare different splitting methods for a system of 100 particles, for a relatively short time integration ($T_{\text{fin}} = 1$). All the methods use fixed step-size, appropriately scaled for each splitting scheme, to require the same number of function evaluations. For the reference method, the V2+MR, we use step size $h = 10^{-1} \times 1/2^i$, for $i = 0, \ldots, 7$, i.e. for the largest step-size $h = 0.1$ one has 10 potential evaluations, thus the x-axis in Figure 3.8 can be interpreted as number of function evaluations as well. Similarly, the sixth-order splitting method $S6_{10}$+RB, with 10 internal stages requiring potential evaluations, is implemented with step-size $h = 1$. The results of the simulation are displayed in Figure 3.8. The methods are implemented using the RB method (solid line) and using the MR method (dash-dotted line). Coalescence of stages is exploited for all methods. The initial conditions for the experiment were taken as follows: the masses m_i are chosen to be 1, $\mathbf{q}_i = N \times \mathtt{randn}(3, 1)$, $N = 100$ being the number of particles, and $\mathtt{randn}(3, 1)$ a vector with random components (gaussian distribution) between -1 and 1; $\mathbf{p}_i = 0, \boldsymbol{m}_i = 0$, $\mathbf{Q_i}$ random orthogonal matrix, $\boldsymbol{\mu}_i = (0, 1, 1)^T$, $\sigma = \epsilon = 1$, with a resulting energy $H_0 = 0.14134185611814$. The moments of inertia are those of water ($I_1 = 1, I_2 = 1.88, I_3 = 2.88$).

In the next numerical example (Figure 3.9), we test the same methods for different energies. The initial conditions are chosen as follows: we take 125 particles that we position on a lattice of dimension $5 \times 5 \times 5$. The initial positions are then perturbed by 1% (Gaussian normal distribution). The initial orientations are random orthogonal matrices. With these parameters, we compute the initial energy and then we change the linear momentum of the particles in positions $\mathbf{q}_1 = (1, 1, 1)^T$ and $\mathbf{q}_{125} = (5, 5, 5)^T$ to achieve the target energy H_0. For each step-size $h = 1, 1/2, 1/4, 1/8$ of the basic method $SR6_{10}$, we perform 100 simulations
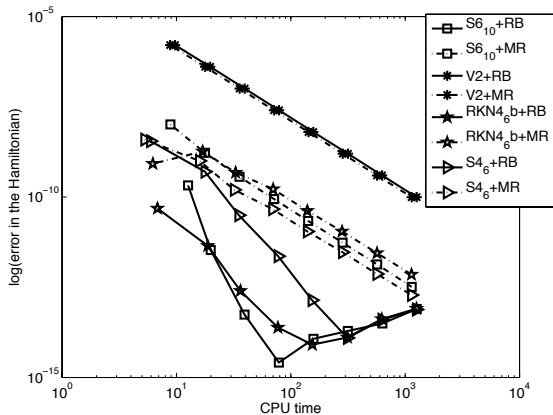
Figure 3.8: Error in the Hamiltoninan versus computational time for 100 particles. Several splitting methods are compared. See text for details.

(choosing every time a different initial condition), and we average the error and the computational time (arithmetic mean).

Finally, having observed that Nyström schemes behave very well for this class of problems, the method $RKN4_6^b$ is compared to $RKN6_{14}^a$ in Figure 3.10. The number of function evaluations for the two methods is the same. The initial conditions as before, except for the number of averages (which is 1), and the time of integration, with $T_{\text{fin}} = 10$.

These experiments indicate that the main source of error for this problem is the splitting $H = T + V$. This seems consistent with conclusions on the water simulations in [30]. In particular, a lower global error as a result of using the exact RB integrator becomes visible only in the step-size asymptotic regime (as $h \to 0$, see Figure 3.8). Furthermore, how small the step-size h must be, to see the positive effect of the exact RB integrator, seems to depend on the total energy of the system. For low energies, the error with the exact method becomes smaller at a larger step-size. For higher energies, the error with the exact method becomes smaller only at very small values of h, see Figures 3.9-3.10.

Our conclusion is that the use of an exact RB integrator is favorable for simulations where higher precision is required (for instance low energy). For higher energies, and the effect of having an exact integrator for the RB part appears to be less relevant unless other techniques are used.
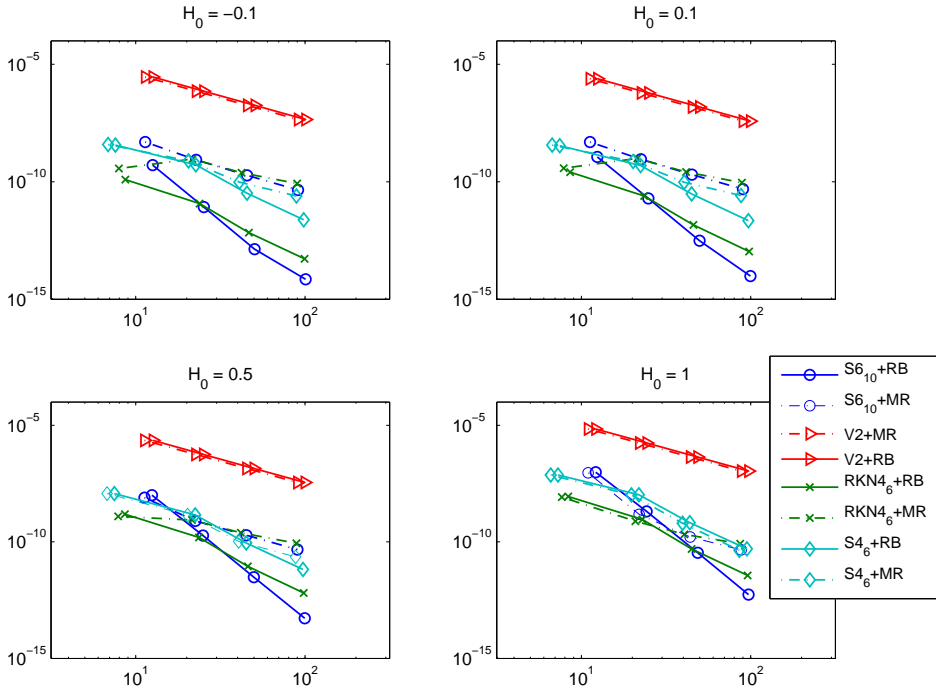
Figure 3.9: Average errors versus CPU time for different values of the energy H_0, 100 runs per each of the step-sizes $1, 1/2, 1/4, 1/8$. Number of particles $N = 125$. For small energy values, the splitting methods based on the exact RB integrator perform better than those with the MR splitting. For higher values of the energy, the error due to the splitting $H = T + V$ is much higher than the error for the RB-part and it dominates the total error.

3.4   Conclusions

The main purpose of this paper has been to understand whether and when the use of exact solution of the free rigid body equations as a component of splitting methods is a competitive geometric integrator.

We have reviewed various algorithms for the computation of the exact solution of the free rigid body equations providing a common framework. We have implemented two concrete approaches based on rotation matrices and quaternions. The algorithms require the computation of a elliptic integral of the third kind, which we either compute to machine accuracy (exact methods) or approximate by Gauss-Legendre quadrature (semi-exact methods). We have preformed numerous experiments comparing these methods to preprocessed discrete Moser–
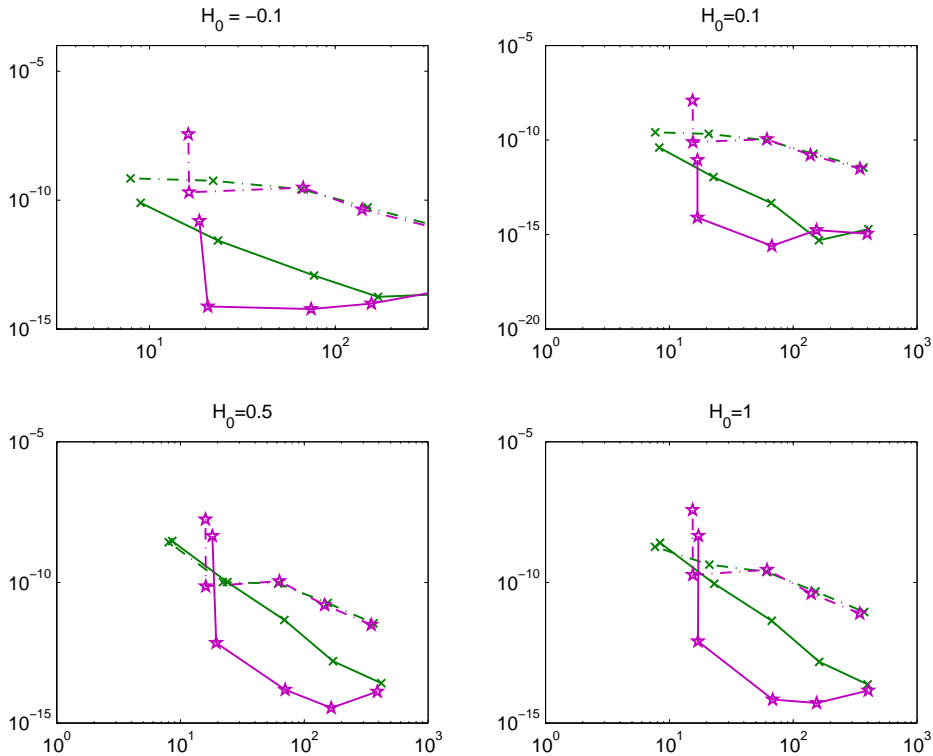
Figure 3.10: Error versus CPU time. Comparison of two RKN splittings of order 4 and 6, on the interval [0,10], 125 particles, for some initial conditions. The sharp increase of the error for the 6th order method is due to the fact that the step-size is too large. The $RKN4_6$ method (crosses with solid and dash-dotted lines) is the same as in Figure 3.9.

Veselov methods (experiments on the free rigid body problem) and to various splitting methods (experiments on torqued rigid bodies).

In conclusion the exact methods, though more expensive, are very robust and behave uniformly well for all choices of the principal moments of inertia and initial conditions, independently of the step-size of integration.

If cost is an issue, *semi-exact* methods are a good compromise. They are much cheaper than the exact ones, while sharing most of the geometric properties[2] and being robust for large step-sizes and arbitrary values of the principal moments

---

[2]Symplecticity is lost, but the methods are time-reversible as long as the underlying quadrature is symmetric. Also the DMV methods are time-reversible but not symplectic.

of inertia. This is an advantage compared to implicit methods using fixed-point iteration, that might require small step-sizes to converge, (e.g. the cheaper DMV).

Our conclusion is that the implementation of the exact solution of the free rigid body is competitive as a numerical approach and has the advantage that it can be used as a building block for splitting methods of high order.

When used as a component of splitting methods the exact and semi-exact methods are definitively of interest in the case of perturbed free rigid body problems. In molecular dynamics simulations, using the exact rigid body motion gives a clear advantage compared to other splittings only in the low energy case. However even in the general case, the cost due to any rigid body integrator (approximate or exact) is growing only linearly as a function of the number of particles while the number of inter-particles force evaluations is growing quadratically and dominates the overall computational cost.

Acknowledgments

Appendices

Jacobi elliptic functions

We collect here a few facts about the elliptic functions we use in the article. Given $0 \leq k < 1$, the function

$$\varphi \mapsto F(\varphi, k) \ := \ \int_0^\varphi \frac{d\theta}{\sqrt{1 - k^2 \sin^2 \theta}} \tag{3.35}$$

is called (incomplete) *elliptic integral of the first type* with modulus k and is a diffeomorphism $\mathbb{R} \to \mathbb{R}$. Its inverse $F(\,\cdot\,, k)$ is an odd function

$$\mathrm{am}(\,\cdot\,, k) : \mathbb{R} \to \left(-\frac{\pi}{2}, \frac{\pi}{2} \right)$$

which is called *amplitude* of modulus k. The *Jacobi elliptic functions* sn and cn of modulus k are the functions $\mathbb{R} \to [-1, 1]$ defined as

$$\mathrm{sn}(u, k) = \sin(\mathrm{am}(u, k)), \qquad \mathrm{cn}(u, k) = \cos(\mathrm{am}(u, k))$$

and are periodic of period $4K(k)$, where $K(k) = F(\frac{\pi}{2}, k)$ (the so called complete elliptic integral of the first type of modulus k). Moreover,

$$\mathrm{dn}(u, k) = \sqrt{1 - k^2 \mathrm{sn}(u, k)^2}, \qquad \mathrm{sd}(u, k) = \frac{\mathrm{sn}(u, k)}{\mathrm{dn}(u, k)}.$$

For given k, the u-derivatives of these functions satisfy $\mathrm{sn}' = \mathrm{cn}\,\mathrm{dn}$, $\mathrm{cn}' = -\mathrm{sn}\,\mathrm{dn}$ and $\mathrm{dn}' = -k^2 \mathrm{sn}\,\mathrm{cn}$.

The (incomplete) *elliptic integral of the third kind* with modulus $0 < k \le 1$ and parameter $n \in \mathbb{R}$ is the function $\Pi(\,\cdot\,, n, k) : (-\frac{\pi}{2}, \frac{\pi}{2}) \to \mathbb{R}$ defined by

$$\Pi(\varphi, n, k) := \int_0^\varphi \frac{d\theta}{(1 - n\sin^2\theta)\sqrt{1 - k^2\sin^2\theta}}, \qquad (3.36)$$

(Legendre form), or equivalently

$$\Pi(\varphi, n, k) = \int_0^{F(\varphi, k)} \frac{ds}{1 - n\,\mathrm{sn}(s, k)^2}.$$

Coefficients of the Gauss quadrature

For completeness, we report the coefficients of the Gaussian quadrature of order 10 shifted to the interval $[0, 1]$.

$$
\begin{aligned}
&a_1 = 0.04691007703067 && b_1 = 0.11846344252809 \\
&a_2 = 0.23076534494716 && b_2 = 0.23931433524968 \\
&a_3 = 0.5 && b_3 = 0.28444444444444 \qquad (3.37) \\
&a_4 = 0.76923465505284 && b_4 = b_2 \\
&a_5 = 0.95308992296933 && b_5 = b_1.
\end{aligned}
$$

For the qudrature of order 6 and 8 the coefficients have closed form and can be found for instace in [1].

Coefficients of the splitting schemes

Given the differential equation

$$y' = F(y) = A(y) + B(y),$$

denote by $\varphi_\tau^{[F]}$ the flow of the vector-field F from time t to time $t + \tau$. Given a numerical approximations $y^{(j)} \approx y(t_j)$, we consider symmetric splitting schemes of the type

$$y^{(j+1)} = \varphi_{a_1 h}^{[A]} \circ \varphi_{b_1 h}^{[B]} \circ \varphi_{a_2 h}^{[A]} \circ \cdots \circ \varphi_{a_{m+1} h}^{[A]} \circ \cdots \circ \varphi_{b_1 h}^{[B]} \circ \varphi_{a_1 h}^{[A]} \; y^{(j)},$$

where $h = t_{j+1} - t_j$. A typical splitting is obtained separating the contributions arising from the from kinetic (A) and potential (B) energy of the system. For this reason, (twice) the number s of the coefficients b_i is called the *stage number* of the splitting method. The effective error is defined as $E_f = s \sqrt[p]{||\mathbf{c}||_2}$, where $\mathbf{c}$ is the vector of coefficients of the elementary differentials of the leading error term and p is the order of the method. We refer to [4, 21] for background and notation.

For completeness, we report the coefficients of the methods used in this paper. Störmer–Verlet scheme (V2):

$$a_1 = 1/2, \qquad b_1 = 1, \tag{3.38}$$

(order 2, one stage).

$S6_{10}$ method (order 6, 10 stages, effective error $E_f = 1.12$):

$$
\begin{aligned}
&a_1 = 0.0502627644003922, &&b_1 = 0.148816447901042, \\
&a_2 = 0.413514300428344, &&b_2 = -0.132385865767784, \\
&a_3 = 0.0450798897943977, &&b_3 = 0.067307604692185, \\
&a_4 = -0.188054853819569, &&b_4 = 0.432666402578175, \\
&a_5 = 0.541960678450780, &&b_5 = 1/2 - (b_1 + \cdots + b_4), \\
&a_6 = 1 - 2(a_1 + \cdots + a_5).
\end{aligned}
\tag{3.39}
$$

$S4_6$ (order 4, 6 stages, effective error $E_f = 0.56$):

$$
\begin{aligned}
&a_1 = 0.07920369643119565, &&b_1 = 0.209515106613362, \\
&a_2 = 0.353172906049774, &&b_2 = 0.143851773179818, \\
&a_3 = -0.04206508035771952, &&b_3 = 1/2 - (b_1 + b_2), \\
&a_4 = 1 - 2(a_1 + a_2 + a_3).
\end{aligned}
\tag{3.40}
$$

The splitting above are generic in the sense that the A and B part are interchangeable. This is not the case for the next methods, which are based on Nyström schemes for separable Hamiltonians.

$RKN4_6^b$ (order 4, (7)6 stages, effective error $E_f = 0.28$):

$$
\begin{aligned}
&b_1 = 0.0829844064174052, &&a_1 = 0.245298957184271, \\
&b_2 = 0.396309801498368, &&a_2 = 0.604872665711080, \\
&b_3 = -0.0390563049223486, &&a_3 = 1/2 - (a_1 + a_2), \\
&b_4 = 1 - 2(b_1 + b_2 + b_3).
\end{aligned}
\tag{3.41}
$$

RKN6$_{14}^a$ (order 6, 14 stages, effective error $E_f = 0.63$):

$$
\begin{aligned}
a_1 &= 0.0378593198406116, & b_1 &= 0.09171915262446165, \\
a_2 &= 0.102635633102435, & b_2 &= 0.183983170005006, \\
a_3 &= -0.0258678882665587, & b_3 &= -0.05653436583288827, \\
a_4 &= 0.314241403071477, & b_4 &= 0.004914688774712854, \\
a_5 &= -0.130144459517415, & b_5 &= 0.143761127168358, \\
a_6 &= 0.106417700369543, & b_6 &= 0.328567693746804, \\
a_7 &= -0.00879424312851058, & b_7 &= 1/2 - (b_1 + \cdots + b_6), \\
a_8 &= 1 - 2(a_1 + \cdots + a_7).
\end{aligned}
\tag{3.42}
$$

Bibliography

[1] M. Abramowitz and I. A. Stegun. *Handbook of mathematical functions with formulas, graphs, and mathematical tables*, volume 55 of *National Bureau of Standards Applied Mathematics Series, 55*. Reprint of the 1972 edition. Dover Publications, Inc., New York, 1992.

[2] P. E. Appell. *Traité de mécanique rationnelle*, volume 2. Gauthier Villars, Paris, 1924/26.

[3] G. Benettin, A. M. Cherubini, and F. Fassò. A changing-chart symplectic algorithm for rigid bodies and other hamiltonian systems on manifolds. *SIAM J. Sci. Comp.*, 23(4):1189–1203, 2001.

[4] S. Blanes and P. C. Moan. Practical symplectic partitioned Runge–Kutta and Runge–Kutta–Nyström methods. *J. Comp. Appl. Math.*, 142(2):313–330, 2002.

[5] P.F. Byrd and M.D. Friedman. *Handbook of elliptic integrals for engineers and scientists.* Die Grundlehren der mathematischen Wissenschaften, Band 67. Springer-Verlag, New York-Heidelberg, second edition edition, 1971.

[6] E. Celledoni and N. Säfstöm. Efficient time-symmetric simulation of torqued rigid bodies using Jacobi elliptic functions. *Journal of Physics A*, 39:5463–5478, 2006.

[7] R. Cushman. No polar coordinates. Lecture notes, MASIE summer school, Peyresq, France, September 2-16, 2000.

[8] A. Dullweber, B. Leimkuhler, and R. McLachlan. Symplectic splitting methods for rigid body molecular dynamics. *J. Chem. Phys.*, 107:5840–5851, 1997.

[9] F. Fassò. Comparison of splitting algorithm for the rigid body. *J. Comput. Phys.*, 189(2):527–538, 2003.

[10] F. Fassò. Superintegrable Hamiltonian systems: geometry and perturbations. *Acta Appl. Math.*, 87(1-3):93–121, 2005.

[11] E. Hairer, C. Lubich, and G. Wanner. *Geometric numerical integration*, volume 31 of *Springer series in compuitational mathematics*. Springer, 2002.

[12] E. Hairer and G. Vilmart. Preprocessed discrete Moser-Veselov algorithm for the full dynamics of a rigid body. *J. Phys. A*, 39:13225–13235, 2006.

[13] C. G. J. Jacobi. Sur la rotation d'un corps. *Crelle Journal für die reine und angewandte Matematik*, Bd. 39:293–350, 1849.

[14] S. H. Morton Jr., J. L. Junkins, and J. N. Blanton. Analytical solutions for Euler parameters. *Celestial Mech.*, 10:287–301, 1974.

[15] I. I. Kosenko. Integration of the equations of a rotational motion of rigid body in quaternion algebra. The Euler case. *J. Appl. Maths Mechs*, 62(2):193–200, 1998.

[16] D. F. Lawden. *Elliptic functions and applications*, volume 80 of *Applied Mathematical Sciences*. Springer-Verlag, New York, 1989.

[17] B. Leimkuhler and S. Reich. *Simulating Hamiltonian Dynamics*, volume 14 of *Cambridge Monographs on Applied and Computational Mathematics*. Cambridge University Press, first edition edition, 2004.

[18] M. Leok, T. Lee, and N.H. McClamroch. Attitude maneuvers of a rigid spacecraft in a circular orbit. In *Proc. American Control Conf.*, pages 1742–1747, 2006.

[19] J. E. Marsden and T. S. Ratiu. *Introduction to mechanics and symmetry*, volume 17 of *Texts in Applied Mathematics*. Springer-Verlag, New York, second edition, 1999. A basic exposition of classical mechanical systems.

[20] R. I. McLachlan. Explicit Lie-Poisson integration and the Euler equations. *Physical Review Letters*, 71:3043–3046, 1993.

[21] R. I. McLachlan and G. R. W. Quispel. Splitting methods. *Acta Numer.*, 11:341–434, 2002.

[22] R. I. McLachlan and A. Zanna. The discrete Moser–Veselov algorithm for the free rigid body, revisited. *Found. of Comp. Math.*, 5(1):87–123, 2005.

[23] J. Wm. Mitchell. *A simplified variation of parameters solution for the motion of an arbirarily torqued mass asymmetric rigid body.* PhD thesis, University of Cincinnati, 2000.

[24] J. Moser and A. Veselov. Discrete versions of some classical integrable systems and factorization of matrix polynomials. *J. of Comm. Math. Phys.*, 139(2):217–243, 1991.

[25] W. H. Press, S. A. Teukolsky, W. T. Vetterling, and B. P. Flannery. *Numerical recipes in Fortran 77 and Fortran 90.* Cambridge University Press, Cambridge, 1996. The art of scientific and parallel computing, Second edition.

[26] S. Reich. Symplectic integrators for systems of rigid bodies. Integration algorithms and classical mechanics (Toronto, ON, 1993). *Fields Inst. Commun.*, 10:181–191, 1996.

[27] A. J. Stone, A. Dullweber, M. P. Hodges, P. L. A. Popelier, and D. J. Wales. ORIENT Version 3.2: A program for studying interaction between molecules.

[28] J. Touma and J. Wisdom. Lie–poisson integrators for rigid body dynamics in the solar system. *Astr. J.*, 107:1189–1202, 1994.

[29] R. van Zon and J. Schofield. Numerical implementation of the exact dynamics of free rigid bodies. *J. of Comput. Phys.*, 225:145–164, 2007.

[30] R. van Zon and J. Schofield. Symplectic algorithms for simulations of rigid body systems using the exact solution of free motion. *Phys. Rev. E*, 75, 2007.

[31] E. T. Whittaker. *A Treatise on the Analytical Dynamics of Particles and Rigid Bodies.* Cambridge University Press, 4th edition, 1937.

[32] H. Yoshida. Construction of higher order symplectic integrators. *Physics Letters A*, 150:262–268, 1990.

Paper III

Modeling and Control of Offshore Pipelay Operations Based on a Finite Strain Pipe Model

G. A. Jensen, N. Säfström, T. D. Nguyen and T. I. Fossen.

Chapter 4

Modeling and Control of Offshore Pipelay Operations Based on a Finite Strain Pipe Model

ABSTRACT. This paper deals with modeling and control of offshore pipelay operations from a dynamically positioned surface vessel where a nonlinear dynamic beam formulation in three dimensions capable of undergoing shearing, twist and bending is used to model the pipe. This pipe model is coupled with a nonlinear vessel model that has been adopted as a standard for vessel control design and analysis purposes. The complete pipelay system is shown to be input-output passive taking the thruster force as the input and the vessel velocity as the output. A nonlinear controller is applied, and using the passivity condition of feedback connection of two passive systems, the closed loop system is stable. Numerical simulations using both PD and PID controllers illustrate the theoretical results.

4.1   Introduction

Over the last decade deepwater pipelaying has gone through a spectacular development. In the early 90s a water depth of 300 meters was considered deep, while today depths of 2000 meters are common practice. The unprecedented global demand for oil and gas is the main drive in the offshore petroleum industry, which in turn demands improved pipeline technology. The installation of pipelines and

flowlines constitute some of the most challenging offshore operations handled, and the required engineering sophistication, as well as the share size and complexity of the vessels used, has developed pipelaying into an engineering discipline of its own accord [13]. Present trends in the marked indicates an increase in deepwater projects as well in length as depth, according to [12].

Purpose build pipelay vessels equipped with dynamic positioning systems are used for installation of offshore pipelines. The pipe is clamped on to the vessel by heavy tension equipment and extended in a production line accommodating either S-lay or J-lay, which are the two main pipelay methods. The S-lay method is fast and economical and dominates the pipelay market. The pipe is extended horizontally and it describes an S-shaped curve to the seabed, see Figure 4.1. The upper part (*overbend*) is supported by a submerged supporting structure called a *stinger* to control curvature and ovalization, and the curvature in the lower curve (*sagbend*) is controlled by pipe tension. The strain must be checked against pipe design parameters to stay within limits for buckling and ovalization. In deep waters, the weight of the pipe makes it difficult to maintain a stinger supported overbend due to the increased pipe tension, but the tension may be reduced by adopting the J-lay method where the pipe is extended near vertically and thus eliminates the overbend. The methods are seen to be complementary [15]. Both methods are well described in recent textbooks such as [2], [7] and [14]. The present trends in deepwater pipelay systems are described in [8] and the references therein.

Mathematical models are vital in pipeline design for analysis of pipelay parameters and for operability analysis. Commercially developed computer tools, e.g., OFFPIPE, RIFLEX and SIMLA, that are based on *finite element* models have become the universal method for modeling pipelay operations in industry. These models capture well the dynamics of the pipe and have replaced simpler models, e.g., the static catenary model and stiffened catenary model [3, 16], which were used in earlier years. These finite element models are not suited in model-based controllers for pipelay operations, as the system may become unstable due to unmodeled system modes, the so-called *spillover* [1], since the passivity analysis is performed on a finite-dimensional model rather than an infinite-dimensional model.

In this paper a mathematical model for the dynamics of pipelay operations is developed, limited to a surface vessel and pipe where the pipe is clamped to the vessel at an arbitrary angle. The pipe dynamics is modeled by a three dimensional finite strain beam formulation obtained from the classical study of rods. This is a geometrically correct model of nonlinear rods capable of undergoing finite extension, shearing, twist and bending. The key feature of this model is the choice of parametrization which yields the momentum equation on a form which strongly resembles the classical Euler equation of rigid body dynamics, and it is
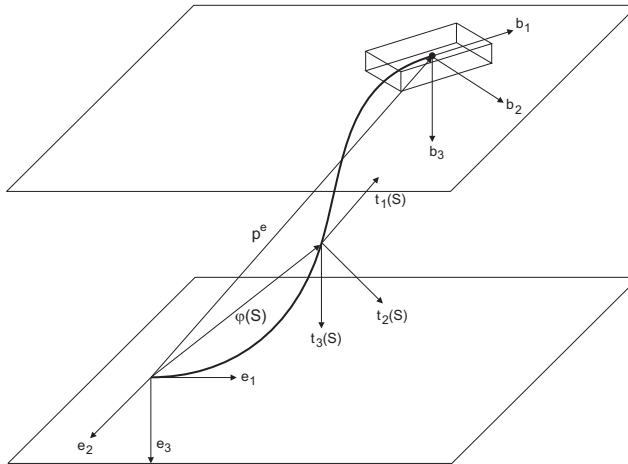
Figure 4.1: A schematic presentation of the pipe and vessel system in a S-lay configuration shown in three degrees of freedom. All the coordinate frames used are shown.

well suited for both mathematical and numerical analysis.

A vessel model on vectorial form using Euler angles is used here since Euler angles are preferred for quantifying attitude in marine applications. The models are coupled by applying the vessel as a boundary condition of the partial differential equation describing the pipe. The system is shown to be input-output passive when the vessel thruster forces are taken as input and the vessel velocity is taken as the output. Hence, stability of the closed loop system follows for a passive controller. Numerical simulations are provided to illustrate the theoretical results.

4.2 Mathematical Model

In this section the mathematical model is developed for the system of a surface vessel with a freely suspended slender pipe string extending from the vessel at a touchdown point at the seabed, see Figure 4.1. The model of the vessel is the familiar system of ordinary differential equations on vectorial form, as presented in [5], and the pipe model is a nonlinear partial differential equation presented in [9], which extends the finite strain beam theory presented by Simo et. al in [17, 18, 19, 20], to apply for a pipeline submerged in a fluid by adding hydrodynamic and hydrostatic effects. The configurations of the pipe are completely defined by specifying the evolution of an orthogonal matrix, and position vector of line of centroids [17].

4.2.1 Notation

Vectors are represented with bold face lower case letters, while bold face upper case letters denote matrices. All vectors are given as coordinate vectors with reference to a frame which is indicated by a superscript, which may be omitted if the frame dependency is evident. A superposed dot denotes the derivative with respect to time, and a prefixed ∂_S indicates the material derivative. The usual inner product is equally defined by $\langle \mathbf{a}, \mathbf{b} \rangle$ and $\mathbf{a}^\mathrm{T}\mathbf{b}$ for all $\mathbf{a}, \mathbf{b} \in \mathbb{R}^n$.

4.2.2 Kinematics

The pipe is in a classical point of view a rod, which is a three-dimensional body whose reference configuration can be described by a smooth curve $\boldsymbol{\varphi}_0$, where planes called *cross-sections* are attached at each point of $\boldsymbol{\varphi}_0$. The curve $\partial_S\boldsymbol{\varphi}_0$ is assumed to be normal to the plane of each cross-section and intersecting the plane at the centroid. Any configuration of the pipe is thus given by a smooth curve $\boldsymbol{\varphi} : [0, L] \rightarrow \mathbb{R}^3$ denoted *line of centroids*, where L is the total length of $\boldsymbol{\varphi}_0$, and thus the undeformed pipe. The cross-sections are assumed to remain unchanged in shape, but do not necessarily remain normal to $\partial_S\boldsymbol{\varphi}$ while the pipe is undergoing motion. This means that the pipe model is capable of undergoing shearing. The outlined kinematic model is known as the constrained two director *Cosserat rod*.

Let $\mathbf{t}$ be an orthonormal frame with base $\mathbf{t}_1, \mathbf{t}_2, \mathbf{t}_3$ with $\mathbf{t}_2$ and $\mathbf{t}_3$ directed along the principal axis of the plane and $\mathbf{t}_1$ normal to the plane in order to form a right-handed system, with the origin O_t at the centroid. In rigid body mechanics the frame $\mathbf{t}$ is called a *body frame*. Let $\mathbf{e}$ be an inertial frame with orthonormal base $\mathbf{e}_1, \mathbf{e}_2, \mathbf{e}_3$ and origin O_e located at the pipe touchdown point fixed on the sea floor. The orientation of $\mathbf{t}$ along $\boldsymbol{\varphi}(S)$ relative to $\mathbf{e}$ is given by the rotation matrix $\mathbf{R}_t^e : [0, L] \rightarrow \mathrm{SO}(3)$, where $\mathrm{SO}(3) \subset \mathbb{R}^3$ denotes the *special orthogonal group* of order three, such that for $i = 1, 2, 3$,

$$\mathbf{t}_i^e = \mathbf{R}_t^e \mathbf{e}_i^e. \tag{4.1}$$

The velocity of the points of $\boldsymbol{\varphi}(S, t)$ is given as $\dot{\boldsymbol{\varphi}}(S, t)$, and the spatial angular velocity of frame $\mathbf{t}$ is given as

$$\dot{\mathbf{R}}_t^e = (\mathbf{w}^e)^\times \mathbf{R}_t^e, \tag{4.2}$$

where $(\cdot)^\times$ is the skew-symmetric operator, and $(\mathbf{w}^e)^\times$ is the *vorticity* in the inertial frame. The associated vector $\mathbf{w}^e \in \mathbb{R}^3$ is the spatial angular velocity of the cross-sections.

Marine vessels moving in six degrees of freedom (DOF) require a minimum of six independent coordinates to uniquely determine position and orientation. Let

b be a body fixed frame with the origin O_b located at the center of gravity of the pipelay vessel and orthonormal base $\mathbf{b}_1, \mathbf{b}_2, \mathbf{b}_3$ directed along the principal axes of symmetry of the vessel. Let the generalized position and orientation of the vessel be given as

$$\boldsymbol{\eta}^e = \begin{bmatrix} \mathbf{p}^{\mathrm{T}} & \boldsymbol{\Theta}^{\mathrm{T}} \end{bmatrix}^{\mathrm{T}} \in \mathbb{R}^6, \tag{4.3}$$

where $\mathbf{p} = [x, y, z]^{\mathrm{T}}$ is the position in the **e** frame, and $\boldsymbol{\Theta} = [\phi, \theta, \psi]^{\mathrm{T}}$ representing the orientation $\mathbf{R}_t^e$ in Euler angles by the *zyx*-convention. The velocity of the vessel $\boldsymbol{\nu}^b$, is expressed in the body-fixed frame **b** such that

$$\boldsymbol{\nu}^b = \begin{bmatrix} \mathbf{v}^{\mathrm{T}} & \boldsymbol{\omega}^{\mathrm{T}} \end{bmatrix}^{\mathrm{T}} \in \mathbb{R}^6. \tag{4.4}$$

where $\mathbf{v} \in \mathbb{R}^3$ represents the linear velocity, and $\boldsymbol{\omega} \in \mathbb{R}^3$ represents the angular velocity. Let the pipe be clamped to the vessel such that O_b coincides with O_t at $S = L$, at an arbitrary fixed angle $\boldsymbol{\beta}$. The rotation matrix $\mathbf{R}_b^e$, rotating from **e** to **b** is

$$\mathbf{R}_b^e = \mathbf{R}_t^e(L) \, \mathbf{R}_b^t(\boldsymbol{\beta}), \tag{4.5}$$

where $\mathbf{R}_b^t$ is a constant. The mapping of velocity between the **e**-frame and the **b**-frame is

$$\dot{\boldsymbol{\eta}}^e = \mathbf{J}(\boldsymbol{\eta}^e) \, \boldsymbol{\nu}^b, \tag{4.6}$$

where $\mathbf{J}(\boldsymbol{\eta}^e) \in \mathbb{R}^{6 \times 6}$ is found as

$$\mathbf{J}(\boldsymbol{\eta}^e) = \begin{bmatrix} \mathbf{R}_b^e & \mathbf{0}_{3 \times 3} \\ \mathbf{0}_{3 \times 3} & \boldsymbol{\Pi}_e^{-1} \mathbf{R}_b^e \end{bmatrix} \in \mathbb{R}^{6 \times 6}, \quad \theta \neq \pm \frac{\pi}{2}. \tag{4.7}$$

The mapping $\boldsymbol{\Pi}_e$ between angular velocity $\mathbf{w}^e$ and the rate of change of the Euler angles $\dot{\boldsymbol{\Theta}}$ is obtained from equation (4.2), such that

$$\mathbf{w}^e = \boldsymbol{\Pi}_e \dot{\boldsymbol{\Theta}} \tag{4.8}$$

where

$$\boldsymbol{\Pi}_e(\boldsymbol{\Theta}) = \begin{bmatrix} \cos\theta \cos\psi & -\sin\psi & 0 \\ \cos\theta \sin\psi & \cos\psi & 0 \\ -\sin\theta & 0 & 1 \end{bmatrix}. \tag{4.9}$$

This parametrization of the rotation with respect to Euler angles by the *zyx*-convention introduces a singularity in pitch for the inverse kinematics. Alternative conventions can be applied to move the singularity, or it can be removed completely by using quaternions.

The superscripts of $\boldsymbol{\eta}^e$ and $\boldsymbol{\nu}^b$ will be omitted for the remainder of this paper.

89

4.2.3 The Vessel Dynamics

The equations of motion of a marine vessel given in the body frame is known from [5] as

$$\mathbf{M}\dot{\boldsymbol{\nu}} + \mathbf{C}(\boldsymbol{\nu})\boldsymbol{\nu} + \mathbf{D}(\boldsymbol{\nu})\boldsymbol{\nu} + \mathbf{g}(\boldsymbol{\eta}) = \boldsymbol{\tau} + \boldsymbol{\chi} + \mathbf{w} \tag{4.10}$$

where

$\mathbf{M}$	- system inertia matrix
$\mathbf{C}(\boldsymbol{\nu})$	- Coriolis-centripetal matrix
$\mathbf{D}(\boldsymbol{\nu})$	- damping matrix
$\mathbf{g}(\boldsymbol{\eta})$	- vector of restoring forces and moments
$\boldsymbol{\tau}$	- vector of control inputs
$\boldsymbol{\chi}$	- vector of forces and moments from the pipe
$\mathbf{w}$	- vector of environmental forces

where $\mathbf{M}$ is symmetric positive definite, $\mathbf{C}(\boldsymbol{\nu})$ is skew-symmetric and $\mathbf{D}(\boldsymbol{\nu})$ is symmetric positive definite. The equation of motion in the inertial frame $\mathbf{e}$ is found by substituting (4.6) into (4.10) such that

$$\mathbf{M}_\eta(\boldsymbol{\eta})\ddot{\boldsymbol{\eta}} + \mathbf{C}_\eta(\boldsymbol{\nu},\boldsymbol{\eta})\dot{\boldsymbol{\eta}} + \mathbf{D}_\eta(\boldsymbol{\nu},\boldsymbol{\eta})\dot{\boldsymbol{\eta}} + \mathbf{g}_\eta(\boldsymbol{\eta})$$
$$= \mathbf{J}^{-\mathrm{T}}(\boldsymbol{\eta})\boldsymbol{\tau} + \mathbf{J}^{-\mathrm{T}}(\boldsymbol{\eta})\boldsymbol{\chi} \tag{4.11}$$

where

$$\mathbf{M}_\eta(\boldsymbol{\eta}) = \mathbf{J}^{-\mathrm{T}}\mathbf{M}\mathbf{J}^{-1} \tag{4.12}$$

$$\mathbf{C}_\eta(\boldsymbol{\nu},\boldsymbol{\eta}) = \mathbf{J}^{-\mathrm{T}}\left[\mathbf{C}(\boldsymbol{\nu}) - \mathbf{M}\mathbf{J}^{-1}\dot{\mathbf{J}}\right]\mathbf{J}^{-1} \tag{4.13}$$

$$\mathbf{D}_\eta(\boldsymbol{\nu},\boldsymbol{\eta}) = \mathbf{J}^{-\mathrm{T}}\mathbf{D}(\boldsymbol{\nu})\mathbf{J}^{-1} \tag{4.14}$$

$$\mathbf{g}_\eta(\boldsymbol{\eta}) = \mathbf{J}^{-\mathrm{T}}\mathbf{g}(\boldsymbol{\eta}) \tag{4.15}$$

The vector of forces and moments from the pipe $\boldsymbol{\chi}$, is presented as the boundary condition for the pipe in the next section. Note that $\boldsymbol{\chi}$ is given in the body fixed frame of the vessel. For the later passivity analysis the following properties of (4.11) hold:

P1) $\mathbf{M}_\eta(\boldsymbol{\eta}) = \mathbf{M}_\eta^{\mathrm{T}}(\boldsymbol{\eta}) > 0, \quad \forall\,\boldsymbol{\eta} \in \mathbb{R}^6$

P2) $\mathbf{s}^{\mathrm{T}}\left[\dot{\mathbf{M}}_\eta(\boldsymbol{\eta}) - 2\mathbf{C}_\eta(\boldsymbol{\nu},\boldsymbol{\eta})\right]\mathbf{s} = 0, \quad \forall\,\mathbf{s},\boldsymbol{\nu},\boldsymbol{\eta} \in \mathbb{R}^6$

P3) $\mathbf{D}_\eta(\boldsymbol{\nu},\boldsymbol{\eta}) > 0, \quad \forall\,\boldsymbol{\nu},\boldsymbol{\eta} \in \mathbb{R}^6$.

Note also that $\mathbf{C}_\eta(\boldsymbol{\nu},\boldsymbol{\eta})$ is not skew-symmetric.

4.2.4 The Pipe Dynamics

The pipe dynamics is modeled by:

$$m_P \ddot{\boldsymbol{\varphi}} = \partial_S \mathbf{n}^e - \mathbf{f}_g^e - \mathbf{R}_t^e \mathbf{f}_D^t, \tag{4.16}$$

$$\mathbf{I}_\rho^e \dot{\mathbf{w}}^e + \mathbf{w}^e \times \mathbf{I}_\rho^e \mathbf{w}^e = \partial_S \mathbf{m}^e + \partial_S \boldsymbol{\varphi} \times \mathbf{n}^e - \mathbf{D}_R \mathbf{w}^e, \tag{4.17}$$

where

m_P	- mass per unit length of the pipe
$\mathbf{R}_t^e \mathbf{f}_D^t$	- transversal hydrodynamic damping vector
$\mathbf{n}^e$	- resultant internal force vector
$\mathbf{f}_g^e$	- restoring force vector
$\mathbf{I}_\rho^e$	- mass moment of inertia matrix
$\mathbf{D}_R$	- rotation damping matrix
$\mathbf{m}^e$	- resultant internal torque vector

and $\mathbf{D}_R > 0$. Due to the buoyancy, the restoring forces given as $\mathbf{f}_g^e = (m_P - \rho_w A) \mathbf{g}^e$, not only depend on the mass and gravitation $\mathbf{g}^e = [0, 0, g]^{\mathrm{T}}$, but also on the mass density of ambient water ρ_w and the cross-section area of the pipe A. The damping is estimated using Morison's equation [4] and is given as

$$\mathbf{f}_D^t = \frac{1}{2} d_o \rho_w \mathbf{D}_T \begin{bmatrix} \left| v_{r_1}^t \right| v_{r_1}^t \\ \left(\left(v_{r_2}^t \right)^2 + \left(v_{r_3}^t \right)^2 \right)^{1/2} v_{r_2}^t \\ \left(\left(v_{r_2}^t \right)^2 + \left(v_{r_3}^t \right)^2 \right)^{1/2} v_{r3}^t \end{bmatrix}, \tag{4.18}$$

where d_o is the outer pipe diameter, $\mathbf{D}_T$ is the symmetric positive definite damping matrix of translational motion and $v_{r_i}^t$ are elements of the relative velocity of the pipe in the water, $\mathbf{v}_r^t = \left(\mathbf{R}_t^e \right)^{\mathrm{T}} (\dot{\boldsymbol{\varphi}} - \mathbf{v}_c^e) \in \mathbb{R}^3$, where $\mathbf{v}_c^e \left(\boldsymbol{\varphi}^{\mathrm{T}} \mathbf{e}_3, t \right)$ is the ocean current velocity at depth $h + \boldsymbol{\varphi}^{\mathrm{T}} \mathbf{e}_3$, where h represents the water depth. Wave excitation forces on the pipe are neglected since they only affect the pipe near to the surface, (typically down to 20m). The time dependent inertia tensor, $\mathbf{I}_\rho^e (S, t)$, is given by

$$\mathbf{I}_\rho^e = \mathbf{R}_t^e \mathbf{J}_\rho^t \left(\mathbf{R}_t^e \right)^{\mathrm{T}}, \quad \mathbf{J}_\rho^t = \mathrm{diag}[J_1, J_2, J_3] \tag{4.19}$$

where $\mathbf{J}_\rho^t \in \mathbb{R}^{3 \times 3}$ is the inertia tensor for the cross section in the reference configuration.

Let the lower end of the pipe be clamped to the seabed, tangent to the $\mathbf{e}_1$-axis, thus the boundary conditions at $S = 0$ are

$$\boldsymbol{\varphi} (0, t) = \boldsymbol{\varphi}_0 = 0, \tag{4.20}$$

$$\mathbf{R}_t^e (0, t) = (\mathbf{R}_t^e)_0 = I_{3 \times 3}, \tag{4.21}$$

and the pipelay vessel represents the boundary conditions at $S = L$, which can explicitly be expressed by inserting (4.10) into

$$
\begin{bmatrix} \mathbf{n}^e|_L \\ \mathbf{m}^e|_L \end{bmatrix} = - \begin{bmatrix} \mathbf{R}_b^e & \mathbf{0}_{3\times 3} \\ \mathbf{0}_{3\times 3} & \mathbf{R}_b^e \end{bmatrix} \boldsymbol{\chi}
\tag{4.22}
$$

with the initial conditions

$$
\mathbf{R}_t^e \left(L, t_0 \right) = \mathbf{R}_b^e \left(t_0 \right) \left(\mathbf{R}_b^t \left(\boldsymbol{\beta} \right) \right)^{\mathrm{T}}.
\tag{4.23}
$$

4.3   Control Design

The stability properties of the system are investigated in this section. Firstly, an input-output passivity check of the pipelay system with the thrusters as the input and the velocity vector as the output is performed, and secondly a stability check of the pipelay system by condition of feedback connection of two passive systems, which are the pipelay vessel with pipeline and the passive thruster controller.

4.3.1   Passivity

Let the thruster force of the vessel $\boldsymbol{\tau}$ be defined as the input, and the output be defined as the vessel speed in the body frame. The total energy of the system $\mathcal{E}$, taken as the storage function is given by

$$
\mathcal{E} = \mathcal{E}_P + \mathcal{E}_V \geq 0
\tag{4.24}
$$

where $\mathcal{E}_P$ and $\mathcal{E}_V$ are the energy of the pipe and vessel respectively. The pipe energy function $\mathcal{E}_P$ is the sum of kinetic energy $\mathcal{T}_P$ and potential energy $\mathcal{U}_P$,

$$
\mathcal{E}_P = \mathcal{T}_P + \mathcal{U}_P
\tag{4.25}
$$

where

$$
\mathcal{T}_P = \frac{1}{2} \int_0^L \left(m_P \left\langle \dot{\boldsymbol{\varphi}}, \dot{\boldsymbol{\varphi}} \right\rangle + \left\langle \mathbf{w}^e, \mathbf{I}_\rho \mathbf{w}^e \right\rangle \right) dS,
\tag{4.26}
$$

$$
\mathcal{U}_P = \int_0^L \boldsymbol{\Psi} \left(\boldsymbol{\gamma}^t, \boldsymbol{\omega}^t \right) dS + \int_0^L \left\langle \mathbf{f}_g^e, \boldsymbol{\varphi} \right\rangle dS,
\tag{4.27}
$$

and the potential energy function $\boldsymbol{\Psi}$ is given by the quadratic form

$$
\boldsymbol{\Psi} \left(S, \boldsymbol{\gamma}^t, \boldsymbol{\omega}^t \right) = \frac{1}{2} [\left(\boldsymbol{\gamma}^t \right)^{\mathrm{T}} \mathbf{C}_T \boldsymbol{\gamma}^t + \left(\boldsymbol{\omega}^t \right)^{\mathrm{T}} \mathbf{C}_R \boldsymbol{\omega}^t],
\tag{4.28}
$$

where $\{\boldsymbol{\gamma}^t, \boldsymbol{\omega}^t\}$ is the strain measure [17], and

$$\mathbf{C}_T = \operatorname{diag}\left[EA, GA_2, GA_3\right] > 0, \tag{4.29}$$

$$\mathbf{C}_R = \operatorname{diag}\left[GJ, EI_2, EI_3\right] > 0. \tag{4.30}$$

The constants E and G are interpreted as the Young's modulus and the shear modulus, A is the cross-sectional area of the pipe, A_2 and A_3 are the effective shear areas, $\{I_2, I_3\}$ are the principal moments of inertia of the cross-section plane relative to principal axes $\mathbf{t}_2, \mathbf{t}_3$ of $\boldsymbol{\varphi}_0$, and J is the *Saint Venant* torsional modulus. Equation (4.28) is only valid for small strains since it does not have proper growth conditions for extreme strains.

The vessel energy function $\mathcal{E}_V$ is likewise the sum of kinetic energy $\mathcal{T}_V$ and potential energy $\mathcal{U}_V$, given as

$$\mathcal{T}_V = \frac{1}{2}\dot{\boldsymbol{\eta}}^{\mathrm{T}}\mathbf{M}_\eta\dot{\boldsymbol{\eta}} \quad \text{and} \quad \mathcal{U}_V = \mathcal{G}\left(\boldsymbol{\eta}\right), \tag{4.31}$$

where $\mathcal{G}\left(\boldsymbol{\eta}\right) : \mathbb{R}^6 \to \mathbb{R}$ is a potential function for $\mathbf{g}_\eta\left(\boldsymbol{\eta}\right)$, such that

$$\nabla\mathcal{G} = \mathbf{g}_\eta \quad \Rightarrow \quad \dot{\mathcal{G}}\left(\boldsymbol{\eta}\right) = \mathbf{g}_\eta^{\mathrm{T}}\left(\boldsymbol{\eta}\right)\dot{\boldsymbol{\eta}}. \tag{4.32}$$

The time derivative of (4.24) is given as

$$\dot{\mathcal{E}} = \dot{\mathcal{E}}_P + \dot{\mathcal{E}}_V, \tag{4.33}$$

where, following [9], $\dot{\mathcal{E}}_P$ is found to be

$$\dot{\mathcal{E}}_P = \left[\langle\mathbf{n}^e, \dot{\boldsymbol{\varphi}}\rangle\right]_0^L + \left[\langle\mathbf{m}^e, \mathbf{w}^e\rangle\right]_0^L$$
$$- \int_0^L \left(\langle\dot{\boldsymbol{\varphi}}, \mathbf{R}_t^e\mathbf{f}_D^t\rangle + \langle\mathbf{w}^e, \mathbf{D}_R\mathbf{w}^e\rangle\right)dS, \tag{4.34}$$

where the two terms of the integral are square damping terms dissipating energy from the system. Without these terms the system is seen to be energy conservative as the energy is only depending on the boundary conditions. The time derivative of $\mathcal{E}_V$ is readily seen to be

$$\dot{\mathcal{E}}_V = \dot{\boldsymbol{\eta}}^{\mathrm{T}}\mathbf{M}_\eta\ddot{\boldsymbol{\eta}} + \frac{1}{2}\dot{\boldsymbol{\eta}}^{\mathrm{T}}\dot{\mathbf{M}}_\eta\dot{\boldsymbol{\eta}} + \mathbf{g}_\eta^{\mathrm{T}}\left(\boldsymbol{\eta}\right)\dot{\boldsymbol{\eta}} \tag{4.35}$$

$$= \dot{\boldsymbol{\eta}}^{\mathrm{T}}\mathbf{J}^{\text{-}\mathrm{T}}\boldsymbol{\tau} + \dot{\boldsymbol{\eta}}^{\mathrm{T}}\mathbf{J}^{\text{-}\mathrm{T}}\boldsymbol{\chi} - \dot{\boldsymbol{\eta}}^{\mathrm{T}}\mathbf{D}_\eta\left(\boldsymbol{\nu}, \boldsymbol{\eta}\right)\dot{\boldsymbol{\eta}} \tag{4.36}$$

where (4.11) and properties **P2** and **P3** have been applied. Thus

$$\dot{\mathcal{E}}_V \leq \boldsymbol{\nu}^{\mathrm{T}}\boldsymbol{\tau} + \boldsymbol{\nu}^{\mathrm{T}}\boldsymbol{\chi} \tag{4.37}$$

which implies that to obtain input-output passivity for the vessel $\boldsymbol{\nu}^{\mathrm{T}}\boldsymbol{\chi}$ vanish.

For the boundary condition at $S = 0$ it is readily seen that

$$\langle \mathbf{n}^e, \dot{\boldsymbol{\varphi}} \rangle \,|_0 = \langle \mathbf{m}^e, \mathbf{w}^e \rangle \,|_0 = 0. \tag{4.38}$$

The remaining terms, $S = L$, are the forces and moments on the pipe from the vessel. Summing the time derivatives of the energy for the vessel (4.36) and pipe (4.34), we obtain

$$\dot{\mathcal{E}} = \boldsymbol{\nu}^{\mathrm{T}}\boldsymbol{\tau} + \boldsymbol{\nu}^{\mathrm{T}}\boldsymbol{\chi} - \dot{\boldsymbol{\eta}}^{\mathrm{T}}\mathbf{D}_\eta \left(\boldsymbol{\nu}, \boldsymbol{\eta} \right) \dot{\boldsymbol{\eta}} \tag{4.39}$$
$$+ \langle \mathbf{n}^e, \dot{\boldsymbol{\varphi}} \rangle \,|_L + \langle \mathbf{m}^e, \mathbf{w}^e \rangle \,|_L$$

$$- \int_0^L \left(\langle \dot{\boldsymbol{\varphi}}, \mathbf{R}_t^e \mathbf{f}_D^t \rangle + \langle \mathbf{w}^e, \mathbf{D}_R \mathbf{w}^e \rangle \right) dS. \tag{4.40}$$

It is readily seen by inserting (4.22), and noting that

$$\boldsymbol{\nu} = \begin{bmatrix} \mathbf{v} \\ \boldsymbol{\omega} \end{bmatrix} = \begin{bmatrix} \mathbf{R}_e^b \dot{\boldsymbol{\varphi}} \\ \mathbf{R}_e^b \mathbf{w}^e \end{bmatrix}, \tag{4.41}$$

that the forces and moments acting between the vessel and the pipe cancel, so that (4.39) reduces to

$$\dot{\mathcal{E}} = \boldsymbol{\nu}^{\mathrm{T}}\boldsymbol{\tau} - \dot{\boldsymbol{\eta}}^{\mathrm{T}}\mathbf{D}_\eta \left(\boldsymbol{\nu}, \boldsymbol{\eta} \right) \dot{\boldsymbol{\eta}}$$

$$- \int_0^L \left(\langle \dot{\boldsymbol{\varphi}}, \mathbf{R}_t^e \mathbf{f}_D^t \rangle + \langle \mathbf{w}^e, \mathbf{D}_R \mathbf{w}^e \rangle \right) dS. \tag{4.42}$$

The properties of the damping terms are known from the previous sections such that $\dot{\mathcal{E}} \leq \boldsymbol{\nu}^{\mathrm{T}}\boldsymbol{\tau}$, and input-output passivity from thruster force to vessel motion of the total system has been shown.

4.3.2 Controller

An important objective in the competitive pipelay industry is to improve the profit margins by optimize the utilization of the equipment by increasing the operational time of the vessel and also to reduce the cost of pipe path preparation on the seabed. The tension from the pipe on the vessel is a function of the water depth, pipe density and bending stiffness, and must be counteracted by the vessel thrusters to obtain a desired pipe configuration. Low tension yields a steep configuration where the touchdown point is located close to the vessel, which reduces free spans and allows for smaller radii of the pipe on the seabed

and thus reduces the need for seabed preparation as the pipe can more easily be placed to avoid obstacles. Also advocating for low tension is the directly proportional relationship to the fuel cost [10]. However, too little tension will cause the pipe string to buckle, this occurs when the strain exceeds the pipe design limit. Finding the optimal tension is an optimization task where the above issues are considered.

A simple and common control strategy is *tension control* which is based on the measured tension of the pipe at the vessel. In this paper a controller is designed to shape the configuration of the pipe. Assume that a desired pipe configuration $\boldsymbol{\varphi}_{ref}$ is known. This may typically be obtained from simulations in tools like SIMLA. There exists a mapping $\mathbf{F}$ from the desired configuration to desired vessel position $\boldsymbol{\eta}_{ref}$ and velocities $\boldsymbol{\nu}_{ref}$;

$$\mathbf{F} : \left(\boldsymbol{\varphi}_{ref}, \mathbf{R}_t^e \right) \rightarrow \left(\boldsymbol{\eta}_{ref}, \boldsymbol{\nu}_{ref} \right). \tag{4.43}$$

Known measurements are the vessel and touchdown point positions and attitudes, the pipe tension at the vessel, the length of the suspended pipe and the stinger configuration for S-lay. In practical applications, the external environmental forces of wind, waves and current must be accounted for in the controller, so the nonlinear PID-controller is suggested

$$\boldsymbol{\tau} = -\mathbf{J}^{\mathrm{T}} \left(\boldsymbol{\eta} \right) \boldsymbol{\tau}_{PID}, \tag{4.44}$$

$$\boldsymbol{\tau}_{PID} = \mathbf{K}_p \tilde{\boldsymbol{\eta}} + \mathbf{K}_d \dot{\tilde{\boldsymbol{\eta}}} + \mathbf{K}_i \int_{t_0}^{t} \tilde{\boldsymbol{\eta}} \left(\tau \right) d\tau, \tag{4.45}$$

where $\tilde{\boldsymbol{\eta}} = \boldsymbol{\eta} - \boldsymbol{\eta}_{ref}$, and the matrices $\mathbf{K}_p$, $\mathbf{K}_d$, $\mathbf{K}_i \in \mathbb{R}^{6 \times 6}$ are controller gains. It is assumed that a wave filter removes the 1st order waves, and the effect of wind is handled as a feed-forward term. The integrator term removes the bias caused by current and 2nd order waves. Assuming the vessel to be fully actuated, the available control input are the vessel thrusters, which are limited to surge, sway and yaw. By choosing a passive controller such as a PD-controller ($\mathbf{K}_i = \mathbf{0}$), the closed loop system is stable by the condition of feedback connection of two passive systems, found in Theorem 6.1 in [11]. However, this property is generally not guaranteed for the PID-controller due to the integrator term, unless the integral action term of the controller is bounded.

4.4 Simulations

A standard Galerkin finite element method, with linear shape functions, is applied on (4.16–4.17) with (4.20–4.22) as boundary conditions. The integration in time is handled by the embedded Matlab ODE-solver `ode15s`, suitable for stiff
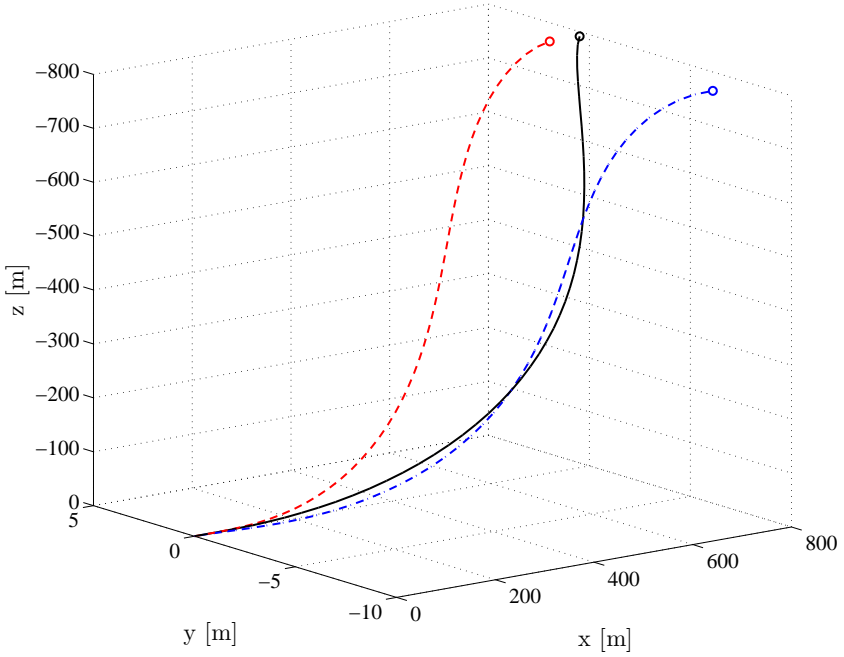
Figure 4.2: The dashed red line is the initial static configuration. Dash dot blue line is at $t = 30s$ where the controller is turned on. Solid black line is configuration at $t = 200s$.

systems, with the timestep set to $0.03s$. To find the static equilibrium configuration, a Newton Raphson iterative scheme [19] is applied to the linearized weak formulation of the static model. Integrals are approximated by using Gauss-quadrature. A linearized model of the vessel (4.10) found in *GNC Toolbox* [6] is used for the pipelay vessel.

The position of the vessel in the static equilibrium is computed to be $\boldsymbol{\eta}_0 =$

$[729.96, 0, -800.38, 0, 0.13, 0]^{\mathrm{T}}$ based on the following parameters:

$$\begin{aligned}
\mathbf{R}_b^t &= \mathbf{I}_{3\times3}, & \boldsymbol{\eta}_{ref} &= [780, 0, 0, 0, 0, 0]^{\mathrm{T}}, \\
n &= 48, & \mathbf{w} &= \left[0, 6\cdot10^5, 0, 0, 0, 0\right]^{\mathrm{T}}, \\
h &= 800\mathrm{m}, & \mathbf{J} &= 10^2\cdot\mathrm{diag}[1, 1, 2]^{\mathrm{T}}, \\
L &= 1200\mathrm{m}, & \mathbf{C}_T &= 10^9\cdot\mathrm{diag}[1, 1, 1]^{\mathrm{T}}, \\
d_i &= 0.57\mathrm{m}, & \mathbf{C}_R &= 10^{11}\cdot\mathrm{diag}[1, 1, 1]^{\mathrm{T}}, \\
d_o &= 0.60\mathrm{m}, & \mathbf{D}_T &= 1.5\cdot\mathrm{diag}[1, 1, 1]^{\mathrm{T}}, \\
\boldsymbol{\beta} &= [0, 0, 0]^{\mathrm{T}}, & \mathbf{D}_R &= 1.5\cdot\mathrm{diag}[1, 1, 1]^{\mathrm{T}}, \\
\rho_a &= 1.200\cdot10^3\mathrm{g/m}^3, & \rho &= (\rho_a - \rho_s)(d_i/d_o)^2 + \rho_s, \\
\rho_w &= 1.025\cdot10^6\mathrm{g/m}^3, & \rho_s &= 7.850\cdot10^6\mathrm{g/m}^3.
\end{aligned}$$

The course of the simulation is as follows. The pipe starts in the static equilibrium. At time $t = 10\ s$ the environmental forces on the vessel $\mathbf{w}$ and linearly shared current velocity profile with surface velocity $0.8\ m/s$ in the $-y$ direction are applied. At time $t = 30\ s$ the controller is turned on. The configurations at the different times are illustrated in Figure 4.2, and Figure 4.3 show the elements of $\boldsymbol{\eta}$ for the vessel when the PD-controller is applied with the following controller gains:

$$\mathbf{K}_p = \mathrm{diag}[0.5\cdot10^6, 0.5\cdot10^6, 0, 0, 0, 0]^{\mathrm{T}}, \qquad (4.46)$$

$$\mathbf{K}_d = \mathrm{diag}[0.4\cdot10^7, 0.4\cdot10^7, 0, 0, 0, 0]^{\mathrm{T}}. \qquad (4.47)$$

In Figure 4.4 a PID-controller has been applied with the following controller gains:

$$\mathbf{K}_p = \mathrm{diag}[0.4\cdot10^6, 0.4\cdot10^6, 0, 0, 0, 10^5]^{\mathrm{T}} \qquad (4.48)$$

$$\mathbf{K}_d = \mathrm{diag}[0.5\cdot10^7, 0.4\cdot10^7, 0, 0, 0, 10^5]^{\mathrm{T}} \qquad (4.49)$$

$$\mathbf{K}_i = \mathrm{diag}[0.1\cdot10^4, 0.5\cdot10^4, 0, 0, 0, 0.2\cdot10^4]^{\mathrm{T}}. \qquad (4.50)$$

Applying a PID-controller removes the bias seen in the PD-controller simulation.

4.5   Conclusions

A mathematical model suitable for pipelay operations from a dynamically positioned surface vessel has been presented in this paper. The pipe string has been modeled by a nonlinear dynamic formulation in three dimensions capable of undergoing shearing, twist, and bending. A nonlinear model of the pipelay vessel
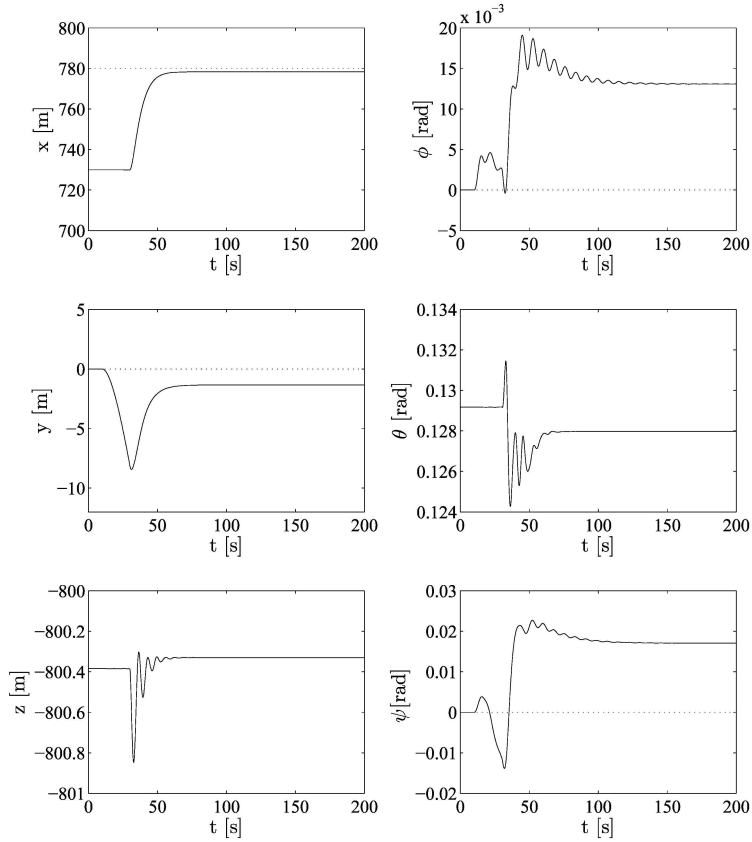
Figure 4.3: Postion and orientation of $\boldsymbol{\eta}$ over the course of the simulation. The PD-controller is enabled at $t = 30s$. The dotted line indicates $\boldsymbol{\eta}_{ref}$ for the controlled states. Note the bias.

has been taken as the upper boundary condition for solving the numerical problem. The pipelay system has been shown to be passive taking the thruster force as input and the vessel velocity as the output. A nonlinear controller considering the kinematics is presented and applied in numerical simulations to illustrate the theoretical results. For future extensions of the pipe model, seabed and stinger interaction forces should be added to the model, and the pipe length should be made a function of time $L(t)$ to handle pay-out of pipe from the vessel.
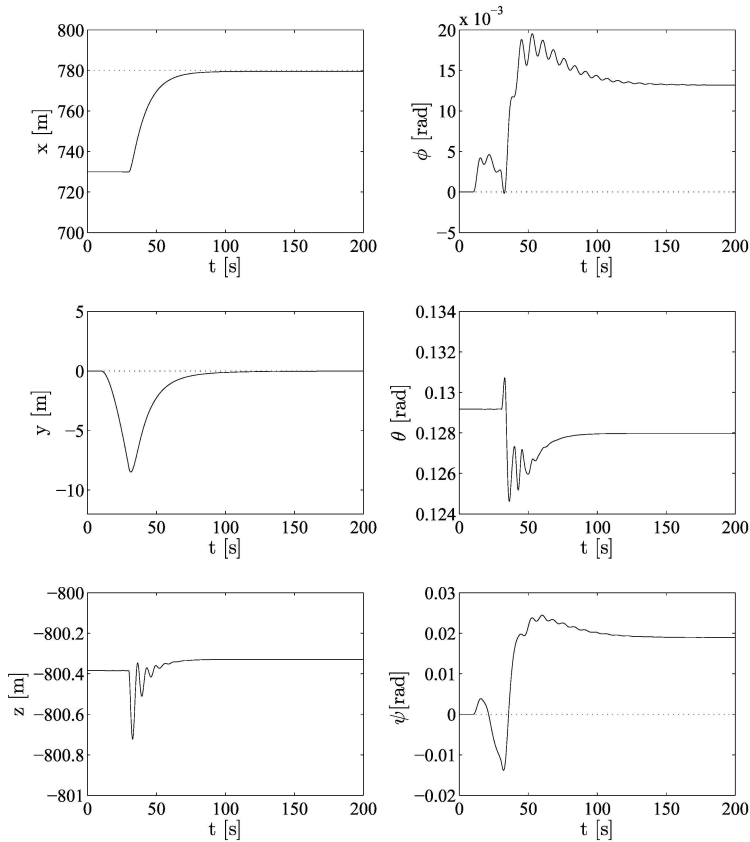
Figure 4.4: Postion and orientation of $\boldsymbol{\eta}$ over the course of the simulation. The PID-controller is enabled at $t = 30s$. The dotted line indicates $\boldsymbol{\eta}_{ref}$ for the controlled states. Note that the integrator term cancels the bias terms seen when the PD-controller was applied.

Bibliography

[1] M. J. Balas. Active control of flexible systems. *Journal Of Optimization Theory And Applications*, 25(3):415–436, 1978.

[2] M. W. Braestrup, J. B. Andersen, L. W. Andersen, M. B. Bryndum, C. J. Christensen, and N. Rishøy. *Design and Installation of Marine Pipelines*. Blackwell Science Ltd, 2005.

[3] D.A. Dixon and D.R. Rutledge. Stiffened catenary calculations in pipeline laying problem. *ASME Journal of Engineering for Industry*, (90):153–160, February 1968.

[4] O. M. Faltinsen. *Sea Loads on Ships and Offshore Structures*. Cambridge University Press, 1990.

[5] Thor I. Fossen. *Marine Control Systems: Guidance, Navigation, and Control of Ships, Rigs and Underwater Vehicles*. Marine Cybernetics, Trondheim Norway, 1st edition, 2002.

[6] Thor I. Fossen and Tristan Perez. Marine systems simulator (MSS). ⟨*www.marinecontrol.org*⟩, 2004.

[7] B. Guo, S. Song, J. Chacko, and A. Ghalambor. *Offshore Pipelines*. Gulf Professional Publishing, 2005.

[8] E.P. Heerema. Recent achievements and present trends in deepwater pipe-lay systems. In *Proceedings of the 37th Offshore Technology Conference*, 2005. OTC 17627.

[9] G. A. Jensen, N. Säfström, T. I. Fossen, and T. D. Nguyen. A nonlinear PDE formulation for offshore vessel pipeline installation. *Ocean Engineering*, 2009. To appear.

[10] M. Kashani and R. Young. Installation load consideration in ultra-deepwater pipeline sizing. *Journal of Transportation Engineering*, 131(8):632–639, August 2005.

[11] H.K. Khalil. *Nonlinear Systems*. Prentice Hall, 3rd edition, 2002.

[12] R. Knight and O. Palathingal. Pipelay market constrained by vessel shortages? In *OTC07 Show Daily 05.02.07*, pages 20–21, 2007.

[13] S. Kyriakides and E. Corona. *Mechanics of Offshore Pipelines, Volume 1: Buckling and Collapse*. Elsevier, 1 edition, 2007.

[14] Andrew C. Palmer and Roger A. King. *Subsea Pipeline Engineering*. PennWell Books, 2nd edition, 2008.

[15] D. Perinet and I. Frazer. J-lay and Steep S-lay: Complementary tools for ultradeep water. In *Proceedings of the 39th Offshore Technology Conference*, 2007. OTC 18669.

[16] R. Plunkett. Static bending stresses in catenaries and drill strings. *Journal of Engineering for Industry*, February 1967.

[17] J. C. Simo. A finite strain beam formulation. The three-dimensional dynamic problem. Part I. *Computer Methods in Applied Mechanics and Engineering*, 49(1):55–70, May 1985.

[18] J. C. Simo, N. Tarnow, and M. Doblare. Non-linear dynamics of three-dimensional rods: Exact energy and momentum conserving algorithms. *International Journal For Numerical Methods in Engineering*, 38:1431–1473, 1995.

[19] J. C. Simo and L. Vu-Quoc. A three-dimensional finite-strain rod model. Part II: Computational aspects. *Computer Methods in Applied Mechanics and Engineering*, 58(1):79–116, October 1986.

[20] J. C. Simo and L. Vu-Quoc. On the dynamics in space of rods undergoing large motions – a geometrically exact approach. *Computer Methods in Applied Mechanics and Engineering*, 66(2):125–161, February 1988.

Paper IV

A Nonlinear PDE Formulation for Offshore Vessel Pipeline Installation

G. A. Jensen, N. Säfström, T. I. Fossen and T. D. Nguyen.
To appear in Journal of Ocean Engineering.

Chapter 5

A Nonlinear PDE Formulation for Offshore Vessel Pipeline Installation

ABSTRACT. In this paper a nonlinear dynamic PDE formulation for a pipe string suspended from a pipelay vessel to the seabed in a pipelay operation is developed. This model extends a three-dimensional beam model capable of undergoing finite extension, shearing, twist and bending, to apply for marine applications by adding the effects of restoring forces, hydrodynamic drag and seabed interaction. The model is validated against the natural catenary equation and the FEM code RI-FLEX. The model is extended to include the pipelay vessel dynamics by applying a potential theory formulation of a surface vessel, suited for dynamic positioning and low speed maneuvering, as a boundary condition for the PDE. This system is found to be input-output passive and stable. Pipeline installation applications where the presented PDE is suited are e.g., analysis and simulation of the installation operation, operabiltiy analysis, hardware-in-the-loop (HIL) testing for vessel control systems, and automation of the pipelay operation.

5.1   Introduction

Slender marine structures are characterized by having a small cross-section area compared to the overall structure length, and in the offshore industry these structures have many applications, such as mooring lines, umbilicals, towers, pipelines and risers, e.g., drilling risers, production risers, export risers and workover risers. Having a good understanding of the dynamics of such structures is important for

marine applications, and this understanding can be acquired from simulations based on mathematical models.

In this paper offshore pipeline installation from a surface vessel, a so-called *pipelay operation*, is considered, see Figure 5.1, where the main objective of the operation is to position a pipeline along a predefined path on the seabed only by means of active control of the pipelay vessel position, while at all times ensuring the structural integrity of the pipe [18]. The different methods used in pipelay operations are well described in recent textbooks on pipelaying, e.g., [4], [13] and [25], while the present trends in deepwater pipelay systems in general are well described by [15] and the references therein.

5.1.1 Pipeline Modelling

In the design phase of an offshore pipeline project, mathematical models for the pipeline dynamics are needed to determine pipe properties, pipelay parameters, and the conditions under which the pipeline can safely be installed. Offshore pipelay operations were first conducted in shallow waters close to shore, where the strains and stresses in the pipe could satisfactory be approximated by analytic models, such as the catenary equation known from cable mechanics [16], and the stiffened catenary equation [27, 5]. As pipelay operations were taken into deeper waters the dynamic behavior of the pipe became significant. Hence, dynamic pipe models based on elastic beam models, known from continuum mechanics, were introduced. These models were discretized, using e.g., the finite element method (FEM) or the finite difference method, and solved numerically using computers.

Today, computer codes based on FEM, e.g., RIFLEX, ABAQUS, OFFPIPE and SIMLA, where FEM models are developed by joining already defined elements, are the method of choice for analysis and simulation of pipelay operations, since these computer codes produce high quality discrete dynamic models. A case-study using ABAQUS is found in [21].

In this paper a nonlinear model for pipe string dynamics is developed by extending a finite strain beam formulation, which is three-dimensional and capable of undergoing finite extension, shearing, twisting and bending, first presented in [31]. The principle of superposition [7] is frequently applied in ocean engineering and is used to extend this model to account for the effects of gravity and buoyancy as well as hydrodynamic drag and seabed interaction. An advantage of this model over FEM codes is that analyses can be performed directly on the continuous system, rather than on a discretized system. This model is then validated against the catenary equation and the commercial computer code RIFLEX [12], which holds an international leading position in FEM analysis for slender marine structures.

A potential theory formulation of a surface vessel, suited for dynamic posi-

tioning and low speed maneuvering, is used as the upper boundary condition to form a system encompassing both pipe and vessel. Hence, analyses where the dynamics of the vessel is integrated can be performed with vessel control forces as inputs. It seems plausible that a computer code for dynamic simulation based on this model may be lighter and faster compared to present alternatives, since the discretization and integration methods can be chosen based on detailed knowledge of the model, see e.g., [29, 3, 22]. Applications related to pipeline installation are e.g., simulation of the installation operation, operabiltiy analysis, hardware-in-the-loop (HIL) testing for vessel control systems, and pipelay operation automation. It seems also plausible that the model is not limited to pipelines, but is valid for many slender marine structures.

5.1.2 Automating Pipelay Operations

Today pipelay operations mostly rely on manually operated dynamic positioning (DP) systems for vessel positioning. Following [18], it seems plausible that introducing automatic control systems can improve the performance in this industry, as it has for several other industries, including the process industry, aerospace industry, and others [1]. Consequently, closed-loop automatic control for pipelay operations is a relatively new application which may now gain more attention as DP systems have become standard for deep-water pipelay operations.

The issue of stability of the closed-loop feedback system arises when FEM computer code models are considered for application in model-based controllers. The pipe model must be shown to be passive, and the potentially large number of states and equations may complicate this analysis. However, mechanical flexible systems are continuous with infinite degrees of freedom, so-called *infinite-dimensional*. In practice these systems are modeled as finite-dimensional with a large number of dimensions, and the fundamental problem of actively controlling such systems is to control the large-dimensional system with a much smaller dimensional controller. This issue was addressed in [2], where the authors showed that such controllers can become unstable when connected to systems with infinite degrees of freedom even if the discrete model is shown to be passive. This is due to the unmodeled modes in the system, named *the spillover*, which the controller does not account for.

In this paper the passivity analysis of the pipe model is performed before the system is discretized by a finite element method. By careful discretization, this property can be preserved, and the closed-loop system will be stable. This model feature indicates that it may be a suitable candidate for implementation in a model-based controller. The passivity analysis is extended to the complete system including the vessel as the upper boundary condition. This result is important in that a necessary property for implementing the model in model-

based controllers is establishes.

5.2 Mathematical Model

The model of the pipe dynamics is a partial differential equation (PDE) extending the nonlinear beam formulation developed and investigated by Simo et al. in a series of papers [31, 33, 34, 32]. The formulation is a reparametrization of the formulation originally developed in [28], and this model again can be regarded as a generalization of a three-dimensional extension of the classical Kirchhoff-Love rod model [20]. The extension includes finite extension and finite shearing of the rod. New to the model in this paper is the hydrodynamic and hydrostatic effects caused by the marine environment as well as the seabed interaction. Pipeline installation is a low speed application, hence it is a reasonable assumption to neglect the acceleration term of the damping as well as the added mass.

A vessel model in the time domain, suitable for low-speed maneuvering and station keeping, is fixed to the surface end of the pipe string as the upper boundary condition. The vessel model is obtained by considering the forces and moments on a rigid body as well as hydrodynamic radiation forces and wave loads and the resulting state space model is a system of ordinary differential equations in the time domain.

In this section, the notation and reference frames are introduced, followed by the kinematics and the dynamics, including the boundary conditions.

5.2.1 Notation

Bold face lower and upper case letters denote vectors and matrices respectively, and a superscript denote the reference frame of coordinate vectors. This may be omitted if the frame dependency is evident. With a small abuse of notation, the derivative with respect to time is denoted by a superposed dot and the derivative with respect to space, the curve parameter S, is denoted by a prefixed ∂_S. The usual inner product of $\boldsymbol{a}, \boldsymbol{b} \in \mathbb{R}^n$ is denoted $\langle \boldsymbol{a}, \boldsymbol{b} \rangle$ or equivalently on vectorial form $\boldsymbol{a}^{\mathrm{T}} \boldsymbol{b}$.

5.2.2 Reference Frames

Three Cartesian reference frames denoted by $\boldsymbol{e}$, $\boldsymbol{t}$ and $\boldsymbol{b}$ are required in the development of the pipelay system model, see Figure 5.1. Let $\boldsymbol{e}$ be an inertial frame with base $\boldsymbol{e}_1, \boldsymbol{e}_2, \boldsymbol{e}_3$, where the origin O_e is fixed to the seabed at $S = 0$. Let $\boldsymbol{t}(S)$ be a body-fixed frame with base $\boldsymbol{t}_1(S), \boldsymbol{t}_2(S), \boldsymbol{t}_3(S)$ and origin $O_t(S)$ located at the centroid of the pipe cross-section at S, where $S \in [0, L]$ is the spatial pipe variable, and L is the total length of the undeformed pipe. The base vector $\boldsymbol{t}_1(S)$
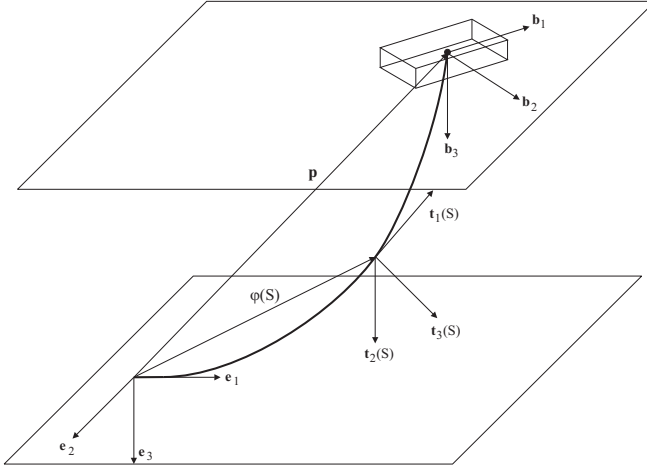
Figure 5.1: Illustration of a J-lay installation in three dimensions with the three reference frames applied. The position of the pipelay vessel center of mass, illustrated by the box, is in the spatial frame $\boldsymbol{e}$ given by $\boldsymbol{p}$.

is directed normal to the cross-section plane, and $\boldsymbol{t}_2\,(S)$ and $\boldsymbol{t}_3\,(S)$ are directed along the principal axis of it. Let $\boldsymbol{b}$ be body-fixed with origin O_b at the pipelay vessel center of mass, and with its basis $\boldsymbol{b}_1, \boldsymbol{b}_2, \boldsymbol{b}_3$ along the principle axes of symmetry for the vessel, in accordance with [35]. The $\boldsymbol{e}$ and $\boldsymbol{t}$ frames are frequently referred to as the *spatial* and *material* frame, respectively.

The coordinate transformation of vectors from one frame to another is given by

$$\mathbf{v}^y = \boldsymbol{R}_x^y \mathbf{v}^x, \quad x,y \in \{\boldsymbol{e}, \boldsymbol{t}, \boldsymbol{b}\}, \quad \mathbf{v} \in \mathbb{R}^3, \tag{5.1}$$

where

$$\boldsymbol{R}_x^y \in SO(3), \quad SO(3) \triangleq \{\boldsymbol{R}_x^y \in \mathbb{R}^{3\times3}\,|\,(\boldsymbol{R}_x^y)^\mathrm{T}\boldsymbol{R}_x^y = \boldsymbol{I}_{3\times3},\ \det \boldsymbol{R}_x^y = 1\}, \tag{5.2}$$

is a so-called *rotation matrix* from y to x, that transforms the vector coordinates of $\mathbf{v}$ in frame x to frame y. This notation is adopted from [6]. In addition to representing the coordinate transformation between the coordinates of a point expressed in two different frames, the rotation matrix is also describing the mutual orientation between two coordinate frames, where the columns of the matrix are the directional cosines of the axes of the rotated frame with respect to the original frame [30]. Transformations between the defined frames $\boldsymbol{e}$, $\boldsymbol{t}$ and $\boldsymbol{b}$ are handled by the rotation matrices

$$\boldsymbol{R}_t^e(S), \boldsymbol{R}_b^e, \boldsymbol{R}_b^t \in SO(3), \tag{5.3}$$
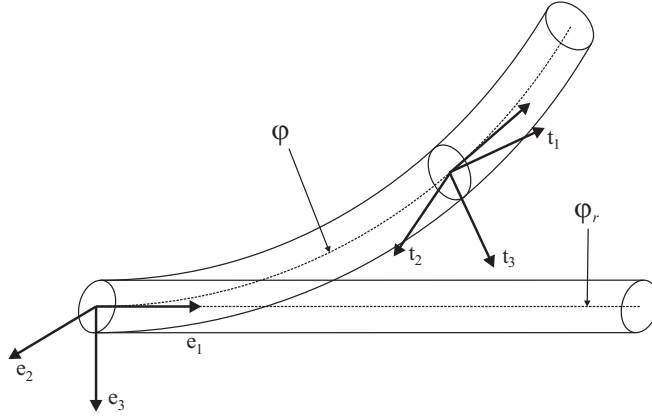
Figure 5.2: The pipe configuration is given by the line of centroids $\boldsymbol{\varphi}$, where the reference configuration is given as $\boldsymbol{\varphi}_r$. The cross-section of the pipe at $\boldsymbol{\varphi}(S)$ is spanned by $\boldsymbol{t}_2(S)$ and $\boldsymbol{t}_3(S)$.

where e.g. $\boldsymbol{R}_t^e$ transforms coordinate vectors from in frame $\boldsymbol{t}$ to frame $\boldsymbol{e}$. Equivalent interpretations are given for $\boldsymbol{R}_b^e$ and $\boldsymbol{R}_b^t$ such that

$$\boldsymbol{t}_i^e(S) = \boldsymbol{R}_t^e(S)\boldsymbol{e}_i^e, \quad \boldsymbol{b}_i^e = \boldsymbol{R}_b^e\boldsymbol{e}_i^e, \quad \boldsymbol{b}_i^t = \boldsymbol{R}_b^t\boldsymbol{t}_i^t. \tag{5.4}$$

A rotation can be expressed as a sequence of partial rotations where each rotation is defined with respect to the preceding one [30]. Hence, a rotation matrix of composite rotations is the product of rotation matrices, and $\boldsymbol{R}_b^e$ can be found by the composite rotations

$$\boldsymbol{R}_b^e = \boldsymbol{R}_t^e(L)\boldsymbol{R}_b^t. \tag{5.5}$$

5.2.3 Model Preliminaries

From a classical point of view the pipeline can be considered similar to a hollow rod, a three-dimensional slender body with uniform density and circular cross-sections. The reference configuration of the pipe is described by a smooth curve $\boldsymbol{\varphi}_r$, connecting the centroids of the cross-section planes, where the tangent of $\boldsymbol{\varphi}_r$ is normal to each cross-section, see Figure 5.2. Any configuration of the pipe can then be given by a smooth curve $\boldsymbol{\varphi} : [0, L] \to \mathbb{R}^3$, the so-called *line of centroids*. The cross-sections are assumed to remain unchanged in shape while the pipe is undergoing motion, but the assumption that the cross-sections remain normal to the tangent $\partial_S\boldsymbol{\varphi}$ known from the Euler-Bernoulli beam theory is relaxed to account for shearing effects. The position of any point along the line of centroids is given by $\boldsymbol{\varphi}(S)$, and the orientation of the cross-section at $\boldsymbol{\varphi}(S)$ is given by $\boldsymbol{R}_t^e(S)$.

Hence, the configurations of the pipe are completely defined by specifying $\boldsymbol{\varphi}(S,t)$ and $\boldsymbol{R}_t^e(S,t)$ along the material variable S and time t. The *configuration space* for the elastic pipe is given by

$$\mathcal{C} \triangleq \left\{ (\boldsymbol{\varphi}, \boldsymbol{R}_t^e) \,|\, S \in [0,L] \to \mathbb{R}^3 \times SO(3) \,|\, \langle \partial_S \boldsymbol{\varphi}(S), \boldsymbol{R}_t^e \boldsymbol{e}_1^e \rangle > 0 \right\}, \qquad (5.6)$$

and the reference configuration is taken as $\left(\boldsymbol{\varphi}_r, \boldsymbol{R}_{t,r}^e \right) \in \mathcal{C}$ such that

$$\boldsymbol{\varphi}_r(S) = S\boldsymbol{e}_1^e, \quad \boldsymbol{R}_{t,r}^e(S) = \boldsymbol{I}_{3\times3}. \qquad (5.7)$$

5.2.4 Kinematics

The derivatives of $\boldsymbol{\varphi}(S,t)$ and $\boldsymbol{R}_t^e(S,t)$ with respect to time t and space S (curve parameter), and the material stress resultant and stress couple are derived in this section.

5.2.4.1 Time and Space Derivatives

Differentiating (5.4) with respect to time t yields

$$\dot{\boldsymbol{t}}_i^e = \boldsymbol{S}(\mathbf{w}^e)\,\boldsymbol{t}_i^e, \quad \boldsymbol{S}(\mathbf{w}^e) = \dot{\boldsymbol{R}}_t^e (\boldsymbol{R}_t^e)^{\mathrm{T}}, \qquad (5.8)$$

where $\boldsymbol{S}(\cdot) : \mathbb{R}^3 \to T_I SO(3)$, is the skew-symmetric map, defined as

$$\boldsymbol{S}(\mathbf{v}) \triangleq \begin{bmatrix} 0 & -v_3 & v_2 \\ v_3 & 0 & -v_1 \\ -v_2 & v_1 & 0 \end{bmatrix}, \quad \mathbf{v} \in \mathbb{R}^3. \qquad (5.9)$$

The *spin* of the moving frame is defined as the skew-symmetric tensor $\boldsymbol{S}(\mathbf{w}^e)$, and the associated axial vector $\mathbf{w}^e(S,t)$ defines the *vorticity*. The time derivative of $\boldsymbol{R}_t^e$ is thus given by the two alternative forms

$$\dot{\boldsymbol{R}}_t^e = \boldsymbol{R}_t^e \boldsymbol{S}(\mathbf{w}^t), \qquad (5.10)$$

$$\dot{\boldsymbol{R}}_t^e = \boldsymbol{S}(\mathbf{w}^e)\,\boldsymbol{R}_t^e. \qquad (5.11)$$

The linear velocity vector is given in the spatial and material frames respectively as

$$\dot{\boldsymbol{\varphi}} \in \mathbb{R}^3, \qquad \boldsymbol{v}^t = (\boldsymbol{R}_t^e)^{\mathrm{T}}\,\dot{\boldsymbol{\varphi}}, \qquad (5.12)$$

where differentiating (5.12) yields the linear acceleration

$$\ddot{\boldsymbol{\varphi}} \in \mathbb{R}^3, \qquad \dot{\boldsymbol{v}}^t = (\boldsymbol{R}_t^e)^{\mathrm{T}}\,\ddot{\boldsymbol{\varphi}} - (\boldsymbol{R}_t^e)^{\mathrm{T}}\,[\mathbf{w}^e \times \dot{\boldsymbol{\varphi}}]. \qquad (5.13)$$

The space derivative of the position vector is simply denoted $\partial_S \boldsymbol{\varphi}(S,t) \in \mathbb{R}^3$, and the corresponding material derivative of $\boldsymbol{R}_t^e$ is, like the time derivative, obtained from (5.4). Hence,

$$\partial_S \boldsymbol{R}_t^e = \boldsymbol{R}_t^e \boldsymbol{S}\left(\boldsymbol{\omega}^t\right), \tag{5.14}$$

$$\partial_S \boldsymbol{R}_t^e = \boldsymbol{S}\left(\boldsymbol{\omega}^e\right) \boldsymbol{R}_t^e, \tag{5.15}$$

where $\boldsymbol{\omega}^t$ and $\boldsymbol{\omega}^e$ represent the curvature or bending in material and spatial form, respectively. Since derivation with respect to time and space are commutative operations, evaluating the identity

$$\partial_S\left(\partial_t \boldsymbol{R}_t^e\right) = \partial_t\left(\partial_S \boldsymbol{R}_t^e\right), \tag{5.16}$$

by taking the spatial derivative of (5.10) and the time derivative of (5.14), yields the following expression relating $\boldsymbol{\omega}$ and $\mathbf{w}$,

$$\dot{\boldsymbol{\omega}}^t = \partial_S \mathbf{w}^t + \boldsymbol{\omega}^t \times \mathbf{w}^t = (\boldsymbol{R}_t^e)^{\mathrm{T}} \left[\partial_S \mathbf{w}^e + \boldsymbol{\omega}^e \times \mathbf{w}^e\right]. \tag{5.17}$$

5.2.4.2 Stress

The material stress resultant $\boldsymbol{n}^t$ and stress couple $\boldsymbol{m}^t$ are obtained from the bilinear quadratic energy function $\boldsymbol{\Psi}(\boldsymbol{\gamma}^t, \boldsymbol{\omega}^t)$ [31],

$$\boldsymbol{n}^t = \frac{\partial}{\partial \boldsymbol{\gamma}^t} \boldsymbol{\Psi}, \quad \boldsymbol{m}^t = \frac{\partial}{\partial \boldsymbol{\omega}^t} \boldsymbol{\Psi}, \tag{5.18}$$

where

$$\boldsymbol{\Psi}(\boldsymbol{\gamma}^t, \boldsymbol{\omega}^t) \triangleq \frac{1}{2} \begin{bmatrix} \boldsymbol{\gamma}^t \\ \boldsymbol{\omega}^t \end{bmatrix}^{\mathrm{T}} \begin{bmatrix} \boldsymbol{C}_T & \boldsymbol{0}_{3\times3} \\ \boldsymbol{0}_{3\times3} & \boldsymbol{C}_R \end{bmatrix} \begin{bmatrix} \boldsymbol{\gamma}^t \\ \boldsymbol{\omega}^t \end{bmatrix}, \tag{5.19}$$

and where extension and shearing $\boldsymbol{\gamma}^t$, defined as

$$\boldsymbol{\gamma}^t = (\boldsymbol{R}_t^e)^{\mathrm{T}} \left(\partial_s \boldsymbol{\varphi} - \boldsymbol{t}_1\right), \tag{5.20}$$

and curvature $\boldsymbol{\omega}^t$ are the material strain measures, and

$$\boldsymbol{C}_T = \operatorname{diag}\left[EA, GA_2, GA_3\right], \tag{5.21}$$

$$\boldsymbol{C}_R = \operatorname{diag}\left[GJ, EI_2, EI_3\right]. \tag{5.22}$$

The constants E and G are interpreted as the Young's modulus and the shear modulus, A is the cross-sectional area of the pipe, A_2 and A_3 are the effective shear areas, I is the unit polar moment of inertia of the cross-section plane, and J is the Saint Venant torsional modulus. Hence in material form

$$\boldsymbol{n}^t = \boldsymbol{C}_T \boldsymbol{\gamma}^t, \tag{5.23}$$

$$\boldsymbol{m}^t = \boldsymbol{C}_R \boldsymbol{\omega}^t, \tag{5.24}$$

and in spatial form

$$\boldsymbol{n}^e = \boldsymbol{R}_t^e \boldsymbol{n}^t = \boldsymbol{R}_t^e \boldsymbol{C}_T \left(\boldsymbol{R}_t^e\right)^{\mathrm{T}} [\partial_S \boldsymbol{\varphi} - \boldsymbol{t}_1^e], \tag{5.25}$$

$$\boldsymbol{m}^e = \boldsymbol{R}_t^e \boldsymbol{m}^t = \boldsymbol{R}_t^e \boldsymbol{C}_R \left(\boldsymbol{R}_t^e\right)^{\mathrm{T}} \boldsymbol{\omega}^e. \tag{5.26}$$

Taking the time derivative of (5.20) yields $\dot{\boldsymbol{\gamma}}^t$ to be

$$\dot{\boldsymbol{\gamma}}^t = -\boldsymbol{S}\left(\mathbf{w}^t\right) \left(\boldsymbol{R}_t^e\right)^{\mathrm{T}} \left(\partial_S \boldsymbol{\varphi}\right) + \left(\boldsymbol{R}_t^e\right)^{\mathrm{T}} \left(\partial_S \dot{\boldsymbol{\varphi}}\right) = \left(\boldsymbol{R}_t^e\right)^{\mathrm{T}} \left[\partial_S \dot{\boldsymbol{\varphi}} - \mathbf{w}^e \times \left(\partial_S \boldsymbol{\varphi}\right)\right]. \tag{5.27}$$

5.2.5 Dynamics

The linear and angular momentum balance equations for a nonlinear elastic beam are derived in [31] as

$$m_P \ddot{\boldsymbol{\varphi}} = \partial_S \boldsymbol{n}^e + \widetilde{\boldsymbol{n}}^e, \tag{5.28}$$

$$\boldsymbol{I}_\rho^e \dot{\mathbf{w}}^e + \mathbf{w}^e \times \boldsymbol{I}_\rho^e \mathbf{w}^e = \partial_S \boldsymbol{m}^e + \left(\partial_S \boldsymbol{\varphi}\right) \times \boldsymbol{n}^e + \widetilde{\boldsymbol{m}}^e, \tag{5.29}$$

where m_P is the mass per unit length, $\widetilde{\boldsymbol{n}}^e$ and $\widetilde{\boldsymbol{m}}^e$ are the resultant external force and torque per unit length, and $\boldsymbol{I}_\rho^e (S,t)$ is the state dependent inertia tensor given by

$$\boldsymbol{I}_\rho^e = \boldsymbol{R}_t^e \boldsymbol{J}_\rho^t \left(\boldsymbol{R}_t^e\right)^{\mathrm{T}}, \quad \boldsymbol{J}_\rho^t = \mathrm{diag}\left[J_1, J_2, J_3\right], \tag{5.30}$$

where $\boldsymbol{J}_\rho^t$ is the constant inertia tensor for the cross-sections in the reference configuration.

In this paper we propose to adopt this model for pipes submerged in water by approximating $\widetilde{\boldsymbol{n}}^e$ and $\widetilde{\boldsymbol{m}}^e$ by

$$\widetilde{\boldsymbol{n}}^e = -\boldsymbol{f}_g^e - \boldsymbol{f}_D^e - \boldsymbol{\sigma}^e, \tag{5.31}$$

$$\widetilde{\boldsymbol{m}}^e = -\boldsymbol{D}_R \mathbf{w}^e, \tag{5.32}$$

where

$\boldsymbol{f}_g^e$ - restoring forces vector (gravitation and buoyancy),
$\boldsymbol{f}_D^e$ - transversal hydrodynamic damping,
$\boldsymbol{D}_R$ - constant damping matrix of rotation,
$\boldsymbol{\sigma}^e$ - seabed interaction force.

Hence, the equations of motion for a nonlinear elastic pipe submerged in water, given as a PDE in the spatial frame, is found by substituting (5.31)–(5.32) into (5.28)–(5.29).

5.2.5.1 Hydrostatic Restoring Terms

The pipe is assumed to be completely submerged in water such that the restoring forces per unit length are the sum of the gravitation and the buoyancy as defined by Archimedes. The restoring forces acts only in the vertical direction $\boldsymbol{e}_3$, and is given in $\boldsymbol{e}$ by

$$\boldsymbol{f}_g^e = (m_P - \rho_w A)\, g\boldsymbol{e}_3, \tag{5.33}$$

where ρ_w is the mass density of ambient water, A is the pipe cross-section area and g is the gravitational constant.

5.2.5.2 Hydrodynamic Damping Terms

The hydrodynamic forces on a submerged slender body are given by Morison's equation as the sum of added mass and drag [23]. For applications involving low velocities such as e.g., risers, mooring lines and pipelay operations, the added mass term is small and can be neglected. An estimate for the remaining drag forces acting on a cylindrical shape in three dimensions are

$$\boldsymbol{f}_D^t = \frac{1}{2} d_o \rho_w \boldsymbol{D}_T \begin{bmatrix} \left| v_{r_1}^t \right| v_{r_1}^t \\ \left(\left(v_{r_2}^t\right)^2 + \left(v_{r_3}^t\right)^2 \right)^{1/2} v_{r_2}^t \\ \left(\left(v_{r_2}^t\right)^2 + \left(v_{r_3}^t\right)^2 \right)^{1/2} v_{r_3}^t \end{bmatrix}, \tag{5.34}$$

where d_o is the outer pipe diameter and

$$\boldsymbol{D}_T = \mathrm{diag}[D_1, D_2, D_3], \tag{5.35}$$

where $D_1, D_2, D_3 \geq 0$ are damping coefficients, which are constant if a constant Reynold's number is assumed. The vector $\boldsymbol{v}_r^t$ is the relative velocity of the pipe in the water,

$$\boldsymbol{v}_r^t = \left(\boldsymbol{R}_t^e\right)^{\mathrm{T}} \left(\dot{\boldsymbol{\varphi}}^e - \boldsymbol{v}_c^e\right), \tag{5.36}$$

where $\boldsymbol{v}_c^e = \boldsymbol{v}_c^e \left(\boldsymbol{\varphi}^{\mathrm{T}} \boldsymbol{e}_3, t\right)$ is the water current vector given in the spatial frame. Let the rotational damping in (5.29) be directly proportional to the angular velocity $\mathbf{w}$, where

$$\boldsymbol{D}_R = \mathrm{diag}[D_4, D_5, D_6], \tag{5.37}$$

and where $D_4, D_5, D_6 \geq 0$ are the damping coefficients.

5.2.6 Seabed Interaction

A seabed interaction force is commonly modeled by a spring and damper pair or simply a spring, since the spring effect will usually dominate the damping effect.

In this paper the damping effect is neglected, and we propose that the seabed interaction force $\boldsymbol{\sigma}^e$ is modeled by a nonlinear spring, acting on the pipeline section that is in contact with the seabed, given by

$$\boldsymbol{\sigma}^e = k_\sigma \left(\kappa \right) \boldsymbol{e}_3, \qquad k_\sigma \left(\kappa \right) = \begin{cases} 0, & \kappa < 0, \\ \dfrac{\|\boldsymbol{f}_g^e\|_2}{(d_o/8 - d_o/40)} \dfrac{10\kappa^2}{d_o}, & 0 \leqslant \kappa \leqslant d_o/20, \\ \dfrac{\|\boldsymbol{f}_g^e\|_2}{(d_o/8 - d_o/40)} (\kappa - d_o/40), & \kappa > d_o/20, \end{cases}$$

(5.38)

where $\kappa = \boldsymbol{\varphi}^\mathrm{T} \boldsymbol{e}_3 + d_o/2$ denotes the vertical seabed penetration. The nonlinear spring $\boldsymbol{\sigma}^e \in \mathcal{C}^1$ is defined such that the pipe is at rest for seabed penetration equal to $1/8$ of the outer pipe diameter, $\kappa = d_o/8$. The spring becomes linear for $\kappa > d_o/20$ and the constants are chosen so that $\boldsymbol{\sigma}^e$ becomes continuously differentiable over $\mathbb{R}$.

5.2.7 Boundary Conditions

The model (5.28)–(5.29) is clamped to the seabed at the lower end and fixed to a surface vessel at the upper end. These boundary conditions are presented in this section, mainly focusing on the surface vessel model.

5.2.7.1 Seabed

The lower end of the pipe is assumed to be fixed to the seabed, and the boundary condition for $S = 0$ is thus given by

$$\boldsymbol{\varphi} \left(0, t \right) = \boldsymbol{\varphi}_0 = 0, \quad \boldsymbol{R}_t^e \left(0, t \right) = \boldsymbol{R}_{t,0}^e = \boldsymbol{I}_{3 \times 3}.$$

(5.39)

5.2.7.2 Vessel

In recent years there has been a significant drive to develop time-domain models for simulation and control system design based on data obtained from seakeeping programs such as VERES [8] and WAMIT [36]. These programs use potential theory to compute the potential coefficients (added mass and potential damping) and the existing wave loads (Froude-Krylov and diffraction forces) for a given vessel design [9] and [11]. In [26], a potential theory formulation for a surface vessel suited for dynamic positioning and low speed maneuvering is developed, and this model is adopted as the boundary condition of the pipe at $S = L$ with some modifications.

Let $\boldsymbol{\eta} \in \mathbb{R}^3 \times \mathcal{S}^3$ be the generalized coordinate position vector using Euler angles given in the spatial frame $\boldsymbol{e}$ and $\boldsymbol{\nu} \in \mathbb{R}^6$ be the generalized velocity vector

given in the body frame $\boldsymbol{b}$, both defined by [9] as

$$\boldsymbol{\eta} = [x, y, z, \phi, \theta, \psi]^{\mathrm{T}} \qquad \text{and} \qquad \boldsymbol{\nu} = [u, v, w, p, q, r]^{\mathrm{T}}. \tag{5.40}$$

For low-speed applications, we can approximate the equations of motion with a linear kinetic model,

$$\boldsymbol{M}\dot{\boldsymbol{\nu}} + \boldsymbol{C}_{RB}\boldsymbol{\nu} + \boldsymbol{C}_A\boldsymbol{\nu} + \boldsymbol{B}\left(\infty\right)\boldsymbol{\nu} + \boldsymbol{\mu} + \boldsymbol{G}\boldsymbol{\eta} = \boldsymbol{\tau}^b, \tag{5.41}$$

while the kinematics use a nonlinear formulation

$$\dot{\boldsymbol{\eta}} = \boldsymbol{J}\left(\boldsymbol{\eta}\right)\boldsymbol{\nu}, \quad \boldsymbol{J}\left(\boldsymbol{\eta}\right) = \begin{bmatrix} \boldsymbol{R}_b^e & \boldsymbol{0}_{3\times 3} \\ \boldsymbol{0}_{3\times 3} & \boldsymbol{T}_\Theta \end{bmatrix}, \tag{5.42}$$

where $\boldsymbol{T}_\Theta$ relates the body-fixed angular velocity to the Euler rate vector. Let

$$\boldsymbol{M} \triangleq \boldsymbol{M}_{RB} + \boldsymbol{M}_A, \tag{5.43}$$

where $\boldsymbol{M}_{RB}$ is the rigid body inertia matrix

$$\boldsymbol{M}_{RB} = \begin{bmatrix} m_V \boldsymbol{I}_{3\times 3} & \boldsymbol{0}_{3\times 3} \\ \boldsymbol{0}_{3\times 3} & \boldsymbol{I}_V^b \end{bmatrix}, \tag{5.44}$$

where m_V is the total vessel mass, and $\boldsymbol{I}_V^b \in \mathbb{R}^{3\times 3}$ is the body inertia tensor. Matrix $\boldsymbol{M}_A = \boldsymbol{A}\left(\infty\right)$ and $\boldsymbol{B}\left(\infty\right)$ are the constant infinite frequency added mass and potential damping matrices. Notice that $\boldsymbol{B}\left(\infty\right) = 0$ for zero-speed applications. As the frame used is not inertial, the Coriolis and centripetal terms for the rigid body $\boldsymbol{C}_{RB}$ and the added mass $\boldsymbol{C}_A$ are accounted for, and appears as

$$\boldsymbol{C}_{RB} \triangleq \boldsymbol{M}_{RB} U \boldsymbol{L} \quad \text{and} \quad \boldsymbol{C}_A \triangleq \boldsymbol{M}_A U \boldsymbol{L}, \tag{5.45}$$

where $U = \|\boldsymbol{v}^e\|$, and

$$\boldsymbol{L} \triangleq \begin{bmatrix} 0 & \cdots & 0 & 0 \\ 0 & \cdots & 0 & 1 \\ 0 & \cdots & -1 & 0 \\ \vdots & \ddots & \vdots & \vdots \\ 0 & \cdots & 0 & 0 \end{bmatrix} \in \mathbb{R}^{6\times 6}. \tag{5.46}$$

The matrix $\boldsymbol{G}$ is the restoring matrix. External forces acting on the pipelay vessel $\boldsymbol{\tau}^b$ are

$$\boldsymbol{\tau}^b = \boldsymbol{\tau}_{\text{control}}^b + \boldsymbol{\tau}_{\text{pipe}}^b + \boldsymbol{\tau}_{\text{env}}^b, \tag{5.47}$$

where $\boldsymbol{\tau}_{\text{pipe}}^b$ is the force from the pipe, $\boldsymbol{\tau}_{\text{control}}^b$ is the applied control force, and $\boldsymbol{\tau}_{\text{env}}^b$ are environmental forces. In the remainder of this paper we assume $\boldsymbol{\tau}_{\text{env}}^b = 0$.

The term $\boldsymbol{\mu}$ is a convolution term representing the fluid memory effects and given for low-speed, i.e. $U = 0$, as

$$\boldsymbol{\mu} \triangleq \int_0^t \boldsymbol{K}\left(t - \xi\right) \boldsymbol{\nu}\left(\xi\right) d\xi, \tag{5.48}$$

where $\boldsymbol{K}\left(t\right)$ is a matrix of retardation functions [24]:

$$\boldsymbol{K}\left(t\right) = \int_0^\infty \boldsymbol{B}\left(\omega\right) \cos\left(\omega t\right) d\omega. \tag{5.49}$$

We can approximate

$$\boldsymbol{\mu}\left(t\right) \approx \boldsymbol{D}_p \boldsymbol{\nu}, \tag{5.50}$$

where $\boldsymbol{D}_p$ is a frequency-independent constant matrix approximating $\boldsymbol{\mu}$ at low frequencies. The resulting linear state-space model becomes

$$\boldsymbol{M}\dot{\boldsymbol{\nu}} + \boldsymbol{C}_{RB}\boldsymbol{\nu} + \boldsymbol{C}_A\boldsymbol{\nu} + \boldsymbol{D}_p\boldsymbol{\nu} + \boldsymbol{G}\boldsymbol{\eta} = \boldsymbol{\tau}^b. \tag{5.51}$$

In hydrodynamics it is common to assume linear superposition [7], hence nonlinear Coriolis and damping terms can be added directly in the time-domain model (5.51) according to:

$$\boldsymbol{M}\dot{\boldsymbol{\nu}} + \boldsymbol{C}\left(\boldsymbol{\nu}\right)\boldsymbol{\nu} + \boldsymbol{D}\left(\boldsymbol{\nu}\right)\boldsymbol{\nu} + \boldsymbol{g}\left(\boldsymbol{\varphi}, \boldsymbol{R}_b^e\right) = \boldsymbol{\tau}^b, \tag{5.52}$$

with relaxations

$$\boldsymbol{G}\boldsymbol{\eta} \longleftrightarrow \boldsymbol{g}\left(\boldsymbol{\varphi}, \boldsymbol{R}_b^e\right), \tag{5.53}$$

$$\boldsymbol{C}_{RB} \longleftrightarrow \boldsymbol{C}_{RB}\left(\boldsymbol{\nu}\right), \tag{5.54}$$

$$\boldsymbol{C}_A \longleftrightarrow \boldsymbol{C}_A\left(\boldsymbol{\nu}\right), \tag{5.55}$$

and

$$\boldsymbol{C}\left(\boldsymbol{\nu}\right) \triangleq \boldsymbol{C}_{RB}\left(\boldsymbol{\nu}\right) + \boldsymbol{C}_A\left(\boldsymbol{\nu}\right), \tag{5.56}$$

$$\boldsymbol{D}\left(\boldsymbol{\nu}\right) \triangleq \boldsymbol{D}_p + \boldsymbol{D}_v\left(\boldsymbol{\nu}\right), \tag{5.57}$$

where $\boldsymbol{D}_v\left(\boldsymbol{\nu}\right)$ is quadratic viscous damping due to cross-flow drag and surge resistance.

The following properties of (5.52) holds for the assumption that $\dot{\boldsymbol{M}} = \boldsymbol{0}$:

P1) $\boldsymbol{M} = \boldsymbol{M}^\mathrm{T} > 0$,

P2) $\boldsymbol{s}^\mathrm{T}\left[\dot{\boldsymbol{M}} - 2\boldsymbol{C}\left(\boldsymbol{\nu}\right)\right]\boldsymbol{s} = 0, \quad \forall\, \boldsymbol{s} \in \mathbb{R}^6$,

P3) $\boldsymbol{D}\left(\boldsymbol{\nu}\right) > 0, \quad \forall\, \boldsymbol{\nu} \in \mathbb{R}^6$.

117

A metacentric stable surface vessel has restoring forces and moments in heave (z), roll (ϕ) and pitch (θ) that will resist inclinations away from the steady-state equilibrium. The restoring forces and moments will depend on the vessel's metacentric height, the location of the center of gravity, the center of buoyancy, and the shape and size of the water plane, denoted by A_{wp}. For every vessel and load a transversal metacentric height $\overline{GM}_T \in \mathbb{R}$ and a longitudinal metacentric height $\overline{GM}_L \in \mathbb{R}$ can be computed [9].

The equilibrium in heave is obtained when the gravity and buoyancy forces balance. A force $\boldsymbol{g}_l^e \in \mathbb{R}^3$ is generated to restore this balance if the heave position $\boldsymbol{\varphi}^{\mathrm{T}}(L,t)\,\boldsymbol{e}_3$ changed due to external forces, or the heave equilibrium z_{eq} changes due to e.g. waves. This force is modeled in the $\boldsymbol{e}$ frame as

$$\boldsymbol{g}_l^e = -A_{wp}\rho_w g \left(\boldsymbol{\varphi}^{\mathrm{T}}(L,t)\,\boldsymbol{e}_3 - z_{eq} \right) \boldsymbol{e}_3, \tag{5.58}$$

where the A_{wp} is assumed to be constant for small changes in heave.

From geometric considerations, the moment arms in roll and pitch can be found to be

$$\boldsymbol{r}_r^b = \begin{bmatrix} -\overline{GM}_L \sin\theta \\ \overline{GM}_T \sin\phi \\ 0 \end{bmatrix}. \tag{5.59}$$

The dependence of Euler angles are removed from (5.59) by observing that

$$\sin\theta = -\left(\boldsymbol{R}_b^e \boldsymbol{e}_1\right)^{\mathrm{T}} \boldsymbol{e}_3, \tag{5.60}$$

$$\sin\phi \approx \cos\theta \sin\phi = \left(\boldsymbol{R}_b^e \boldsymbol{e}_2\right)^{\mathrm{T}} \boldsymbol{e}_3, \tag{5.61}$$

where the applied approximation $\cos\theta = 1$ is generally true for small pitch angles, hence (5.59) is approximated by without Euler angles as

$$\widetilde{\boldsymbol{r}}_r^b \triangleq \begin{bmatrix} \overline{GM}_L \left(\boldsymbol{R}_b^e \boldsymbol{e}_1\right)^{\mathrm{T}} \boldsymbol{e}_3 \\ \overline{GM}_T \left(\boldsymbol{R}_b^e \boldsymbol{e}_2\right)^{\mathrm{T}} \boldsymbol{e}_3 \\ 0 \end{bmatrix} \approx \boldsymbol{r}_r^b, \tag{5.62}$$

such that the restoring moment term becomes

$$\begin{aligned} \boldsymbol{g}_r^e &= \widetilde{\boldsymbol{r}}_r^e \times \boldsymbol{f}_r^e \\ &= \left(\boldsymbol{R}_b^e \widetilde{\boldsymbol{r}}_r^b \right) \times \left(m_V g \boldsymbol{e}_3 \right). \end{aligned} \tag{5.63}$$

It is assumed that there is no moment due to heave. Consequently, the nonlinear restoring forces term of (5.52) is given in the body frame $\boldsymbol{b}$ as

$$\boldsymbol{g}^b \left(\boldsymbol{\varphi}(L,t), \boldsymbol{R}_b^e(t) \right) = \begin{bmatrix} \left(\boldsymbol{R}_b^e\right)^{\mathrm{T}} \boldsymbol{g}_t^e \\ \left(\boldsymbol{R}_b^e\right)^{\mathrm{T}} \boldsymbol{g}_r^e \end{bmatrix}. \tag{5.64}$$

For the remainder of this paper, let the pipe be fixed to the center of gravity of the vessel such that

$$
\boldsymbol{\nu} = \begin{bmatrix} (\boldsymbol{R}_b^e)^\mathrm{T} \, \dot{\boldsymbol{\varphi}} \, (L,t) \\ (\boldsymbol{R}_b^e)^\mathrm{T} \, \mathbf{w}^e \, (L,t) \end{bmatrix} \quad \text{and} \quad \dot{\boldsymbol{\nu}} = \begin{bmatrix} (\boldsymbol{R}_b^e)^\mathrm{T} \, \ddot{\boldsymbol{\varphi}} \, (L,t) \\ (\boldsymbol{R}_b^e)^\mathrm{T} \, \dot{\mathbf{w}}^e \, (L,t) \end{bmatrix}. \tag{5.65}
$$

Forces and moments acting between the pipe and the vessel are considered as internal forces in the total system, and by Newton's third law the following relationship holds:

$$
\begin{bmatrix} \boldsymbol{R}_b^e & \mathbf{0}_{3\times3} \\ \mathbf{0}_{3\times3} & \boldsymbol{R}_b^e \end{bmatrix} \boldsymbol{\tau}_{\mathrm{pipe}}^b = - \begin{bmatrix} \overline{\boldsymbol{n}}^e (L,t) \\ \overline{\boldsymbol{m}}^e (L,t) \end{bmatrix}. \tag{5.66}
$$

5.3 Passivity

The passivity properties of the developed model, with and without boundary conditions, are considered in this section. Passivity provides a useful tool for the analysis of nonlinear systems which relates nicely to Lyapunov and $\mathcal{L}_2$ stability [19]. The main passivity theorem states that the negative feedback connection of two passive systems is passive. By proving passivity of the pipelay system and choosing a passive controller, the feedback connection is thus known to be stable, which is necessary for control applications.

Theorem 5.3.1. *The system (5.28)–(5.29) is input-output passive, where the input $\overline{\boldsymbol{\tau}}$ and output $\overline{\boldsymbol{\nu}}$ are taken as*

$$
\overline{\boldsymbol{\tau}} \triangleq [\overline{\boldsymbol{n}}^e (0,t), \overline{\boldsymbol{m}}^e (0,t), \overline{\boldsymbol{n}}^e (L,t), \overline{\boldsymbol{m}}^e (L,t)]^T \in \mathbb{R}^{12} \tag{5.67}
$$

$$
\overline{\boldsymbol{\nu}} \triangleq [-\dot{\boldsymbol{\varphi}} (0,t), -\mathbf{w}^e (0,t), \dot{\boldsymbol{\varphi}} (L,t) \, \mathbf{w}^e (L,t)]^T \in \mathbb{R}^{12} \tag{5.68}
$$

and assuming that $|v_{c,i}^e| \le |\dot{\varphi}_i|$, for $i = 1, \ldots, 3$ (5.36).

Proof. The total system energy $\mathcal{E}_P$ of (5.28)–(5.29), is given by

$$
\mathcal{E}_P = \mathcal{T}_P + \mathcal{U}_P, \tag{5.69}
$$

where this pipe energy function is the sum of kinetic energy $\mathcal{T}_P$ and potential energy $\mathcal{U}_P$ [33],

$$
\mathcal{T}_P = \frac{1}{2} \int_0^L m_p \, \|\dot{\boldsymbol{\varphi}}\|_2^2 + \left\langle \mathbf{w}^e, \boldsymbol{I}_\rho^e \mathbf{w}^e \right\rangle dS, \tag{5.70}
$$

$$
\mathcal{U}_P = \int_0^L \boldsymbol{\Psi} \left(\boldsymbol{\gamma}^t, \boldsymbol{\omega}^t \right) dS + \int_0^L \left(\left\langle \boldsymbol{f}_g^e, \boldsymbol{\varphi} \right\rangle + \int_0^\kappa k_\sigma(\xi) \, d\xi \right) dS. \tag{5.71}
$$

Differentiating (5.69) with respect to time, the kinetic energy term yields

$$
\dot{\mathcal{T}}_P = \int\limits_0^L \langle \dot{\boldsymbol{\varphi}}, m_p \ddot{\boldsymbol{\varphi}} \rangle + \langle \mathbf{w}^e, \boldsymbol{I}_\rho^e \dot{\mathbf{w}}^e \rangle \, dS, \tag{5.72}
$$

which by substituting by (5.28)–(5.29) can be rewritten as

$$
\dot{\mathcal{T}}_P = \int\limits_0^L \left\langle \dot{\boldsymbol{\varphi}}, \left[\partial_S \boldsymbol{n}^e - \boldsymbol{f}_g^e - \boldsymbol{f}_D^e - \boldsymbol{\sigma}^e \right] \right\rangle \, dS +
$$

$$
\int\limits_0^L \left\langle \mathbf{w}^e, \left[(\boldsymbol{I}_\rho^e \mathbf{w}^e) \times \mathbf{w}^e + \partial_S \boldsymbol{m}^e + (\partial_S \boldsymbol{\varphi}) \times \boldsymbol{n}^e - \boldsymbol{D}_R \mathbf{w}^e \right] \right\rangle \, dS. \tag{5.73}
$$

The potential energy rate of change yields by differentiation

$$
\dot{\mathcal{U}}_P = \int\limits_0^L \langle \boldsymbol{n}^t, \partial_t \boldsymbol{\gamma}^t \rangle + \langle \boldsymbol{m}^t, \partial_t \boldsymbol{\omega}^t \rangle \, dS + \int\limits_0^L \langle \boldsymbol{f}_g^e, \dot{\boldsymbol{\varphi}} \rangle + \langle \boldsymbol{\sigma}^e, \dot{\boldsymbol{\varphi}} \rangle \, dS \tag{5.74}
$$

which by substituton of (5.27) for $\partial_t \boldsymbol{\gamma}^t$ and (5.17) for $\partial_t \boldsymbol{\omega}^t$, is rewritten as

$$
\dot{\mathcal{U}}_P = \int\limits_0^L \langle \boldsymbol{n}^e, [\partial_S \dot{\boldsymbol{\varphi}} - (\mathbf{w}^e \times (\partial_S \boldsymbol{\varphi}))] \rangle \, dS + \int\limits_0^L \langle \boldsymbol{m}^t, [\partial_S \mathbf{w}^t + (\boldsymbol{\omega}^t \times \mathbf{w}^t)] \rangle \, dS +
$$

$$
\int\limits_0^L \langle \boldsymbol{f}_g^e, \dot{\boldsymbol{\varphi}} \rangle + \langle \boldsymbol{\sigma}^e, \dot{\boldsymbol{\varphi}} \rangle \, dS. \tag{5.75}
$$

Since

$$
\partial_S \mathbf{w}^e = \partial_S \left(\boldsymbol{R}_t^e \mathbf{w}^t \right) = \boldsymbol{R}_t^e \boldsymbol{S} \left(\boldsymbol{\omega}^t \right) \mathbf{w}^t + \boldsymbol{R}_t^e \partial_S \mathbf{w}^t = \boldsymbol{R}_t^e \left[\partial_S \mathbf{w}^t + \left(\boldsymbol{\omega}^t \times \mathbf{w}^t \right) \right],
$$

and the fact that $\langle \boldsymbol{m}^t, (\boldsymbol{R}_t^e)^{\mathrm{T}} \partial_S \mathbf{w}^e \rangle = \langle \boldsymbol{m}^e, \partial_S \mathbf{w}^e \rangle$, the second term in (5.75) is simplified and, by integration by parts, the equation (5.75) is finally rewritten as

$$
\dot{\mathcal{U}}_P = \langle \overline{\boldsymbol{n}}^e, \dot{\boldsymbol{\varphi}} \rangle \big|_0^L + \langle \overline{\boldsymbol{m}}^e, \mathbf{w}^e \rangle \big|_0^L - \int\limits_0^L \langle \partial_S \boldsymbol{n}^e, \dot{\boldsymbol{\varphi}} \rangle + \langle \partial_S \boldsymbol{m}^e, \mathbf{w}^e \rangle \, dS +
$$

$$
\int\limits_0^L \langle \mathbf{w}^e, (\partial_S \boldsymbol{\varphi}) \times \boldsymbol{n}^e \rangle \, dS + \int\limits_0^L \langle \boldsymbol{f}_g^e, \dot{\boldsymbol{\varphi}} \rangle + \langle \boldsymbol{\sigma}^e, \dot{\boldsymbol{\varphi}} \rangle \, dS. \tag{5.76}
$$

Hence, the change of energy of the pipe string $\dot{\mathcal{E}}_P$ can then be found by summing (5.73) and (5.76) as

$$\dot{\mathcal{E}}_P = \langle \overline{\boldsymbol{n}}^e, \dot{\boldsymbol{\varphi}} \rangle \big|_0^L + \langle \overline{\boldsymbol{m}}^e, \mathbf{w}^e \rangle \big|_0^L - \int_0^L \langle \dot{\boldsymbol{\varphi}}, \boldsymbol{f}_D^e \rangle \, dS - \int_0^L \langle \mathbf{w}^e, \boldsymbol{D}_R \mathbf{w}^e \rangle \, dS, \quad (5.77)$$

where the energy is seen to depend on the boundary conditions and the transversal and rotational damping. Investigating the integral term for the rotational damping it is readily seen that

$$\int_0^L \langle \mathbf{w}^e, \boldsymbol{D}_R \mathbf{w}^e \rangle \, dS = \int_0^L \left(\sum_{i=1}^3 D_{i+3} \left(\mathbf{w}_i^e \right)^2 \right) dS \geq 0, \quad \forall \, \mathbf{w}^e, \quad (5.78)$$

such that this term will always dissipate energy. The restoring term is rewritten into

$$\int_0^L \langle \dot{\boldsymbol{\varphi}}, \boldsymbol{f}_D^e \rangle \, dS = \frac{1}{2} d\rho_w \int_0^L \langle \dot{\boldsymbol{\varphi}}, \boldsymbol{\Pi}(\dot{\boldsymbol{\varphi}} - \boldsymbol{v}_c^e) \rangle \, dS \geq 0, \quad \forall \, \left| v_{c,i}^e \right| \leq \left| \dot{\varphi}_i \right|, \quad (5.79)$$

where

$$\boldsymbol{\Pi} = \boldsymbol{R}_t^e \boldsymbol{D}_T \boldsymbol{\Gamma} \left(\boldsymbol{R}_t^e \right)^{\mathrm{T}} \geq 0, \quad (5.80)$$

$$\boldsymbol{\Gamma} = \mathrm{diag}\left[\left| v_{r_1}^t \right|, \left(\left(v_{r_2}^t \right)^2 + \left(v_{r_3}^t \right)^2 \right)^{1/2}, \left(\left(v_{r_2}^t \right)^2 + \left(v_{r_3}^t \right)^2 \right)^{1/2} \right] \geq 0. \quad (5.81)$$

Hence, from (5.77) and the assumption $\left| v_{c,i}^e \right| \leq \left| \dot{\varphi}_i \right|$, it follows

$$\dot{\mathcal{E}}_P \leq \langle \overline{\boldsymbol{n}}^e, \dot{\boldsymbol{\varphi}} \rangle \big|_0^L + \langle \overline{\boldsymbol{m}}^e, \mathbf{w}^e \rangle \big|_0^L = \overline{\boldsymbol{\tau}}^{\mathrm{T}} \overline{\boldsymbol{\nu}}. \quad (5.82)$$

$\square$

This theorem can be extended to include also the boundary conditions.

Theorem 5.3.2. *The system* (5.28)–(5.29) *with boundary condition* (5.39) *for* $S = 0$ *and* (5.66) *for* $S = L$ *is input-output passive, with input* $\boldsymbol{\tau}_{\mathrm{control}}^b$ (5.47) *and output* $\boldsymbol{\nu}$ (5.40), *and assuming that* $|v_{c,i}^e| \leq |\dot{\varphi}_i|$, *for* $i = 1, \ldots, 3$.

Proof. The total energy $\mathcal{E}$ of the pipelay system is given by the sum of the total energy of the pipe $\mathcal{E}_P$ and the surface vessel $\mathcal{E}_V$,

$$\mathcal{E} = \mathcal{E}_P + \mathcal{E}_V \geq 0, \quad (5.83)$$

$$\mathcal{E}_V = \mathcal{T}_V + \mathcal{U}_V, \quad (5.84)$$

The vessel energy function is the sum of kinetic $\mathcal{T}_V$ and potential energy $\mathcal{U}_V$,

$$\mathcal{T}_V = \frac{1}{2}\boldsymbol{\nu}^{\mathrm{T}}\boldsymbol{M}\boldsymbol{\nu} \tag{5.85}$$

$$\mathcal{U}_V = \frac{1}{2}A_{wp}\rho_w g \left(\boldsymbol{\varphi}^{\mathrm{T}}(L,t)\,\boldsymbol{e}_3 + h_{ref}\right)^2 +$$
$$\frac{1}{2}m_V g\left\{\overline{GM}_L\left[(\boldsymbol{R}_b^e\boldsymbol{e}_1)^{\mathrm{T}}\boldsymbol{e}_3\right]^2 + \overline{GM}_T\left[(\boldsymbol{R}_b^e\boldsymbol{e}_2)^{\mathrm{T}}\boldsymbol{e}_3\right]^2\right\}, \tag{5.86}$$

where $\mathcal{U}_V$ is the sum of the potential functions derived from (5.58) and (5.64). By differentiating (5.85) and (5.86) with respect to time, substituting in (5.52) and finally applying property **P2**, the change of energy for the vessel is found to be

$$\dot{\mathcal{T}}_V = \boldsymbol{\nu}^{\mathrm{T}}\boldsymbol{\tau}^b - \boldsymbol{\nu}^{\mathrm{T}}\boldsymbol{D}\boldsymbol{\nu} - \boldsymbol{\nu}^{\mathrm{T}}\boldsymbol{g}^b, \tag{5.87}$$

$$\dot{\mathcal{U}}_V = \boldsymbol{\nu}^{\mathrm{T}}\boldsymbol{g}^b. \tag{5.88}$$

Since $\dot{\mathcal{E}}_V = \dot{\mathcal{T}}_V + \dot{\mathcal{U}}_V$ we get

$$\dot{\mathcal{E}}_V = \boldsymbol{\nu}^{\mathrm{T}}\boldsymbol{\tau}^b - \boldsymbol{\nu}^{\mathrm{T}}\boldsymbol{D}\boldsymbol{\nu}. \tag{5.89}$$

Applying property **P3** to (5.89) yields $\dot{\mathcal{E}}_V \leq \boldsymbol{\nu}^{\mathrm{T}}\boldsymbol{\tau}^b$ showing that the vessel is itself input-output passive with input $\boldsymbol{\tau}$ and output $\boldsymbol{\nu}$. Hence, the derivative of the energy (5.83) can be found by summing (5.77) and (5.89),

$$\dot{\mathcal{E}} = \langle\overline{\boldsymbol{n}}^e, \dot{\boldsymbol{\varphi}}\rangle\,\big|_0^L + \langle\overline{\boldsymbol{m}}^e, \mathbf{w}^e\rangle\,\big|_0^L - \int_0^L \langle\dot{\boldsymbol{\varphi}}, \boldsymbol{f}_D^e\rangle\,dS$$

$$-\int_0^L \langle\mathbf{w}^e, \boldsymbol{D}_R\mathbf{w}^e\rangle\,dS + \boldsymbol{\nu}^{\mathrm{T}}\boldsymbol{\tau}^b - \boldsymbol{\nu}^{\mathrm{T}}\boldsymbol{D}\boldsymbol{\nu}, \tag{5.90}$$

where the lower boundary condition $S = 0$, known from (5.39), implies

$$\langle\overline{\boldsymbol{n}}^e, \dot{\boldsymbol{\varphi}}\rangle\,|_0 = \langle\overline{\boldsymbol{m}}^e, \mathbf{w}^e\rangle\,|_0 = 0, \tag{5.91}$$

and the upper boundary condition is given by (5.66) where the pipe is connected to the vessel in the center of gravity, as defined in (5.65), such that the total rate of change of energy of the pipe and vessel system reduces to

$$\dot{\mathcal{E}} = -\int_0^L \langle\dot{\boldsymbol{\varphi}}, \boldsymbol{f}_D^e\rangle\,dS - \int_0^L \langle\mathbf{w}^e, \boldsymbol{D}_R\mathbf{w}^e\rangle\,dS - \boldsymbol{\nu}^{\mathrm{T}}\boldsymbol{D}\boldsymbol{\nu} + \boldsymbol{\nu}^{\mathrm{T}}\boldsymbol{\tau}_{\text{control}}, \tag{5.92}$$

which implies that $\dot{\mathcal{E}} \leq \boldsymbol{\nu}^{\mathrm{T}}\boldsymbol{\tau}_{\text{control}}$, and the system is input-output passive. $\qquad\square$

Corollary 5.3.3. *Finally, it can be concluded the combined system of pipeline and vessel is stable since $\mathcal{E} \geq 0$, $\|\mathcal{E}\| \to \infty$ due to unbounded system states, and $\dot{\mathcal{E}} \leq 0$ which implies that*

$$\mathcal{E}(t) - \mathcal{E}(0) \leq 0. \tag{5.93}$$

If a *passive* controller $\boldsymbol{\tau}_{\text{control}}$ is applied, this analysis shows that the complete system is input-output passive and stable.

5.4 Model Validation

A scenario of installing a $30''$ $(0.762m)$ OD (outer diameter) steel pipe at a water depth of 900 meters using the J-lay method, as illustrated in Figure 5.1, is considered in this section for validation. Static and dynamic pipe analyses are performed in this case-study using both the proposed pipe model, as well as the catenary equation and RIFLEX. The catenary equation is the classic nonlinear solution of the static deflection curve for a string loaded by its own weight, and is well known from cable mechanics [16], while RIFLEX is a recognized FEM program for static and dynamic analysis of slender marine structures developed by MARINTEK and SINTEF in cooperation with the Norwegian University of Science and Technology (NTNU) as a joint industry project. The physical constants and material pipe properties given in Tables 5.1 and 5.2 are used for all the analyses.

Constant	Notation	Value	Unit
Density of water	ρ_w	$1.025 \cdot 10^3$	kg/m^3
Earth gravity	g	9.80665	m/s^2
Young's modulus steel	E	$206 \cdot 10^9$	N/m^2
Shear modulus steel	G	$7.9231 \cdot 10^{10}$	N/m^2

Table 5.1: Physical constants.

5.4.1 Numerical Implementation

A finite element method is applied on (5.28)–(5.29) for the numerical simulations, following the same procedure as in [34]. A Galerkin weak form of the initial boundary problem (5.28)–(5.29) with boundary conditions (5.39) and (5.66), is developed by taking the inner product with admissible test functions $\boldsymbol{u}, \boldsymbol{\vartheta}$. Let the space of test functions $\mathcal{V}$ be defined as

$$\mathcal{V} = \{(\boldsymbol{u}, \boldsymbol{\vartheta}) \,|\, S \in [0, L] \to \mathbb{R}^3 \times \mathbb{R}^3 \,|\, (\boldsymbol{u}, \boldsymbol{\vartheta})\big|_{S=0} = (\boldsymbol{0}, \boldsymbol{0})\}. \tag{5.94}$$

123

Parameter	Notation	Value	Unit
Outer pipe diameter	d_o	0.762	m
Wall thickness	WT	0.033	m
Undeformed pipe length	L	1500	m
Unit mass of empty pipe	m_p	593.2818	kg
Moments of inertia	I_1	78.9851	$kg \cdot m^2$
	$I_2 = I_3$	39.4925	$kg \cdot m^2$
Unit polar moments of inertia	I	$5.0309 \cdot 10^{-3}$	m^4
	J	$1.0062 \cdot 10^{-2}$	m^4
Axial stiffness	EA	$1.5569 \cdot 10^{10}$	Nm^2
Shear stiffness	GA	$9.0330 \cdot 10^9$	Nm^2
Torsional stiffness	GJ	$7.9720 \cdot 10^8$	Nm^2
Bending stiffness	EI	$1.0364 \cdot 10^9$	Nm^2

Table 5.2: Parameters for a $30''$ OD (outer diameter) steel pipe.

Admissible variations associated with any pipe configuration $(\boldsymbol{\varphi}, \boldsymbol{R}_t^e) \in \mathcal{C}$ span the tangent space $T_{(\boldsymbol{\varphi}, \boldsymbol{R}_t^e)}\mathcal{C}$ given by

$$T_{(\boldsymbol{\varphi}, \boldsymbol{R}_t^e)}\mathcal{C} \triangleq \{(\boldsymbol{u}, \boldsymbol{S}(\boldsymbol{\vartheta})\boldsymbol{R}_t^e) \,|\, (\boldsymbol{u}, \boldsymbol{\vartheta}) \in \mathcal{V}\}. \tag{5.95}$$

Hence, the weak formulation is found to be

$$G_{\text{dyn}}(\boldsymbol{\varphi}, \boldsymbol{R}_t^e; \boldsymbol{u}, \boldsymbol{\vartheta}) \triangleq \int_0^L \langle m_P \ddot{\boldsymbol{\varphi}}, \boldsymbol{u} \rangle + \langle [\boldsymbol{I}_\rho \dot{\mathbf{w}}^e + \mathbf{w}^e \times (\boldsymbol{I}_\rho \mathbf{w}^e)], \boldsymbol{\vartheta} \rangle \, dS +$$

$$\int_0^L \langle [\boldsymbol{f}_D^e + \boldsymbol{\sigma}^e], \boldsymbol{u} \rangle + \langle \boldsymbol{D}_R \mathbf{w}^e, \boldsymbol{\vartheta} \rangle \, dS + G_{\text{stat}}(\boldsymbol{\Phi}, \boldsymbol{R}_t^e; \boldsymbol{u}, \boldsymbol{\vartheta}) +$$

$$\left. \left\langle [\boldsymbol{M}\dot{\boldsymbol{\nu}} + \boldsymbol{C}(\boldsymbol{\nu})\boldsymbol{\nu} + \boldsymbol{D}(\boldsymbol{\nu})\boldsymbol{\nu}], (\boldsymbol{u}^{\mathrm{T}}, \boldsymbol{\vartheta}^{\mathrm{T}})^{\mathrm{T}} \right\rangle \right|_{S=L} = 0, \quad (5.96)$$

for all test functions $(\boldsymbol{u}, \boldsymbol{\vartheta}) \in \mathcal{V}$, where the static part G_{stat} is given by

$$G_{\text{stat}}(\boldsymbol{\varphi}, \boldsymbol{R}_t^e; \boldsymbol{u}, \boldsymbol{\vartheta}) \triangleq \int_0^L \left\langle \boldsymbol{n}^e, \left[\frac{d\boldsymbol{u}}{dS} + \boldsymbol{S}(\partial_S \boldsymbol{\varphi})\boldsymbol{\vartheta} \right] \right\rangle + \left\langle \boldsymbol{m}^e, \frac{d\boldsymbol{\vartheta}}{dS} \right\rangle dS +$$

$$\int_0^L \langle \boldsymbol{f}_g^e, \boldsymbol{u} \rangle \, dS + \left. \left\langle \boldsymbol{g}(\boldsymbol{\varphi}, \boldsymbol{R}_b^e), (\boldsymbol{u}^{\mathrm{T}}, \boldsymbol{\vartheta}^{\mathrm{T}})^{\mathrm{T}} \right\rangle \right|_{S=L}. \tag{5.97}$$

Let the rotation matrix $\boldsymbol{R}_t^e$ be parameterized in Euler angles $\boldsymbol{\Theta} = (\phi, \theta, \psi)^{\mathrm{T}} \to \boldsymbol{R}_t^e(\boldsymbol{\Theta})$ by the zxy-convention, which is locally diffeomorphic to $SO(3)$. Hence, $\boldsymbol{R}_t^e$ is given by

$$\boldsymbol{R}_t^e(\boldsymbol{\Theta}) = \boldsymbol{R}_{\boldsymbol{e}_2}(\theta)\boldsymbol{R}_{\boldsymbol{e}_1}(\phi)\boldsymbol{R}_{\boldsymbol{e}_3}(\psi), \tag{5.98}$$

where the elementary rotations about the $\boldsymbol{e}_1$, $\boldsymbol{e}_2$ and $\boldsymbol{e}_3$ axes are given by

$$\boldsymbol{R}_{\boldsymbol{e}_1}(\phi) = \begin{bmatrix} 1 & 0 & 0 \\ 0 & \mathrm{c}\,\phi & -\mathrm{s}\,\phi \\ 0 & \mathrm{s}\,\phi & \mathrm{c}\,\phi \end{bmatrix}, \quad \boldsymbol{R}_{\boldsymbol{e}_2}(\theta) = \begin{bmatrix} \mathrm{c}\,\theta & 0 & \mathrm{s}\,\theta \\ 0 & 1 & 0 \\ -\mathrm{s}\,\theta & 0 & \mathrm{c}\,\theta \end{bmatrix},$$

$$\boldsymbol{R}_{\boldsymbol{e}_3}(\psi) = \begin{bmatrix} \mathrm{c}\,\psi & -\mathrm{s}\,\psi & 0 \\ \mathrm{s}\,\psi & \mathrm{c}\,\psi & 0 \\ 0 & 0 & 1 \end{bmatrix}, \tag{5.99}$$

where $\mathrm{s}\,(\cdot)$ and $\mathrm{c}\,(\cdot)$ denotes $\sin(\cdot)$ and $\cos(\cdot)$. Adopting the zxy-convention instead of the more common xyz-convention moves the singularity inherent to Euler angles from pitch to roll, which is more suitable for the presented model. This choice of parametrization yields the transformations

$$\begin{aligned} \mathbf{w}^e &= \boldsymbol{\Pi}_e \dot{\boldsymbol{\Theta}}, & \dot{\mathbf{w}}^e &= \boldsymbol{\Pi}_e \ddot{\boldsymbol{\Theta}} + \dot{\boldsymbol{\Pi}}_e \dot{\boldsymbol{\Theta}}, \\ \partial_S \boldsymbol{\omega}^e &= \boldsymbol{\Pi}_e (\partial_S \boldsymbol{\Theta}), & \boldsymbol{\Theta} &= (\phi, \theta, \psi)^{\mathrm{T}}, \end{aligned} \tag{5.100}$$

where

$$\boldsymbol{\Pi}_e = \begin{bmatrix} \cos\theta & 0 & \cos\phi \sin\theta \\ 0 & 1 & -\sin\phi \\ -\sin\theta & 0 & \cos\phi \cos\theta \end{bmatrix}. \tag{5.101}$$

Following the parametrization in Euler angles, the configuration space $\mathcal{C}$ can be reformulated as

$$\widetilde{\mathcal{C}} \triangleq \{(\boldsymbol{\varphi}, \boldsymbol{\Theta}) \,|\, S \in [0, L] \to \mathbb{R}^3 \times \mathbb{R}^3 \,|\, \langle \partial_S \boldsymbol{\varphi}(S), \boldsymbol{R}_t^e(\boldsymbol{\Theta}) \boldsymbol{e}_1 > 0\}, \tag{5.102}$$

with test functions

$$\widetilde{\mathcal{V}} \triangleq \{(\boldsymbol{u}, \widetilde{\boldsymbol{\vartheta}}) \,|\, S \in [0, L] \to \mathbb{R}^3 \times \mathbb{R}^3 \,|\, (\boldsymbol{u}, \widetilde{\boldsymbol{\vartheta}})\big|_{S=0} = (\boldsymbol{0}, \boldsymbol{0})\}, \tag{5.103}$$

and the new tangent space becomes

$$T_{(\boldsymbol{\varphi}, \boldsymbol{\Theta})} \widetilde{\mathcal{C}} \triangleq \{(\boldsymbol{u}, \widetilde{\boldsymbol{\vartheta}}) \,|\, (\boldsymbol{u}, \widetilde{\boldsymbol{\vartheta}}) \in \widetilde{\mathcal{V}}\}. \tag{5.104}$$

The weak formulation (5.96) for the configuration space (5.102) is semi-discretized with N equidistant nodes, $\bigcup_{i=1}^{N-1}[S_i, S_{i+1}] = [0, L]$, using linear shape functions $N_h^i(S)$ such that

$$\begin{aligned} \boldsymbol{\varphi} \approx \boldsymbol{\varphi}_h &= \sum_{i=1}^{N} \boldsymbol{\varphi}_i(t) N_h^i(S), & \boldsymbol{\Theta} \approx \boldsymbol{\Theta}_h &= \sum_{i=1}^{N} \boldsymbol{\Theta}_i(t) N_h^i(S), \\ \boldsymbol{u}_h &= \sum_{i=1}^{N} \boldsymbol{u}_i N_h^i(S), & \widetilde{\boldsymbol{\vartheta}}_h &= \sum_{i=1}^{N} \widetilde{\boldsymbol{\vartheta}}_i N_h^i(S), \end{aligned} \tag{5.105}$$

125

and the integrals in the weak formulation $G_{\mathrm{dyn}}(\boldsymbol{\varphi}, \boldsymbol{R}_t^e(\boldsymbol{\Theta}); \boldsymbol{u}, \widetilde{\boldsymbol{\vartheta}})$ (5.96) are approximated using two point Gaussian quadrature for each interval $[S_i, S_{i+1}] \subset [0, L]$, except for the stiffness integral

$$\int_0^L \left\langle \boldsymbol{n}^e, \left[\frac{d\boldsymbol{u}}{dS} + \boldsymbol{S}(\partial_S \boldsymbol{\varphi}) \widetilde{\boldsymbol{\vartheta}} \right] \right\rangle + \left\langle \boldsymbol{m}^e, \frac{d\widetilde{\boldsymbol{\vartheta}}}{dS} \right\rangle dS, \qquad (5.106)$$

which is approximated by a reduced one point Gaussian quadrature, to avoid shear locking [33]. The semi discretized problem is finally obtained in the form

$$\overline{\boldsymbol{M}}_h(\dot{\boldsymbol{x}}_j, \boldsymbol{x}_j)\ddot{\boldsymbol{x}}_i + \overline{\boldsymbol{C}}_h(\dot{\boldsymbol{x}}_j, \boldsymbol{x}_j)\dot{\boldsymbol{x}}_i + \overline{\boldsymbol{K}}_h(\boldsymbol{x}_j)\boldsymbol{x}_i = \boldsymbol{0}, \qquad \text{for} \quad i, j = 1, \ldots, N, \quad (5.107)$$

where

$$\boldsymbol{x}_i = [\boldsymbol{\varphi}_i, \boldsymbol{\Theta}_i]^{\mathrm{T}}, \qquad (5.108)$$

is the state vector, and $\overline{\boldsymbol{M}}_h$, $\overline{\boldsymbol{C}}_h$ and $\overline{\boldsymbol{K}}_h$ are the semi discretized system mass-, damping- and stiffness matrix, respectively. This form is well known in marine control engineering. In the simulations Matlab is applied, and the embedded ODE-solver `ode23tb` is used to solve the semi discretized problem (5.107).

To approximate the static solution, $G_{\mathrm{stat}}(\boldsymbol{\varphi}, \boldsymbol{R}_t^e; \boldsymbol{u}, \boldsymbol{\vartheta}) = 0$, the Newton-Raphson strategy described in [33] is applied. For the approximated static solution (5.97), let the averaged error estimate be given by

$$\varepsilon^N \triangleq \frac{1}{N} \sum_{i=1}^N \|(\boldsymbol{\varphi}_i, \boldsymbol{\Theta}_i) - (\boldsymbol{\varphi}^{\mathrm{ref}}(S_i), \boldsymbol{\Theta}^{\mathrm{ref}}(S_i))\|_2, \qquad (5.109)$$

where the approximated solution from a fine gridded discretization is taken as a reference solution

$$(\boldsymbol{\varphi}^{\mathrm{ref}}(S), \boldsymbol{\Theta}^{\mathrm{ref}}(S)) \triangleq \sum_{i=1}^N (\boldsymbol{\varphi}_i, \boldsymbol{\Theta}_i) N_h^i(S). \qquad (5.110)$$

The convergence of ε^N is shown in Figure 5.3.

5.4.2 Static Pipe Model Validation

The static analysis are performed in the vertical plane spanned by $\{\boldsymbol{e}_1, \boldsymbol{e}_3\}$ where different values for the horizontal tension $H = \{200, 400, 800\}\ kN$ are applied to the top node in the $\boldsymbol{e}_1$-direction. For the pipe model $N = 740$, such that element length is approximately 2 meters. To validate the model against the catenary, the bending stiffness in the pipe model is set to zero, i.e., $EI = 0$, and the computed static configurations are plotted in Figure 5.4, where the pipe model and the catenary configurations can hardly be distinguished. The hang-off angle β and

Horizontal tension	H	200	400	800	kN
Pipe model without bending stiffness, $EI = 0$					
Hang-off angle	β	81.22	74.64	65.24	*deg*
Lay-back distance	l_h	412.25	645.10	975.51	*m*
Catenary					
Hang-off angle	β	81.22	74.64	65.24	*deg*
Lay-back distance	l_h	415.25	649.41	982.24	*m*

Table 5.3: Static analyses results for the pipe model without bending stiffness e.g. $EI = 0$ and the catenary.

Horizontal tension	H	200	400	800	kN
Pipe model					
Hang-off angle	β	80.97	74.30	64.87	*deg*
Lay-back distance	l_h	467.92	679.76	996.29	*m*
RIFLEX					
Hang-off angle	β	81.0	74.4	65.0	*deg*
Lay-back distance	l_h	477	686	1001	*m*

Table 5.4: Static analyses results for the pipe model including the effects of bending stiffness and RIFLEX.

the lay-back distance l_h, the horizontal distance from hang-off to touchdown, for the PDE and the catenary are presented in Table 5.3, and are seen to correspond well. The difference in lay-back distance may be explained from the effect of the seabed interaction of the pipe model. Comparing the pipe model configuration with and without bending stiffness, see Figure 5.5. The effect of the bending stiffness is seen in the touchdown area and at the hang-off angle. The computed static configurations including bending stiffness for $H = \{200, 400, 800\}\, kN$ for the PDE and RIFLEX are plotted in Figure 5.6. The hang-off angles and lay-back distances for RIFLEX and our code are presented in Table 5.3, and are in very good agreement. The curvature along the pipe configurations of Figure 5.6 are plotted in Figure 5.7, and show that the forces also agree in the two models.

5.4.3 Dynamic Pipe Model Validation

In the dynamic analysis, the static configuration for $H = 400\, kN$ and $N = 100$ with elements of equal lengths is taken as the initial configuration. No lateral or axial seabed friction is assumed. The pipe at $S = 0$ is horizontally clamped to the seabed, and it is fixed to the center of gravity of the vessel, where it is free to rotate, for $S = L$. A linearized vessel model is used where the coefficient matrices

are obtained from the *Marine Systems Simulator* (MSS) available at [10]. A DP system is implemented by a nonlinear PID controller, found in [17], to allow the surface vessel to track a circular motion with period $T = 10s$ and radius $r = 2.5m$ before returning to its initial position, see Figure 5.8, which imposes a spiraling motion to the pipe. The control reference is ramped to limit accelerations. The position of the pipe tip over the course of 60 seconds of simulation is given as input to RIFLEX, as RIFLEX does not include the surface vessel dynamics. The displacement envelopes, bending moment envelopes and axial tension envelope along the pipe, produced by the proposed model and RIFLEX, are compared in Figures 5.9, 5.10 and 5.11. The dynamic position and bending moment as a function of time for node $N = 25$, which is close to the touchdown point, is shown in Figure 5.12. The pipe overall length is a sensitive parameter, and Figure 5.13 indicates a very good dynamic correlation of the results, as well as nominal values are in agreement. By considering these analysis results, the difference between the results obtained are not more than what can be expected from different numerical implementation, and the dynamics of the proposed model is very close to that obtained by RIFLEX both with respect to displacement and forces.

5.4.4   Model Convergence

For a practical applications of the numerical implementation, the convergence must be considered. The number of nodes in a simulation should be small to optimize computation time, while at the same time capture the main dynamic behavior of the system. The dynamic simulation scenario, given in the previous section, is repeated for $N = 10, 20, 40, 80$ nodes, and plotted against $N = 100$, used in the dynamic validation, see Figure 5.14. Visually, the configurations of $N = 80$ and $N = 100$ cannot be distinguished, while the configuration for $N = 40$ can only be distinguished at some locations. For $N = 20$, the main dynamics are kept, while for $N = 10$, the oscillations differs much from that of $N = 100$. To improve the dynamics without increasing the number of nodes, variable element lengths can be introduced, such that sensitive regions along the pipe, i.e., the touchdown and the hang-off area, may have shorter elements than the less sensitive regions.

5.5   Conclusions

A dynamic model for a freely suspended pipe string with bending stiffness has been developed. This pipe model has been shown to be input-output passive by a passivity check. Further, the model has been extended to include the dynamics of a surface pipelay vessel, and passivity and stability of the combined system has been shown from considering the total energy of the system. A numerical im-

plementation of the proposed PDE model has been successfully validated against the catenary equation and RIFLEX, which proves that the PDE model can be used to analyze and simulate slender marine structures, such as a pipe string suspended from a surface vessel to the seabed. The range of analysis that can be performed using the proposed model extends that of RIFLEX, since the dynamics of the surface vessel is included in the model. Hence, it may be used to e.g., analyze the interaction between a pipe string and a motion control systems for the surface vessel.

The numerical implementation in this paper was done in Matlab, using equidistant distributed nodes and traditional ODE solvers to integrate in time, and real-time simulations could not be achieved. For future work, it would be an advantage to consider a more "sophisticated" numerical implementation to improve the code, e.g., applying a geometric method [14], which usually show good stability properties and excellent behavior in long-time simulations. Implementing a dedicated method rather than using built-in solvers, may also improve computation time. Finally, by implementing the discretized model in a more suited compilable language will speed up the execution of the computations.

Future extensions to the model can be envisioned: Adding lateral and longitudinal seabed friction, allow for uneven seabed by using bathymetry maps, allow pipe elongation my relaxing the fixed pipe length property so that $L = L(t)$.

Acknowledgments

5.6 Figures
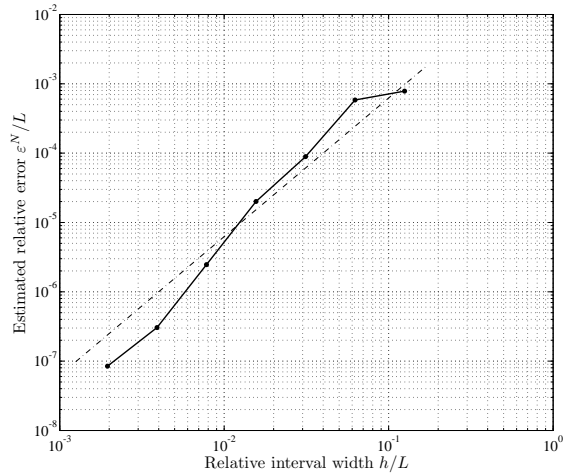
Figure 5.3: The estimated relative error ε^N/L for the static solution approximations where the number of elements $N-1 = 8, 16, 32, 64, 128, 256, 512$, against relative interval width $h/L = 1/(N-1)$, where an approximated solution with $N-1 = 1024$ is taken as the reference. The results compare well to the quadratic auxiliary line.
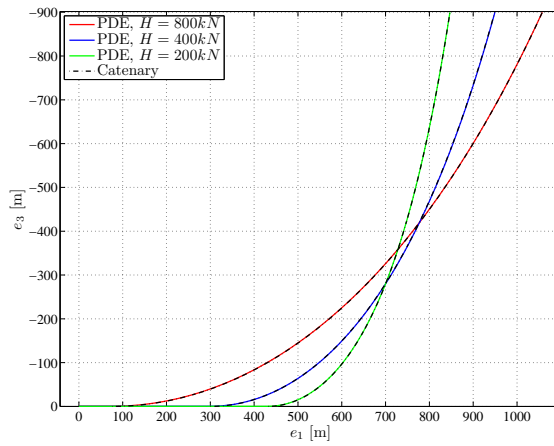

Figure 5.4: Static pipe configuration without bending stiffness of the pipe model validated against the catenary.
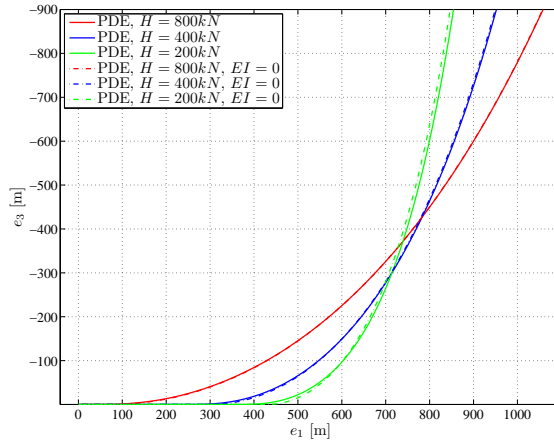
Figure 5.5: Pipe model configurations with and without bending stiffness compared.
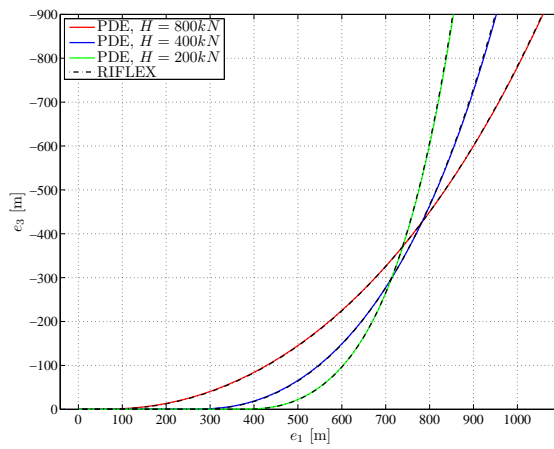
Figure 5.6: Static pipe configuration of the pipe model validated against RIFLEX.

131
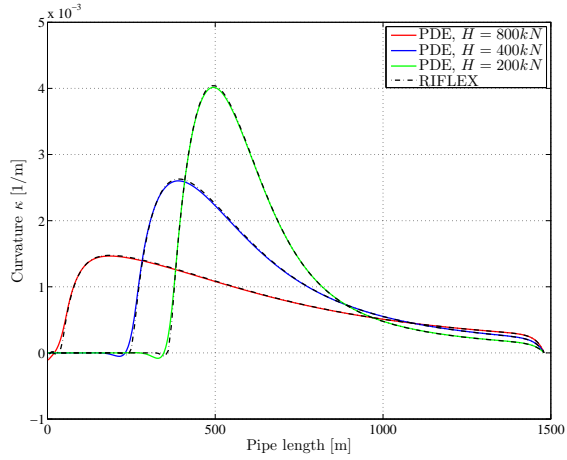
Figure 5.7: Comparing the curvature κ of the pipe model and RIFLEX.
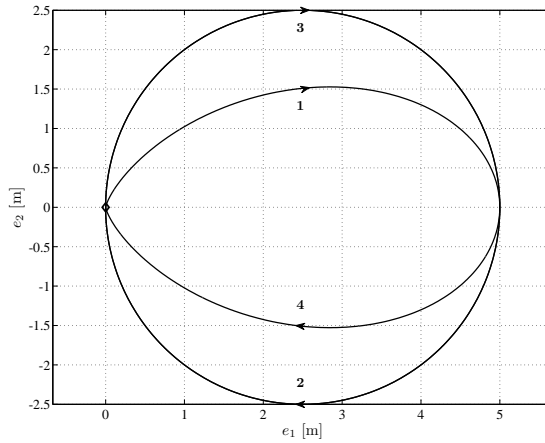
Figure 5.8: The path followed by the surface vessel. The vessel starts in $(0,0)$, which represents the surface position for the static solution where $H = 400kN$. The path is made up of three completes circles with ramps to limit acceleration at the beginning and end. The sequence and direction is indicated by the arrows and numbers 1–4. After completing the third circle, the vessel remains fixed at $(0,0)$.
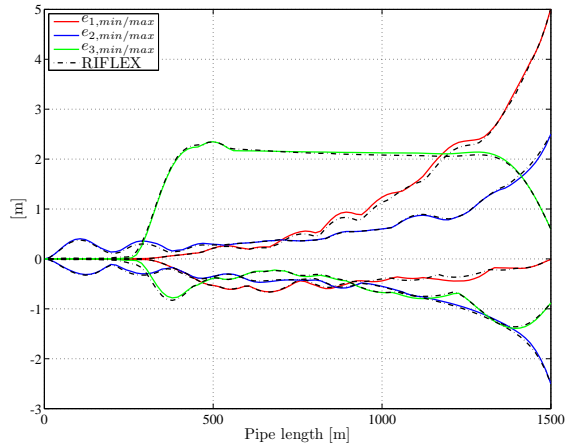
Figure 5.9: Relative displacement envelope in the e_1, e_2 and e_3 directions for the proposed model compared to RIFLEX.
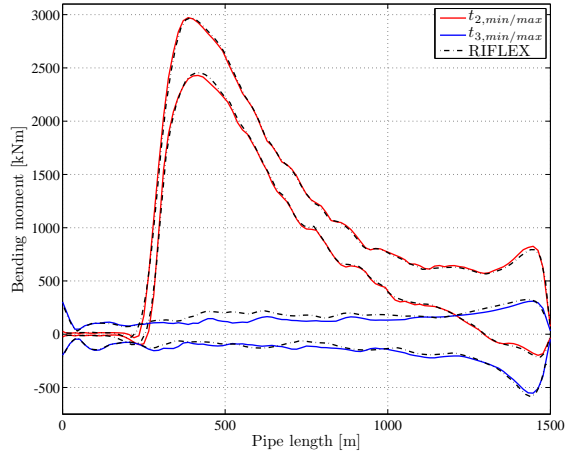
Figure 5.10: Bending moment envelope about the t_2 and the t_3 axis along the pipe. This value is represented in the PDE by the min/max values for m_2^t and m_3^t along S. The results are compared to RIFLEX.

133
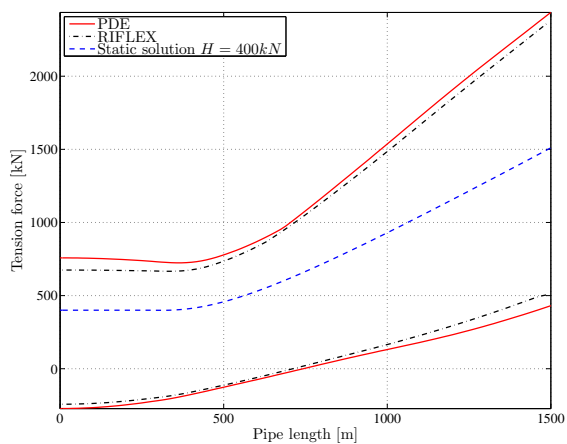
Figure 5.11: Axial tension envelope, includeing the static axial tension for $H = 400kN$.
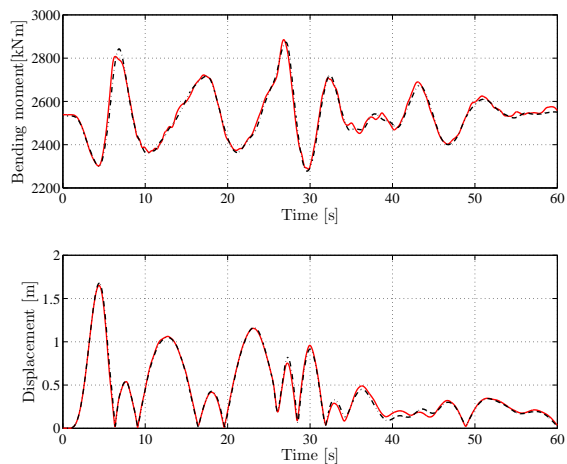
Figure 5.12: Dynamic bending moment *(top)* and relative displacement *(bottom)* for a node ($N = 25$) close to the touchdown point.
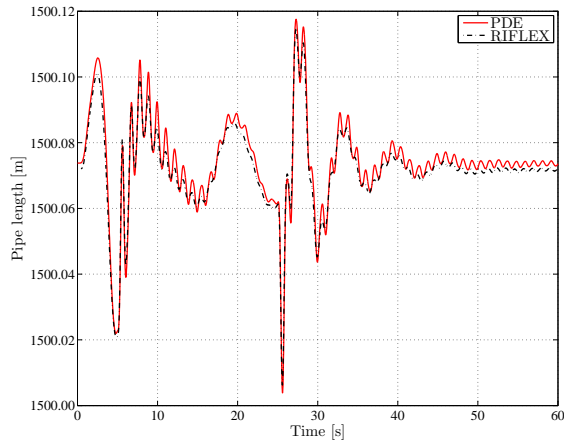
Figure 5.13: Pipe length.
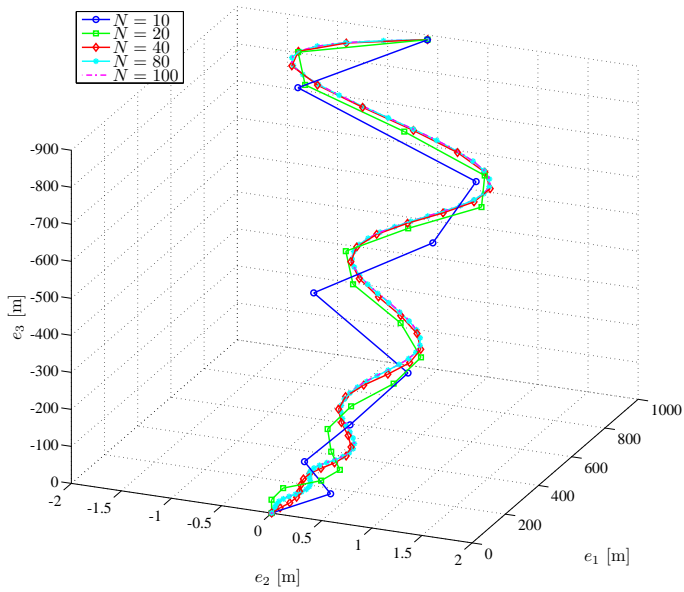
Figure 5.14: Pipe configurations at $t = 15s$ for $N = 10, 20, 40, 80, 100$.

135

Bibliography

[1] Karl Johan Åström. *Automatic control: A perspective*, pages 1–26. Colloquium on Automatic Control, Vol. 215 of Lecture Notes in Control and Information Sciences. Springer Berlin / Heidelberg, 1996.

[2] M. J. Balas. Active control of flexible systems. *Journal Of Optimization Theory And Applications*, 25(3):415–436, 1978.

[3] P. Betsch and P. Steinmann. Frame-indifferent beam finite elements based upon the geometrically exact beam theory. *International Journal for Numerical Methods in Engineering*, 54(12):1775–1788, 2002.

[4] M. W. Braestrup, J. B. Andersen, L. W. Andersen, M. B. Bryndum, C. J. Christensen, and N. Rishøy. *Design and Installation of Marine Pipelines*. Blackwell Science Ltd, 2005.

[5] D.A. Dixon and D.R. Rutledge. Stiffened catenary calculations in pipeline laying problem. *ASME Journal of Engineering for Industry*, (90):153–160, February 1968.

[6] Olav Egeland and Jan Tommy Gravdahl. *Modeling and Simulation for Automatic Control*. Marine Cybernetics, 1st edition, 2002.

[7] O. M. Faltinsen. *Sea Loads on Ships and Offshore Structures*. Cambridge University Press, 1990.

[8] D. Fathi. ShipX Vessel Responses (VERES). *MARINTEK Trondheim, www.marintek.sintef.no*, 2004.

[9] Thor I. Fossen. *Marine Control Systems: Guidance, Navigation, and Control of Ships, Rigs and Underwater Vehicles*. Marine Cybernetics, Trondheim Norway, 1st edition, 2002.

[10] Thor I. Fossen and Tristan Perez. Marine systems simulator (MSS). *www.marinecontrol.org*, 2004.

[11] Thor I Fossen and Øyvind N. Smogeli. Nonlinear time-domain strip theory formulation for low-speed manoeuvering and station-keeping. *Modeling, Identification and Control*, 25(4):201–221, 2004.

[12] I Fylling, C. M. Larsen, N. Sødahl, E Passano, A. Bech, A. G. Engseth, H. Lie, and H Ormberg. RIFLEX User's Manual 3.6, MARINTEK, Trondheim, Norway. 2008.

[13] B. Guo, S. Song, J. Chacko, and A. Ghalambor. *Offshore Pipelines*. Gulf Professional Publishing, 2005.

[14] E. Hairer, C. Lubich, and G. Wanner. *Geometric numerical integration*, volume 31 of *Springer series in computational mathematics*. Springer, 2002.

[15] E.P. Heerema. Recent achievements and present trends in deepwater pipe-lay systems. In *Proceedings of the 37th Offshore Technology Conference*, 2005. OTC 17627.

[16] H. Max Irvine. *Cable Structures*. The MIT Press, 1981.

[17] G. A. Jensen, N. Säfström, T. D. Nguyen, and T. I. Fossen. Modeling and control of offshore pipelay operations based on a finite strain pipe model. In *Proceedings of the 2009 American Control Conference, St. Louis, USA*, 2009.

[18] Gullik A. Jensen, Morten Breivik, and Thor. I. Fossen. Offshore pipelay operations from a control perspective. In *Proceedings of the 28th OMAE, Honolulu, Hawaii, USA*, 2009.

[19] H.K. Khalil. *Nonlinear Systems*. Prentice Hall, 3rd edition, 2002.

[20] A. E. H. Love. *The Mathematical Theory of Elasticity*. Dover, New York, 1944.

[21] M. Martinsen. A finite element model for pipeline installation. Master's thesis, Stavanger University College for JP Kenny A/S, 1998.

[22] F.A. McRobie and J. Lasenby. Simo-vu quoc rods using clifford algebra. *International Journal for Numerical Methods in Engineering*, 45(4):377–398, 1999.

[23] J. R. Morison, M. P. O'Brien, J. W. Johnson, and S. A. Schaaf. The force exerted by surface waves on piles. *Petroleum Transactions AIME*, 189:149–189, 1950.

[24] T. Francis Ogilvie. Recent progress toward the understanding and prediction of ship motions. In *Proc. Fifth Symposium on Naval Hydrodynamics, Bergen, Norway*, volume ACR-112, pages 3–79. ONR, 1964.

[25] Andrew C. Palmer and Roger A. King. *Subsea Pipeline Engineering*. PennWell Books, 2nd edition, 2008.

[26] Tristan Perez and Thor Inge Fossen. Kinematic models for manoeuvring and seakeeping of marine vessels. *Modeling, Identification and Control*, 28(1):19–30, 2007.

[27] R. Plunkett. Static bending stresses in catenaries and drill strings. *Journal of Engineering for Industry*, February 1967.

[28] E. Reissner. Some remarks on the problem of column buckling. *Ingenieur-Archiv*, 52:115–119, 1982.

[29] I. Romero and F. Armero. An objective finite element approximation of the kinematics of geometrically exact rods and its use in the formulation of an energy-momentum conserving scheme in dynamics. *International Journal for Numerical Methods in Engineering*, 54(12):1683–1716, 2002.

[30] L. Sciavicco and B. Siciliano. *Modelling and Control of Robot Manipulators*. Springer, 2nd edition, 2001.

[31] J. C. Simo. A finite strain beam formulation. The three-dimensional dynamic problem. Part I. *Computer Methods in Applied Mechanics and Engineering*, 49(1):55–70, May 1985.

[32] J. C. Simo, N. Tarnow, and M. Doblare. Non-linear dynamics of three-dimensional rods: Exact energy and momentum conserving algorithms. *International Journal For Numerical Methods in Engineering*, 38:1431–1473, 1995.

[33] J. C. Simo and L. Vu-Quoc. A three-dimensional finite-strain rod model. Part II: Computational aspects. *Computer Methods in Applied Mechanics and Engineering*, 58(1):79–116, October 1986.

[34] J. C. Simo and L. Vu-Quoc. On the dynamics in space of rods undergoing large motions – a geometrically exact approach. *Computer Methods in Applied Mechanics and Engineering*, 66(2):125–161, February 1988.

[35] SNAME. Nomenclature for treating the motion of a submerged body through a fluid. *Technical and Research Bulletin*, 1950. No. 1-5.

[36] WAMIT. *WAMIT User Manual*. www.wamit.com, 2004.

Paper V

Hamiltonian and multi-symplectic structure of a rod model using quaternions

Celledoni and N. Säfström.

Chapter 6

Hamiltonian and multi-symplectic structure of a rod model using quaternions

ABSTRACT. The geometrically exact model of an elastic rod, formulated in [21] has been investigated. We present a constrained Hamiltonian formulation of the elastic rod model as well as a constrained multi-symplectic formulation of the model. In both formulations, quaternions are used to represent the group of rotations. The resulting Hamiltonian PDE and multi-symplectic formulation have simple looking formats involving constant structure matrices.

6.1 Introduction

In this paper we consider an elastic rod model first formulated in [21]. This model is a variant of the classical Kirchoff-Love model [17], when allowing for finite extension and shearing effects. Internal stress forces in the body depend linearly on the stress measures, and the material therefore possesses a hyper-elastic behavior. The equations of motion are a system of partial differential equations (PDEs) on a manifold, and, in many respects, they resemble the Euler equations of rigid body dynamics. The first numerical discretization methods designed and applied to this model, aimed at obtaining numerical approximations

lying on the configuration manifold, see [23] (static case) and [24] (dynamical case). An energy-momentum method was later presented in [11]. One of the main motivations for developing the energy-momentum method was the disappointing performance of conventional methods in long time simulations. Even methods usually regarded as very stable exhibited unacceptable numerical instability [11]. Numerical approximations for the model have later been studied by many authors, in particular energy-conserving and dissipative schemes based on finite element strategies, see for example [6, 7, 1, 2].

One important issue in the numerical simulation of this model is the choice of coordinates used to describe the configuration manifold, consisting of a cartesian product of the vector space $\mathbb{R}^3$ and the group of rotations, $SO(3)$. In [23], and in many papers later on, rotation matrices were used, while in [2] the authors choose directors reducing the amount of computations and the memory requirements: a rotation can be identified by two orthonormal vectors of $\mathbb{R}^3$ and represented by 6 parameters satisfying two length constraints and one orthogonality constraint. In [6], [16] instead the kinematic constraints are imposed via appropriate algebraic equations and Lagrange multipliers.

In the recent paper [12] this model is employed for modeling pipe-lay offshore operations and the rod equations are coupled to a controlled rigid body (representing the vessel conducting the pipe-lay operations). In the same paper the configuration manifold is described using Euler angles and the choice of appropriate *conventions* (coordinate charts) is very important for the performance of the method. A robust implementation of this approach should allow for changes of chart when necessary.

The main contribution of the present work is the derivation of a Hamiltonian and a multi-symplectic formulation of the model in quaternions. We choose to represent rotations as unit quaternions (Euler parameters), we realize unit quaternions as vectors of $\mathbb{R}^4$ subjected to one length constraint. Compared to Euler angles, which give a local coordinatization of $SO(3)$ and allow to represent rotations with a minimal number of coordinates, unit quaternions use just one extra coordinate. The advantage is that we avoid the difficulties of local coordinatizations and changing of charts, see for example [14], [4] for a discussion of local vs global formulations of Hamiltonian systems and their symplectic integration. A Hamiltonian formulation of an elastic Cosserat rod has earlier been investigated in [13].

The resulting Hamiltonian PDE has a simple looking format involving the canonical (constant) structure matrix typical of finite dimensional Hamiltonian systems, and it is subjected to kinematic constraints.

The new formulation has the advantage that strightforward finite-difference/ finite-element discretizations in space lead to canonical Hamiltonian semi-discretized ODE systems with constraints. The semi-discrete Hamiltonian system is

obtained by first discretizing the Hamiltonian function in space, using a consistent approximation. The obtained discrete energy function is then used for defining a finite dimensional canonical Hamiltonian system, approximating the problem.

Multi-symplecticity is a generalization of classical symplecticity for finite-dimensional Hamiltonian systems to the infinite-dimensional case. Besides global preservation of energy and momentum, the multi-symplectic formulation of a Hamiltonian PDE implies local energy and momentum conservation properties. Following a procedure described in [10], from the Hamiltonian formulation we derive a multi-symplectic formulation of our problem by defining a new Hamiltonian function via a Legendre transform. For more details on multi-symplectic PDE's and multi-symplectic integrators, see e.g. [8, 9, 15].

6.2 Background

6.2.1 The elastic rod model

Here we give a short review of the elastic rod model formulated in [21]. For a given configuration of the elastic rod, the set occupied in $\mathbb{R}^3$ by its body $\mathcal{B} \subset \mathbb{R}^3$ is described by

$$\mathcal{B} = \{X(S, \xi_2, \xi_3) = \boldsymbol{\varphi}(S) + \xi_2 \boldsymbol{t}_2(S) + \xi_3 \boldsymbol{t}_3(S) \in \mathbb{R}^3 \,|\, (S, \xi_2, \xi_3) \in [0, L] \times A\},$$

where $[0, L] \times A = \mathcal{R} \in \mathbb{R}^3$ is the reference body, A is the cross section area, L its reference length and $\boldsymbol{t}_2(S)$, $\boldsymbol{t}_3(S)$ are mutually orthonormal vectors lying in the rod cross section plane at $\boldsymbol{\varphi}(S)$. Hence, the rod is fully described by the curve of centroids $\boldsymbol{\varphi}(S)$ and the orientation of its cross sections, defined by the orthonormal frame $\boldsymbol{t}_i$, $i = 1, 2, 3$,

$$\boldsymbol{t}_i = \boldsymbol{\Lambda} \mathbf{e}_i, \quad \boldsymbol{\Lambda} \in \mathrm{SO}(3),$$

attached to each point of the curve of centroids, where $\boldsymbol{t}_1(S)$ is normal to the plane cross section at $\boldsymbol{\varphi}(S)$, see figure 6.1. The configuration space $\mathcal{C}$ of the elastic rod, letting the normal to the cross section be $\boldsymbol{t}_1 = \boldsymbol{\Lambda} \mathbf{e}_1$, is given by the set of functions

$$\mathcal{C} = \{(\boldsymbol{\varphi}, \boldsymbol{\Lambda}) \,:\, S \in [0, L] \to \mathbb{R}^3 \times \mathrm{SO}(3) \,|\, \langle \boldsymbol{\varphi}'(S), \boldsymbol{\Lambda} \mathbf{e}_1 \rangle > 0\} = \mathbb{R}^3 \times \mathrm{SO}(3). \quad (6.1)$$

As reference configuration, $(\boldsymbol{\varphi_r}, \boldsymbol{\Lambda_r}) \in \mathcal{C}$ we assume that the rod is aligned along the spatial basis axis $\mathbf{e}_1$ such that

$$\boldsymbol{\varphi_r}(S) = S\mathbf{e}_1, \quad \boldsymbol{\Lambda_r}(S) = \mathbb{1},$$

where $\mathbb{1}$ is the 3×3 identity matrix [21] (letting the rod reference configuration be aligned along $\mathbf{e}_1$ instead of $\mathbf{e}_3$).

143
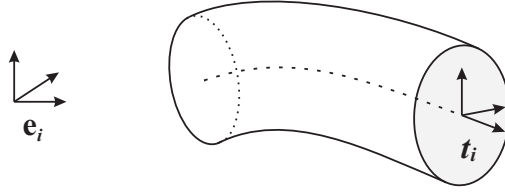
Figure 6.1: The body frame $\boldsymbol{t}_i(S)$, $i = 1,\ldots,3$, relative to the spatial frame for a given rod configuration.

Following the notation by Simo et al. [23], the *material* coordinate vectors given in material basis $\boldsymbol{t}_i$ will be denoted by upper-case letters, while lower case letters are used to denote the vectors in the *spatial* basis $\mathbf{e}_i$. Let $\boldsymbol{W}$ be the body angular velocity, $\boldsymbol{\Omega}$ be the bending and torsional strain in body frame. Hence, the spatial vectors will be related to their material vectors by the expression

$$\boldsymbol{\omega} = \boldsymbol{\Lambda}\boldsymbol{\Omega}, \quad \mathbf{w} = \boldsymbol{\Lambda}\boldsymbol{W}.$$

This will give us the kinematics for the orientation of the cross sections along the line of centroids $\boldsymbol{\varphi}(S,t)$, $(S,t) \in [0, L] \times \mathbb{R}_+$,

$$\partial_S \boldsymbol{\Lambda}(S,t) = \widehat{\boldsymbol{\omega}}\boldsymbol{\Lambda} = \boldsymbol{\Lambda}\widehat{\boldsymbol{\Omega}}, \tag{6.2}$$

$$\partial_t \boldsymbol{\Lambda}(S,t) = \widehat{\mathbf{w}}\boldsymbol{\Lambda} = \boldsymbol{\Lambda}\widehat{\boldsymbol{W}}, \tag{6.3}$$

where the hat map $\widehat{} : \mathbb{R}^3 \to \mathfrak{so}(3)$, sends the axial vector $\boldsymbol{v}$ to its associated skew-symmetric matrix $\widehat{\boldsymbol{v}}$, i.e.

$$\boldsymbol{v} = \begin{bmatrix} v_1 \\ v_2 \\ v_3 \end{bmatrix}, \quad \widehat{\boldsymbol{v}} = \begin{bmatrix} 0 & -v_3 & v_2 \\ v_3 & 0 & -v_1 \\ -v_2 & v_1 & 0 \end{bmatrix}.$$

The assumption of an hyperelastic material behavior, corresponds to allowing for a bilinear quadratic energy function $\boldsymbol{\Psi}(\boldsymbol{\gamma}, \boldsymbol{\omega})$,

$$\boldsymbol{\Psi}(\boldsymbol{\gamma}, \boldsymbol{\omega}) = \frac{1}{2} \left[\langle \boldsymbol{\gamma}, \boldsymbol{D}_N \boldsymbol{\gamma} \rangle + \langle \boldsymbol{\omega}, \boldsymbol{D}_M \boldsymbol{\omega} \rangle \right],$$

$$\boldsymbol{D}_N = \boldsymbol{\Lambda} \boldsymbol{C}_N \boldsymbol{\Lambda}^T, \quad \boldsymbol{D}_M = \boldsymbol{\Lambda} \boldsymbol{C}_M \boldsymbol{\Lambda}^T, \tag{6.4}$$

and

$$\boldsymbol{C}_N = \mathrm{diag}([EA, GA_1, GA_2]), \quad \boldsymbol{C}_M = \mathrm{diag}([GJ, EI_1, EI_2]), \tag{6.5}$$

where

$$\boldsymbol{\gamma} = \partial_S \boldsymbol{\varphi}(S,t) - \boldsymbol{t}_1 = \partial_S \boldsymbol{\varphi}(S,t) - \boldsymbol{\Lambda}(S,t)\mathbf{e}_1, \tag{6.6}$$

is the strain measure for extension and shearing, and $\boldsymbol{\omega}$ gives the measure for twisting and bending.

The constants E and G are interpreted as the Young's modulus and the shear modulus, A is the cross-sectional area of the rod, A_2 and A_3 are the effective shear areas, I_2 and I_3 the polar moments of inertia of the cross section plane relative to the principal axes, and J is the Saint Venant torsional modulus.

The internal stress resultant $\boldsymbol{n}$ and stress couple $\boldsymbol{m}$ are obtained by differentiation from the bilinear quadratic energy function $\boldsymbol{\Psi}(\boldsymbol{\gamma}, \boldsymbol{\omega})$,

$$n = \frac{\partial}{\partial \boldsymbol{\gamma}} \boldsymbol{\Psi} = \boldsymbol{D}_N \boldsymbol{\gamma}, \tag{6.7}$$

$$m = \frac{\partial}{\partial \boldsymbol{\omega}} \boldsymbol{\Psi} = \boldsymbol{D}_M \boldsymbol{\omega}. \tag{6.8}$$

Stress forces in material form are given in upper-case letters,

$$\boldsymbol{N} = \boldsymbol{\Lambda}^T \boldsymbol{n} = \boldsymbol{C}_N \boldsymbol{\Gamma}, \qquad \boldsymbol{\Gamma} = \boldsymbol{\Lambda}^T \boldsymbol{\gamma} = \boldsymbol{\Lambda}^T \partial_S \boldsymbol{\varphi} - \mathbf{e}_1,$$
$$\boldsymbol{M} = \boldsymbol{\Lambda}^T \boldsymbol{m} = \boldsymbol{C}_M \boldsymbol{\Omega}.$$

The spatial form of the local, linear and angular, momentum balance equations are written, see e.g. [21, 24],

$$\rho_A \partial_{tt} \boldsymbol{\varphi} = \partial_S \boldsymbol{n} + \tilde{\boldsymbol{n}}, \tag{6.9}$$
$$\boldsymbol{I}_\rho \partial_t \mathbf{w} + \mathbf{w} \times (\boldsymbol{I}_\rho \mathbf{w}) = \partial_S \boldsymbol{m} + (\partial_S \boldsymbol{\varphi}) \times \boldsymbol{n} + \tilde{\boldsymbol{m}}, \tag{6.10}$$

for $(\boldsymbol{\varphi}(S,t), \boldsymbol{\Lambda}(S,t)) \in \mathcal{C}$ and external forces $\tilde{\boldsymbol{n}}, \tilde{\boldsymbol{m}}$. Here $\rho_A(S)$ is the mass per unit length of the rod in reference length, and $\boldsymbol{I}_\rho(S,t)$ is the time dependent inertia tensor in spatial basis

$$\boldsymbol{I}_\rho = \boldsymbol{\Lambda} \boldsymbol{J}_\rho \boldsymbol{\Lambda}^T, \quad \boldsymbol{J}_\rho = \mathrm{diag}([J_1, J_2, J_3]), \tag{6.11}$$

where $\boldsymbol{J}_\rho$ is the constant inertia tensor for the cross section in the reference configuration.

In the absence of external forces $\tilde{\boldsymbol{n}}$ and $\tilde{\boldsymbol{m}}$, we assume pure displacement boundary conditions, such that $\boldsymbol{\varphi}$ and $\boldsymbol{\Lambda}$ are described at the boundaries $S = 0$ and $S = L$. Then the total energy E (Hamiltonian) [22, 11] of the problem (6.9)–(6.10) is given by

$$E = T + U = \frac{1}{2} \int_0^L \langle \dot{\boldsymbol{\varphi}}, \rho_A \dot{\boldsymbol{\varphi}} \rangle + \langle \mathbf{w}, \boldsymbol{I}_\rho \mathbf{w} \rangle \, dS + \frac{1}{2} \int_0^L \langle \boldsymbol{\gamma}, \boldsymbol{D}_N \boldsymbol{\gamma} \rangle + \langle \boldsymbol{\omega}, \boldsymbol{D}_M \boldsymbol{\omega} \rangle \, dS, \tag{6.12}$$

where the first integral in the sum is the kinetic energy T and the second is the potential energy U.

145

6.2.2 Quaternions

We here review briefly the main properties of quaternions and introduce some notations that will be used throughout this paper, more information on this subject is found in e.g. [20]. The quaternions,

$$\mathbb{H} := \{\mathbb{q} = (q_0, \boldsymbol{q}) \in \mathbb{R} \times \mathbb{R}^3,\ \boldsymbol{q} = (q_1, q_2, q_3)^T\} \cong \mathbb{R}^4,$$

is a strictly skew field [3]. Addition and multiplication of two quaternions, $\mathbb{p} = (p_0, \boldsymbol{p})$, $\mathbb{q} = (q_0, \boldsymbol{q}) \in \mathbb{H}$, are defined by

$$\mathbb{p} + \mathbb{q} = (p_0 + q_0, \boldsymbol{p} + \boldsymbol{q})$$

and

$$\mathbb{p}\mathbb{q} = (p_0 q_0 - \boldsymbol{p}^T \boldsymbol{q}, p_0 \boldsymbol{q} + q_0 \boldsymbol{p} + \boldsymbol{p} \times \boldsymbol{q}), \tag{6.13}$$

respectively. For $\mathbb{q} \neq (0, \boldsymbol{0})$ there exist an inverse

$$\mathbb{q}^{-1} = \mathbb{q}^c / \|\mathbb{q}\|^2, \quad \|\mathbb{q}\| = \sqrt{q_0^2 + \|\boldsymbol{q}\|_2^2},$$

where $\mathbb{q}^c = (q_0, -\boldsymbol{q})$ is the conjugate of $\mathbb{q}$, such that $\mathbb{q}\mathbb{q}^{-1} = \mathbb{q}^{-1}\mathbb{q} = \mathbb{e} = (1, \boldsymbol{0})$. In the sequel we will consider $\mathbb{q} \in \mathbb{H}$ as a vector $\mathbb{q} = (q_0, q_1, q_2, q_3)^T \in \mathbb{R}^4$. The multiplication rule (6.13) can then be expressed by means of a matrix-vector product in $\mathbb{R}^4$. Namely, $\mathbb{p}\mathbb{q} = L(\mathbb{p})\mathbb{q} = R(\mathbb{q})\mathbb{p}$, where

$$L(\mathbb{p}) = \begin{bmatrix} p_0 & -\boldsymbol{p}^T \\ \boldsymbol{p} & (p_0 \mathbb{1} + \widehat{\boldsymbol{p}}) \end{bmatrix}, \quad R(\mathbb{q}) = \begin{bmatrix} q_0 & -\boldsymbol{q}^T \\ \boldsymbol{q} & (q_0 \mathbb{1} - \widehat{\boldsymbol{q}}) \end{bmatrix} \tag{6.14}$$

and $\mathbb{1}$ is the 3×3 identity matrix. Note that $R(\mathbb{q})$ and $L(\mathbb{p})$ commutes, i.e. $R(\mathbb{q})L(\mathbb{p}) = L(\mathbb{p})R(\mathbb{q})$.

Three-dimensional rotations in space can be represented by unit quaternions, sometimes referred to as Euler parameters,

$$\mathbb{S}^3 = \{\mathbb{q} \in \mathbb{H} \,|\, \|\mathbb{q}\| = 1\}.$$

$\mathbb{S}^3$ with the quaternion product is a Lie group, and $\mathbb{q}^{-1} = \mathbb{q}^c$ while $\mathbb{e} = (1, \boldsymbol{0})$ is the identity. There is a (surjective 2 : 1) group homomorphism (the Euler-Rodriguez map) $\mathcal{E} : \mathbb{S}^3 \to SO(3)$, defined by

$$\mathcal{E}(\mathbb{q}) = \mathbb{1} + 2q_0 \widehat{\boldsymbol{q}} + 2\widehat{\boldsymbol{q}}^2,$$

and therefore $\mathbb{S}^3$ is a double-covering of $SO(3)$. The Euler-Rodriguez map can be explicitly written as

$$\mathcal{E}(\mathbb{q}) = \begin{bmatrix} 1 - 2(q_2^2 + q_3^2) & 2(q_1 q_2 - q_0 q_3) & 2(q_0 q_2 + q_1 q_3) \\ 2(q_0 q_3 + q_1 q_2) & 1 - 2(q_1^2 + q_3^2) & 2(q_2 q_3 - q_0 q_1) \\ 2(q_1 q_3 - q_0 q_2) & 2(q_0 q_1 + q_2 q_3) & 1 - 2(q_1^2 + q_2^2) \end{bmatrix}. \tag{6.15}$$

A rotation in $\mathbb{R}^3$,

$$\mathbf{w} = Q\mathbf{v}, \quad Q \in SO(3), \quad \mathbf{v}, \mathbf{w} \in \mathbb{R}^3,$$

can, for some $\mathbb{q} \in \mathbb{S}^3$, be expressed in quaternionic form as

$$W = L(\mathbb{q})R(\mathbb{q}^c)V = R(\mathbb{q}^c)L(\mathbb{q})V, \quad V = (0, \mathbf{v}),\ W = (0, \mathbf{w}) \in \mathbb{H}_{\mathcal{P}}, \quad (6.16)$$

where $\mathbb{H}_{\mathcal{P}} = \{\mathbb{q} \in \mathbb{H} \,|\, q_0 = 0\} \cong \mathbb{R}^3$ is the set of so called pure quaternions. It also follows from straightforward computations that

$$L(\mathbb{q})R(\mathbb{q}^c) = R(\mathbb{q}^c)L(\mathbb{q}) = \begin{bmatrix} 1 & \mathbf{0}^T \\ \mathbf{0} & \mathcal{E}(\mathbb{q}) \end{bmatrix}, \quad \mathbf{0} = (0,0,0)^T \in \mathbb{R}^3.$$

It is also evident that $\forall\, \mathbb{q} \in \mathbb{S}^3$, $L(\mathbb{q}), R(\mathbb{q}) \in O(4)$ are orthogonal matrices, such that $L(\mathbb{q})L(\mathbb{q})^T = L(\mathbb{q})L(\mathbb{q}^c) = \mathbb{1}_{4\times4}$, $R(\mathbb{q})R(\mathbb{q})^T = R(\mathbb{q})R(\mathbb{q}^c) = \mathbb{1}_{4\times4}$.

6.2.2.1 The Lie algebra $\mathfrak{s}^3$

If $\mathbb{q} \in \mathbb{S}^3$, it follows from $\mathbb{q}\mathbb{q}^c = \mathbb{e}$ that

$$\mathfrak{s}^3 := T_{\mathbb{e}}\mathbb{S}^3 = \mathbb{H}_{\mathcal{P}}.$$

The Lie algebra $\mathfrak{s}^3$, associated to $\mathbb{S}^3$, is equipped with a Lie bracket $[\,\cdot\,,\cdot\,]_{\mathfrak{s}} : \mathfrak{s}^3 \times \mathfrak{s}^3 \to \mathfrak{s}^3$,

$$[\,V\,,W\,]_{\mathfrak{s}} := [L(V)W - L(W)V] = (0, 2\mathbf{v} \times \mathbf{w}) \in \mathfrak{s}^3,$$

where $V = (0, \mathbf{v})$, $W = (0, \mathbf{w}) \in \mathfrak{s}^3$.

The derivative map of $\mathcal{E}$ is $\mathcal{E}_* = T_{\mathbb{e}}\mathcal{E} : \mathfrak{s}^3 \to \mathfrak{so}(3)$ is given by

$$\mathcal{E}_*(V) = 2\widehat{\mathbf{v}}, \quad V = (0, \mathbf{v}) \in \mathfrak{s}^3, \quad (6.17)$$

and it is a Lie algebra isomorphism. Assume now that $\mathbb{q} \in \mathbb{S}^3$ is such that $\mathcal{E}(\mathbb{q}(S,t)) = \mathbf{\Lambda}(S,t)$, then $L(\mathbb{q}^c)\dot{\mathbb{q}} \in \mathfrak{s}^3$, $\mathbf{\Lambda}^T\dot{\mathbf{\Lambda}} \in \mathfrak{so}(3)$ and

$$\mathcal{E}_*(L(\mathbb{q}^c)\dot{\mathbb{q}}) = \mathbf{\Lambda}^T\dot{\mathbf{\Lambda}}. \quad (6.18)$$

Further, it can be shown that

$$\mathcal{E}_*(L(\mathbb{q})R(\mathbb{q}^c)V) = 2\widehat{\mathcal{E}(\mathbb{q})\mathbf{v}} \qquad \forall\, \mathbb{q} \in \mathbb{S}^3,\ V = (0, \mathbf{v}) \in \mathfrak{s}^3, \quad (6.19)$$

and as a consequence of (6.18) and (6.19) the kinematics of the cross sections (6.2) and (6.3) can be formulated in unit quaternions $\mathbb{S}^3$ as

$$\dot{\mathbb{q}} = \frac{1}{2}L(\mathbb{q})W = \frac{1}{2}R(\mathbb{q})\mathbb{w}, \quad \mathbb{q}' = \frac{1}{2}L(\mathbb{q})\Omega = \frac{1}{2}R(\mathbb{q})\omega, \quad (6.20)$$

$$W = 2L(\mathbb{q}^c)\dot{\mathbb{q}}, \quad \Omega = 2L(\mathbb{q}^c)\mathbb{q}', \quad \mathbb{w} = 2R(\mathbb{q}^c)\dot{\mathbb{q}}, \quad \omega = 2R(\mathbb{q}^c)\mathbb{q}', \quad (6.21)$$

where $W = (0, \boldsymbol{W})$, $\mathbb{w} = (0, \mathbf{w})$, $\Omega = (0, \boldsymbol{\Omega})$, $\omega = (0, \boldsymbol{\omega}) \in \mathfrak{s}$.

147

6.2.3 Hamiltonian formulation of the free rigid body

Following [18] we write an Hamiltonian formulation of the free rigid body motion in unit quaternions $\mathbb{S}^3$, see also [5] for constrained formulation of the rigid body in quaternions.

Having in mind the expression for the angular velocity in unit quaternions (6.21), the kinetic energy (total energy) is defined by,

$$L = \frac{1}{2}\langle \mathrm{W}, \widetilde{\boldsymbol{J}}\mathrm{W}\rangle = 2\langle \dot{\mathbb{q}}, L(\mathbb{q})\widetilde{\boldsymbol{J}}L(\mathbb{q}^c)\dot{\mathbb{q}}\rangle,$$

where

$$\widetilde{\boldsymbol{J}} = \begin{bmatrix} \alpha & \mathbf{0}^T \\ \mathbf{0} & \boldsymbol{J} \end{bmatrix}, \quad \alpha \in \mathbb{R}, \tag{6.22}$$

is the constant inertia matrix $\boldsymbol{J} = \mathrm{diag}([J_1, J_2, J_3])$ extended to $\mathbb{R}^{4\times 4}$. From the Legendre transformation one obtains the conjugate momenta

$$\mathbb{p} := \frac{\partial \mathcal{L}}{\partial \dot{\mathbb{q}}} = 4L(\mathbb{q})\widetilde{\boldsymbol{J}}L(\mathbb{q}^c)\dot{\mathbb{q}} \in T_{\mathbb{q}}^*\mathbb{S}^3, \tag{6.23}$$

and the map $T_{\mathbb{q}}\mathbb{S}^3 \to T_{\mathbb{q}}^*\mathbb{S}^3$ (6.23) is invertible for any α. Infact, $\mathbb{q} \in \mathbb{S}^3$ implies $\langle \mathbb{q}, \dot{\mathbb{q}}\rangle = 0$ and $L(\mathbb{q}^c)\dot{\mathbb{q}} \in \mathbb{H}_{\mathcal{P}}$. Consequently, α has no significance when $\mathbb{q} \in \mathbb{S}^3$. Taking $\alpha \neq 0$ we can write the Hamiltonian formulation of the free rigid body

$$\mathbb{p} = \frac{1}{4}L(\mathbb{p})\widetilde{\boldsymbol{J}}L(\mathbb{q}^c)\dot{\mathbb{q}},$$

$$\dot{\mathbb{q}} = \frac{1}{4}L(\mathbb{q})\widetilde{\boldsymbol{J}}^{-1}L(\mathbb{q}^c)\mathbb{p}.$$

This motivates a similar extension of the matrices $\boldsymbol{J}_\rho$ and $\boldsymbol{C}_M$ in the sections that follow.

6.3 Formulation of the Hamiltonian in quaternions

We will obtain the augmented Hamiltonian formulation on the cotangent bundle of $\mathbb{R}^3 \times \mathbb{H}$ with the holonomic constraint $g(\mathbb{q}) := \|\mathbb{q}\|^2 - 1 = 0$, from the augmented Lagrangian

$$\mathcal{L}(\boldsymbol{u}, \boldsymbol{u}_t, \boldsymbol{u}_S) = T - U - \lambda(\|\mathbb{q}\|^2 - 1), \quad \boldsymbol{u} = (\boldsymbol{\varphi}, \mathbb{q})^T \in \mathbb{R}^3 \times \mathbb{H}. \tag{6.24}$$

We extend for convenience the inertia tensor $\boldsymbol{J}_\rho \in \mathbb{R}^{3\times 3}$ to $\widetilde{\boldsymbol{J}}_\rho \in \mathbb{R}^{4\times 4}$, and analogously $\boldsymbol{C}_M \in \mathbb{R}^{3\times 3}$ to $\widetilde{\boldsymbol{C}}_M \in \mathbb{R}^{4\times 4}$ invertible 4×4-matrices, so that the

new Lagrangian becomes regular on $T(\mathbb{R}^3 \times \mathbb{H})$. In particular

$$\widetilde{\boldsymbol{J}}_\rho = \begin{bmatrix} \alpha & \mathbf{0}^T \\ \mathbf{0} & \boldsymbol{J}_\rho \end{bmatrix}, \quad \widetilde{\boldsymbol{C}}_M = \begin{bmatrix} \alpha & \mathbf{0}^T \\ \mathbf{0} & \boldsymbol{C}_M \end{bmatrix}, \quad \alpha \neq 0,$$

and accordingly

$$\widetilde{\boldsymbol{I}}_\rho = L(\mathbb{q})R(\mathbb{q}^c)\widetilde{\boldsymbol{J}}_\rho L(\mathbb{q}^c)R(\mathbb{q}), \quad \widetilde{\boldsymbol{D}}_M = L(\mathbb{q})R(\mathbb{q}^c)\widetilde{\boldsymbol{C}}_M L(\mathbb{q}^c)R(\mathbb{q}). \qquad (6.25)$$

This is convinient for the actual inversion of the Legendre transform when constructing the augmented Hamiltonian and multi-symplectic Hamiltonian, respectively. See [19] for general framework of constrained multi-symplectic theory.

The kinetic- and potential energy density functions, (6.12), are expressed in quaternions by

$$T = \frac{1}{2}\left[\langle \dot{\boldsymbol{\varphi}}, \rho_A \dot{\boldsymbol{\varphi}} \rangle + 4\langle \dot{\mathbb{q}}, R(\mathbb{q})\widetilde{\boldsymbol{I}}_\rho R(\mathbb{q}^c)\dot{\mathbb{q}} \rangle \right], \qquad (6.26)$$

$$U = \frac{1}{2}\left[\langle \boldsymbol{\gamma}, \boldsymbol{D}_N \boldsymbol{\gamma} \rangle + 4\langle \mathbb{q}', R(\mathbb{q})\widetilde{\boldsymbol{D}}_M R(\mathbb{q}^c)\mathbb{q}' \rangle \right], \qquad (6.27)$$

see also [22, 11, 24]. Here w, $\omega \in \mathbb{H}_{\mathcal{P}}$ are defined as in (6.21) and

$$\boldsymbol{\gamma} = \boldsymbol{\varphi}' - \mathcal{E}(\mathbb{q})\mathbf{e}_1.$$

We now introduce the conjugate variables, $\boldsymbol{p}_\varphi$ and $\mathbb{p}$, via the Legendre transform

$$\boldsymbol{p}_\varphi := \frac{\partial \mathcal{L}}{\partial \dot{\boldsymbol{\varphi}}} = \rho_A \dot{\boldsymbol{\varphi}}, \qquad (6.28)$$

$$\mathbb{p} := \frac{\partial \mathcal{L}}{\partial \dot{\mathbb{q}}} = 4L(\mathbb{q})\widetilde{\boldsymbol{J}}_\rho L(\mathbb{q}^c)\dot{\mathbb{q}} = 4R(\mathbb{q})\widetilde{\boldsymbol{I}}_\rho R(\mathbb{q}^c)\dot{\mathbb{q}} \in T^*\mathbb{H}, \qquad (6.29)$$

and finally obtain the augmented Hamiltonian

$$\mathcal{H} = \int_0^L h(\boldsymbol{u}, \boldsymbol{p}, \boldsymbol{u}_S)\, dS, \quad \boldsymbol{p} = (\boldsymbol{p}_\varphi, \mathbb{p}), \qquad (6.30)$$

where h is the energy density function,

$$h(\boldsymbol{u}, \boldsymbol{p}, \boldsymbol{u}_S) = \langle \boldsymbol{p}_\varphi, \dot{\boldsymbol{\varphi}}(\boldsymbol{p}_\varphi) \rangle + \langle \mathbb{p}, \dot{\mathbb{q}}(\mathbb{q}, \mathbb{p}) \rangle - \mathcal{L}(\boldsymbol{u}, \boldsymbol{u}_t(\boldsymbol{u}, \boldsymbol{p}), \boldsymbol{u}_S)$$

$$= \frac{1}{2}\left[\langle \boldsymbol{p}_\varphi, \rho_A^{-1}\boldsymbol{p}_\varphi \rangle + \frac{1}{4}\langle \mathbb{p}, R(\mathbb{q})\widetilde{\boldsymbol{I}}_\rho^{-1} R(\mathbb{q}^c)\mathbb{p} \rangle \right]$$

$$+ \frac{1}{2}\left[\langle \boldsymbol{\gamma}, \boldsymbol{D}_N \boldsymbol{\gamma} \rangle + 4\langle \mathbb{q}', R(\mathbb{q})\widetilde{\boldsymbol{D}}_M R(\mathbb{q}^c)\mathbb{q}' \rangle \right] + \lambda(\|\mathbb{q}\|^2 - 1), \qquad (6.31)$$

and

$$\dot{\boldsymbol{\varphi}}(\boldsymbol{p}_\varphi) = \rho_A^{-1}\boldsymbol{p}_\varphi, \quad \dot{\mathbb{q}}(\mathbb{q},\mathbb{p}) = \frac{1}{4}R(\mathbb{q})\widetilde{\boldsymbol{I}}_\rho^{-1}R(\mathbb{q}^c)\mathbb{p}. \tag{6.32}$$

The abstract form of the equation of motion for the constrained Hamiltonian problem is stated as

$$\partial_t\boldsymbol{x} = \mathcal{J}\frac{\delta\mathcal{H}}{\delta\boldsymbol{x}}, \qquad \mathcal{J} := \begin{bmatrix} 0 & \mathbb{1} \\ -\mathbb{1} & 0 \end{bmatrix} \in \mathbb{R}^{14\times 14}, \tag{6.33}$$

$$g(\boldsymbol{x}) = 0, \qquad g(\boldsymbol{x}) := \|\mathbb{q}\|^2 - 1, \tag{6.34}$$

where $\mathbb{1}$ is the 7×7 identity matrix, $\boldsymbol{x} = (\boldsymbol{u},\boldsymbol{p})^T \in \mathbb{R}^{14}$, $\boldsymbol{u} = (\boldsymbol{\varphi},\mathbb{q})^T \in \mathbb{R}^7$ and $\boldsymbol{p} = (\boldsymbol{p}_\varphi,\mathbb{p})^T \in \mathbb{R}^7$. In other words, a constrained system of partial differential equations

$$\partial_t\boldsymbol{u} = \begin{bmatrix} \dot{\boldsymbol{\varphi}} \\ \dot{\mathbb{q}} \end{bmatrix} = \begin{bmatrix} \rho_A^{-1}\boldsymbol{p}_\varphi \\ (1/4)R(\mathbb{q})\widetilde{\boldsymbol{I}}_\rho^{-1}R(\mathbb{q}^c)\mathbb{p} \end{bmatrix}, \tag{6.35}$$

$$\partial_t\boldsymbol{p} = \begin{bmatrix} \dot{\boldsymbol{p}}_\varphi \\ \dot{\mathbb{p}} \end{bmatrix} = \begin{bmatrix} -\partial h/\partial\boldsymbol{\varphi} + \partial_S(\partial h/\partial\boldsymbol{\varphi}') \\ -\partial h/\partial\mathbb{q} + \partial_S(\partial h/\partial\mathbb{q}') \end{bmatrix}, \tag{6.36}$$

$$0 = \|\mathbb{q}\|^2 - 1. \tag{6.37}$$

Here, the equation for $\boldsymbol{p}_\varphi$ in (6.36) is

$$\dot{\boldsymbol{p}}_\varphi = [\boldsymbol{D}_N,\widehat{\boldsymbol{\omega}}]\,\boldsymbol{\gamma} - \boldsymbol{D}_N\boldsymbol{\gamma}', \tag{6.38}$$

where $[\,\cdot\,,\,\cdot\,]$ is the usual commutator for 3×3-matrices ($[A,B] = AB - BA$),

$$\boldsymbol{\gamma}' = \boldsymbol{\varphi}'' - \widehat{\boldsymbol{\omega}}\mathcal{E}(\mathbb{q})\mathbf{e}_1$$

and

$$\boldsymbol{\omega}(\mathbb{q},\mathbb{q}') = 2(q_0\boldsymbol{q}' - q_0'\boldsymbol{q} + \widehat{\boldsymbol{q}}\boldsymbol{q}') = 2\left[-\boldsymbol{q} \;\; (q_0\mathbb{1} - \widehat{\boldsymbol{q}})\right]\mathbb{q}'.$$

The equation for $\mathbb{p}$, (6.36), becomes

$$\dot{\mathbb{p}} = \frac{1}{4}R(\mathbb{q})L(\mathbb{p})L(\mathbb{q}^c)\widetilde{\boldsymbol{I}}_\rho^{-1}R(\mathbb{q}^c)\mathbb{p} + R(\mathbb{q})\left[L(\boldsymbol{\varphi}') - R(\boldsymbol{\varphi}')\right]\begin{bmatrix} 0 \\ \boldsymbol{D}_N\boldsymbol{\gamma} \end{bmatrix}$$

$$+ 2R(\mathbb{q})\left[L(\omega)\widetilde{\boldsymbol{D}}_M\omega + \widetilde{\boldsymbol{D}}_M\omega'\right] + 2\langle(\mathcal{E}(\mathbb{q}) - \mathbb{1})\boldsymbol{\varphi}',\boldsymbol{D}_N\boldsymbol{\gamma}\rangle\mathbb{q} - 2\lambda\mathbb{q}. \tag{6.39}$$

Detailed calculations for the equations of motions can be found in the appendix 6.5.1.1–6.5.1.2, as well as the solution for the Lagrange multiplier (6.5.2),

$$\lambda = -\langle\omega,\widetilde{\boldsymbol{D}}_M\omega\rangle - \langle(\mathbb{1} - \mathcal{E}(\mathbb{q}))\boldsymbol{\varphi}',\boldsymbol{D}_N\boldsymbol{\gamma}\rangle.$$

Substituting the above expression for λ in (6.39) and multiplying with $(1/2)R(\mathbb{q}^c)$ from the left and using (6.29), one reproduces (6.10) (formulated in quaternions). Equation (6.9) is reproduced from (6.38) by using (6.28).

6.4 Multi-symplectic formulation

6.4.1 Review of multi-symplectic PDEs

A PDE is said to be multi-symplectic if it can be written as a linear system of first order equations of the type

$$M\boldsymbol{z}_t + K\boldsymbol{z}_x = \nabla_{\boldsymbol{z}}\mathcal{S}(\boldsymbol{z}), \tag{6.40}$$

where $\boldsymbol{z} \in \mathbb{R}^d$, M and K are skew-symmetric $d \times d$-matrices and $\mathcal{S} : \mathbb{R}^d \to \mathbb{R}$ is a smooth function, see [8] and [9] for a comprehensive description. Defining the two-forms

$$\omega := \mathrm{d}\boldsymbol{z} \wedge M\mathrm{d}\boldsymbol{z}, \quad \kappa := \mathrm{d}\boldsymbol{z} \wedge K\mathrm{d}\boldsymbol{z}, \tag{6.41}$$

any solution $\mathrm{d}\boldsymbol{z}$, of the variational equation associated with (6.40), will satisfy the multi-symplectic conservation law

$$\partial_t\omega + \partial_x\kappa = 0. \tag{6.42}$$

The equation (6.40) also obeys the local energy and momentum conservation laws, i.e.

$$\partial_t e(z) + \partial_x f(z) = 0, \quad \text{and} \quad \partial_t i(z) + \partial_x g(z) = 0, \tag{6.43}$$

where

$$e(z) = \mathcal{S}(z) - \frac{1}{2}z_x^T K^T z, \quad f(z) = \frac{1}{2}z_t^T K^T z, \tag{6.44}$$

$$g(z) = \mathcal{S}(z) - \frac{1}{2}z_t^T M^T z, \quad i(z) = \frac{1}{2}z_x^T M^T z. \tag{6.45}$$

Integrating the densities $f(z)$ and $i(z)$ over the spatial domain one obtains, for suitable boundary conditions, the global conservative quantities of energy $E(z)$ (6.12) and momentum $I(z)$,

$$E(z) = \int_0^L e(z)\,dx, \quad \text{and} \quad I(z) = \int_0^L i(z)\,dx, \tag{6.46}$$

such that $(d/dt)E(z) = (d/dt)I(z) = 0$.

6.4.2 The multi-symplectic formulation $\mathcal{S}$

We construct the constrained multi-symplectic formulation in quaternions by defining

$$\mathcal{S}(\boldsymbol{u}, \boldsymbol{p}, \boldsymbol{v}) = \langle \boldsymbol{p}, \boldsymbol{u}_t(\boldsymbol{p}) \rangle + \langle \boldsymbol{v}, \boldsymbol{u}_S(\boldsymbol{v}) \rangle - \mathcal{L}(\boldsymbol{u}, \boldsymbol{u}_t(\boldsymbol{p}), \boldsymbol{u}_S(\boldsymbol{v})), \tag{6.47}$$

151

where $\mathcal{L}(\boldsymbol{u}, \boldsymbol{u}_t(\boldsymbol{p}), \boldsymbol{u}_S(\boldsymbol{v}))$ is the Lagrangian (6.24) defined in the previous section, $\boldsymbol{p} = (\boldsymbol{p}_\varphi, \mathbb{p})^T \in \mathbb{R}^7$ are given by the former Legendre transforms (6.28)–(6.29) and $\boldsymbol{v} = (\boldsymbol{v}_\varphi, \mathbb{v})^T \in \mathbb{R}^7$ are the second conjugate variables defined by

$$\boldsymbol{v}_\varphi := \frac{\partial \mathcal{L}}{\partial \boldsymbol{\varphi}'} = -\boldsymbol{D}_N \boldsymbol{\gamma} = -\boldsymbol{n}, \tag{6.48}$$

$$\mathbb{v} := \frac{\partial \mathcal{L}}{\partial \mathbb{q}'} = -4L(\mathbb{q})\widetilde{\boldsymbol{C}}_M L(\mathbb{q}^c)\mathbb{q}' = -4R(\mathbb{q})\widetilde{\boldsymbol{D}}_M R(\mathbb{q}^c)\mathbb{q}' \in T^*\mathbb{H} \tag{6.49}$$

such that

$$\boldsymbol{\varphi}'(\mathbb{q}, \boldsymbol{v}_\varphi) = -\boldsymbol{D}_N^{-1}\boldsymbol{v}_\varphi + \mathcal{E}(\mathbb{q})\mathbf{e}_1, \tag{6.50}$$

$$\mathbb{q}'(\mathbb{q}, \mathbb{v}) = -\frac{1}{4}R(\mathbb{q})\widetilde{\boldsymbol{D}}_M^{-1}R(\mathbb{q}^c)\mathbb{v}. \tag{6.51}$$

We can write the Lagrangian as a function of first and second conjugate variables $\boldsymbol{p}$ and $\boldsymbol{v}$,

$$\mathcal{L}(\boldsymbol{u}, \boldsymbol{u}_t(\boldsymbol{p}), \boldsymbol{u}_S(\boldsymbol{v})) = \frac{1}{2}\left[\langle \boldsymbol{p}_\varphi, \rho_A^{-1}\boldsymbol{p}_\varphi \rangle + \frac{1}{4}\langle \mathbb{p}, R(\mathbb{q})\widetilde{\boldsymbol{I}}_\rho^{-1}R(\mathbb{q}^c)\mathbb{p} \rangle\right]$$
$$-\frac{1}{2}\left[\langle \boldsymbol{v}_\varphi, \boldsymbol{D}_M^{-1}\boldsymbol{v}_\varphi \rangle + \frac{1}{4}\langle \mathbb{v}, R(\mathbb{q})\widetilde{\boldsymbol{D}}_M^{-1}R(\mathbb{q}^c)\mathbb{v} \rangle\right]$$
$$-\lambda(\|\mathbb{q}\|^2 - 1), \tag{6.52}$$

and consequently

$$\mathcal{S}(\boldsymbol{u}, \boldsymbol{p}, \boldsymbol{v}) = \frac{1}{2}\left[\langle \boldsymbol{p}_\varphi, \rho_A^{-1}\boldsymbol{p}_\varphi \rangle + \frac{1}{4}\langle \mathbb{p}, R(\mathbb{q})\widetilde{\boldsymbol{I}}_\rho^{-1}R(\mathbb{q}^c)\mathbb{p} \rangle\right]$$
$$-\frac{1}{2}\left[\langle \boldsymbol{v}_\varphi, \boldsymbol{D}_N^{-1}\boldsymbol{v}_\varphi - 2\mathcal{E}(\mathbb{q})\mathbf{e}_1 \rangle + \frac{1}{4}\langle \mathbb{v}, R(\mathbb{q})\widetilde{\boldsymbol{D}}_M^{-1}R(\mathbb{q}^c)\mathbb{v} \rangle\right]$$
$$+\lambda(\|\mathbb{q}\|^2 - 1). \tag{6.53}$$

Hence, the equations of motion are

$$\frac{\partial \mathcal{S}}{\partial \boldsymbol{u}} = -\partial_t \boldsymbol{p} - \partial_S \boldsymbol{v}, \tag{6.54}$$

$$\frac{\partial \mathcal{S}}{\partial \boldsymbol{p}} = \partial_t \boldsymbol{u}, \tag{6.55}$$

$$\frac{\partial \mathcal{S}}{\partial \boldsymbol{v}} = \partial_S \boldsymbol{u}, \tag{6.56}$$

$$0 = \|\mathbb{q}\|^2 - 1. \tag{6.57}$$

Let $\boldsymbol{z} = (\boldsymbol{u}, \boldsymbol{p}, \boldsymbol{v}, \lambda)^T \in \mathbb{R}^{22}$, then (6.54)–(6.57) can be written in the general multi-symplectic form (6.40) where

$$
M = \begin{bmatrix} 0 & -\mathbb{1} & 0 & 0 \\ \mathbb{1} & 0 & 0 & 0 \\ 0 & 0 & 0 & 0 \\ 0 & 0 & 0 & 0 \end{bmatrix}, \quad K = \begin{bmatrix} 0 & 0 & -\mathbb{1} & 0 \\ 0 & 0 & 0 & 0 \\ \mathbb{1} & 0 & 0 & 0 \\ 0 & 0 & 0 & 0 \end{bmatrix} \in \mathbb{R}^{22 \times 22},
$$

and $\mathbb{1}$ is the 7×7 identity matrix. The partial derivatives of S with respect to $\boldsymbol{\varphi}$ and $\mathbb{q}$ (6.54), respectively, are:

$$
\frac{\partial \mathcal{S}}{\partial \boldsymbol{\varphi}} = 0, \tag{6.58}
$$

and

$$
\begin{aligned}
\frac{\partial \mathcal{S}}{\partial \mathbb{q}} = {}&- \frac{1}{4} R(\mathbb{q}) L(\mathbb{p}) L(\mathbb{q}^c) \widetilde{\boldsymbol{I}}_\rho^{-1} R(\mathbb{q}^c) \mathbb{p} + \frac{1}{4} R(\mathbb{q}) L(\mathbb{v}) L(\mathbb{q}^c) \widetilde{\boldsymbol{D}}_M^{-1} R(\mathbb{q}^c) \mathbb{v} \\
&+ R(\mathbb{q}) \left[L(\boldsymbol{v}_\varphi) - R(\boldsymbol{v}_\varphi) \right] \begin{bmatrix} 0 \\ \boldsymbol{D}_N^{-1} \boldsymbol{v}_\varphi - \mathcal{E}(\mathbb{q}) \mathbf{e}_1 \end{bmatrix} \\
&+ 2 \langle (\mathcal{E}(\mathbb{q}) - \mathbb{1}) \boldsymbol{v}_\varphi, \boldsymbol{D}_N^{-1} \boldsymbol{v}_\varphi - \mathcal{E}(\mathbb{q}) \mathbf{e}_1 \rangle \mathbb{q} + 2\lambda \mathbb{q}.
\end{aligned} \tag{6.59}
$$

Equations (6.55) and (6.56) are given by (6.32) and (6.50)–(6.51), respectively. Differentiating the constraint $g(\mathbb{q}) = 0$ twice, see appendix 6.5.3.1, yields

$$
\lambda = - \langle (\mathcal{E}(\mathbb{q}) - \mathbb{1}) \boldsymbol{v}_\varphi, \boldsymbol{D}_N^{-1} \boldsymbol{v}_\varphi - \mathcal{E}(\mathbb{q}) \mathbf{e}_1 \rangle.
$$

Analogously to the Hamiltonian case, by a similar procedure as the one in the end of section 6.3, one can verify that the multi-symplectic formulation is reformulation of the original equations (6.9)–(6.10) in quaternions.

6.5 Appendix

6.5.1 Equations of motions: The Hamiltonian formulation

Detailed calculations for the variational derivative $\delta\mathcal{H}/\delta\boldsymbol{u}$ (6.33)

$$
\frac{\delta\mathcal{H}}{\delta\boldsymbol{\varphi}} = \frac{\partial h}{\partial\boldsymbol{\varphi}} - \partial_S \frac{\partial h}{\partial\boldsymbol{\varphi}'}, \qquad \text{and} \qquad \frac{\delta\mathcal{H}}{\delta\mathbb{q}} = \frac{\partial h}{\partial\mathbb{q}} - \partial_S \frac{\partial h}{\partial\mathbb{q}'}. \tag{6.60}
$$

6.5.1.1 Variational derivative with respect to $\delta\boldsymbol{\varphi}$

Straight forward computations give the second term in first equation of (6.60),

$$
\frac{\partial h}{\partial\boldsymbol{\varphi}'} = \frac{\partial}{\partial\boldsymbol{\varphi}'} \left[\frac{1}{2} \langle \boldsymbol{\gamma}, \boldsymbol{D}_N \boldsymbol{\gamma} \rangle \right] = \boldsymbol{D}_N \boldsymbol{\gamma} = \boldsymbol{n}. \tag{6.61}
$$

Since $\boldsymbol{\gamma} = \boldsymbol{\varphi}' - \mathcal{E}(\mathbb{q})\mathbf{e}_1$, we can compute the second term in the first equation (6.60)

$$\partial_S \frac{\partial h}{\partial \boldsymbol{\varphi}'} = \boldsymbol{D}_N' \boldsymbol{\gamma} + \boldsymbol{D}_N \boldsymbol{\gamma}' = [\widehat{\boldsymbol{\omega}}, \boldsymbol{D}_N]\,\boldsymbol{\gamma} + \boldsymbol{D}_N \boldsymbol{\gamma}' \tag{6.62}$$

where $[\,\cdot\,,\,\cdot\,]$ denotes the usual commutator for 3×3-matrices, $\boldsymbol{\gamma}' = \boldsymbol{\varphi}'' - \widehat{\boldsymbol{\omega}}\mathcal{E}(\mathbb{q})\mathbf{e}_1$ and

$$\boldsymbol{\omega}(\mathbb{q}, \mathbb{q}') = 2(q_0\boldsymbol{q}' - q_0'\boldsymbol{q} + \widehat{\boldsymbol{q}}\boldsymbol{q}') = 2 \begin{bmatrix} q_0 q_1' - q_0' q_1 - q_3 q_2' + q_2 q_3' \\ q_0 q_2' - q_0' q_2 - q_1 q_3' + q_3 q_1' \\ q_0 q_3' - q_0' q_3 - q_2 q_1' + q_1 q_2' \end{bmatrix}.$$

Finally $\partial h/\partial\boldsymbol{\varphi} = 0$, and the first equation of (6.60) follows

$$\frac{\delta\mathcal{H}}{\delta\boldsymbol{\varphi}} = [\widehat{\boldsymbol{\omega}}, \boldsymbol{D}_N]\,\boldsymbol{\gamma} + \boldsymbol{D}_N \boldsymbol{\gamma}'. \tag{6.63}$$

6.5.1.2   Variational derivative with respect to $\delta\mathbb{q}$

Differentiating the terms of the Hamiltonian density function h (6.31) with respect to $\mathbb{q}$. We have

$$\frac{\partial}{\partial\mathbb{q}}\langle \mathbb{p}, R(\mathbb{q})\widetilde{\boldsymbol{I}}_\rho^{-1} R(\mathbb{q}^c)\mathbb{p}\rangle = \frac{\partial}{\partial\mathbb{q}}\langle L(\mathbb{q}^c)\mathbb{p}, \widetilde{\boldsymbol{J}}_\rho^{-1} L(\mathbb{q}^c)\mathbb{p}\rangle$$

$$= 2\left(\frac{\partial(L(\mathbb{q}^c)\mathbb{p})}{\partial\mathbb{q}}\right)^T \widetilde{\boldsymbol{J}}_\rho^{-1} L(\mathbb{q}^c)\mathbb{p}$$

$$= -2R(\mathbb{q})L(\mathbb{p})L(\mathbb{q}^c)\widetilde{\boldsymbol{I}}_\rho^{-1} R(\mathbb{q}^c)\mathbb{p}, \tag{6.64}$$

and similarly

$$\frac{\partial}{\partial\mathbb{q}}\langle \mathbb{q}', R(\mathbb{q})\widetilde{\boldsymbol{D}}_M R(\mathbb{q}^c)\mathbb{q}'\rangle = -2R(\mathbb{q})L(\mathbb{q}')L(\mathbb{q}^c)\widetilde{\boldsymbol{D}}_M R(\mathbb{q}^c)\mathbb{q}'$$

$$= -\frac{1}{2}R(\mathbb{q})L(\omega)\widetilde{\boldsymbol{D}}_M \omega. \tag{6.65}$$

Further, differentiation of $\langle\boldsymbol{\gamma}, \widetilde{\boldsymbol{D}}_N\boldsymbol{\gamma}\rangle = \langle\boldsymbol{\Gamma}, \widetilde{\boldsymbol{C}}_N\boldsymbol{\Gamma}\rangle$, where $\boldsymbol{\Gamma} = \mathcal{E}(\mathbb{q})^T\boldsymbol{\varphi}' - \mathbf{e}_1$, with respect to $\mathbb{q}$ gives

$$\frac{\partial}{\partial\mathbb{q}}\langle\boldsymbol{\gamma}, \widetilde{\boldsymbol{D}}_N\boldsymbol{\gamma}\rangle = 2 \begin{bmatrix} \mathbf{0} & \left(\dfrac{\partial\boldsymbol{\Gamma}}{\partial\mathbb{q}}\right)^T \end{bmatrix} \begin{bmatrix} 0 \\ C_N\boldsymbol{\Gamma} \end{bmatrix}$$

$$= 4 \begin{bmatrix} 0 & -(\boldsymbol{q}\times\boldsymbol{\varphi}')^T \\ \mathbf{0} & \widehat{\boldsymbol{q}\times\boldsymbol{\varphi}'} - q_0\widehat{\boldsymbol{\varphi}'} - \widehat{\boldsymbol{\varphi}'}\widehat{\boldsymbol{q}} \end{bmatrix} \begin{bmatrix} 0 \\ C_N\boldsymbol{\Gamma} \end{bmatrix}. \tag{6.66}$$

The above expression (6.66) can be simplified and written in a more convenient form

$$4\begin{bmatrix} 0 & -\widehat{(\boldsymbol{q}\times\boldsymbol{\varphi}')^T} \\ \boldsymbol{0} & \widehat{\boldsymbol{q}\times\boldsymbol{\varphi}'}-q_0\widehat{\boldsymbol{\varphi}'}-\widehat{\boldsymbol{\varphi}'\boldsymbol{q}} \end{bmatrix}\begin{bmatrix} 0 \\ C_N\boldsymbol{\Gamma} \end{bmatrix}=$$
$$2R(\mathbb{q})\left[R(\varphi')-L(\varphi')\right]\begin{bmatrix} 0 \\ \boldsymbol{D}_N\boldsymbol{\gamma} \end{bmatrix}+4\langle(\mathbb{1}-\mathcal{E}(\mathbb{q}))\boldsymbol{\varphi}',\boldsymbol{D}_N\boldsymbol{\gamma}\rangle\mathbb{q},\quad(6.67)$$

where $\varphi'=(0,\boldsymbol{\varphi}')\in\mathbb{H}_{\mathcal{P}}$.

To find an explicit expression for the second term $\partial_S(\partial h/\partial\mathbb{q}')$ (6.60) we first have

$$\partial_S\left(L(\mathbb{q})R(\mathbb{q}^c)\right)=L(\mathbb{q}')R(\mathbb{q}^c)+L(\mathbb{q})R((\mathbb{q}^c)'),$$

and, since $L(\mathbb{q})L(\mathbb{q}^c)=R(\mathbb{q})R(\mathbb{q}^c)=\mathbb{1}_{4\times4}$, one has $L(\mathbb{q}')L(\mathbb{q}^c)=-L(\mathbb{q})L((\mathbb{q}^c)')$, $R(\mathbb{q}')R(\mathbb{q}^c)=-R(\mathbb{q})R((\mathbb{q}^c)')$. So, from $\omega=2R(\mathbb{q}^c)\mathbb{q}'$, it follows

$$\partial_S\left(L(\mathbb{q})R(\mathbb{q}^c)\right)=\frac{1}{2}\left[L(\omega)-R(\omega)\right]L(\mathbb{q})R(\mathbb{q}^c).$$

The latter identity yields

$$\partial_S\widetilde{\boldsymbol{D}}_M=\frac{1}{2}\left[(L(\omega)-R(\omega)),\widetilde{\boldsymbol{D}}_M\right],\quad(6.68)$$

where $[\cdot,\cdot]$ is the usual commutator for 4×4-matrices. Thus, we have

$$\frac{\partial h}{\partial\mathbb{q}'}=\frac{\partial}{\partial\mathbb{q}'}\left[2\langle\mathbb{q}',R(\mathbb{q})\widetilde{\boldsymbol{D}}_MR(\mathbb{q}^c)\mathbb{q}'\rangle\right]=4R(\mathbb{q})\widetilde{\boldsymbol{D}}_MR(\mathbb{q}^c)\mathbb{q}'=2R(\mathbb{q})\widetilde{\boldsymbol{D}}_M\omega,$$
$$(6.69)$$

and using the identity (6.68)

$$\partial_S\frac{\partial h}{\partial\mathbb{q}'}=2R(\mathbb{q}')\widetilde{\boldsymbol{D}}_M\omega+R(\mathbb{q})\left[(L(\omega)-R(\omega)),\widetilde{\boldsymbol{D}}_M\right]\omega+2R(\mathbb{q})\widetilde{\boldsymbol{D}}_M\omega'$$
$$=R(\mathbb{q})\left(L(\omega)\widetilde{\boldsymbol{D}}_M\omega+2\widetilde{\boldsymbol{D}}_M\omega'\right).\quad(6.70)$$

Finally, with aid from the above results we obtain the equation for $\delta\mathcal{H}/\delta\mathbb{q}=\partial h/\partial\mathbb{q}-\partial_S(\partial h/\partial\mathbb{q}')$ (6.60), where h is the density function (6.31),

$$\frac{\delta\mathcal{H}}{\delta\mathbb{q}}=-\frac{1}{4}R(\mathbb{q})L(\mathbb{p})L(\mathbb{q}^c)\widetilde{\boldsymbol{I}}_\rho^{-1}R(\mathbb{q}^c)\mathbb{p}-2R(\mathbb{q})\left(L(\omega)\widetilde{\boldsymbol{D}}_M\omega+\widetilde{\boldsymbol{D}}_M\omega'\right)+2\lambda\mathbb{q}$$
$$+R(\mathbb{q})\left[R(\varphi')-L(\varphi')\right]\begin{bmatrix} 0 \\ \boldsymbol{D}_N\boldsymbol{\gamma} \end{bmatrix}+2\langle(\mathbb{1}-\mathcal{E}(\mathbb{q}))\boldsymbol{\varphi}',\boldsymbol{D}_N\boldsymbol{\gamma}\rangle\mathbb{q}.\quad(6.71)$$

155

6.5.2   Solution of the Lagrange multiplier λ

Differentiating the constraint $g(\mathbb{q}) := \|\mathbb{q}\|^2 - 1 = 0$ with respect to t, $\partial_t g(\mathbb{q}) = 2\langle \dot{\mathbb{q}}, \mathbb{q} \rangle = 0$, inserting the expression for $\dot{\mathbb{q}} = (1/4)R(\mathbb{q})\widetilde{\boldsymbol{I}}_\rho^{-1}R(\mathbb{q}^c)\mathbb{p}$ (6.32),

$$\partial_t g(\mathbb{q}) = \frac{1}{2}\langle R(\mathbb{q})\widetilde{\boldsymbol{I}}_\rho^{-1}R(\mathbb{q}^c)\mathbb{p}, \mathbb{q}\rangle = \frac{1}{2}\langle \widetilde{\boldsymbol{I}}_\rho^{-1}R(\mathbb{q}^c)\mathbb{p}, \mathbb{e}\rangle = \frac{1}{2}\langle \mathbb{q}, \mathbb{p}\rangle,$$

gives the second constraint

$$\frac{1}{2}\langle \mathbb{q}, \mathbb{p}\rangle = 0. \tag{6.72}$$

Differentiating (6.72) once again,

$$\frac{1}{2}\left[\langle \dot{\mathbb{q}}, \mathbb{p}\rangle + \langle \mathbb{q}, \dot{\mathbb{p}}\rangle\right] = 0,$$

and plugging in the equations for $\dot{\mathbb{p}}$ and $\dot{\mathbb{q}}$,

$$\frac{1}{2}\left[\langle \dot{\mathbb{q}}, \mathbb{p}\rangle + \langle \mathbb{q}, \dot{\mathbb{p}}\rangle\right] = \frac{1}{2}\left[\langle \mathrm{w}, \widetilde{\boldsymbol{I}}_\rho \mathrm{w}\rangle - \langle \mathrm{w}, \widetilde{\boldsymbol{I}}_\rho \mathrm{w}\rangle\right] - \langle \omega, \widetilde{\boldsymbol{D}}_M \omega\rangle - \langle (\mathbb{1}-\mathcal{E}(\mathbb{q}))\boldsymbol{\varphi}', \boldsymbol{D}_N \boldsymbol{\gamma}\rangle - \lambda$$

gives the solution for the Lagrange multiplier λ

$$\lambda = -\langle \omega, \widetilde{\boldsymbol{D}}_M \omega\rangle - \langle (\mathbb{1} - \mathcal{E}(\mathbb{q}))\boldsymbol{\varphi}', \boldsymbol{D}_N \boldsymbol{\gamma}\rangle. \tag{6.73}$$

6.5.3   Equations for the rotation $\mathbb{q}$: The multi-symplectic formulation

The calculations are similar as for the Hamiltonian formulation. In particular, note that

$$\langle \boldsymbol{v}_\varphi, \boldsymbol{D}_N^{-1}\boldsymbol{v}_\varphi - 2\mathcal{E}(\mathbb{q})\mathbf{e}_1\rangle = \langle \mathcal{E}(\mathbb{q})^T \boldsymbol{v}_\varphi, \boldsymbol{C}_N^{-1}\mathcal{E}(\mathbb{q})^T \boldsymbol{v}_\varphi - 2\mathbf{e}_1\rangle$$

and

$$\frac{\partial}{\partial \mathbb{q}}\langle \boldsymbol{v}_\varphi, \boldsymbol{D}_N^{-1}\boldsymbol{v}_\varphi - 2\mathcal{E}(\mathbb{q})\mathbf{e}_1\rangle = 2\begin{bmatrix} \mathbf{0} & \left(\dfrac{\partial (\mathcal{E}(\mathbb{q})^T \boldsymbol{v}_\varphi)}{\partial \mathbb{q}}\right)^T \end{bmatrix}\begin{bmatrix} 0 \\ \boldsymbol{C}_N^{-1}\mathcal{E}(\mathbb{q})^T \boldsymbol{v}_\varphi - \mathbf{e}_1 \end{bmatrix}$$

$$= 4\begin{bmatrix} 0 & -(\boldsymbol{q}\times\boldsymbol{v}_\varphi)^T \\ \mathbf{0} & \widehat{\boldsymbol{q}\times\boldsymbol{v}_\varphi} - q_0\widehat{\boldsymbol{v}_\varphi} - \widehat{\boldsymbol{v}_\varphi}\widehat{\boldsymbol{q}} \end{bmatrix}\begin{bmatrix} 0 \\ \boldsymbol{C}_N^{-1}\mathcal{E}(\mathbb{q})^T \boldsymbol{v}_\varphi - \mathbf{e}_1 \end{bmatrix}.$$

Comparing with (6.67) in the Hamiltonian case, we see that the above expression can be rewritten,

$$\frac{\partial}{\partial \mathbb{q}}\langle \boldsymbol{v}_\varphi, \boldsymbol{D}_N^{-1}\boldsymbol{v}_\varphi - 2\mathcal{E}(\mathbb{q})\mathbf{e}_1\rangle = 2R(\mathbb{q})\left[R(\boldsymbol{v}_\varphi) - L(\boldsymbol{v}_\varphi)\right]\begin{bmatrix} 0 \\ \boldsymbol{D}_N^{-1}\boldsymbol{v}_\varphi - \mathcal{E}(\mathbb{q})\mathbf{e}_1 \end{bmatrix}$$

$$+ 4\langle (\mathbb{1} - \mathcal{E}(\mathbb{q}))\boldsymbol{v}_\varphi, \boldsymbol{D}_N^{-1}\boldsymbol{v}_\varphi - \mathcal{E}(\mathbb{q})\mathbf{e}_1\rangle\mathbb{q}.$$

156

6.5.3.1 Solution for the Lagrange multiplier in the multi-symplectic case

Differentiation of the constraint, $g(\mathbb{q}) := \|\mathbb{q}\|^2 - 1 = 0$, in time and space, respectively, gives two hidden constraints

$$\langle \mathbb{p}, \mathbb{q} \rangle = 0, \qquad \langle \mathbb{v}, \mathbb{q} \rangle = 0. \tag{6.74}$$

Differentiating twice yields

$$\begin{aligned}
(\partial_t^2 + \partial_S^2)g(\mathbb{q}) &= \langle \mathbb{q}, \mathbb{v}' + \dot{\mathbb{p}} \rangle + \langle \mathbb{q}', \mathbb{v} \rangle + \langle \dot{\mathbb{q}}, \mathbb{p} \rangle \\
&= \langle (\mathcal{E}(\mathbb{q}) - \mathbb{1})\boldsymbol{v}_\varphi, \boldsymbol{D}_N^{-1}\boldsymbol{v}_\varphi - \mathcal{E}(\mathbb{q})\mathbf{e}_1 \rangle + \lambda = 0. \tag{6.75}
\end{aligned}$$

Bibliography

[1] F. Armero and I. Romero. An objective finite element approximation of the kinematics of geometrically exact rods and its use in the formulation of an energy-momentum conserving scheme in dynamics. *Internat. J. Num. Meth. Engrg.*, 54(12):1683–1716, 2002.

[2] F. Armero and I. Romero. Energy-dissipative momentum-conserving time-stepping algorithms for the dynamics of nonlinear cosserat rods. *Comp. Mech.*, 31:3–26, 2003.

[3] A. Baker. *Matrix groups. An introduction to Lie group theory.* SUMS. Springer-Verlag, 2002.

[4] G. Benettin, A.M. Cherubini, and F. Fassó. A changing-chart symplectic algorithm for rigid bodies and other hamiltonian systems on manifolds. *SIAM J. Sci. Comp.*, 23(4):1189–1203, 2001.

[5] P. Betsch and R. Siebert. Rigid body dynamics in terms of quaternions: Hamiltonian formulation and conserving numerical integration. *Internat. J. Numer. Methods Engrg.*, 79(4):444–473, 2009.

[6] P. Betsch and P. Steinmann. Frame-indifferent beam finite elements based upon the geometrically exact beam theory. *Internat. J. Numer. Methods Engrg.*, 54(12):1775–1788, 2002.

[7] P. Betsch and P. Steinmann. Constrained dynamics of geometrically exact beams. *Comp. Mech.*, 31(1-2):49–59, 2003.

[8] T. J. Bridges. Multi-symplectic structures and wave propagation. *Math. Proc. Cambridge Philos. Soc.*, 121(1):147–190, 1997.

[9] T. J. Bridges and S. Reich. Multi-symplectic integrators: numerical schemes for Hamiltonian PDEs that conserve symplecticity. *Phys. Lett. A*, 284(4-5):184–193, 2001.

[10] J. Frank. Geometric space-time integration of ferromagnetic materials. *Appl. Numer. Math.*, 48(3-4):307–322, 2004.

[11] N. Tarnow J. C Simo and M. Doblare. Non-linear dynamics of three-dimensional rods: Exact energy and momentum conserving algorithms. *Internat. J. Numer. Methods Engrg.*, 38:1431–1473, 1995.

[12] G. A. Jensen, N. Säfström, T. I. Fossen, and T. D. Nguyen. A nonlinear PDE formulation for offshore vessel pipeline installation. *Ocean Engineering*, 2009. To appear.

[13] S. Kehrbaum and J. H. Maddocks. Elastic rods, rigid bodies, quaternions and the last quadrature. *Phil. Trans. R. Soc. A*, 355(1732):2117–2136, 1997.

[14] B. Leimkuhler and S. Reich. Symplectic integration of constrained Hamiltonian systems. *Math. Comp.*, 63(208):589–605, 1994.

[15] Benedict Leimkuhler and Sebastian Reich. *Simulating Hamiltonian dynamics*, volume 14 of *Cambridge Monographs on Applied and Computational Mathematics*. Cambridge University Press, Cambridge, 2004.

[16] S. Leyendecker, P. Betsch, and P. Steinmann. The discrete null space method for the energy-consistent integration of constrained mechanical systems. Part III: Flexible multibody dynamics. *Multibody Syst. Dyn..*, 19:45–72, 2008.

[17] A. E. H. Love. *Mathematical theory of elasticity*. Dover, fourth edition, 1944.

[18] A. J. Maciejewski. Hamiltonian formalism for Euler parameters. *Celestial Mech.*, 37:47–57, 1985.

[19] J. E. Marsden, S. Pekarsky, and S. Shkoller. Variational methods, multi-symplectic geometry and continuum mechanics. *J. Geom. Phys*, 38:253–284, 2001.

[20] J. E. Marsden and T. S. Ratiu. *Introduction to mechanics and symmetry*. Texts in applied mathematics. Springer, 1999.

[21] J. C. Simo. A finite strain beam formulation. The three-dimensional dynamic problem. Part I. *Comput. Methods Appl. Mech. Engrg.*, 49(1):55–70, 1985.

[22] J. C. Simo, J. E. Marsden, and P. S. Krishnaprasad. The Hamiltonian structure of nonlinear elasticity: The material and convective representations of solids, rods, and plates. *Arch. Rat. Mech. Anal.*, 104(2):125–183, 1988.

[23] J. C. Simo and L. Vu-Quoc. A three-dimensional finite-strain rod model. Part II: Computational aspects. *Comput. Methods Appl. Mech. Engrg.*, 58(1):79–116, 1986.

[24] J. C. Simo and L. Vu-Quoc. On the dynamics in space of rods undergoing large motions – a geometrically exact approach. *Comput. Methods Appl. Mech. Engrg.*, 66(2):125–161, 1988.